

Interference Experiment with Slow Neutrons

A Feasibility Study of Lloyd's Mirror
at the Institut Laue-Langevin

Hanno Filter

Dissertation
Technische Universität
Wien

Interference Experiment with Slow Neutrons:

A Feasibility Study of Lloyd's Mirror
at the Institut Laue-Langevin.

Hanno Filter

DISSERTATION

Interference Experiment with Slow Neutrons:

A Feasibility Study of Lloyd's Mirror
at the Institut Laue-Langevin.

Ausgeführt zum Zwecke der Erlangung des akademischen Grads eines Doktors der
Naturwissenschaften unter Leitung von

Univ. Prof. Dr. Hartmut Abele

E141 — Atominstitut

eingereicht an der Technischen Universität Wien
Fakultät für Physik

von

Dipl.-Phys. Hanno Marius Filter

Matrikelnummer 1128460

Keilgasse 8, A-1030 Wien



Kurzfassung

Lloyd's Spiegel wie er von Humphrey Lloyd 1831 beschrieben wurde ist ein vielseitiges optisches Instrument. Heutzutage findet es vor allem in den Gebieten der Unterwasserakustik und der optischen Oberflächenanalyse Verwendung. In dieser Arbeit wird die Machbarkeit einer Umsetzung von Lloyd's Spiegel mit sehr kalten Neutronen untersucht. Aufgrund offener Fragen wie z.B. der scheinbaren Inkompatibilität von Allgemeiner Relativitätstheorie und Quantenmechanik, dem Phänomen der Dunklen Materie und der Dunklen Energie, und der Antimaterie-Materie Asymmetrie, werden neuartige Experimente benötigt, die Einblick geben in bisher nicht untersuchte Parameterbereiche. Eine Umsetzung von Lloyd's Spiegel mit sehr kalten Neutronen könnte einen solchen Einblick eröffnen, wie in Pokotilovski (2011) und in Pokotilovski (2013b) vorgeschlagen. In dieser Arbeit wird das quantenmechanische Verhalten von Neutronen untersucht, die eine Region mit einem vertikal ausgerichteten Spiegel durchqueren, um Bedingungen einer experimentellen Umsetzung abzuleiten. Darauf aufbauend wird eine Simulation des erwarteten Interferogram vorgestellt, um die benötigte Messzeit abzuschätzen. In Übereinstimmung mit den theoretischen Überlegungen wird ein Neutronenoptik Aufbau, wie er am Institut Laue-Langevin umgesetzt wurde und welcher den Neutronenstrahl für das Interferometer aufbereitet, vorgestellt. Abschließend werden Entwicklungen einer orts aufgelösten Detektion von Neutronen mithilfe von Bor-beschichteten CR39 Plättchen präsentiert, wie sie für dieses Experiment benötigt werden.

Abstract

The Lloyd's mirror as described by Humphrey Lloyd in 1831 is a simple but powerful instrument in optical studies. Today's foremost applications are the optical inspection of flat surfaces and as a tool in underwater acoustics. This thesis discusses and investigates the feasibility of an implementation of Lloyd's mirror with very-cold neutrons. Due to current open questions in physics as for example the apparent incompatibility of general relativity and quantum mechanics, the phenomenon of dark energy and dark matter, and matter antimatter asymmetry, novel experimental insights into yet unexplored parameter spaces are needed. Lloyd's mirror realized with matter wave especially very-cold neutrons could offer such new insights as proposed in Pokotilovski (2011) and in Pokotilovski (2013b). In this thesis the quantum mechanical behavior of neutrons that transverse a region in front of a mirror is studied theoretically to infer the requirements of an experimental realization. It is concluded with a simulation of the expected interferogram to estimate the required measurement time. In accordance with the theoretical studies, the results of an experimental realization of the required beam preparation section at the very-cold neutron beam at the PF2 at the Institut Laue-Langevin are presented. Finally, a spatial detection mechanism using boron-based CR39 imaging plates adapted to the needs of this experiment is demonstrated.

Contents

I. Introduction and Neutron Physics	1
1. Introduction	3
2. Selected Open Questions in Physics	7
2.1. Dark Matter	7
2.2. Dark Energy	10
2.3. Matter/Antimatter Asymmetry	12
2.4. Hypothetical Scenarios	12
3. The Neutron	17
3.1. Neutron Characteristics	17
3.2. Neutron Energy Range	18
3.3. Very-Cold Neutrons	19
II. Lloyd's Mirror	27
4. Introduction	29
4.1. A Brief Overview of Interferometry	29
4.2. Motivation of this Thesis	31
5. Theory	33
5.1. Interactions of the Neutron	33
5.2. Matter Wave Dynamics	35
5.3. Kirchhoff Diffraction Formula	36
5.3.1. Fraunhofer-Diffraction: Single Slit	39
5.3.2. Fresnel-Diffraction: Straight Edge	40
5.4. Green's Formalism	42

5.5. Lloyd’s Mirror	44
5.5.1. Plane Wave Reflection	45
5.5.2. Wave Function Using Green’s Function	48
5.6. Phase Shifting Effects	59
5.6.1. Phase Shifts in Interferometry	59
5.6.2. Sensitivity to a Small Shift	61
5.6.3. Systematic Phase Shifting Effects	64
5.6.4. Non-Standard Model Effects	70
5.7. Summary	76
6. Dimensioning and Simulation	79
6.1. Measurement Procedure	80
6.1.1. Theoretical Framework Verification	80
6.1.2. Single-slit Scan with Varying Phase	83
6.2. Measurement Constraints	84
6.2.1. Angular Constraints	85
6.2.2. Spatial Distribution	89
6.2.3. Wavelength Distribution	91
6.2.4. Statistical Constraints	91
6.3. Measurement Estimation	97
6.3.1. Interferogram Simulation	97
6.3.2. Additional Systematic Effects	103
6.4. Summary	107
III. Selected Experiments	109
7. Experimental Setup and First Measurements	111
7.1. Experimental Implementation	112
7.1.1. Very-Cold Neutron Beam at the PF2	115
7.1.2. Angular Preparation	121
7.1.3. Wavelength Selection	122
7.1.4. Expected Intensity in Front of S1	124
7.2. Lloyd’s Interferometer	128
7.2.1. Entrance Slit	129
7.2.2. Main Mirror	130

7.2.3. Monitoring Scheme	131
7.2.4. Background Intensity	133
7.3. Summary	134
8. Spatial Neutron Detection	137
8.1. Spatial Resolving Neutron Detection	137
8.1.1. CR39-based Detector Design	138
8.1.2. Detector Production and New Developments	142
8.2. Radiating CR39 Detectors with Neutrons	145
8.2.1. Lower Limit for Neutron Exposure	145
8.2.2. Upper Limit for Neutron Exposure:	146
8.3. Post-Processing of a CR39 Detector	148
8.3.1. Chemical Treatment	148
8.3.2. Image Capture and Image Processing	148
8.3.3. Track detection	151
8.3.4. Machine Vision Based Detection	152
8.4. Summary	161
IV. Prospects and Conclusion	165
9. Future Prospects	167
9.1. Proposed Implementation at the PF2	167
9.2. Refined Theoretical Model for Lloyd’s Mirror	169
9.3. Probing Physics beyond the Standard Model of Particle Physics	170
9.4. Future Developments	170
9.4.1. CR39-based Detection	171
9.4.2. Detector Coating	171
10. Conclusion	173
Appendices	179
A. Supplemental Information	179
A.1. Collected Figures	179
A.1.1. Optical Lloyd’s Mirror	179
A.1.2. Simulation Fit Residuals	180

Contents

A.1.3. CR39 Example	181
A.1.4. CR39Analyse.m	182
A.2. Neutron Energy Availability	186
A.3. The H18 Beam at the Institut Laue-Langevin	187
A.4. Constants and Calculation Parameter	188
A.5. Beam Parameter Definition	191
A.6. Function Definition	192
A.7. Wave Function of Lloyd’s Mirror in Green’s Formalism	194
A.7.1. Slit and Reflecting Half-Plane — Static	198
A.7.2. Slit and Reflecting Half-Plane — Time-Dependent	207
A.8. Calculation of the Phase Shifts in Lloyd’s Mirror	214
A.8.1. General Phase Shift Calculation	214
A.8.2. Phase Shift due to the Casimir-Effect	215
A.8.3. Phase Shift due to a Magnetic Field	221
B. Thesis Information	229
B.1. Developed Software	229
B.2. Supervised Theses	230
List of Tables	233
List of Figures	235
Acknowledgement	251

Part I.

Introduction and Neutron Physics

1. Introduction

Matter wave diffraction phenomena are at the heart of experimental physics and the theoretical development of quantum mechanics. One of the most prominent examples is the diffraction of a wave at a double-slit setup and the resulting pattern on a viewing screen. The observable interference pattern due to the superposition of a wave originating from each slit was realized experimentally with a variety of different waves, i.e. sound-waves, water-waves, electromagnetic-waves and matter waves. For classical waves this is expected but in the case of particles diffraction it has been a matter of controversy leading to the development of quantum mechanics with the Schrödinger-equation at its center

$$\hat{H}\Psi(\vec{r}, t) = \frac{\hbar}{i} \frac{\partial}{\partial t} \Psi(\vec{r}, t). \quad (1.1)$$

Here \hat{H} is the hermitian Hamiltonian and $\Psi(\vec{r}, t)$ is the wave function which solves this equation. Up until now quantum mechanics is in agreement with all experimental tests and is therefore an excellent and preferable tool¹ to investigate nature to highest accuracy. Quantum mechanics on the dynamical side is joined on the kinematical side by the Standard Model of particle physics. There the three known elementary forces, i.e. weak, strong, and the electromagnetic force, are unified to describe the kinematics of the known elementary particles. Despite the robustness of quantum mechanics and the Standard Model of particle physics they fail to incorporate the fourth known force — gravity. Gravity is successfully modeled with general relativity as a geometry property of space-time. It can account for even the smallest effects from the macroscopic to the astronomic scale. General relativity and its central equations, the Einstein field equations, have been introduced in Einstein (1916). They connect an energy density to the curvature of space-time

$$\mathcal{G}_{\mu\nu} + \Lambda g_{\mu\nu} = \frac{8\pi G}{c^4} \mathcal{T}_{\mu\nu}. \quad (1.2)$$

¹Experimental results that deviate from quantum mechanical predictions and that are not caused by an experimental error, would either hint at a breakdown of the axioms of quantum mechanics or at a not yet considered novel fundamental effect.

1. Introduction

Here $\mathcal{G}_{\mu\nu} = R_{\mu\nu} - \frac{1}{2}Rg_{\mu\nu}$ denotes the Einstein tensor, $\mathcal{T}_{\mu\nu}$ denotes the stress-energy tensor, $g_{\mu\nu}$ is the metric tensor, $R_{\mu\nu}$ is the Ricci tensor, R is the Ricci scalar, G is Newtons gravitational constant, and finally Λ denotes the cosmological constant. Again, the validity of the theory has been checked rigorously for astronomical and macroscopic scales. While both theories asymptotically pass over to classical dynamics and kinematics, no connecting fundamental theory is known. Several candidates for an encompassing theory are currently developed but lack experimental backing. This is even true in light of still unexplained phenomena that seem to imply a failure of each of the two theories. For example, there are cases in cosmology and astronomy where observations hint at the phenomena of dark matter and dark energy, but also the question of the observed matter/antimatter asymmetry in the Universe. The latter does not agree with the behavior expected from the Standard Model of particle physics where each elementary particle obtains a corresponding antiparticle with the same quantum numbers but inverted charge. As the majority of processes in the Standard Model of particle physics are symmetric under **Charge-Parity** conjugation, only a slight imbalance of the abundance of matter and antimatter is expected. Either the Standard Model of particle physics does have additional CP-symmetry breaking processes or the initial condition of the universe did favor matter over antimatter.² While CP-symmetry breaking processes are at least present in the Standard Model of particle physics, the first two observations i.e. dark matter and dark energy do not even fit in the framework all together. Thus, either to resolve the strong CP problem or to explain the dark-sector there is the possibility of novel particles and interactions that up until now elude experimental observations.

In the following chapter 2, three open questions in physics are presented that persist to this day and do motivate additional experimental and theoretical endeavors. On the experimental side, experiments investigating novel physical effects can offer new insights to our understanding of nature, but also experiments examining a well-known effect in a new context can contribute valuable insights.

Thesis Outline In this thesis the feasibility of an implementation of Lloyd's mirror with matter waves i.e. very-cold neutrons is investigated. Lloyd's mirror consists of a vertical mirror on which parts of an incoming beam are reflected back onto the unreflected part producing an interference pattern. Opposed to the well-known implementation using photons, the implementation with neutrons as proposed in Pokotilovski (2011) and

²This argument, that the asymmetry is due to initial conditions while the baryon number is conserved, is not compatible with a model of the universe which includes an inflation period after the Big Bang. This is argued in Dolgov, 1992. Thank you, Prof. Snow for pointing this out.

in Pokotilovski (2013b) has the potential to cover a not yet investigated parameter space on the intersection of linearized-gravity and quantum mechanics. Due to the particularity of a massive mirror in the setup, candidates for physics beyond the Standard Model of particle physics can be probed. In chapter 2 section 2.4 the relevant hypothetical scenarios beyond the Standard Model of particle physics are shortly introduced.

The overall outline of the thesis is as follows. Part I shortly introduces some fundamental concepts which are needed for the following argumentation. In the subsequent chapter 2 current open questions in the field of physics are summarized and in chapter 3 properties of the neutron and the concept of very-cold neutrons are introduced. Part II of this thesis introduces concepts in diffraction theory and the application to Lloyd's mirror. After chapter 4, where Lloyd's mirror is put into an historical context, the concept itself is theoretically described in chapter 5. There, the solution of Lloyd's mirror in the framework of diffraction theory is given and the phase shifts for several external effects are presented. Chapter 6 applies the theoretical deliberations to calculate requirements for parameters of a realistic neutron beam. Part III selectively presents some experimental realizations connected to Lloyd's mirror. In chapter 7 the realization of a setup is presented which satisfies the required characteristics of an incoming beam. Chapter 8 concludes the experimental section by presenting the enhanced procedure of spatial neutron detection using boron-based CR39 imaging plates. Finally, part IV advises on future developments in chapter 9 and concludes this thesis in chapter 10.

2. Selected Open Questions in Physics

This chapter discusses open questions in physics that greatly motivate the implementation of novel experiments throughout all disciplines of physics.

Questions arise whenever experiments give observations conflicting with a well established theoretical model. Currently this is the case for observations on the astronomical length scale and beyond, compared to the microscopical length scale and below and the corresponding established theoretical models.

The three open questions which are relevant in this thesis center around the phenomena of dark matter, dark energy, and the matter/antimatter asymmetry. They are presented briefly in the following sections.

2.1. Dark Matter

The Standard Model of particle physics together with Newton's gravity does accurately model¹ nature up to macroscopic length scales². It covers the known particles as shown in figure 2.1 and joins the weak, strong, and electromagnetic force into a potent framework. The success of this model stands in contrast to astronomical observations that indicate the existence of massive objects that do not or that interact only weakly with the known constituents of the Standard Model of particle physics, as extensively reviewed in Patrignani (2016). The postulation³ of dark matter hinges on several observations with galaxy rotational curves, the observation of the bullet cluster, and fluctuations in the microwave background being the most prominent examples. It has to be emphasized that despite

¹Currently a few observations that challenge the Standard Model of particle physics exist. For example the observation of a non-zero mass of neutrinos which is accounted for by artificially adding a corresponding term as is discussed in Patrignani (2016). Despite this the Standard Model of particle physics offers unprecedented predictive power and no contradicting observations are known.

²Here macroscopic length scale are specified to correspond to scales of everyday life and below astronomical scales at which effects of general relativity become emerge.

³Alternatively, to postulating particles that only interact with the Standard Model of particle physics via gravity, gravity itself can be tuned as it is done in the so called **Modified Newtonian Gravity**. As stated in Patrignani (2016) this can explain some but not all observations contributed to dark matter while being a classical model.

2. Selected Open Questions in Physics

indirect gravitational observation no direct detection of a dark matter particle has been discovered to date.

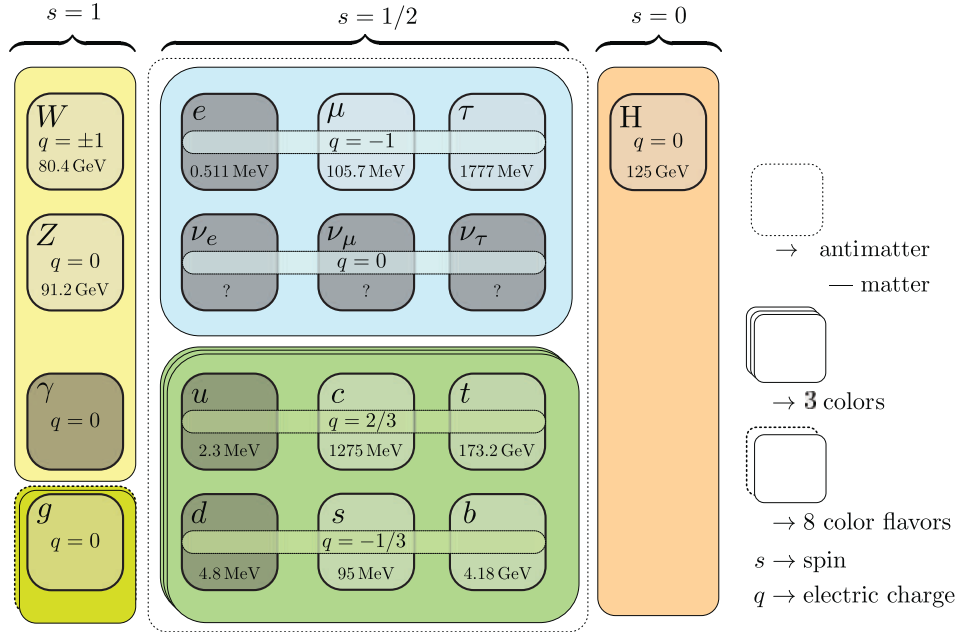


Figure 2.1.: Constituents of the Standard Model of particle physics. Values taken from Patrignani (2016). Decimal places of masses are provided up to the uncertainty of the observation. The boson row is divided between particles which interact via the electroweak interaction and the strong interaction in the case of gluons. The darker boxes correspond to particles that can be found in “stable” states at standard conditions.

Galaxy Rotational Curves The distance dependency of the rotational velocity of stars in a galaxy does not fit the prediction if only the luminous mass is taken into account. Assuming Newtonian gravity the rotational velocity scales with the square root of the mass $M(r)$. Here $M(r)$ is the mass that is enclosed by an orbit within the galaxy with radius r measured to the galactic center. Thus, the rotational velocity is given as

$$v(r) \propto \sqrt{M(r)/r}. \quad (2.1)$$

If the present matter density is proportional to the density of stars one would expect a significant drop-off of $v(r)$ at the edge of the galaxy. This is not observed. On the contrary $v(r)$ stays rather constant, which implies a non-observable or dark matter density extending beyond the galaxy’s edge. This argument is taken from Patrignani (2016).

Bullet Cluster 1E 0657–558 In Clowe, Bradač and Gonzalez (2006) a gravitational weak-lensing analysis of two galaxy clusters that collided and passed through each other is presented. The mass distribution and the X-ray emitting plasma density is measured independently. The first by gravitational lensing and the second by conventional astronomical means. Intriguingly, the interacting plasma that is the dominant baryonic contribution⁴ to these clusters did decelerate and aggregate significantly shifted from the mass density centroid. It is concluded that most of the mass in these clusters is not visible and dominantly interacts via gravity.

Microwave Background Studying the fluctuations of the microwave background⁵ as measured for example by Planck-Collaboration et al. (2015) provides an estimate of the cold non-baryonic matter density parameter of the universe to be

$$\Omega_c h^2 = 0.1187 \pm 0.0022, \quad (2.2)$$

which is significantly bigger than the baryonic matter density parameter of $\Omega_b h^2 = 0.02226 \pm 0.00023$. Here, $H_0 = (67.81 \pm 0.92) \text{ km s}^{-1} \text{ Mpc}^{-1}$ is the Hubble constant which gives $h = H_0 / (100 \text{ km s}^{-1} \text{ Mpc}^{-1}) = 0.6781 \pm 0.0092$, as stated in Planck-Collaboration et al. (2015). Both quantities are a result of a fit which is based on a model of the baryogenesis in the early stages of the universe. See Planck-Collaboration et al. (2015) for the analysis and figure 2.2 for the derived overall energy budget of the universe.

Local Dark Matter Density The current estimate for the local dark matter density is highly model dependent. For a homogeneous distribution along the galactic disc the dark matter density at the position of the solar system is given⁶ in Patrignani (2016) as

$$\rho_{\text{DM}}^{\text{local}} \approx (0.47 \pm 0.28) \text{ GeV/cm}^3. \quad (2.3)$$

The local dark matter density is discussed in Read (2014) in more detail.

⁴This is true even for highly uncertain stellar masses as is argued in Clowe, Bradač and Gonzalez (2006).

⁵See section 2.2 for further details.

⁶The derivation in Patrignani (2016) is based on Catena and Ullio (2010).

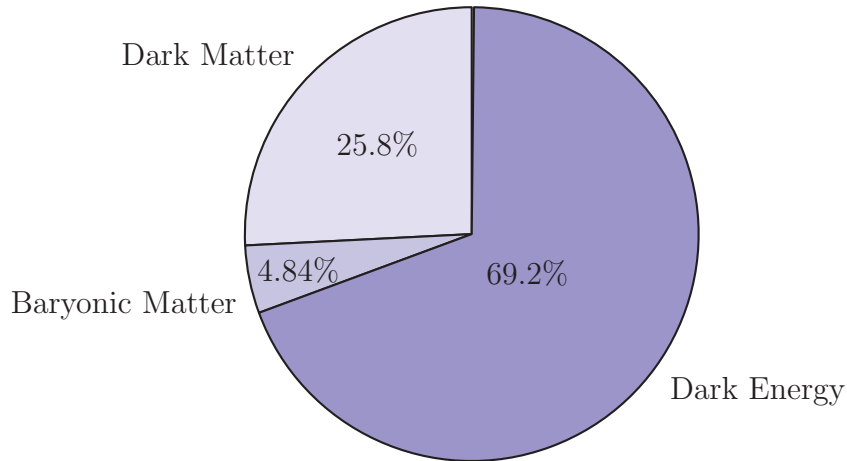


Figure 2.2.: Energy budget of the universe as given in Patrignani (2016). Used are the values for the TT+lowP+lensing dataset analysis. *TT* stands for the temperature power spectrum, *lowP* stands for low *l*-likelihood, thus only multipoles up to $l = 29$ are considered, and *lensing* stands for a correction of weak gravitational lensing by the foreground. The graphic does not add exactly to 100% because contributions like Ω_γ for photons, Ω_ν for neutrinos, and Ω_l for leptons are neglected. For example, $\Omega_\gamma + \Omega_\nu \approx 0.11$.

2.2. Dark Energy

The observation of the movement of extra-galactic objects has shown that the universe is expanding in Hubble (1929) and later that this expansion is accelerating in Riess et al. (1998). This accelerated expansion is surprising, as one would expect a deceleration for a matter-dominated universe. Something seems to apply a negative pressure acting against the attraction by the gravity of matter. Thus, observations justify and even require the addition of the cosmological constant in the Einstein field equations which are shown in equation (1.2). Instead of writing the constant on the left hand side of the equation, one can also move it to the right hand side — the mass/energy side. There it then can be interpreted as a kind of vacuum energy applying a constant pressure

$$R_{\mu\nu} - \frac{1}{2}Rg_{\mu\nu} = \frac{8\pi G}{c^4} (\mathcal{T}_{\mu\nu} + \mathcal{T}_{\text{vac}, \mu\nu}), \quad (2.4)$$

where $\mathcal{T}_{\text{vac}, \mu\nu} = \frac{\Lambda c^4}{8\pi G} g_{\mu\nu}$. Einstein did famously introduce this mathematically allowed cosmological constant in his equations in Einstein (1916) in order to arrive at a static solution. Due to the observation of accelerated expansion this constant does now have a central relevance in modeling the evolution of the universe using general relativity.

An important observation is the in section 2.1 summarized measurement of the **Cosmic Microwave Background**, which supports and extends the analysis of extra-galactic objects and was first reported in Penzias and Wilson (1965). The microwave background is an almost isotropic photon radiation with a blackbody spectrum around $T = (2.72548 \pm 0.00057)$ K, as stated in Fixsen (2009). Intriguingly, its characteristics and most importantly its isotropy fluctuations match a radiation that is expected from an epoch at a redshift⁷ $z \approx 1100$ in which protons and helium cores combine with electrons out of a plasma. While hydrogen and helium form the first atoms, the cross-section with photons is reduced and photons consequently begin to propagate freely without scattering. Thus, the CMB can be interpreted as an afterglow of a much denser epoch of the universe than today. When the CMB is decomposed in angular harmonic components one can analyze the relative magnitude of different multipoles l . The resulting oscillations of the magnitude of individual components over l are formed by the acoustic characteristics of the dense photon-baryon plasma and thus the dominating interactions and particles in that epoch. A comprehensive overview is provided in Patrignani (2016). Extractable results⁸, among others, are the approximate flatness of the curvature of the universe, the fact that besides baryonic particles, also a substantial part of the overall universe energy budget is bound to dark matter; the fact that dark energy is the main contribution to the overall energy budget; and that thermalization in the universe covers a super-Hubble volume⁹, as stated in Patrignani (2016). The most recent CMB survey is presented in Planck-Collaboration et al. (2015). The measured overall energy content of the universe is provided in figure 2.2. The fraction of dark energy of the energy budget of the universe is determined in Planck-Collaboration et al. (2015) to be

$$\Omega_{\Lambda} = \frac{\rho_{\text{DE}}}{\rho_c} = 0.692 \pm 0.007 \quad (2.5)$$

where $\rho_c = \frac{3H_0^2}{8\pi G} = 8.5 \cdot 10^{-27} \text{ kg/cm}^3$ is the critical density, H_0 is the Hubble constant, G is the gravitational constant, and $\rho_{\text{DE}} = \frac{\Lambda c^2}{8\pi G}$ is the dark energy density as given

⁷This corresponds roughly to an age of the universe of $\tau = 400\,000$ a, as stated in Patrignani (2016).

⁸The currently most successful model which combine these and other results is the Λ CDM which among others is based on general relativity, initial conditions for cosmic inflation, a flat universe, cold dark matter, and a cosmological constant as indicated by state of the art observations, as stated in Patrignani (2016).

⁹The Hubble volume is defined as the sphere given by the radius $r_H = c/H_0$. Points outside of this region recede faster than the speed of light from the observer in the middle due to the expansion of the universe. A volume bigger than the Hubble volume is called a super Hubble volume.

2. Selected Open Questions in Physics

in Patrignani (2016). The dark energy density of the vacuum which will be used later is thus given as

$$\rho_{\text{DE}} = \rho_c \Omega_\Lambda h c = (3.3 \pm 0.03) \text{ keV/cm}^3 \quad (2.6)$$

where h is the Planck constant and c is the speed of light.

2.3. Matter/Antimatter Asymmetry

Figure 2.1 shows all elementary particles currently known. Particles inside the dashed enclosure have a antiparticle equivalent under charge conjugation. For example, for an electron this results in the positron which carries an electric charge of $q = +1e$ and a magnetic moment of $\mu_{e^+} = -\mu_e$. This was first discovered in Anderson (1933). For the up quark a charge conjugation results in the antiup quark which has an electric charge of $q_{e^-} = -2/3e$ and the corresponding anti-color. Almost all known physical processes are symmetric under combined charge and parity transformation¹⁰ and thus do not favor matter or antimatter, as stated in Patrignani (2016).

Surprisingly, almost all matter that surrounds us seems to be constituted by matter particles. Note that while evidence for large scale antimatter domains does not exist, the question is still discussed as for example in Grobov and Rubin (2015)¹¹.

Thus, missing large scale antimatter observations indicate that the universe is constituted primarily by matter. This is in contrast to only a small number of CP-symmetry violating processes and to their low probability. The strong interaction, despite theoretical able to break CP-symmetry, does seem to conserve CP-symmetry. This fact is called the strong CP problem. An efficient process that prefers matter over antimatter that did elude detection up until now could explain why matter dominates in our universe.

2.4. Hypothetical Scenarios

The arguments presented in section 2.1, section 2.2, and section 2.3 pose fundamental questions regarding the current understanding of nature. To resolve these issues one can introduce additional fields and particles.

¹⁰CP-symmetry is not conserved in rare weak processes in the quark sector as summarized in Patrignani (2016). Note that CP-symmetry violation is not known to be present in the strong, electromagnetic, and gravitational sector, as stated in Patrignani (2016).

¹¹In Grobov and Rubin (2015) a theoretical model is proposed that is compatible with current observations and allows for large scale antimatter domains.

The Chameleon Field To address the question of dark energy in Khoury and Weltman (2004) a scalar field, the chameleon, can be introduced. In Khoury and Weltman (2004) it is argued that in order to still satisfy experimental equivalence principle tests, the field may have a dependency on the local matter density and thus vanish in the vicinity of an experimental apparatus. In particular the mass m_{cham} of the field is dependent on the local density and will increase with growing density, effectively screening the field to massive objects. One simple possible effective potential of the field is given by the Ratra-Peebles potential, as stated in Joyce et al. (2014) and in Ivanov, Höllwieser et al. (2013) defined as

$$U(\phi) = \Lambda_{\text{scale}} + \frac{\Lambda_{\text{scale}}^{4+n}}{\phi^n} \quad (2.7)$$

where $\phi(x, y, z)$ is the chameleon field, n the Ratra-Peebles index, and $\Lambda_{\text{scale}} \approx 2.24 \text{ meV}$ the dark energy scale¹². The mass for this particular implementation is given as

$$m_{\text{cham}}^2 = n(n+1) \frac{\Lambda_{\text{scale}}^{4+n}}{\phi_{\text{min}}^{n+2}} \quad (2.8)$$

and the minimum of the chameleon field as

$$\phi_{\text{min}} = \Lambda_{\text{scale}} \left(\frac{n M_{\text{pl}} \Lambda_{\text{scale}}^3}{\beta \rho} \right)^{\frac{1}{n+1}} \propto \rho^{-\frac{1}{n+1}} \rightarrow m_{\text{cham}}^2 \propto \rho^{\frac{n+2}{n+1}} \quad (2.9)$$

with the local density ρ , the Planck mass M_{pl} , and the coupling constant β . While in the vicinity of a high density the field is massive and thus very short-range (screened) in empty space it will be very light and can act on cosmological scales. Note that several recent experiments restrict the possible parameter space for n and β as for example most recently in Jaffe et al. (2017). This is further discussed in section 5.6.4.1.

Gravitational Torsion In the general theory of relativity the gravitational “force” is a consequence of the curvature of spacetime by the energy density. In a similar fashion it could be argued that the quantity spin could have an effect on spacetime, namely gravitational torsion. The Einstein-Cartan-Sciama-Kibble theory does include torsion into general relativity, as stated in Cartan (1922). Conveniently, the Ricci scalar can be expressed as $\mathcal{R} = R + \mathcal{K}^2$ where \mathcal{K} is the contorsion tensor, as stated in Ivanov and Wellenzohen (2016).

¹²Note that this is a phenomenological estimation. More generally Λ_{scale} could take another value but is restricted amongst others by Adelberger et al. (2007) to a mass scale coinciding with the scale for dark energy, as stated in Jaffe et al. (2017).

2. Selected Open Questions in Physics

In Poplawski (2011) it is argued that torsion could be connected to questions regarding inflation, dark energy, and even matter/antimatter asymmetry. The connection to dark energy is given in Ivanov and Wellenzohen (2016) as

$$p_{\text{tors}} = -\Lambda_C M_{\text{PL}}^2 \quad (2.10)$$

by using the hypothetical chameleon field. Here M_{PL} is the Plank mass, Λ_C the cosmological constant, and p_{tors} the torsion pressure which can be identified as the torsion or dark energy density $\rho_{\text{tors}} = -p_{\text{tors}}$.

The Axion The axion is a hypothetical, light, weakly coupling, electrical neutral, and spin-less particle which can be introduced to address the strong CP problem and was first introduced in Peccei and Quinn (1977). It offers a mechanism to cancel theoretically expected CP-symmetry violating processes mediated by the strong interaction as discussed in Afach et al. (2015). It is based on the introduction of the Peccei-Quinn symmetry and features a strict relationship between mass m_{ax} and the scale of the Peccei-Quinn symmetry breaking f_{ax} by

$$m_{\text{ax}} = \frac{f_{\pi} m_{\pi}}{f_{\text{ax}}} \frac{\sqrt{z}}{z+1} \quad (2.11)$$

with the ratio $z = m_u/m_d = 0.56$, m_{π} the pion mass, and $f_{\pi} = 92 \text{ MeV}$, as stated in Patrignani (2016). Additionally, the axion could be a constituent of dark matter due to their very weak cooling, as stated in Patrignani (2016). The mass range which is favored by theoretical considerations is given as $10^{-12} < m_{\text{ax}} < 10^6$ as presented in Pokotilovski (2011). For $f_{\text{ax}} \gg v_{\text{weak}}$ where $v_{\text{weak}} = 247 \text{ GeV}$ is the electroweak symmetry breaking scale, the axion model is not yet excluded, as stated in Patrignani (2016). Nevertheless, constraints from astronomic observations as presented in Berenji, Gaskins and Meyer (2016) exclude the mass range for the axion to be

$$m_{\text{ax}} < 7.9 \cdot 10^{-2} \text{ eV}. \quad (2.12)$$

These and other limits restrict the possible mass range tightly and lead to models of axion-like particles for which the mass-scale dependency in equation (2.11) is relaxed, as stated in Patrignani (2016) and in Aprile et al. (2014). Thus, experiments are required to

exclude a bigger parameters space of coupling constants as for example the pseudo-scalar coupling between axion and fermion

$$g_{s, \text{ax}, f} = \frac{C_f m_f}{f_{\text{ax}}} \quad (2.13)$$

and axion masses as would be necessary for the original proposed model, as stated in Patrignani (2016). Here C_f is a model dependent factor and m_f is the mass of the fermion.

3. The Neutron

3.1. Neutron Characteristics

The neutron is a composite particle, which is one of the main building blocks of ordinary matter in the observable universe. It is in general the not-stable ground state of $|udd\rangle$ which can be stabilized if bound to protons via the strong force in an atomic core. The current accepted value for the mean lifetime of the free neutron is $\tau_n = (880.2 \pm 1.1) \text{ s}$ as given in Patrignani (2016), which opens a reasonably wide time window to study the free neutron.

The name historically originates from its electric neutrality. It was discovered that atoms have an electrically positive charged heavy core and an equally negatively charged light exterior as presented in Rutherford (1920). Accounting for the known proton mass $m_p = 938.27 \frac{\text{MeV}}{c^2}$ an almost equal mass could not be associated with a known particle. This was resolved with J. Chadwicks discovery of a neutral particle with a mass comparable to the proton Chadwick (1932) which was named neutron. The neutron can

Quantity	Value/Info
Spin	$s = 1/2$
Mean lifetime	$\tau_n = (880.2 \pm 1.1) \text{ s}$
Mass	$m_n = (939.5654133 \pm 0.0000058) \frac{\text{MeV}}{c^2}$
Magnetic moment	$\mu_n = (-1.91304273 \pm 0.00000045) \mu_N$
Electric charge	$ q < 1.1 \cdot 10^{-21} \text{ qe}$. Consistent with zero, as stated in Baumann et al. (1988).
Electric dipole moment	$ d_e < 3.0 \cdot 10^{-26} \text{ qe} \cdot \text{cm}$. Consistent with zero, as stated in Harris et al. (1999).
Electric polarizability	$\alpha_n = (11.8 \pm 1.1) \cdot 10^{-4} \text{ fm}^3$. The electric dipole moment is given as $\vec{D} = 4\pi\alpha_N\epsilon_0\vec{E}$.

Table 3.1.: Neutron characteristic properties as given in Patrignani (2016). If the source is deviating, it is stated.

interact by several mechanisms described in the Standard Model of particle physics i.e.

3. The Neutron

with its spin $s = 1/2$ via the electromagnetic interaction, by its quark-structure via the strong or weak interaction, and by its mass $m_n \approx 939.565 \frac{\text{MeV}}{c^2}$ via gravity. The currently accepted characteristic properties are given in Patrignani (2016) and are summarized in table 3.1.

3.2. Neutron Energy Range

Typically, neutrons are produced in a nuclear fission reactor as for example at Institut Laue-Langevin in Grenoble, France, or a spallation neutron source as for example at Paul Scherrer Institut near Zurich, Switzerland, in practical quantities. Neutrons arising from a fission reaction are called *fission neutrons*, they have kinetic energies of the order of $E_{\text{kin}} = 2 \cdot 10^6 \text{ eV} = 2 \text{ MeV}$ and a $|\vec{v}| = 10^7 \text{ m/s}$, as stated in Dianoux (2003).

A reactor's basic principle rests on moderating fission neutrons down to thermal energies by scattering at a moderator as for example hydrogen. The energy spectrum of these *thermal neutrons* is a Maxwell-Boltzmann spectrum with a mean energy of $\bar{E} \approx 20 \cdot 10^{-3} \text{ eV} = 20 \text{ meV}$. For most experiments lower energies are desired in order to enlarge the cross-section with matter and to make use of emerging

optical properties of the neutron. Neutrons with lower energies than thermal neutrons are called *sub-thermal neutrons* and can be selectively produced by using a low temperature moderator. An example is Deuterium at $T = 25 \text{ K}$. It is used at the Institut Laue-Langevin to enhance the flux of neutrons with a wavelength of $\lambda = 0.2 \text{ nm}$ and an energy $E_{\text{kin}} = 20 \text{ meV}$ as described in Laue-Langevin (2008).

By selecting only the low-energy part of one of the thermal distributions a *very-cold neutron* beam can be created. The energy range of very-cold neutrons is a matter

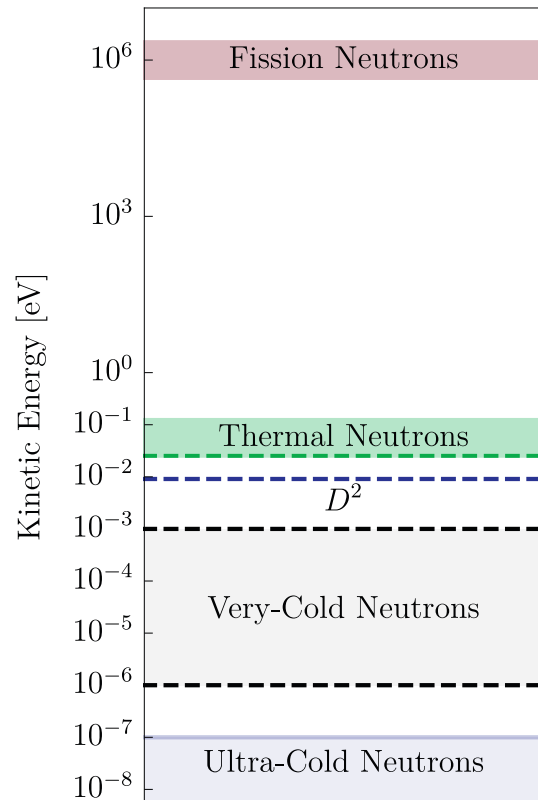


Figure 3.1.: Neutron energies and thermal characterization. The very-cold neutron energy range is specified in Eder et al. (1989).

of definition. A sensible range is given by Eder et al. (1989) as the energy range for which standard optical components can be used as opposed to crystal optics for thermal neutrons and total reflecting optics for ultra-cold neutron. The full energy range of commonly used neutrons is shown in table 3.2. Figure 3.1 gives an overview of accessible neutron energies and the thermal nomenclature.

	Fission Neutrons	Thermal Neutrons	D ² @25 K Neutrons	Very-Cold Neutrons	Ultra-Cold Neutrons
E_{kin}	2 MeV	56 meV	0.9 meV	(1 → 10 ⁻³) meV	< 100 neV
$ \vec{v} $	10 ³ km/s	3.3 km/s	1.3 km/s	(400 → 8) m/s	4.3 m/s
Source:	Dianoux	Laue-Langevin		Eder et al.	Golub et al., 1991
λ	4 · 10 ⁻⁴ nm	0.12 nm	0.3 nm	(1 → 50) nm	92 nm

Table 3.2.: Thermal neutron scale for frequently used energy regions. Note that the energy of thermal neutrons are commonly set to be $v_{term} = 2200$ km/s as it is used as a standard parameter in cross-section measurements. See Dianoux (2003) for additional information.

In this thesis very-cold neutrons are of special importance due to their optical properties. The following chapter will provide an insight in the production of sub-thermal neutrons.

3.3. Very-Cold Neutrons

Neutrons with a kinetic energy $E_{kin} < V_{opt}$ smaller than the optical potential of a surface, totally reflect under every incident angle. This is called total reflection and defines the upper bound of the energy range for ultra-cold neutrons, as stated in Golub, Lamoureux and Richardson (1991). Table A.6 summarizes the neutron optical potential for some frequently used materials. For the materials used in this thesis, the potential has values of the order of $V_{opt} \sim 100$ neV. Some neutron optical characteristics of the used materials are summarized in table A.5.

As the kinetic energy of very-cold neutrons is generally higher than the optical potential, they totally reflect only for angles below the critical angle α_{crit} . It is given as

$$\alpha_{crit} = \arctan \left[\left(\left(\frac{E_{kin}}{V_{opt}} \right)^2 - 1 \right)^{-1/2} \right], \quad (3.1)$$

3. The Neutron

is discussed in more detail in section 5.1, and is applied in section 6.2.1. Experiments with very-cold neutrons frequently have setups with extensions well over several meters, thus their gravitational drop has to be accounted for in experimental realizations. The gravitational drop is given as

$$\Delta x = \frac{g}{2} \left(\frac{L}{v} \right)^2, \quad (3.2)$$

where g is Earth's local acceleration and acts in x -direction, v is the velocity component in either y or z -direction, and L is the flight path. See figure 3.2 for the gravitational

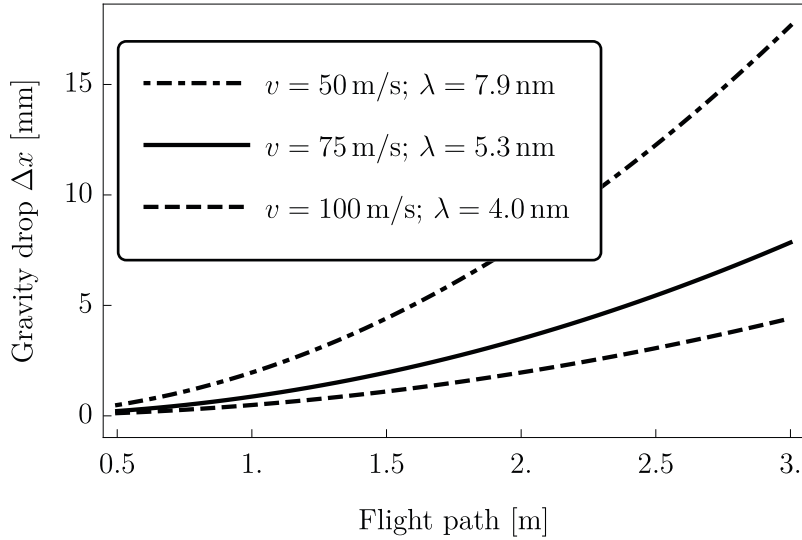


Figure 3.2.: Vertical displacement for a given flight path of neutrons of different energies due to gravitation.

drop Δx for different energies. For a typical very-cold neutron setup, neutrons fall on the order of a few millimeter. Therefore, for sufficiently long setups the alignment has to compensate accordingly.

Institut Laue-Langevin The Institut Laue-Langevin¹ is built around a high flux reactor where neutrons are extracted by neutron guide tubes into several experimental zones. The reactor core is made up by a single uranium fuel element contained in a heavy water moderator. Neutrons that thermalize at the moderator have a mean wavelength of $\lambda = 1.2 \text{ \AA}$ as stated in Laue-Langevin (2008) and thus fall in the category of thermal neutrons. For shifted spectra additional moderator regions are present around the fuel element, as for example two vessels which contain liquid D_2 . They are called the vertical and horizontal cold source. The neutrons thermalized at these sources have a mean wavelength around $\lambda = 3 \text{ \AA}$, as stated in Laue-Langevin (2008). From the vertical cold source a curved neutron beam guide extends to the upper most level of the reactor building, namely “Level D” as shown in figure 3.3. There, the beam guide leads to the turbine which converts the spectrum of roughly half of the beam further down as presented in Steyerl (1975).

The other half of the beam with an area of $A = (34 \times 70) \text{ mm}^2$ bypasses the turbine wheel in a slightly curved guide, exiting the turbine vessel again and guiding the beam to the very-cold neutron cabin. The combination of the turbine and the four ultra-cold neutron beams and the very-cold neutron beam form the PF2 instrument.

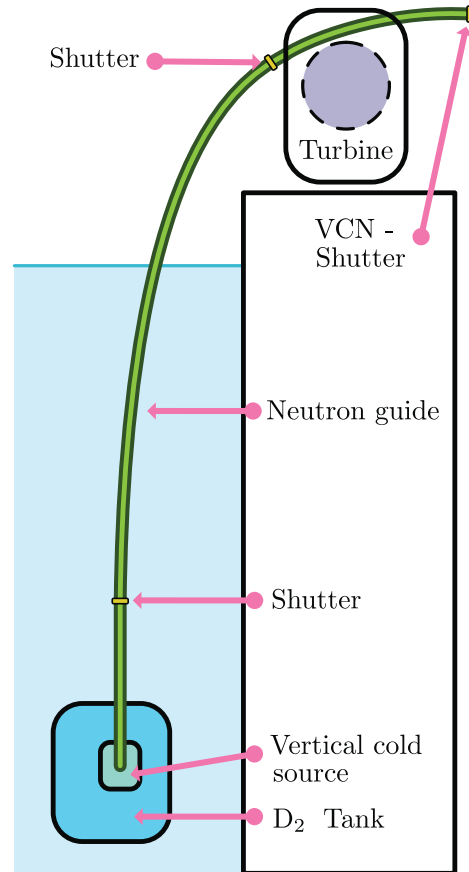


Figure 3.3.: Schematic depiction of the guide that connects the cold source with the turbine at the PF2 instrument at the ILL. The graphic follows the similar graphical representation of the *Instrument Layout* in Laue-Langevin (2008).

¹Institut Laue-Langevin is abbreviated in the following with simply ILL.

3. The Neutron

Quantity	Value
Coating	Ni
Length	$l = 12.8$ m
Curvature	$r = 13$ m
Size	$A = (70 \times 70)$ mm ²
Wavelength	$(2 < \lambda < 40)$ nm
Speed	$(10 < v < 200)$ m/s

Table 3.3.: Characteristic quantities of the vertical neutron beam guide leading to level D taken from Laue-Langevin (2008).

Very-Cold Neutron Port at the PF2

The scheme of the very-cold neutron cabin at the PF2 is shown in figure 3.4 and its characteristics are given in table 3.4. The longitudinal axis of the cabin has a slight angle relative to the neutron beam of $\alpha = 18.2^\circ$ which enters the cabin at a height of 1020 mm. At the front of the cabin a fixed table is used for the pre-setup components as for example a chopper and, most importantly a neutron super-mirror to deflect the beam to be aligned with the cabin.

The cabin is thermally insulated from the climatized experimental area on level D which also provides basic isolation from air vibrations and electromagnetic radiation. Directly left of the cabin the experimental platforms for ultra-cold neutron based experiments are set up. If these employ strong magnetic fields or electromagnetic switching mechanisms, electromagnetic fluctuations will still be measurable in the cabin. The very-cold neutron-beam port supplies central equipment to measurements, as for example a spatially resolving wire chamber detector, namely the BiDim-26, and basic alignment equipment. The BiDim-26 is the main detector

used in chapter 7 and its parameters are given in appendix A.4 in table A.3 and table 3.4. A particular challenge at this beam port is the high spatial dependency of the wavelength spectrum. This is measured and discussed in Oda et al. (2017). Figure 3.5 shows an image taken from Oda et al. (2017) that depicts the wavelength spectrum at different positions in the beam. More in-depth information regarding this beam port is given in chapter 7.

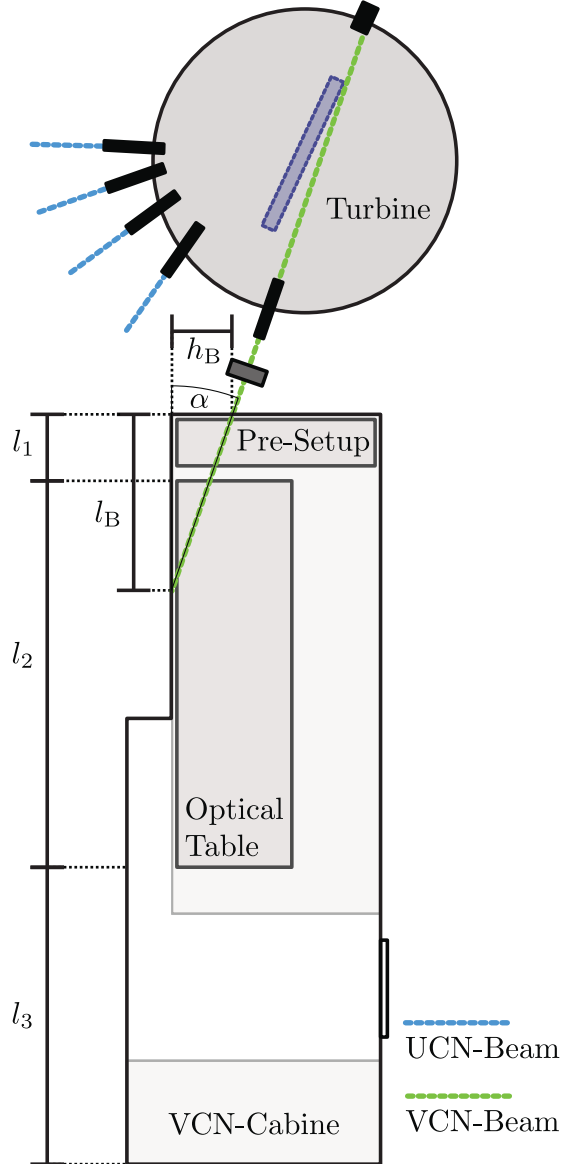


Figure 3.4.: PF2 UCN-Turbine, VCN-Cabin and VCN-Beam. See table 3.4 for the numerical values of the defined quantities.

3. The Neutron

Name	Value	Information
A	(70×34) mm	Beam size at the entrance port of the cabin, as stated in Laue-Langevin (2008).
α	18.2°	Geltenbort (2013, priv. comm.)
l_1	775 mm	First platform length is $l_{Pre} = 650$ mm and the distance between table top and this platform is 125 mm.
l_2	3600 mm	Length of the table top plate.
l_3	3255 mm	Remaining free space in the cabin.
$l_1 + l_2 + l_3$	7630 mm	Geltenbort (2013, priv. comm.)
l_B	2090 mm	Geltenbort (2013, priv. comm.)
h_B	690 mm	Geltenbort (2013, priv. comm.)
A	(265×265) mm	Active area of the BiDim-26 detector. See Manzin (2011)
ζ_{BiDim26}	(2×2) mm	Pixel size of the BiDim-26 detector. See Manzin (2011).
$d_{\text{Conv., BiDim26}}$	3 cm	Conversion gap of the BiDim-26 detector. The gas used is 500 mbar(^3He) + 1.5 bar(CF_4). See Manzin (2011).
$d_{\text{Win., BiDim26}}$	4 mm	Window thickness of the BiDim-26 detector. See Manzin (2011).
$T_{\text{Off}}(10 \text{ Hz})$	(3.69 ± 0.01) ms	Measured during beam-time 3-14-320 in 2013. The measurement was performed using a laser diode and a fast photo diode. The uncertainty stated is the statistical uncertainty.
$T_{\text{Off}}(20 \text{ Hz})$	(1.852 ± 0.009) ms	
$T_{\text{Off}}(30 \text{ Hz})$	(1.238 ± 0.0001) ms	

Table 3.4.: PF2 dimension table. See figure 3.4 for a graphical representation.

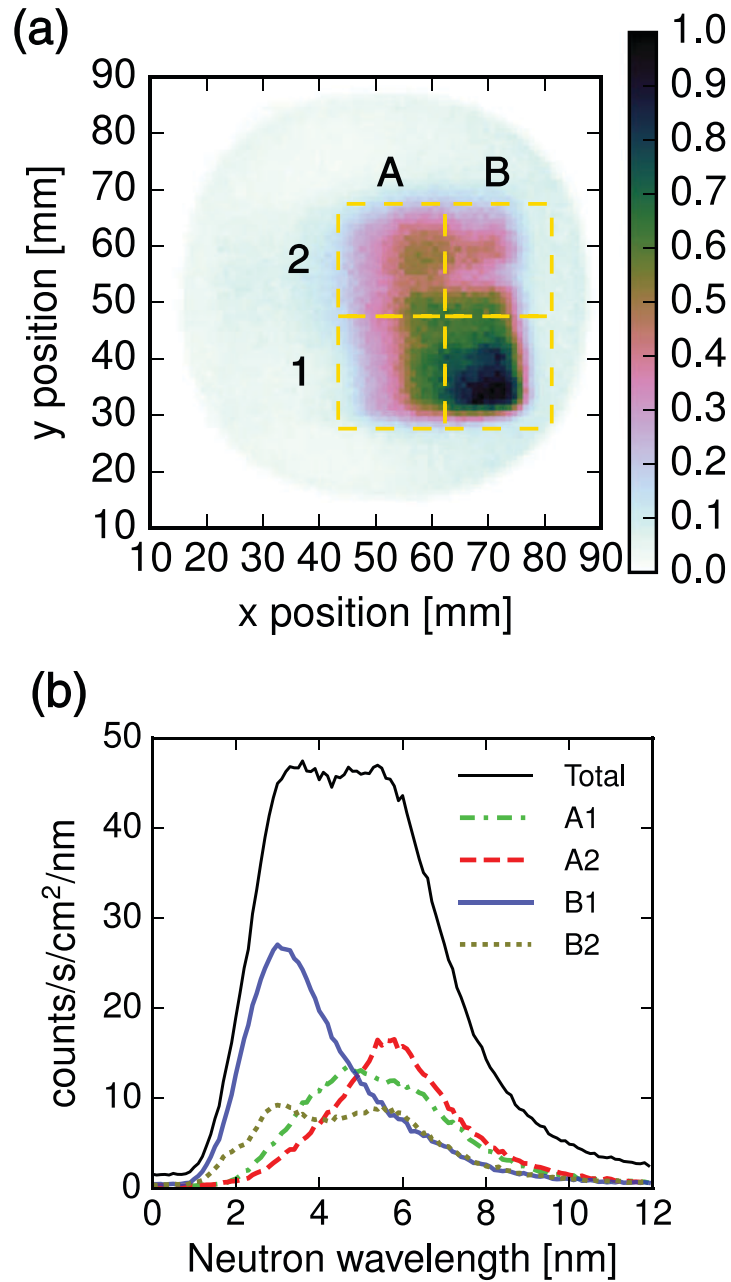


Figure 3.5.: Subfigure (a) shows the cross-section of the very-cold neutron beam after an flight path of $L = 750$ mm between chopper and detector. The dashed yellow rectangles depict regions of interest to calculate wavelength spectra. Subfigure (b) shows wavelength spectra for different extraction positions at the very-cold neutron beam at the PF2. Both images are taken from Oda et al. (2017).

Part II.

Lloyd's Mirror

4. Introduction

This section provides a brief summary of historical wave optics and the introduction of the Lloyd's interferometer by H. Lloyd.

4.1. A Brief Overview of Interferometry

Optics between 1700 and 1800 was dominated by a debate about the 'nature' of light, where the question was if light is made out of corpuscle or undulations (solid particles vs. waves). Despite extensive diffraction experiments the consequence of interference was not clear and both sides had prominent supporters with a variety of arguments¹.

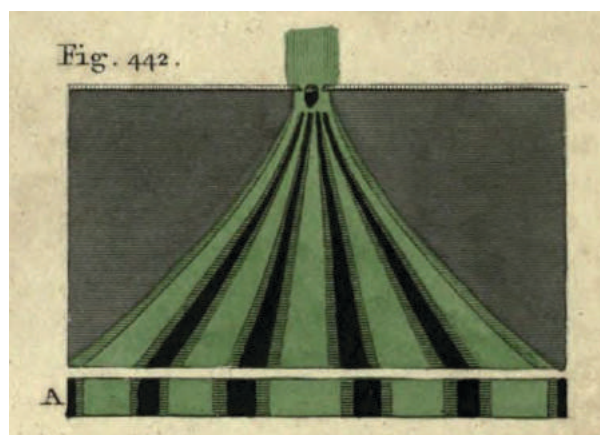


Figure 4.1.: Depiction of the interference pattern and schematic setup of the double-slit experiment and seen interference pattern by Young (1807).

The most famous experiment that shifted the debate in favor to an undulation theory is the double-slit experiment by Young (1807) for which the interference pattern is shown in figure 4.1. Despite this and additional experiments by A. Fresnel, the counter argument that the appeared interference might be explained by the interaction of light with the

¹Examples of prominent supporters of the corpuscle theory of light: Isaac Newton, Siméon Denis Poisson, Examples of prominent supporters of the undulation theory of light are Thomas Young, Augustin Jean Fresnel, Humphrey Lloyd, James Clerk Maxwell (See Born and Wolf (1970), Wikipedia (2017), Young (1807) and Lloyd (1831) for more details)

4. Introduction

edges of the slit or the glass, needed to be refuted as is argued in Born and Wolf (1970) and Lloyd (1831).

To strengthen the understanding of the undulatory theory, in Lloyd (1831) an interferometer is proposed where a reflected beam interferes with a direct beam as shown in figure 4.2. The implementation with light verified, that interference is not due to structure in the entrance slit.

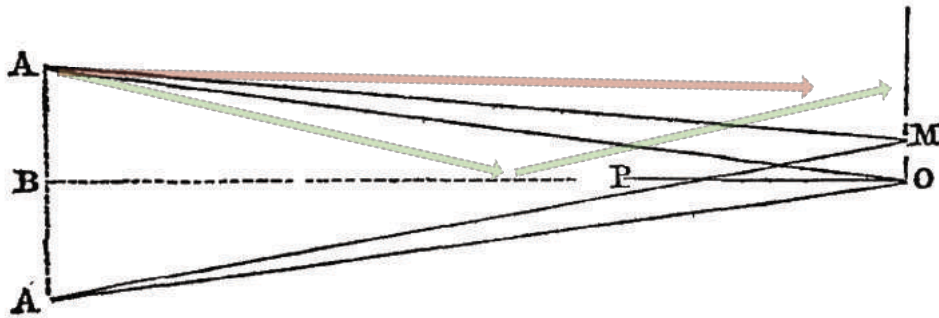


Figure 4.2.: Original schematic depiction of Lloyd's mirror taken from Lloyd (1831). On the left line is a candle that is masked by a thin slit at position A . From P a mirror surface perpendicular to the picture plane extends to point O . A wave will propagate from A to O by direct path or by reflecting at the mirror. The interference pattern at the imaging plane on the right side (plane through O and M) is determined by the ratio of the distance between B and O and the distance between A and B . To simplify the calculation A' , that acts as reflected source is, added. Finally, the green arrows depict the reflected beam a and the red arrows depict the direct beam a' .

In order to describe the intensity pattern H . Lloyd calculated the intensity to be

$$I = A^2 = a^2 + 2aa' \cos 2\pi \left(\frac{\delta' - \delta}{\lambda} \right) + a'^2 \quad (4.1)$$

where $\delta' - \delta$ is the transverse path difference between reflected beam and direct beam, a is the intensity in the direct beam, and a' the intensity in the reflected beam.

With the formulation of Maxwell's equations of electrodynamics the wave-theory of light received a framework which accurately described diffraction effects with light (Born and Wolf, 1970). The argument between corpuscle or undulations was finally settled by Einstein (1905), by showing that wave properties and particle properties are simultaneously needed to explain the photoelectric effect. Thus, joining both sides of the argument by proposing the wave-particle duality of light which was extended to massive particles as proposed in de Broglie (1924). The wave-particle duality today is a corner stone of

quantum mechanics and appears in a wide variety of systems as for example matter wave diffraction. This closes the discussion to the mentioned experiments at the beginning.

4.2. Motivation of this Thesis

Lloyd's mirror for light is frequently used as a tool to investigate planar surfaces as is discussed in Langenbeck (2014). The main prospects of Lloyd's mirror with very-cold neutrons, are possible tests of physics beyond the Standard Model. For example, chameleon fields, axions, symmetrons and gravitational torsion are proposed areas of interest. See Pokotilovski (2013b), Pokotilovski (2013a), Pokotilovski (2011) and Ivanov (2016, priv. comm.) for more details. In section 5.6 the phase shifts due to different hypothetical scenarios in Lloyd's mirror are discussed and measurement scenarios are analyzed. For certain scenarios, for example the chameleon field, the size of the introduced phase shift can be rather large, depending on the exact value of the parameters of the model. The interferometer could offer a general tool to investigate physics beyond the Standard Model as it can combine gravitational effects, quantum mechanical effects and an intriguing comparison between neutrons and a massive macroscopic mirror. This demands a rigorous analysis of the feasibility of specific measurement schemes. Further, the realization of Lloyd's mirror with neutrons would be a novelty on its own and thus it is difficult to predict what possible applications may arise.

In regard to hypothetical models in Foot, Lew and Volkas (1992) a fitting motivation for experiments for or against charge quantization in the Standard Model of particle physics and its extensions is given:

This type of naturalness puzzle suggests that it is more likely for nature to have chosen an extension of the standard model which guarantees charge quantization, rather than opting for dequantization. However, we should be circumspect in treating theoretical prejudices such as this as inviolate principles; only experiment can provide the ultimate answer. Foot, Lew and Volkas (1992)

If theoretical deliberations seem to make an experiment obsolete, one has to remember that only an experiment can supply the ultimate test of nature. This thought can be applied to many situations and in this particular instance to the case of Lloyd's Mirror. As already noted, Lloyd's mirror is a free space diffraction experiment. Interpreting an interference pattern can be particularly hard, if different phase shifts need to be disentangled. An example is the famous COW-experiment by Cowley (1995). There the

4. Introduction

phase shift due to gravity was probed by slightly rotating a single-crystal silicon interferometer. Accompanying the phase shift due to gravity is a shift due to the bending of the interferometer which needed to be measured simultaneously by using x-ray diffraction. In general and depending on the effect under investigation the setup has to be adapted for the specific situation to disentangle different effects. In some cases the effect can be turned on and off or even reversed and one can realize a Null experiment i.e. an experiment where the default outcome is no phase shift. Thus, the concrete sensitivity to an effect is dependent on the question whether systematic effects can be disentangled or suppressed. In the case of Lloyd's Mirror a similar situation as in the COW-experiment is to be expected if different interferograms are to be compared. The reason are several significant phase shifts, which are presented in section 5.6. If on the other hand only a small part of the interferogram is probed for a tunable shift the situation simplifies significantly. For such measurements, section 5.6 presents phase-shift magnitudes and their expected sensitivity. A concrete measurement scenario and its constraints are discussed in section 6.1. Finally, a simulation and experimental work is presented in section 6.3 and chapter 7. Most importantly, the theoretical foundations of Lloyd's mirror are discussed in the following chapter and several important solutions that are needed for the analysis are introduced.

5. Theory

5.1. Interactions of the Neutron

In chapter 3 the basic properties and interactions of the neutron are briefly summarized. For neutron optical experiments especially interactions mediated by the strong force between a neutron and nuclear cores is of importance. This kind of interactions lead to effects analogous to light optics and thus not only to functional similar components, such as beam splitters, mirrors, and prisms, but also analogous quantum-mechanical experiments as single-slit diffraction by Shull (1969), double-slit diffraction by Anton Zeilinger et al. (1988) or experiments in classical optics such as focusing setups by Kumakhov and Sharov (1992) and Eskildsen et al. (1998). The general topic of neutron optics is covered broadly in A. G. Klein and S. A. Werner (1983), Sears (1982) and Bergmann and Schäfer (1992).

For the following discussion, force-free matter wave propagation and propagation in a medium, diffraction at an object and nuclear reactions with matter are of relevance and will be briefly discussed.

Nuclear Interaction The interaction of a neutron with an atom core is to first order based on the strong force and can be described by the interaction with a Fermi pseudo potential, as stated in Helmut Rauch and Samuel A. Werner (2015). For a homogeneous surface the interaction can be well approximated by the mean over point-like interactions at atomic sites, if the wavelength of the neutron is much bigger than the inter-atomic distance $d_a \sim \text{fm}$. See for example Golub, Lamoureux and Richardson (1991). This is the case for thermal and low-energy neutrons and leads to the

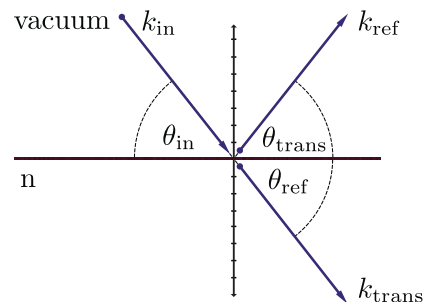


Figure 5.1.: Surface interaction geometry. A neutron incident under the angle θ_{in} on a solid non-magnetic surface.

5. Theory

concept of the neutron optical potential. Thus, many results of regular optics can be applied in the case of non-magnetic interactions with a neutron. See Helmut Rauch and Samuel A. Werner (2015) for a complete in-depth description. The neutron optical potential is defined by

$$V_{\text{opt}} = \frac{2\pi}{m} \hbar^2 b_c \hat{N} \quad (5.1)$$

where b_c is the coherent scattering length and \hat{N} is the number density. The index of refraction for a neutron in a medium follows as

$$n = 1 - \frac{\lambda^2 \hat{N}}{2\pi} \sqrt{b_c^2 - \left(\frac{\sigma_T}{2\lambda}\right)^2} + i \frac{\sigma_T \hat{N} \lambda}{4\pi} \quad (5.2)$$

where $\sigma_T = \sigma_{\text{abs}} + \sigma_{\text{incoh}}$ is the total cross-section, σ_{abs} the absorption cross-section, and σ_{incoh} the incoherent scattering cross-section. If a neutron transverses a medium, the absorbed fraction will be given by the Beer–Lambert law

$$A = 1 - e^{-d\hat{N}\sigma_T} \quad (5.3)$$

with the transversed distance d . If the neutron hits the surface of a material under an angle θ_{in} as shown in figure 5.1, the reflectivity of a thick substrate is stated in Dianoux (2003) to be

$$R = \left(\frac{q - \sqrt{q^2 - q_c^2}}{q + \sqrt{q^2 - q_c^2}} \right)^2 \quad (5.4)$$

with the wave vector transfer $q = 2k_{\text{in}} \sin(\theta_{\text{in}})$, the critical wave vector transfer $q_c = \sqrt{(16\pi b_c \hat{N})}$, k_{in} the incoming wave vector, and θ_{in} the angle of the incoming wave measured to the surface.

Electromagnetic Interaction The neutron has a fractional-spin of $s = 1/2$ and thus can interact electromagnetically. The potential is stated in Helmut Rauch and Samuel A. Werner (2015) as

$$V_{\text{mag}} = -\mu \vec{\sigma} \cdot \vec{B}(\vec{r}) \quad (5.5)$$

where $\vec{\sigma}$ is the Pauli spin operator, μ is the magnetic moment, and $\vec{B}(\vec{r})$ is the magnetic field. For magnetic materials this leads to a polarization dependency of scattering quantities and for a present inhomogeneous magnetic field this leads to a force as $\vec{F} = \mu \nabla(\vec{\sigma} \cdot \vec{B}(\vec{r}))$. In the following, the spin interaction will only sparsely be discussed

as the focus is on quantum dynamical phenomena without magnetic or electric fields present and on propagation in non-magnetic materials.

5.2. Matter Wave Dynamics

As shown first by H. Rauch, Treimer and Bonse (1974), neutrons will exhibit matter wave behavior in a single-silicon crystal interferometer with macroscopic dimensions by the splitting of amplitude of the wave function. This is also true for wavefront splitting interferometers as mentioned in the introduction of section 5.1.

In force-free space a simple non-trivial solution to the Schrödinger equation are plane waves

$$\Psi_{\text{P}} = \Psi_0 e^{i\vec{k}\vec{x} + \varphi + i\omega t} \quad (5.6)$$

and spherical waves

$$\Psi_{\text{S}} = \Psi_0 \frac{e^{ik \cdot r + \varphi + i\omega t}}{r}. \quad (5.7)$$

Ψ_{P} evolves in \vec{k} direction with a specific wavenumber $k = |\vec{k}|$. Ψ_0 is the amplitude at the origin, r is the radial distance to the origin, while \vec{x} is a point in space, ω is the frequency with which the wave evolves in time and φ is an arbitrary phase. This is not sufficient to describe the propagation of a particle in space as neither wave is localized and thus both are not normalizable. This is solved by using the concept of a wave packet which is a weighed superposition of plane waves, as is used in Helmut Rauch and Samuel A. Werner (2015). Thus, wave properties can be related to neutron properties by the de Broglie relations that connect the neutrons momentum \vec{p} with the wave vector \vec{k} by $\vec{p} = \hbar\vec{k}$ and the neutron kinetic energy E with the frequency ω over $E = \hbar\omega$. Additionally, for a force-free particle the frequency ω and the wavelength λ are related by $|\vec{k}| = 2\pi/\lambda = \sqrt{2m\omega/\hbar^2}$. Thus, a force-free neutron with $|\vec{v}| = 75 \text{ m/s}$ will have

$$\omega = \frac{1}{2\hbar} m_n \vec{v}^2 \approx 45 \text{ GHz} \quad (5.8)$$

and

$$\lambda = \frac{h}{m_n |\vec{v}|} \approx 5.3 \text{ nm}. \quad (5.9)$$

In the following the wavelength in analogy to optics is used to characterize the neutron kinetic energy. For both solutions the time dependence can be separated, if the Hamiltonian is not time dependent.

5.3. Kirchhoff Diffraction Formula

The topic of diffraction of waves at various objects is covered extensively in the literature. For example, in Bergmann and Schäfer (1992), Cowley (1995) and Helmut Rauch and Samuel A. Werner (2015). For the topic of stationary matter wave diffraction I closely follow these three sources.

As superpositions of solutions to the Schrödinger equation are again a solution, one can use results as given in section 5.2 (for example $\Psi_{\text{In}} = \Psi_{\text{P}}$) to build up more complicated compositions Ψ_{Out} .

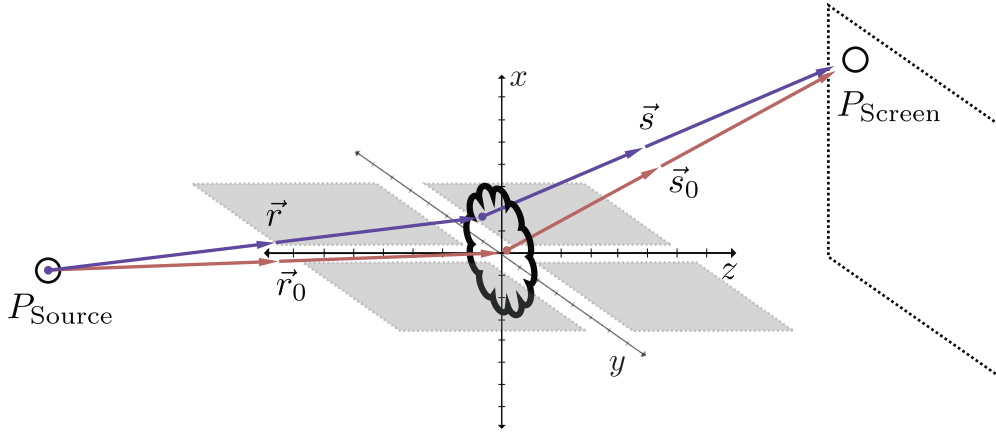


Figure 5.2.: Relevant geometric quantities for diffraction at a thin object. A wave originating from P_{Source} travels along \vec{r} to an object through an arbitrary point in the object plane, gets diffracted and travels along \vec{s} to P_{Screen} . \vec{r}_0 and \vec{s}_0 connect the source point P_{Source} and the screen point P_{Screen} with the origin in the object plane. The arrows indicate the propagation direction.

If a thin object is radiated from a point source at P_{Source} with $\lambda \ll (r_0, s_0)$, the transmitted wave Ψ_{Out} viewed at P_{Screen} can be expressed by

$$\Psi_{\text{Out}} = \frac{i}{2\lambda} \iint S[x, y] \frac{e^{-i\vec{k}(\vec{r}+\vec{s})}}{|\vec{r}||\vec{s}|} (\cos[\vec{n} \cdot \vec{r}] + \cos[\vec{n} \cdot \vec{s}]) dy dz \quad (5.10)$$

which is the Kirchhoff-diffraction formula, as stated in Cowley (1995). Here x and y are the object-plane coordinates, $S[x, y]$ is the object transmission function, $|\vec{k}| = k = 2\pi/\lambda$ the wave vector, λ is the neutron's wavelength, \vec{n} is the normal vector on the object's surface, \vec{r} & \vec{s} are the source vector and the imaging vector respectively and $|\vec{r}| = r$ & $|\vec{s}| = s$ are the vector magnitudes. See figure 5.2 for a graphical representation.

Depending on the placement of the source plane and imaging plane compared to the size of the object and its wavelength, one can distinguish two well explored regimes:

Regime Distinction — Far vs. Near Field If the size of the object D is very small compared to the distance to source r_0 and image s_0

$$\frac{2\lambda}{D^2} \gg \frac{1}{s_0} + \frac{1}{r_0} \quad (5.11)$$

one can replace r and s in the denominator by their not shifted analog r_0 and s_0 . Also \vec{r} and \vec{s} are then almost parallel to the object's normal vector \vec{n} which points in z -direction and thus by only considering forward propagation $\cos[\vec{n} \cdot \vec{r}] \approx \cos[\vec{n} \cdot \vec{s}] \approx 1$. equation (5.10) can then be simplified to

$$\Psi = \frac{i}{\lambda} \iint S[x, y] \frac{e^{-ik(r+s)}}{r_0 s_0} dx dy. \quad (5.12)$$

One can write

$$r = \sqrt{(x - x_{so})^2 + (y - y_{so})^2 + (z_{so})^2} \quad (5.13)$$

$$s = \sqrt{(x - x_{sc})^2 + (y - y_{sc})^2 + (z_{sc})^2} \quad (5.14)$$

and approximate the roots to different orders of x & y depending on the distance between object and source. The coordinates χ_{so} belong to the source plane and the coordinates χ_{sc} to the screen plane. If one finally writes $(r + s) = (r_0 + s_0) + \Delta(x, y)$ the previous equation becomes

$$\Psi = \frac{i}{\lambda} \frac{e^{-ik(r_0+s_0)}}{r_0 s_0} \iint S[x, y] e^{-ik\Delta(x,y)} dx dy. \quad (5.15)$$

Here $\Delta(x, y)$ is the path difference between the path defined by \vec{r} & \vec{s} and the path defined by \vec{r}_0 & \vec{s}_0 . Using the concept of the Fresnel number F one can distinguish different regions. F compares the phase shift between two maximal positions in the objects at the imaging plane by

$$F = \frac{D^2}{s_0 \lambda} \quad (5.16)$$

where D is the characteristic size of the transmissible part of the object. Beware that this distinguishes only coherent diffraction processes. If the incoming wave is not coherent, a pattern will be strongly damped and, depending on the homogeneity of the incoming beam, even be distorted.

5. Theory

Fraunhofer Diffraction — Far Field If the imaging distance is very large, $F \gg 1$ only $\Delta[x]$ and $\Delta[y]$ contribute only to first order. One can write equation (5.15) as

$$\Psi = \frac{i}{\lambda} \frac{e^{-ik(r_0+s_0)}}{r_0 s_0} \iint S[x, y] e^{-ik\Delta(x, y)} dx dy \quad (5.17)$$

with

$$-\Delta[x, y] \approx \left(\frac{x_{so}}{r_0} + \frac{x_{sc}}{s_0} \right) + y \left(\frac{y_{so}}{r_0} + \frac{y_{sc}}{s_0} \right). \quad (5.18)$$

Fresnel Diffraction — Near Field For not too small distances, reasonably sized objects and $F \approx 1$, one has to account for second order contributions which will dominate $\Delta(x, y)$. The diffracted wave function can be expressed as

$$\Psi = \frac{i}{\lambda} \frac{e^{-ik(r_0+s_0)}}{r_0 s_0} \iint S(y, z) e^{-ik(\Delta(y, z))} dy dz. \quad (5.19)$$

If the object has a finite extension in the y -dimension and an infinite extension in the x -dimension the integral over x can be executed. Using $\Delta(x, y) \approx \frac{1}{2}(x^2 + y^2)(\frac{1}{r_0} + \frac{1}{s_0})$ the integral over x is

$$A_x = \int_{-\infty}^{\infty} e^{-ik\left(\frac{1}{r_0} + \frac{1}{s_0}\right)\frac{x^2}{2}} dx = \left(\frac{1}{2} - \frac{i}{2} \right) \sqrt{k \frac{1}{r_0 + s_0}} \quad (5.20)$$

and equation (5.19) becomes

$$\Psi = \frac{i}{\lambda} A_x \frac{e^{-ik(r_0+s_0)}}{r_0 s_0} \int S(y) e^{-ik\left(\frac{1}{r_0} + \frac{1}{s_0}\right)\frac{y^2}{2}} dy. \quad (5.21)$$

The following subsections will give an example for each region, first for the ‘Fraunhofer-Diffraction’ which is represented by a single slit and then for the ‘Fresnel-Diffraction’ which is represented by a straight edge.

5.3.1. Fraunhofer-Diffraction: Single Slit

Following Bergmann and Schäfer (1992) and Shull (1969) the intensity distribution of neutrons Fraunhofer diffracted at a single thin slit is given by

$$I(\beta) = I_0 \frac{\sin^2 [(\pi D/\lambda) \sin(\beta)]}{((\pi D/\lambda) \sin(\beta))^2} \quad (5.22)$$

where β is the diffraction angle, D is the slit opening, λ the neutron wavelength and I_0 the total intensity of the beam in the entrance slit. The angular position of the zero crossings is given by

$$\beta_n = \arcsin \left[\frac{n\lambda}{D} \right] \quad (5.23)$$

where n is the order of the crossing. The resulting pattern can be seen in figure 5.3 which shows a measurement by Anton Zeilinger et al. (1988) in (a) and the calculation in (b). Additionally, this is experimentally verified by Shull (1969).

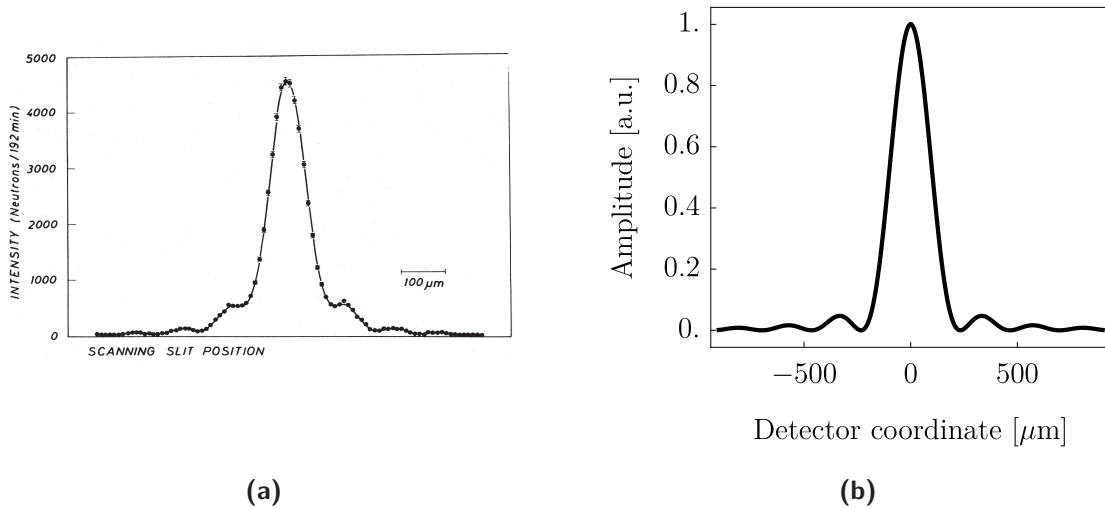


Figure 5.3.: Neutron far field single-slit diffraction pattern. The left figure (a) is a measurement taken by Anton Zeilinger et al. (1988) for a $90 \mu\text{m}$ slit with $L = 5 \text{ m}$. The right figure (b) is a calculation of an ideal pattern at a distance $L = 0.5 \text{ m}$ for $D = 10 \mu\text{m}$, $I_0 = 1$, $\lambda = 6.34 \text{ nm}$ and $F = 0.02$.

5.3.2. Fresnel-Diffraction: Straight Edge

The straight edge has to be treated with the approximations of the Fresnel diffraction, as in one dimension the integration region is not bound to a small area to the axis. $\Delta(y, x)$ will be dominated by terms which are quadratic in y and x . For an edge with an infinite extension in the x -dimension the problem becomes two-dimensional as shown in figure 5.4 and the wave function is given by

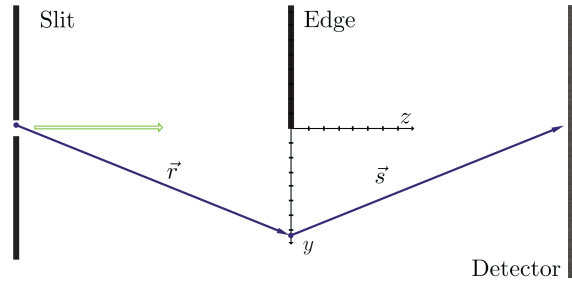


Figure 5.4.: Straight edge diffraction geometry.

This equation can be expressed with Fresnel integrals $\mathcal{C}(u)$ and $\mathcal{S}(u)$ as written in equation (A.11) which can be evaluated numerically

$$\Psi(y_{sc}) = A e^{-i \frac{2\pi^2}{\lambda} (s_0 + r_0)} \int_0^\infty e^{-i \frac{\pi}{2\lambda} (y - y_{sc})^2 \left(\frac{1}{s_0} + \frac{1}{r_0} \right)} dy \quad (5.24)$$

where s_0 is the distance between edge and the point of observation, y_{sc} is the coordinate in the detector plane, and the dependency of the distance to the source is dropped as it is taken to be constant.

This equation can be expressed with Fresnel integrals $\mathcal{C}(u)$ and $\mathcal{S}(u)$ as written in equation (A.11) which can be evaluated numerically

$$\Psi(y_{sc}) = A e^{-i \frac{4\pi^2}{\lambda} s_0} \left(1 + (1 + i) \mathcal{F}_C \left[y_{sc} \frac{1}{\sqrt{s_0 \lambda}} \right] + (1 - i) \mathcal{F}_S \left[y_{sc} \frac{1}{\sqrt{s_0 \lambda}} \right] \right). \quad (5.25)$$

The corresponding normalized probability density $|\Psi|^2$ is

$$|\Psi(y_{sc})|^2 = \left| \left(\frac{1}{4} + \frac{1}{2} \mathcal{F}_C[\xi](1 + \mathcal{F}_C[\xi]) + \frac{1}{2} \mathcal{F}_S[\xi](1 + \mathcal{F}_S[\xi]) \right) \right|. \quad (5.26)$$

with $\xi = y_{sc} \frac{1}{\sqrt{s_0 \lambda}}$. In the experiment performed by R. Gähler, A. G. Klein and A. Zeilinger (1981) and corresponding calculations the beam has finite divergence, is not monochromatic and the entrance slit has a finite size. An ideal pattern and the measured pattern by R. Gähler, A. G. Klein and A. Zeilinger (1981) can be seen in figure 5.5.

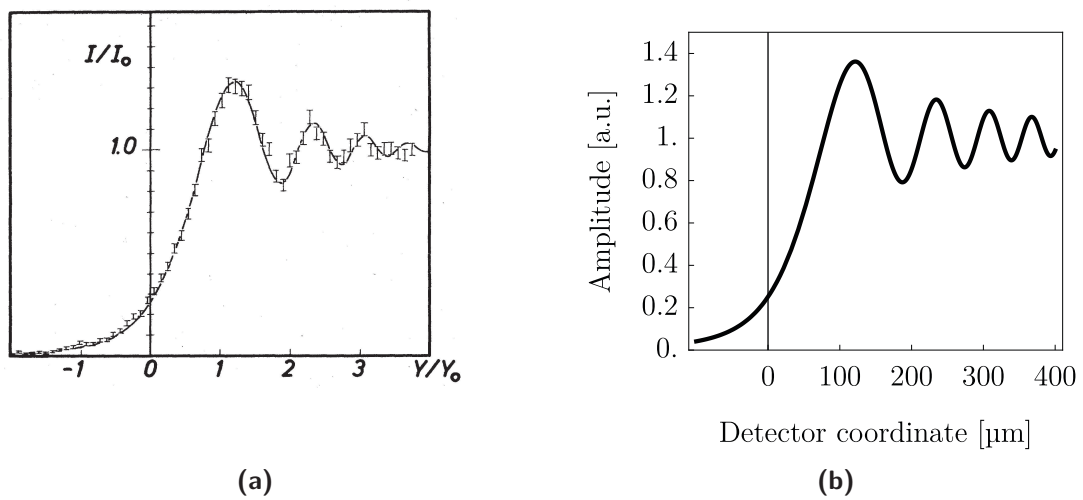


Figure 5.5.: On the left (a) is the straight edge as measured by R. Gähler, A. G. Klein and A. Zeilinger (1981) with very-cold neutrons. A wavelength of $\lambda = (2 \pm 0.5)$ nm is used in the original experiment and the scale in the measurement by Gähler is given as $Y_0 = 100 \mu\text{m}$. On the right (b) is the ideal Fresnel diffraction with similar geometric dimensions but infinitesimal entrance slit size, no beam divergence and for a monochromatic beam.

5.4. Green's Formalism

In some cases the basic structure of the Kirchhoff diffraction formula i.e. that a spherical incoming wave produces spherical waves which will be summed in a diffraction area, is not convenient. In particular the Kirchhoff diffraction formula assumes a diffraction object without significant extension along the propagation direction. If the object has a significant extension and specific symmetries are present in a system, the Green's formalism is more convenient¹.

The Green's function $G(\vec{r}; \vec{r}', t')$ is introduced as the impulse response to an point source at position \vec{r}' at the time t' that is observed at \vec{r} at a time t . In the case of force-free motion and without diffraction at an object the response is called G_0 . By using G_0 to build up more complicated constructs one can incorporate geometrical features and even arrive at the Kirchhoff integral. Green's function in general can be used to incorporate geometrical features directly by demanding boundary conditions. The prerequisites for the following section can be found in Morse and Feshbach (1953) and Arfken and Weber (2013). Especially important is Brukner and Anton Zeilinger (1997) as it discusses various time-dependent single-slit, double-slit and edge phenomena using Green's function.

Starting point is the Schrödinger equation and, as subsequent boundary conditions and potentials will not be time dependent, the stationary Schrödinger equation is sufficient. By adding a source term², the Schrödinger equation will become the inhomogeneous Helmholtz equation

$$\nabla^2 \psi(\vec{r}) + k^2 \psi(\vec{r}) = -4\pi \rho(\vec{r}), \quad (5.27)$$

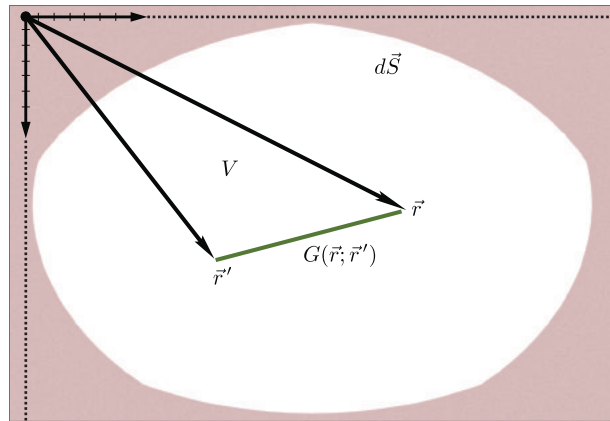


Figure 5.6.: Geometry of the principle of a Green's function. V denotes the region for which the Green's function is defined and $d\vec{S}$ is the boundary surface. The boundary is denoted in brown.

¹Green's formalism produces as a special case the Kirchhoff diffraction formula 5.10 if a Green's function of a point source without added symmetries is used.

²This term is not physical and is only needed for the construction of the solution after which it is dropped.

as stated in Morse and Feshbach (1953). This equation can be solved uniquely with a Green's function, if the source is a delta distribution and if boundary (Dirichlet and/or Neumann) and initial conditions are given

$$\nabla^2 G(\vec{r}, \vec{r}') + k^2 G(\vec{r}, \vec{r}') = -4\pi\delta(\vec{r} - \vec{r}'). \quad (5.28)$$

For a force-free particle where the boundary conditions at the surface \vec{S}

$$G_0(\vec{r}, \vec{r}')|_{\vec{r} \in S} = 0 \quad (5.29)$$

are set at infinity and a Green's function can be given as

$$G(\vec{r}, \vec{r}') = G_0(\vec{r}, \vec{r}') = \frac{e^{i|k|(|\vec{r}-\vec{r}'|)}}{|\vec{r} - \vec{r}'|}, \quad (5.30)$$

as shown in Morse and Feshbach (1953). $G_0(\vec{r}, \vec{r}')$ gives the response of a point source to three-dimensional force-free empty space. With this and given initial conditions $\psi_0(\vec{r}')$ the wave function $\psi(\vec{r})$ at position \vec{r}' becomes

$$\psi(\vec{r}) = \int_V \psi_0(\vec{r}') G(\vec{r}, \vec{r}') dV'. \quad (5.31)$$

For the a scalar wave equation³ as for example the Helmholtz equation at hand, equation (5.31) can be expressed as

$$\begin{aligned} \Psi(\vec{r}) &= \int dV' G \rho(\vec{r}') \\ &+ \frac{1}{4\pi} \oint d\vec{S}' \cdot (G \text{grad}' \Psi(\vec{r}') - \Psi(\vec{r}') \text{grad}' G) \end{aligned} \quad (5.32)$$

by using Green's theorem. If only inhomogeneous Dirichlet type boundary conditions are given as for example $\Psi(\vec{r})|_{\vec{r}' \in S' \wedge \vec{r} \in S} = \Psi_0(\vec{r}_0)$ one can set $G(\vec{r}, \vec{r}')|_{\vec{r}' \in S' \wedge \vec{r} \in S} = 0$ at the surface and thus the previous equation reduces to

$$\psi(\vec{r}) = -\frac{1}{4\pi} \oint \psi'(\vec{r}') \text{grad}' G(\vec{r}, \vec{r}') d\vec{A}'. \quad (5.33)$$

The basic structure of equation (5.33) is very similar to the Kirchhoff-Diffraction integral but with the important difference that $G(\vec{r}, \vec{r}')$ can have a more complex form than just

³For the more general time dependent case see Morse and Feshbach (1953) or appendix A.7.

5. Theory

a point source i.e. $G_0(\vec{r}, \vec{r}')$. This can be shown if $G_0(\vec{r}, \vec{r}')$ is inserted in Term 5.32. Considering the fact that λ is much smaller than the geometrical quantities and if the problem can be reduced to a thin two-dimensional diffraction region, the wave function can be described as

$$\begin{aligned} \Psi(x, y) = & \frac{i}{2\lambda} \iint \frac{e^{-2i\pi\vec{k}\vec{r}}}{|\vec{r}|} q(x', y') \\ & \times \frac{e^{-2i\pi\vec{k}\vec{r}'}}{|\vec{r}'|} (\cos(\vec{e}_z\vec{r}) + \cos(\vec{e}_z\vec{r}')) dx' dy' \end{aligned} \quad (5.34)$$

where $q(x', y')$ is the function which describes the transmission through the diffraction object.

5.5. Lloyd's Mirror

The following subsection give the well-known plane wave solution of Lloyd's mirror and states some simple implications. In particular higher order terms in a frequently made approximation are considered.

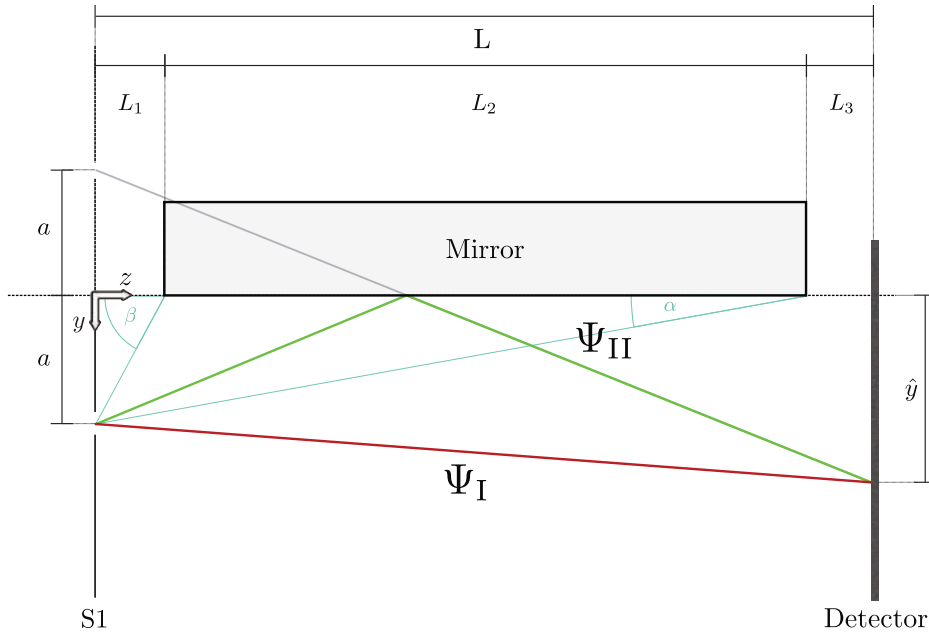


Figure 5.7.: Lloyd's mirror setup sketch for plane wave calculation of the interference pattern. For the first part of the calculation the mirror is supposed to be infinitely extended.

5.5.1. Plane Wave Reflection

A plane monochromatic wave Ψ that passes in front of an infinitely extended reflective plane will give rise to a mirror image of itself, which it will then interfere with. The geometry can be seen in figure 5.7. This plane wave approximation yields an interference pattern with a period constant over the y -dimension. The intensity⁴ $I_{\text{pl}}(\hat{y})$ at a specific section of the mirror and as a function of distance from the mirror \hat{y} can be calculated by

$$I_{\text{pl}}(\hat{y}) \propto |\Psi_{\mathcal{L}}^*(\hat{y})\Psi_{\mathcal{L}}(\hat{y})| = |(\Psi_{\text{I}}^* + \Psi_{\text{II}}^*)(\Psi_{\text{I}} + \Psi_{\text{II}})| \quad (5.35)$$

where $\Psi_{\mathcal{L}}(\hat{y})$ is the wave function of Lloyd's mirror. Subsequently \hat{y} will be named y for simplicity. An incoming monochromatic plane wave $\Psi_{\text{In}} = Ae^{-ikr}$ will accumulate an additional phase φ_{I} in path I of $\varphi_{\text{I}} = -k\sqrt{L^2 + (a - y)^2}$ and φ_{II} in path II $\varphi_{\text{II}} = -k\sqrt{L^2 + (a + y)^2}$.

The wave function in the corresponding path is then given by $\Psi_{\text{I}}(y) = A_{\text{I/II}}e^{-ikr+i\varphi_{\text{I/II}}}$. Additionally, the reflected wave function does accumulate a phase shift of $\Delta\varphi_{\text{ref}} \approx -\pi$ because of the neutron-mirror interaction which is added to the reflected path $\varphi'_{\text{II}} = \varphi_{\text{II}} + \Delta\varphi_{\text{ref}}$.

The phase geometrical difference $\Delta\varphi_{\text{geo}}$ can be expanded by

$$\Delta\varphi_{\text{geo}} = \varphi_{\text{I}} - \varphi_{\text{II}} = -k\frac{2ay}{\sqrt{a^2 + 4L^2}} + \frac{16aL^2y^3}{5\sqrt{a^2 + 4L^2}} + \mathcal{O}(y)^5 \quad (5.36)$$

which in first order and if $L \gg a$ can be approximated by

$$\Delta\varphi_{\text{geo}} \approx -k \cdot 2\frac{ay}{L}. \quad (5.37)$$

This is identical to the phase shift as presented in Pokotilovski (2013a).

⁴This is not a probability distribution as the plane wave solution is not normalizable.

5. Theory

The interference pattern⁵ becomes

$$\begin{aligned}
 I_{\text{pl}}(y) &\propto 2 \left(1 + \frac{e^{i(\varphi_{\text{I}} - \varphi'_{\text{II}})} + e^{-i(\varphi_{\text{I}} - \varphi'_{\text{II}})}}{2} \right) \\
 &\propto 1 + \cos [\Delta\varphi_{\text{geo}} - \Delta\varphi_{\text{ref}}] \\
 &\approx 1 + \cos \left[4\pi \frac{ay}{\lambda L} + \pi \right] = 1 + \cos \left[2\pi \frac{y}{\lambda_{\mathcal{L}}} + \pi \right]
 \end{aligned} \tag{5.38}$$

and

$$\lambda_{\mathcal{L}} = \frac{L\lambda}{2a} \tag{5.39}$$

is the period of the resulting pattern. The pattern is depicted in figure 5.8.

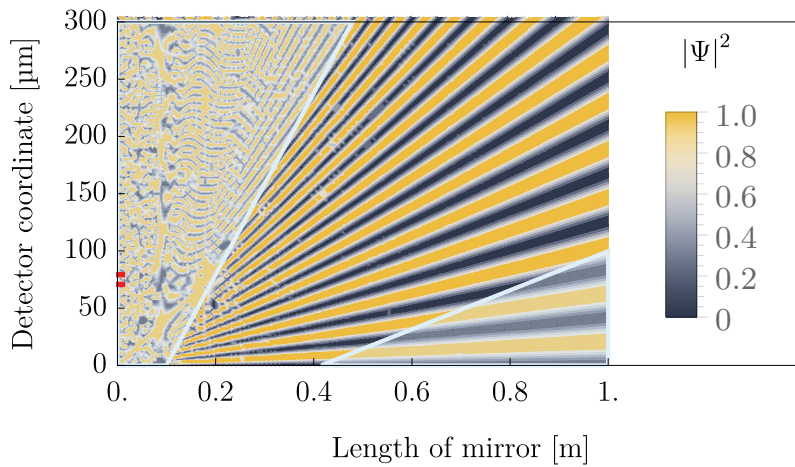


Figure 5.8.: Interference pattern of Lloyd's mirror for $a = 53 \mu\text{m}$, $\lambda = 6.3 \text{ nm}$. The interferogram can be recovered by cutting at a specific mirror length parallel to the y -axis. The region shaded in light blue is not geometrically reachable by the reflected wave. For the calculation the mirror starts $L_1 = 10 \text{ mm}$ behind the entrance slit-screen and the mirror has a length of $L = 0.315 \text{ m}$. The entrance slit is marked in red. The irregular pattern on the left of the plot is a Moire pattern due to the finite plot resolution. See appendix A.4 for the parameters used.

Finite Mirror Length For a finite mirror and a gap between mirror and slit as shown in figure 5.7, the interfering pattern will be constrained from both sides at the screen. Figure 5.8 overlays the plane wave interference pattern with the geometrical shadow⁶ due to the finite mirror and slit restriction to the incoming wave.

⁵In literature Pokotilovski (2013a) an intensity $I \propto \sin\left(\frac{\pi y}{\lambda_{\mathcal{L}}}\right)^2$ is stated. Remembering $\sin(x/2) = \sqrt{(1 + \cos(x))/2}$ the here stated equation is consistent.

⁶Important to note is that diffraction at the slit and at the mirror are neglected at this point. Additional diffraction effects are accounted for in section 5.5.2.

Two restrictions can be derived: first, one for the shallowest angle possible and secondly, one for the steepest possible angle. The shallowest angle α will restrict the interference in the region near the mirror and defines the lowest point y_α that will be geometrically illuminated by the reflected beam as

$$y_\alpha = L_3 \frac{a}{L_1 + L_2} \quad (5.40)$$

where L_1 is the distance between slit-screen and mirror, L_2 is the length of the mirror and L_3 is the distance between mirror and viewing-screen. The steepest angle β which is allowed⁷, restricts the highest distance from the mirror the reflected wave can geometrically illuminate y_β which is given as

$$y_\beta = (L_2 + L_3) \frac{a}{L_1}. \quad (5.41)$$

For a finite sized slit with width S_1 , a has to be changed to either $a \rightarrow a + S_1/2$ or $a \rightarrow a - S_1/2$. Later in section 6.2 it will be shown that a finite sized mirror and entrance slit is a significant constraint of the observability of Lloyd's mirror interference pattern. Thus, the following section will introduce a calculation which accounts for both restrictions.

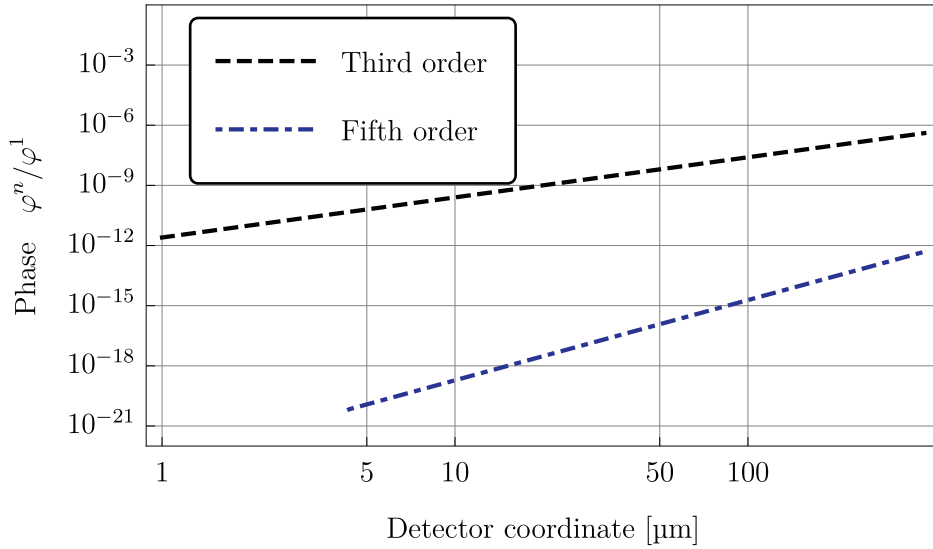


Figure 5.9.: Relative n th-order expansion. Shown are the relative phase change of the third and fifth-order contribution in equation (5.36) for standard parameters as defined in appendix A.4.

⁷Note that this does not mean that no neutron can reach this region. It states that one cannot expect Lloyd's interference fringes in this region.

Higher Order Phase Expansion In equation (5.36) an approximation to the first order is introduced. It is reasonable to check the contribution of the higher order expansions, thus equation (5.36) is developed to the third and fifth-order. Figure 5.9 shows the relative contribution φ^n/φ^1 of next order expansions. The fifth-order term does not contribute significantly but the third-order needs to be accounted for, if the phase-sensitivity should ever reach values below $\delta\varphi < 10^{-7}$. The following section gives a more sophisticated method of calculating the relevant wave function, where an expansion is not needed.

5.5.2. Wave Function Using Green's Function

It is possible to define a Green's function respecting the boundary conditions of the geometry of Lloyd's mirror as shown in figure 5.10. It has to be kept in mind that the vertical boundary condition is idealized as very-cold neutrons do not reflect under every incidence angle. Nevertheless, this geometry is the general approach and it would be possible to incorporate partial reflection and angle dependencies⁸.

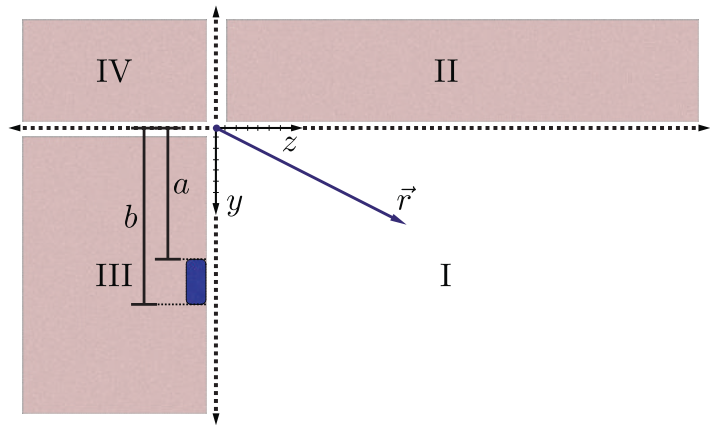


Figure 5.10.: Geometry for Lloyd's mirror to calculate Green's Function. In blue is the position of the source and region I is the region which is to be considered.

For $G_{\mathcal{L}}(\vec{r}, \vec{r}')$ to be uniquely defined, the behavior of $G_{\mathcal{L}}(\vec{r}, \vec{r}')$ at a given boundary S has to be specified, for example for the force-free particle $G_0(\vec{r}, \vec{r}')$ in section 5.4. The position of the chosen boundary S is indicated in figure 5.11. It is required that $G_{\mathcal{L}}(\vec{r}, \vec{r}')$ vanishes on the boundary and thus

$$G_{\mathcal{L}}(\vec{r}, \vec{r}') = 0 \quad \text{for } \vec{r} \in \vec{S} \quad (5.42)$$

⁸An incident under a non-normal angle is calculated in section A.7.1.3.

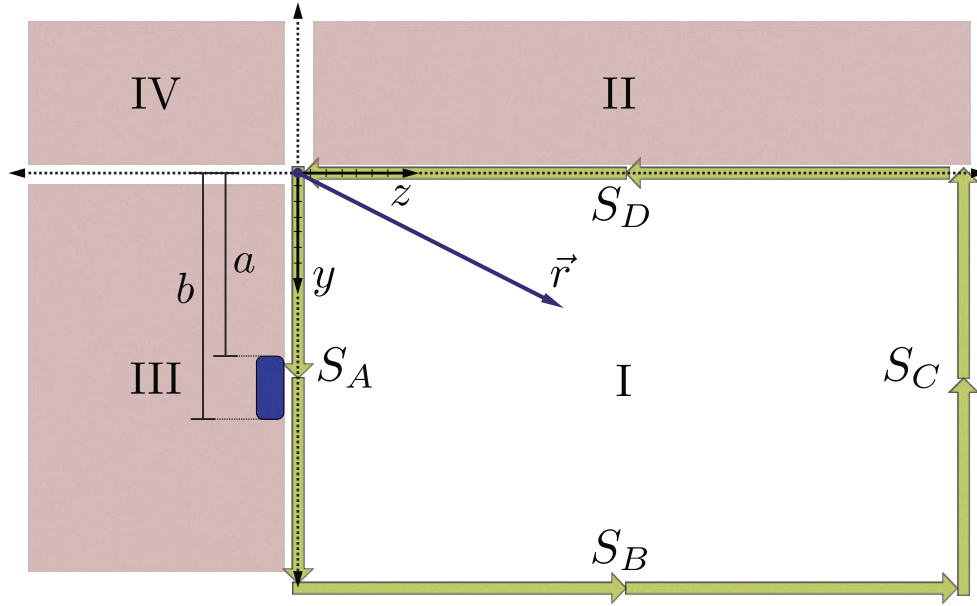


Figure 5.11.: Boundary for Lloyd's mirror geometry. S_B and S_C are evaluated for $\lim |\vec{r}| \rightarrow \infty$.

A Green's function that respects these conditions can be constructed by using the method of images analogue to electrostatics

$$\begin{aligned}
 G_{\mathcal{L}}(r, r') = & G_0 - G_0(|x - x'|, |y + y'|, |z - z'|) \\
 & - G_0(|x - x'|, |y - y'|, |z + z'|) \\
 & + G_0(|x - x'|, |y + y'|, |z + z'|)
 \end{aligned}$$

where G_0 is the Green's function of a force-free particle as given in equation (5.30). Demanding that $\Psi(\vec{r})$ vanishes on the boundary except next to the source region gives

$$\Psi(\vec{r}) = \begin{cases} 0 & \text{for } \vec{r} \in S_D \wedge \vec{r} \in S_B \wedge \vec{r} \in S_C \\ 0 & \text{for } \vec{r} \in S_A \wedge b < y \& y < a \\ 1 & \text{for } \vec{r} \in S_A \wedge b > y > a . \end{cases} \quad (5.43)$$

5. Theory

Using $G_{\mathcal{L}}(r, r')$ with equation (5.33), solves⁹ the integral equation and gives

$$\Psi_{\mathcal{L},st}(\vec{r}) = \Psi_{\text{Green}}(y, z) = A \frac{iz|\vec{k}|}{2} e^{i|\vec{k}|z} \times \left(\int_a^b dy' \frac{\mathcal{H}_1^{(1)} \left[|\vec{k}| \sqrt{(y-y')^2 + z^2} \right]}{\sqrt{(y-y')^2 + z^2}} - \int_a^b dy' \frac{\mathcal{H}_1^{(1)} \left[|\vec{k}| \sqrt{(y+y')^2 + z^2} \right]}{\sqrt{(y+y')^2 + z^2}} \right) \quad (5.44)$$

with amplitude A and $|\vec{k}| = 2\pi/\lambda$.

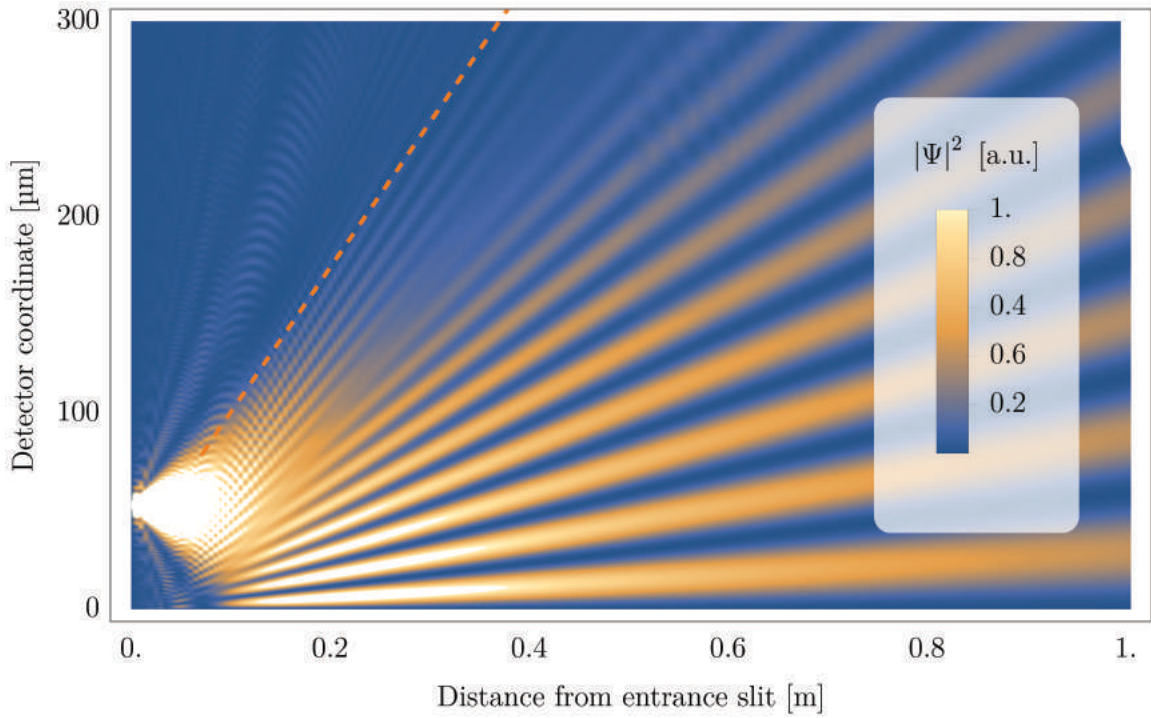


Figure 5.12.: Lloyd's mirror probability density calculated using a Green's identity and by taking advantage of present symmetries. The function is normalized to the first maximum on the bottom of the plot. For the calculation standard parameters as given in appendix A.4 were used. On the left a $S_1 = 8.5 \mu\text{m}$ wide slit on an opaque screen is the starting point of a single-slit diffraction pattern that reflects on a reflecting plane on the bottom. The orange line in the upper right corner corresponds to maximal position of geometrical illumination y_β as given in equation (5.41).

⁹See appendix A.7 for a detailed calculation.

The resulting diffraction pattern for parameters as defined in appendix A.4 is shown in figure 5.12 and a comparison between the plane wave and this approach at one specified mirror length is shown in figure 5.13.

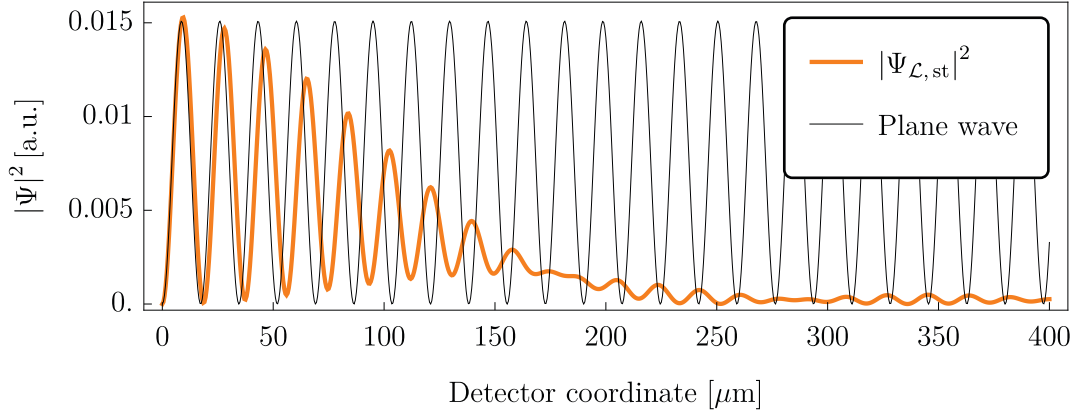


Figure 5.13.: Interference pattern comparison for $a = 53 \mu\text{m}$, $\lambda = 6.3 \text{ nm}$, $L = 0.34 \text{ m}$. The thin line represents the plane wave approach and the red line $|\Psi_{\mathcal{L},st}|^2$ is the result of the calculation using Green's functions as presented in section 5.5.2. For the calculation standard parameters as given in appendix A.4 were used.

The comparison of the plane wave solution and $|\Psi_{\mathcal{L},st}|^2$ yields three interesting facts. Firstly, the period $\lambda_{\mathcal{L}}$ of the interference pattern of the plane wave approach and the one using a Green's function only slightly deviate from each other near the mirror surface. For subsequent chapters it is convenient to calculate additional effects in Lloyd's mirror with a plane wave approach first. Only if effects are considered, which lead to significant deviations from the plane wave solution, a more rigorous approach has to be considered. Secondly, before interacting with the mirror the interference pattern is a single-slit pattern as described in section 5.5.1 and can be seen in figure 5.12 on the left side. The mirror will be irradiated only after the single-slit pattern overlaps with the mirror. The angle under which the minima of the single-slit pattern propagate is given in equation (5.23). Thus, the distance between the slit and the incident position on the mirror is defined by $L_n = (a + D/2) / \arcsin(n\lambda/D)$. With the parameters used in figure 5.12 this yields $L_1 \approx 72 \text{ mm}$, which agrees with the position of the start of the interference pattern in the lower left corner of the graphic. Combining this result with equation (5.41), the maximal distance from the mirror that is geometrically illuminated is given by $y_\beta = az/L_1$ and is depicted in the graphic as dashed orange line. Indeed, y_β does correspond with the upper boundary of the single slit maximum in which the interference pattern is embedded. As $\Psi_{\mathcal{L},st}$ does describe an infinitely extended mirror, the restriction which defines a shadow region after the mirror cannot be reproduced.

5. Theory

Thirdly, the pattern of Lloyd's mirror as seen here can be roughly approximated by the combination of the plane wave case and the single-slit diffraction pattern.

5.5.2.1. Finite Mirror Length

In section 5.5.1 it is discussed that for a setup which has a flight path beam upwards and beam downwards from the mirror, the illuminated region will shrink. It is of interest how the interference pattern will change with a propagation region beam downwards from the mirror. More importantly, it is to be answered whether the resulting pattern can still be identified as one produced by diffraction at a mirror. This can be done by employing Huygens-principle analogously to the problem of the wave function following a channel as in Hartmut Lemmel (2006). In figure 5.14 the vertical red/black dashed line corresponds to the plane defined by the end of the mirror at $z = L$ which is called the cut-off plane $\mathcal{S}_{x,y,z=L}$. At $\mathcal{S}_{x,y,z=L}$ every point gives rise to a spherical wave which is weighted with the amplitude of the wave function as defined in equation (5.44)

$$\begin{aligned} \Psi_{\mathcal{L},\text{F}}(y, z) &\approx \frac{k}{2\pi i} \int_0^\infty dy' \int_{-\infty}^\infty dx' \Psi_{\text{Green}}(\vec{r}')|_{\mathcal{S}_L} \frac{e^{ik|\vec{r}'|}}{|\vec{r}'|} \\ &\approx A \frac{ik^2 L}{4} \int_0^\infty dy' \mathcal{H}_1^{(0)} \left[k \sqrt{(y - y')^2 + (z - L)^2} \right] \\ &\quad \times \left(\int_{y'+a}^{y'+b} dy'' \frac{\mathcal{H}_1^{(1)} \left[k \sqrt{y''^2 + L^2} \right]}{\sqrt{y''^2 + L^2}} - \int_{y'-a}^{y'-b} dy'' \frac{\mathcal{H}_1^{(1)} \left[k \sqrt{y''^2 + L^2} \right]}{\sqrt{y''^2 + L^2}} \right). \end{aligned} \quad (5.45)$$

$$(5.46)$$

The resulting pattern which uses the static solution up to the point L and then continues with the propagated solution can be seen in figure 5.14.

Note that $\Psi_{\mathcal{L},\text{F}}(y, z)$ is only valid for $z > L$. Further, $\Psi_{\mathcal{L},\text{F}}(y, z)$ is **not** a valid approximation, if the wave function is built up by considerable back reflection. As the static solution at a specific $z = L$ is built up partly by waves which originate beam downwards at the mirror $z > L$ it is necessary to check the size of this contribution as only the forward traveling wavefront should be propagated further. Indeed, back reflection does only contribute marginally as is explained in detail in the following section 5.5.2.2. Thus, using the static solution as the wavefront at the end of the mirror is sufficient¹⁰.

¹⁰See the following section 5.5.2.3 which presents an optical measurement of the interference pattern for further verification.

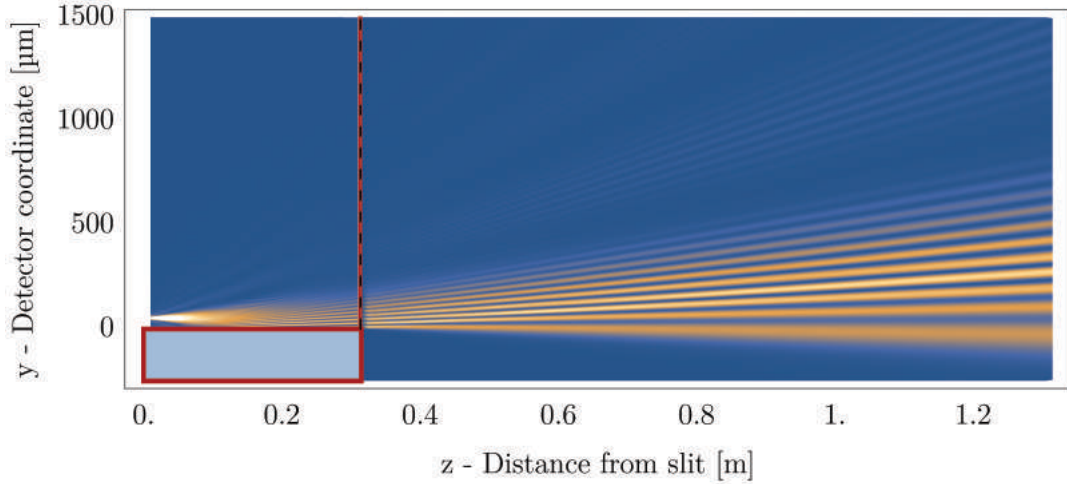


Figure 5.14.: Composition of a static solution $|\Psi_{\mathcal{L},st}|^2$ and a propagated static solution using Huygen's principle $|\Psi_{\mathcal{L},F}|^2$. The left part of the pattern along the mirror is calculated using equation (5.44) and the second is the static solution propagated using Huygen's principle. The static solution is taken along the plane (black-red dashed line) at the end of the mirror (red) as shown in equation (5.46).

An interesting, but not surprising point is that the period $\lambda_{\mathcal{L},F}(L_2)$ of the propagated solution does indeed follow $\lambda_{\mathcal{L}}(L_2)$. See figure 5.15 which compares a cut at $z = L_2$ of the propagated solution with the pattern of the static solution using a mirror with length L_2 . The period of both patterns is almost identical, therefore $\lambda_{\mathcal{L}}$ is used for future calculations as the period estimate.

This is reasonable as long as it is considered, that the pattern will be slightly deformed and partially degrade/lose visibility by propagating beam downwards from the end of the mirror¹¹. See section A.7.1.4 for a more detailed derivation.

5.5.2.2. Time-Dependent Solution

The static solution does contain the superposition of all possible emitted waves¹² in the geometry of an infinitely long mirror. For a specific $z = L$ this includes waves originating from the mirror further down up until $z \rightarrow \infty$. It is not immediately clear that the pattern is mostly formed by forward traveling waves at every possible z . Especially for the applicability of Huygen's principle, using the static solution hinges on vanishing back reflection.

¹¹The plane at the edge of the mirror that separates the mirror region and the downwards propagation region is depicted as red/black dashed line in figure 5.15.

¹²The solution is constructed with the barrier forming the slit and the mirror being perfectly reflecting.

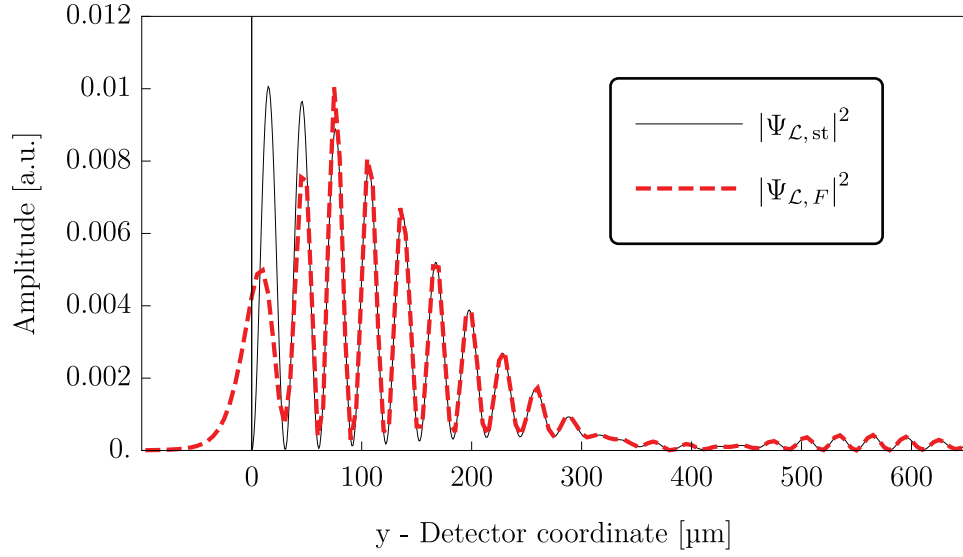


Figure 5.15.: z -slice of the propagated interference pattern. Shown in black is a slice at $L = 0.415\text{m}$ through the pattern shown in figure 5.14. The red dashed line corresponds to equation (5.44) at an equivalent mirror length. Both patterns are normalized to have a unit enclosed probability.

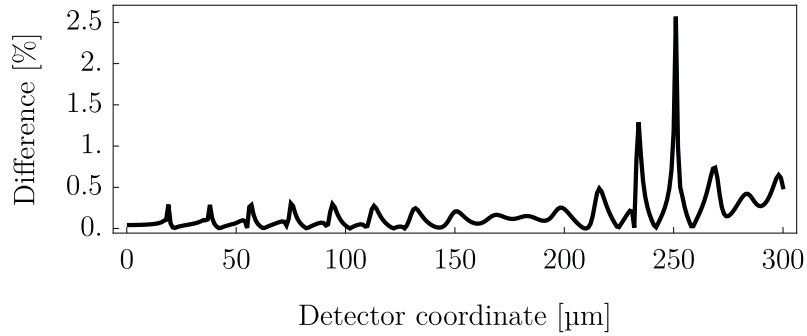


Figure 5.16.: Shown is the normalized difference of the time-dependent and the static solution at $t = \mathcal{T}_c(L)$ and $z = L$. It is calculated for standard parameters as defined in table A.3.

To estimate the back-reflected part¹³ one can compare the time-dependent solution $\Psi_{\mathcal{L},\mathcal{T}_c}$ sliced at the classical propagation time \mathcal{T}_c with the static solution both fixed at $z = L$. The classical propagation time for a particle in a plane is given by $\mathcal{T}_L = \frac{m\lambda}{2\pi\hbar} \sqrt{L^2 + y^2}$. The time-dependent solution of Lloyd's mirror is given in appendix A.7.2 by equation (A.98). Figure 5.16 shows the normalized difference between $\Psi_{\mathcal{L},\mathcal{T}_c}$ and $\Psi_{\mathcal{L},st}$ evaluated at $t = \mathcal{T}_c(L)$ and $z = L$. For the dominant first few maxima the deviation is below 0.4% and not of further interest, if the propagation distance for the finite mirror calculation is not too big. The deviation in the second cluster of maxima can reach several percent but is not of further interest either as this region is suppressed, if the finite $\Delta\lambda/\lambda$ is taken into account. This is even more apparent if the difference is integrated. The fraction of the wave that is back-reflected cannot be much bigger than

$$\int_0^{y_{\max}} (|\Psi_{\mathcal{T}_c,\mathcal{L}}|^2 - |\Psi_{,\mathcal{L}}|^2) < 0.06\% \quad (5.47)$$

where both patterns are normalized to the unit area. y_{\max} is the maximum point of the calculated pattern. In summary, the contribution from back-reflections in the region of interest is only a few per-mill and does not need to be corrected for.

5.5.2.3. Optical Lloyd's Mirror

Using the same setup as presented in section 7.2 which is optimized for neutrons and exchanging the slit assembly, a Lloyd's mirror with light using the same mirror can be implemented. Instead of a layer which is transparent for neutrons, the slit is a gap produced by placing S1= $(155 \pm 0.1) \mu\text{m}$ spacers between the mirror and a boron-steel sheet. The relevant parameters are summarized in table 5.1. The setup consist of a

Quantity	Value	Information
S1	$(155 \pm 0.14) \mu\text{m}$	Thickness of a brass spacer.
a	$(810.5 \pm 0.14) \mu\text{m}$	Thickness of a plastic spacer and half a brass spacer.
β	$\approx -200 \mu\text{rad}$	Estimated from data.
λ	$(653 \pm 0.3) \text{nm}$	The bandwidth should be well below 1 nm.
L	$(0.34 \pm 0.001) \text{m}$	Length of the mirror region.
L_D	30 mm	Distance between mirror and CMOS camera.

Table 5.1.: Parameters that are used to calculate the theoretical pattern for the measurement of an optical Lloyd's mirror as shown in figure 5.17.

¹³At least for back-reflection not in the local area of the time-dependent solution.

5. Theory

laser pointer at $\lambda = (653 \pm 0.3)$ nm, aligning optics, the slit and the mirror, and finally a CMOS camera to capture the interferogram. The setup itself is shown in appendix A in figure A.1. The measurement and the pattern which are predicted by equation (5.44) and equation (5.46) are shown in figure 5.17. Indeed, $|\Psi_{\mathcal{L},F,\beta}|^2$ does describe the measured pattern over a major area correctly. While the measurement itself is not perfect as for example the slit assembly used has an extension of 2 mm and thus deviations from the ideal model are expected, the overall shape of the pattern is correctly reproduced. More importantly, even smaller structures as for example the period of the pattern, relative peak height, and the propagation behavior beam downwards from the mirror region are in agreement. Incorrect is the structure of the first pattern breakdown at $y = 800 \mu\text{m}$ which can be further enlarged by using an even deeper¹⁴ (30 mm) entrance slit. Thus, this deviation is most probably due to a superimposed pattern in the slit region.

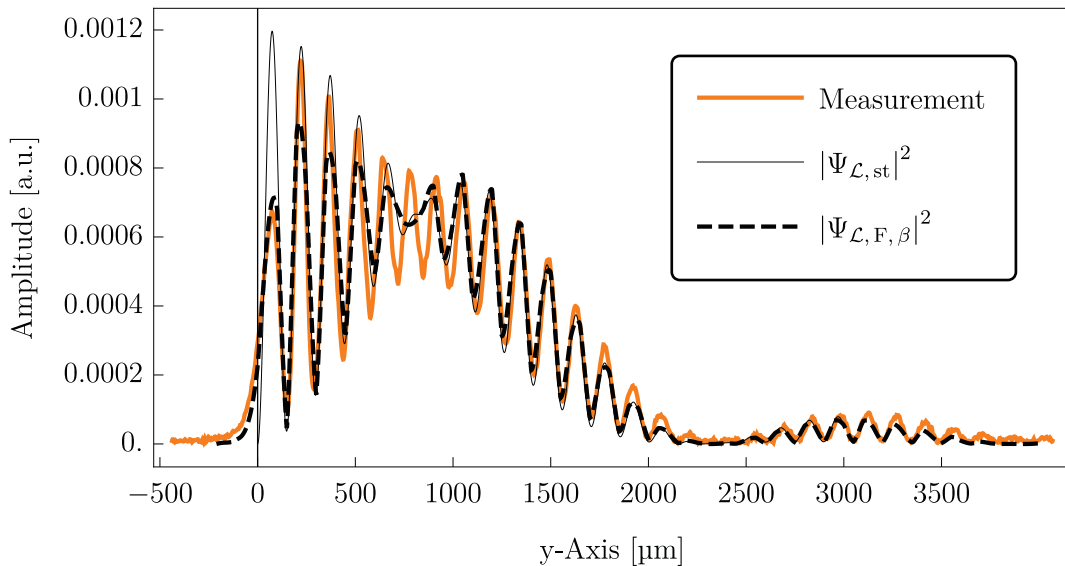


Figure 5.17.: The orange line shows the normalized interference pattern of an optical Lloyd's mirror as measured using a $\lambda = (653 \pm 0.3)$ nm laser and an CMOS camera. From the camera image a region of ROI= $(60 \mu\text{m} \times 4 \text{ mm})$ is cut as the slit parameters $(S1, a)$ are not constant over the vertical extension of the slit. Both patterns are normalized to the area under the curve and the y dimension is fixed by the position of the second maximum. No further data manipulations are applied. The black dashed line is the theoretical exception for the same parameters but using an infinitesimal slit using equation (5.46) and a slight angular misalignment of the incoming beam.

For this measurement the finite length model as presented in equation (5.46) is extended to include a small angle β between incoming wave and slit S1 as it is described in in section A.7.1.3 for the static model $\Psi_{\mathcal{L},st}$.

¹⁴Measured along the z -direction.

5.5.2.4. Detector Influence

Both $\Psi_{\mathcal{L},F}$ and $\Psi_{\mathcal{L},st}$ describe a wave function that is not disturbed by a detector present in the setup. As in the previous paragraph, back-reflection at the mirror contributes marginally to the build-up of the first interference peaks in $\Psi_{\mathcal{L},st}$. $\Psi_{\mathcal{L},F}$ follows only for a forward propagating wavefront, thus it is necessary to address reflections at the detector. The detector that will be presented later in chapter 8 has a ^{10}B coating to absorb neutrons with high efficiency followed by a thin $d < 50$ nm copper layer for stress relief. The reflectivity is given in equation (5.4) and the values for the reflectivity are given in table 5.2 for the boron, copper, and CR39-layers which are the detector materials¹⁵. For neutrons around $\lambda = 6$ nm the reflectivity of the coating in use can be

Layer function	Compound	b_c [fm]	R
Neutron Converter	^{10}B & ^{11}B	0.14	$< 2.8 \cdot 10^{-7}$
Intermediate	Cu	7.7	$< 2.7 \cdot 10^{-5}$
Substrate	CR39	59	$< 4.2 \cdot 10^{-6}$

Table 5.2.: Summary of the reflectivity R of the different layers of the CR39-based detector. R is given for the wavelength range $1 \text{ nm} < \lambda < 10 \text{ nm}$ and at the normal incident $\theta_{\text{in}} \approx \frac{\pi}{2}$.

neglected as the reflected fraction is below $R < 10^{-5}$. See figure 5.18 for a plot of the absorption and reflectivity in the wavelength region of interest.

5.5.2.5. Straight Edge vs. Lloyd's Mirror

An interesting question is, whether Lloyd's mirror offers a significantly different diffraction phenomenon compared to the effect of a straight edge as described in section 5.3.2. For a mirror that is as long as the propagation length after the edge, figure 5.19 shows the resulting pattern for the edge, Lloyd's mirror, and the approximation for a finite mirror. In Roland Gähler and Anton Zeilinger (1991) it is verified that in the case of a straight edge the position of the first maximum relative to the edge is given by

$$P_{1,\text{max}} = 1.22F = 1.22\sqrt{\lambda L} \quad (5.48)$$

where F is the first Fresnel zone. For the identical parameters in the case of $\Psi_{\mathcal{L},st}$, the position of the first maximum is given by $\lambda_{\mathcal{L}}/2 = L\lambda/(4a)$ and it is closer to the surface of the diffraction object as long as $a > 0.2\sqrt{L\lambda}$. Another comparison can be made to $\Psi_{\mathcal{L},F}$ where the first maximum propagates in the shadow region but the overall

¹⁵Ordered by starting from the neutron exposed side.

5. Theory

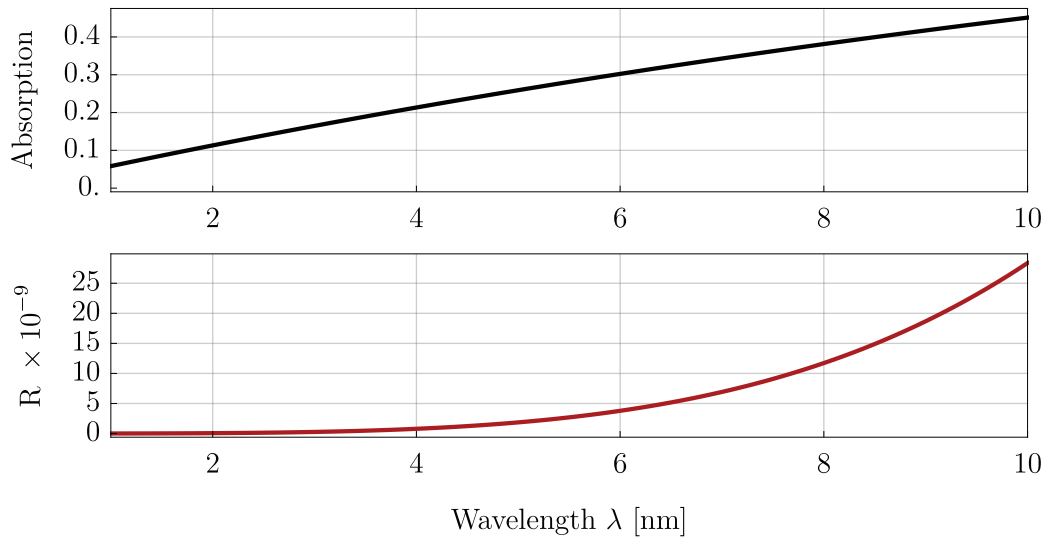


Figure 5.18.: Reflection and absorption probability of a neutron with a wavelength λ at the boron-coated detector surface. The coating is a mixture of 95% ^{10}B and $\approx 5\%$ ^{11}B . The incident of the wave on the surface is normal $\theta_{\text{in}} \approx \frac{\pi}{2}$ to the surface.

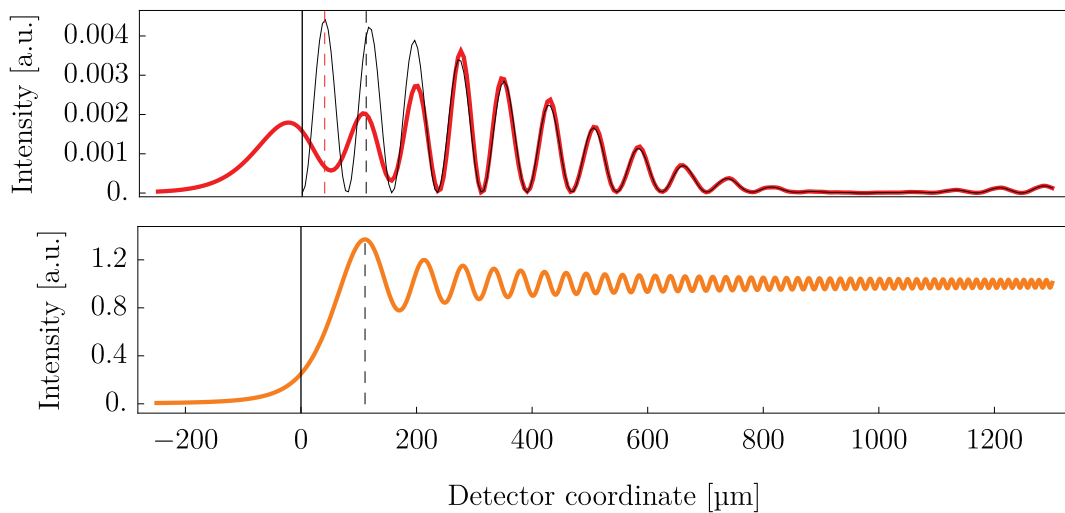


Figure 5.19.: The lower figure is the straight edge diffraction pattern. The upper is the diffraction pattern of Lloyd's mirror with a mirror length equal to the propagation length in the straight edge case. The black line corresponds to $\Psi_{\mathcal{L},\text{st}}$ for $L = 1.34$ m, $\lambda = 6.3$ nm, and standard parameters. The red line corresponds to $\Psi_{\mathcal{L},\text{F}}$ for $L_2 = 0.34$ m and $L_3 = 1$ m. The orange line corresponds to the straight edge with a propagation length of $s_0 = 1.34$ m.

characteristics of Lloyd's mirror are conserved. In conclusion, the vertical mirror adds substantial deviation from a straight edge diffraction. Most notable are the position of the first maximum which probes the closer to the diffraction object surface and a more stable interferogram period. While in the case of a straight edge the period will decrease rapidly over y , for the case of Lloyd's mirror the region which can reasonably be probed for a given detector resolution is much bigger.

5.6. Phase Shifting Effects

Both the very simplified plane wave approach in section 5.5.1 and the Green's function approach in section 5.5.2, describe Lloyd's mirror in a force-free environment. For the investigation of the usage of Lloyd's mirror as a probe for physics beyond the Standard-Model it is necessary to consider fundamental systematic effects and the sensitivity to hypothetical scenarios.

The standard treatment of phase-changing effects is discussed extensively in the literature for example in Helmut Rauch and Samuel A. Werner (2015) and in Berman (1997). Phase shifts specific to Lloyd's mirror are first proposed and discussed in Pokotilovski (2011) and further investigated in Pokotilovski (2013b). The following section starts with a short recapitulation of the general treatment. After that, a paragraph discussing phase shifts due to gravity, due to the Sagnac effect, and other standard effects follows. Section 5.6.4 then discusses phase shifts due to hypothetical forces and particles. Finally, section 5.7 concludes this chapter and gives a summary of the discussed effects. It is important to note that each phase shift depends on the specific experimental realization and thus in general not all effects will be present in every setup.

5.6.1. Phase Shifts in Interferometry

Following S. A. Werner (1994) the phase shift $\varphi(\vec{r}, t)$ in a two-path interferometer in one path is given by the line integral in space-time as

$$\varphi(\vec{r}, t) = \frac{1}{\hbar} \int L dt' \quad (5.49)$$

where $L = \vec{p} \cdot \vec{v} - \hat{H}$ is the Lagrangian, \hat{H} the Hamiltonian of the system, \vec{p} the canonical momentum, and $\vec{v} = \frac{d\vec{s}}{dt}$ the classical group velocity.

5. Theory

The phase shift in both paths can be expressed as

$$\varphi_{I,II}(\vec{r}, t) = \frac{1}{\hbar} \int_{\vec{r}_0}^{\vec{r}} \vec{p}_{I,II} \cdot d\vec{s} - \frac{1}{\hbar} \int_{t_0}^t \hat{H}_{I,II} dt'. \quad (5.50)$$

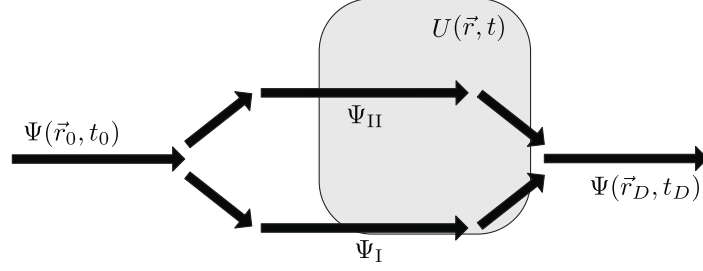


Figure 5.20.: Scheme of a two-path interferometer with a general potential $U(\vec{r}, t)$. See Helmut Rauch and Samuel A. Werner (2015).

See figure 5.20 for a simplified sketch. The phase shift caused by a potential $U(\vec{r}, t)$ is given by the difference between the phase shifts of an interferometer with potential and of the same interferometer without potential. Thus, the phase shift is

$$\begin{aligned} \Delta\varphi_U &= \varphi_I(\vec{r}, t) - \varphi_{II}(\vec{r}, t) - (\varphi_I(\vec{r}, t) - \varphi_{II}(\vec{r}, t))|_{U(\vec{r}, t)=0} \quad (5.51) \\ &= \frac{1}{\hbar} \int_{\vec{r}_0}^{\vec{r}} \Delta\vec{p}_I \cdot d\vec{s} - \frac{1}{\hbar} \int_{t_0}^t \Delta\hat{H}_I dt' \\ &\quad - \frac{1}{\hbar} \int_{\vec{r}_0}^{\vec{r}} \Delta\vec{p}_{II} \cdot d\vec{s} + \frac{1}{\hbar} \int_{t_0}^t \Delta\hat{H}_{II} dt' \quad (5.52) \end{aligned}$$

with $\Delta\hat{H}_{I/II} = \hat{H}_{I/II} - (\hat{H}_{I/II})|_{U(\vec{r}, t)=0}$ and $\Delta\vec{p}_{I/II} = \vec{p}_{I/II} - (\vec{p}_{I/II})|_{U(\vec{r}, t)=0}$. If the Hamiltonian \hat{H} is time-independent the time integration drops out, the phase shift due to the potential becomes the integral along the interferometer path through the potential region $\mathcal{R}(U)$

$$\Delta\varphi_U = \frac{1}{\hbar} \oint_{\mathcal{R}(U)} \Delta\vec{p} \cdot d\vec{s} \quad (5.53)$$

with the change of the kinetic momentum $\Delta\vec{p}$ in the region where the potential is present $\mathcal{R}(U)$.

5.6.2. Sensitivity to a Small Shift

Having calculated the phase shift $\Delta\varphi(y)$ for an effect, it is of interest to calculate the statistical sensitivity of a measurement using Lloyd's mirror for a small shift that can be tuned. The basic premise is to compare two situations and in the most basic implementation to compare the pattern between the case with effect and without effect. For the measurement a scanning slit is moved at the detector position along the y -coordinate, thus giving an intensity $\mathcal{I} = N/T$ at every point. N is the neutron count collected in a integration time T . Figure 5.21 shows the shift of a normalized pattern due to a small additional phase shift $\Delta\varphi(y)$. For the measurement it is not necessary to probe the full pattern, but only to compare the

situation with and without shift while the slit is positioned at the point of the steepest slope $y_s = y_{\pi/4(2n+1)}$ in the not shifted case. Here n is the number of the slope counting from the mirror and starting at zero. Following for example Durstberger-Rennhofer, Jenke and Abele (2011) a Taylor-Expansion is used to approximate the pattern at y_s to the first order, as only small deviations $\Delta y \ll \lambda_{\mathcal{L}}$ are considered. Thus, comparing the not-shifted $\mathcal{I}(y, 0)$ and the shifted intensity $\mathcal{I}(y, \Delta\varphi)$ of the interferogram at y_s gives

$$\mathcal{I}(y_s, 0) - \mathcal{I}(y_s, \Delta\varphi) = \Delta y \left(\mathcal{I}_{\max} \frac{\partial}{\partial y} P(y, 0) \Big|_{y_s} \right) \quad (5.54)$$

$$\Rightarrow \Delta y = (\mathcal{I}(y_s, 0) - \mathcal{I}(y_s, \Delta\varphi)) \left(\mathcal{I}_{\max} \frac{\partial}{\partial y} P(y, 0) \Big|_{y_s} \right)^{-1} \quad (5.55)$$

where \mathcal{I}_{\max} is the intensity at the maximum. For a measurement using a scanning slit, the size of the slit has to be accounted for by convoluting $P(y) = A|\Psi(y)|^2 * \mathcal{T}(y)$ where \mathcal{T} is the transmission function of the slit, A is the normalization constant, and $\Psi(y)$

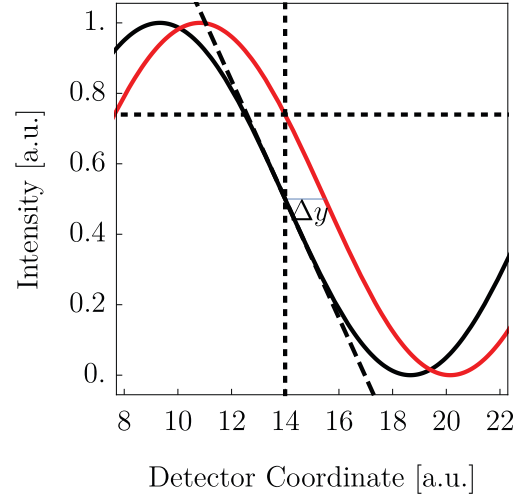


Figure 5.21.: Scheme to calculate the sensitivity for a certain phase shift. The black line corresponds to $\mathcal{I}(y, 0)$ and the red line corresponds to $\mathcal{I}(y, \Delta\varphi)$. For this representation $\mathcal{I}_{\max} = 1$ is chosen.

5. Theory

already includes the wavelength distribution. The statistical uncertainty δy of Δy is then given by

$$\delta y \approx \sqrt{(\delta\mathcal{I}(y_s, 0))^2 + (\delta\mathcal{I}(y_s, \Delta\varphi))^2} \left(\frac{N_{\max}}{T} \frac{\partial}{\partial y} P(y, 0) \Big|_{y_s} \right)^{-1} \quad (5.56)$$

$$\approx \sqrt{\left(\frac{\sqrt{N_{\max}}}{2} \right)^2 + \left(\frac{\sqrt{N_{\max}}}{2} \right)^2} \left(N_{\max} \frac{\partial}{\partial y} P(y, 0) \Big|_{y_s} \right)^{-1} \quad (5.57)$$

$$\approx \frac{1}{\sqrt{2N_{\max}}} \left(\frac{\partial}{\partial y} P(y, 0) \Big|_{y_s} \right)^{-1} \quad (5.58)$$

where $\delta\mathcal{I}(y_s, \Delta\varphi) = \frac{\sqrt{N_{\max}}}{T} P(y_s, \Delta\varphi)$ and $P(y_s, 0) \approx P(y_s, \Delta\varphi) \approx 1/2$ is used. For equation (5.58) the derivative $\frac{\partial}{\partial y} P(y)$ of the pattern $P(y, 0)$ has to be calculated. This is shown in figure 5.22 for a setup without additional phase shifting effects and calculated for standard parameters.

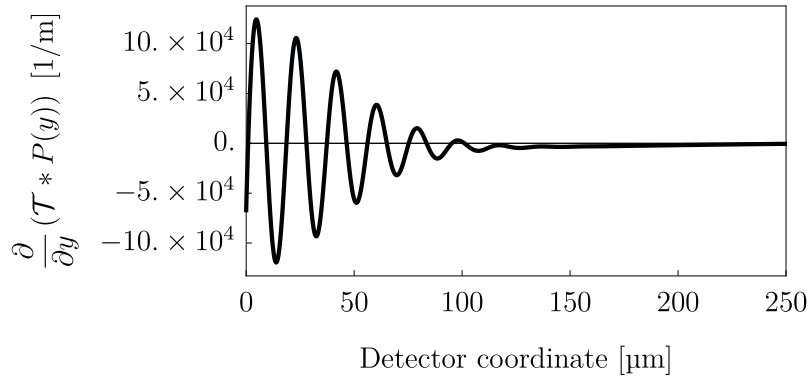


Figure 5.22.: Derivative of the pattern $P(y)$ as seen at the detector calculated for standard parameters as defined in appendix A.4. Note that by anticipating section 6.3.1.1 the wavelength bandwidth is already incorporated in $P(y)$. A rectangular transmission function \mathcal{T} with a width $b_{\text{Scan}} = 10 \mu\text{m}$ is assumed and shortly discussed in section 6.1.2.

The wave function that describes the static case of Lloyd's mirror and is explained in detail in section A.7.1.1 is based on Hankel-functions. Hankel-functions do not have a product relation as exponential functions do

$$\mathcal{H}_p^{(q)}[\varphi_{\text{I}}] \mathcal{H}_p^{(q)}[\varphi_{\text{II}}] \neq \mathcal{H}_p^{(q)}[\varphi_{\text{I}} + \varphi_{\text{II}}], \quad (5.59)$$

thus an easy treatment of a phase shifting effect is not possible in this description¹⁶. As only small shifts are considered, it is assumed that the derivative does not change significantly due to an effect. The phase shift $\Delta\varphi(y)$ is approximated by using the asymptotic form for big arguments which is the plane wave solution given in equation (5.38). The explicit calculation of the asymptotic solution is given in section A.7.1.2 and in Filter, Pitschmann and Abele (2018).

The shift $\Delta\varphi = \Delta y \frac{2\pi}{\lambda\mathcal{L}}$ and its dependency on quantities of interest ξ can be calculated for different effects but it is only applicable if the effect can be turned on and off. If this is not the case, more elaborate measurement schemes have to be employed. Nevertheless, $\Delta\varphi$ is an important quantity which is given for several different effects in the following paragraphs and subsections. The sensitivity to a small shift due to an arbitrary quantity ξ is calculated by solving

$$\Delta\varphi(\xi)|_{y=y_s} \approx \frac{1}{\sqrt{2N_{\max}}} \frac{2\pi}{\lambda\mathcal{L}} \left(\left. \frac{\partial}{\partial y} P(y, 0) \right|_{y_s} \right)^{-1} \quad (5.60)$$

for ξ . The phase sensitivity multiplied by the neutron count at the maximum $\delta\varphi \cdot \sqrt{N_{\max}}$ is a useful quantity to estimate the sensitivity for arbitrary effects and is shown in figure 5.23. Additionally, the sensitivity per measurement day is frequently used which is valid only for a specific intensity.

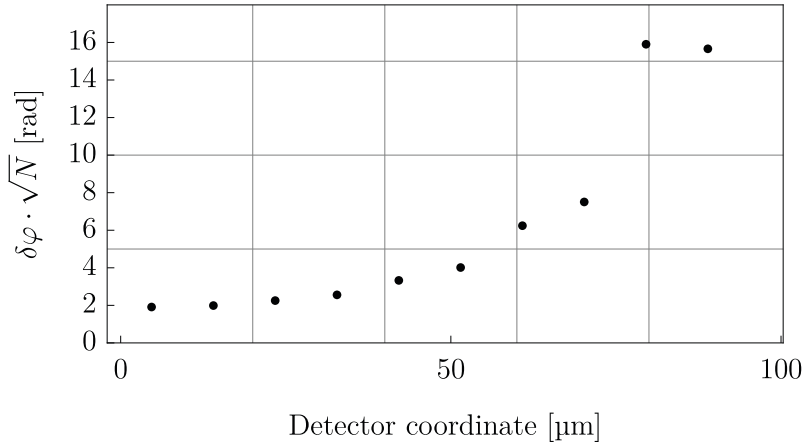


Figure 5.23.: Phase sensitivity calculated for standard parameters as defined in appendix A.4.

¹⁶This not surprising. A rigorous approach would need to calculate the wave function with an additional potential present and then compare this to the case without it.

5.6.3. Systematic Phase Shifting Effects

The following subsection discusses phase shifting effects which are due to known phenomena and can be treated as systematic effects or noise.

5.6.3.1. Mirror Reflection Phase Shift

Geometrically, the reflection at the mirror introduces a π phase shift. In case of the reflection of a neutron at the finite mirror potential there will be a y -coordinate dependent deviation, as stated in Pokotilovski (2013b).

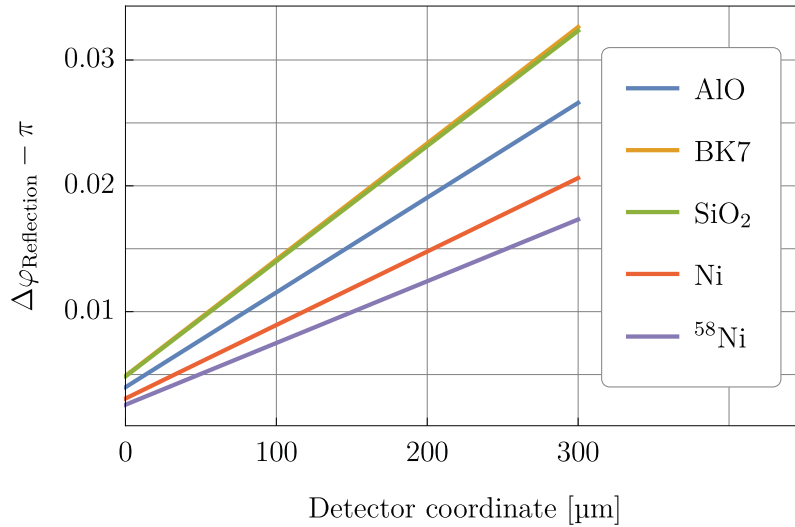


Figure 5.24.: Shown is the phase shift $\Delta\varphi_{\text{reflection}} - \pi$ due to the reflection of the neutron at a mirror. Aluminumoxid, silicdioxid, and nickel are frequently used mirror coatings while BK7 is the material of the bulk. Phase shifts are calculated for standard parameters as defined in appendix A.4.

The phase shift due to the reflection in the plane wave case is given as

$$\Delta\varphi_{\text{reflection}} = 2 \arccos(k_{\perp}/k_b) = \pi - \frac{k(a+y)}{k_b L} \quad (5.61)$$

with $k_b = \sqrt{4\pi\hat{N}b_c}$, \hat{N} the number density of the mirror, and b_c the coherent scattering length. The resulting phase shifts for different mirror materials are shown in figure 5.24. The part of the phase shift which is proportional to y is expected to be of the order $\varphi \sim 30 \cdot 10^{-3}$ and thus has to be considered for precision measurements. On the other hand, this effect is not time dependent and is negligible if measurements are implemented which investigate a tune-able effect which does not effect this shift. In general this phase shift can be incorporated in the interferometer model by setting the boundary

condition for the wave function at the mirror surface S_D not to zero but to match it to an exponential decay in the mirror

$$\Psi(\vec{r})|_{S_D} = Ae^{-ky}. \quad (5.62)$$

5.6.3.2. Gravitational Phase Shift

As has been shown in Cowley (1995) and is reviewed in S. A. Werner (1994) the linear gravitational potential $U_g = m\vec{g} \cdot \vec{r}$ will induce a phase shift in a neutron interferometer that is proportional to the enclosed area $A = aLy/(a + y)$ of the interferometer of

$$\Delta\varphi_{\text{gravity}} = \frac{g\lambda}{2\pi} \left(\frac{m}{\hbar}\right)^2 A \sin(\theta) \quad (5.63)$$

$$= \frac{g\lambda}{2\pi} \left(\frac{m}{\hbar}\right)^2 \frac{ayL}{a + y} \sin(\theta). \quad (5.64)$$

θ is the angle between the local gravity vector g and the mirror surface. This result is also stated in Pokotilovski (2013b) specifically for Lloyd's Mirror. Figure 5.25 shows the gravitational phase shift for standard parameters, as stated in appendix A.4. As the gravitational phase shift can get bigger than the geometrical phase shift it could dominate the interference pattern, therefore it is crucial to minimize a misalignment of the mirror relative to gravity.

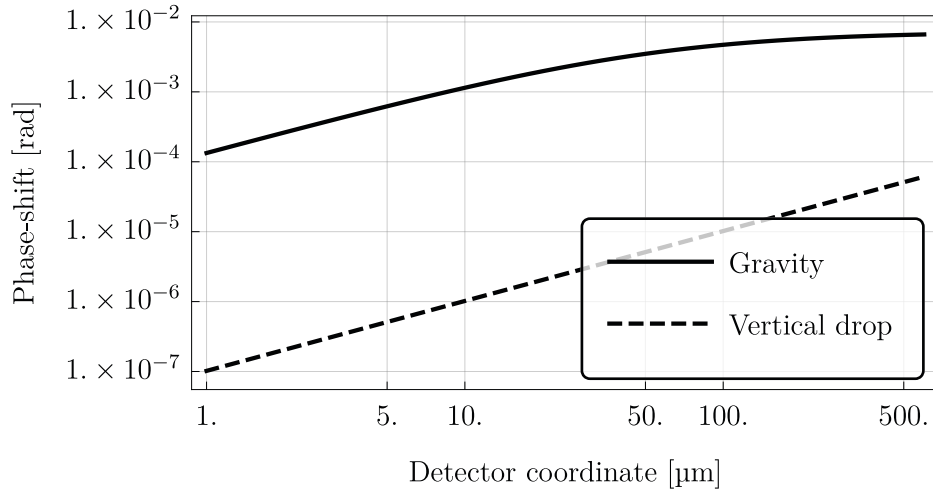


Figure 5.25.: Phase shifts induced by gravity. Shown are the standard phase shifts due to gravity namely φ_{gravity} and due to the vertical drop of neutrons in the gravitational field namely $\varphi_{\text{vertical}}$. An small misalignment of $\theta = 0.01^\circ$ is assumed.

Vertical Drop Additionally, neutrons will fall differently depending on their flight path length and thus their path difference will be altered, breaking the assumption that the problem is strictly two-dimensional. In Pokotilovski (2013b) the phase shift $\varphi_{\text{vertical}}$ due to different flight paths in the gravitational field is given as

$$\Delta\varphi_{\text{vertical}} = \frac{2\pi}{\lambda v^4} g^2 a L y \quad (5.65)$$

with the particle velocity v . The corresponding phase shift for a standard parameter setup can be seen in figure 5.25.

Time-Dependency of g Due to the expected low intensity, measurements can span over several days and thus temporal variations of g have to be taken into consideration. Variations of g due to density variations as for example solid tides, atmospheric movement, and even movement near the experimental area. Table 5.3 gives a not complete overview of sources of variations in g and their magnitude based on Peters, Chung and Chu (2001). The effect with the highest magnitude is the effect of solid tides with $\Delta g \sim 3 \cdot 10^{-6}$ m/s. Using equation (5.60), the sensitivity to a small change in g is given as

$$\delta g \approx \frac{1}{\sqrt{2N_{\text{max}}}} \frac{2\pi}{\lambda} \left(\frac{\hbar}{m}\right)^2 \frac{(a+y)}{ayL \sin(\Theta)} \frac{2\pi}{\lambda_{\mathcal{C}}} \left(\left.\frac{\partial}{\partial y} P(y, 0)\right|_{y_s}\right)^{-1}. \quad (5.66)$$

As the gravitational phase shift depends on the coordinate y , the most sensitive point is

Effect	Magnitude [m/s ²]	Uncertainty	Timescale/Info
Solid Earth Tides	$3 \cdot 10^{-6}$	0.1%	Daily
Ocean Loading	$200 \cdot 10^{-9}$	1%	Daily
Air Pressure	$80 \cdot 10^{-9}$	63%	< Daily
Polar Motion	$100 \cdot 10^{-9}$	0.1%	~ Yearly

Table 5.3.: Magnitude of Time-dependent contributions to g . The table closely resembles Table 4 in Peters, Chung and Chu (2001).

not the point of the steepest slope but slightly shifted. The point of minimal sensitivity can be found at $y_s = y_{5\pi/4} = 23 \mu\text{m}$, the third flank of the pattern, to be

$$\delta g \cdot \sqrt{N_{\text{max}}} \approx 10 \cdot 10^3 \text{ m/s}^2 \quad (5.67)$$

in the case of $\Theta = 0.01^\circ$ and to be

$$\delta g \cdot \sqrt{N_{\max}} \approx 1.7 \text{ m/s}^2 \quad (5.68)$$

in the case of $\Theta = 90^\circ$. Table 5.4 summarizes the expected sensitivity for two specific intensities derived from equation (6.19). For a mirror that is vertically aligned and

$\delta g \left[\frac{\text{m}}{\text{s}^2 \sqrt{\text{day}}} \right]$	Θ	$\mathcal{I}_{\max} \cdot 10^{-6} \left[\frac{\#/\text{s}}{\text{bin}} \right]$
3827	0.01°	159
605	0.01°	40×159
0.67	90°	159
0.11	90°	40×159

Table 5.4.: The sensitivity of Lloyd’s mirror is given for standard parameters and already include the restrictions presented in the following chapter. The point of minimal sensitivity is found at $n = 2$ and thus $y_s = y_{5\pi/4}$. Θ is the angle between the gravitational vector and the mirror surface. The intensity $\mathcal{I}_{\max} = 159 \cdot 10^{-6} \#/\text{s}$ is calculated from equation (7.17) for a $1.2 \mu\text{m}$ scanning slit. $\mathcal{I}_2 = 40 \cdot \mathcal{I}_{\max}$ is given, as this is the brilliance without the specific monochromatization setup and gives a benchmark for the case that the monochromatization can be implemented without losses.

with given intensity \mathcal{I}_{\max} and \mathcal{I}_2 , the interferometer is rather insensitive to deviations on g that are aligned with the gravitational vector and even on g itself. Note that the optical setup will tilt slightly over time as quantified in table 7.8. As this tilt is smaller than the considered minimal misalignment relative to the gravitational field $\Theta = 0.01^\circ = 175 \mu\text{rad} \gg 10 \mu\text{rad}$, this systematic effect can be neglected. The situation is different for a horizontally aligned mirror where the interferometer gains in sensitivity but not enough to resolve Earth tides which is the major contribution of temporal deviations. In the present case of very-cold neutrons at the PF2 these effects can be neglected as measurements will be constrained statistically¹⁷.

5.6.3.3. Sagnac Effect Phase Shift

Due to Earth’s rotation a phase shift $\Delta\varphi_{\text{sagnac}}$ caused by the Sagnac effect is introduced as for example discussed in Helmut Rauch and Samuel A. Werner (2015)

$$\Delta\varphi_{\text{sagnac}} = \frac{2m}{\hbar} \vec{\omega}_e \vec{A} \quad (5.69)$$

¹⁷Even if a measurement could be performed on a level where these effects would be significant, they can be corrected as it is, for example frequently done for Earth tides as also used in Peters, Chung and Chu (2001).

5. Theory

where ω_e is the Earth's angular rotational vector and A the enclosed area. The enclosed area was already stated in the previous section as

$$\Delta\varphi_{\text{sagnac}} = \frac{2m}{\hbar} |\vec{\omega}_e| |\vec{A}| \cos(\theta) \quad (5.70)$$

$$= \frac{2m}{\hbar} |\vec{\omega}_e| \frac{aLy}{a+y} \cos(\theta) \quad (5.71)$$

where $|\vec{\omega}_e| = (7.292115 \cdot 10^{-5} \pm 1 \cdot 10^{-11}) \text{ rad/s}$ ¹⁸ is the mean angular speed of Earth's rotation and $\theta = (0.781801 \pm 2 \cdot 10^{-6}) \text{ rad}$ is the angle between Earth's rotational vector and the normal vector of the enclosed area \vec{n}_A at the experimental position at the ILL¹⁹. Using standard parameters and $y = y_{\varphi=1/4\pi(2n+1)}$ the phase shift becomes

$$\Delta\varphi_{\text{sagnac}} = 15 \cdot 10^{-3}, \quad (5.72)$$

thus it has to be precisely modeled if the full interferogram is to be interpreted for the composition of the total phase shift.

5.6.3.4. Phase Shift due to a Magnetic-Field

As long as only a homogeneous magnetic field \vec{B} is present no phase shift will be introduced. An example for an inhomogeneous field is investigated in H. Rauch, Zeilinger et al. (1975) where a field is present in one interferometer path of a single silicon crystal interferometer. In appendix A.8.3 phase shifts due to different orientations of a magnetic field gradient relative to the interferometer plane are calculated. For example, one can assume a magnetic field

$$\vec{B} = \begin{pmatrix} B_x(y) \\ 0 \\ 0 \end{pmatrix}. \quad (5.73)$$

that acts in a single direction and in this case the y -direction. The phase shift for the spin up component is given by equation (A.150) as

$$- \frac{\hbar^2 k \Delta\varphi_{\text{Mag,+}}}{m\mu_n} = \frac{\cos \alpha_I L}{y-a} \int_a^y d\hat{y} B_x(\hat{y}) - \frac{\cos \alpha_{II} L}{y+a} \left(\int_0^a d\hat{y} B_x(\hat{y}) + \int_0^y d\hat{y} B_x(\hat{y}) \right) \quad (5.74)$$

¹⁸Note that $|\vec{\omega}_e|$ is not a constant but is varying due to tidal effects. For the given value and a model of variational effects see Petit and Luzum (2010).

¹⁹The Institut Laue-Langevin reactor is at a latitude of 45.206112° . The stated uncertainty is estimated from the uncertainty of the exact experiment position.

where α_n is the angle between axis and momentum of the neutron in path I or path II and μ_n is the magnetic moment of the neutron. Assuming a linear field gradient of $\frac{\partial}{\partial y}B_x(y) = b$ the phase shift becomes

$$\Delta\varphi_{\text{Mag},\pm} = \mp \frac{m}{\hbar^2 k} \mu_n b \frac{ayL}{a+y} \quad (5.75)$$

as stated in equation (A.152). Note that this shift is identical to the gravitational phase shift in the case $\theta = \pi/2$ in which gravity acts perpendicular to the mirror plane. Due to the smallness of this phase shift earth's magnetic field can be neglected as systematic influence in the interferometer. In general, magnetic contributions can be neglected as long as no component introduce strong gradients in the experiment. The ambient magnetic field strength as measured in the interferometer setup without shielding during beam-time *Test-2455* is below $B < 40 \mu\text{T}$ and changes over time on the level of $\Delta B \approx 2\%$. By unrealistically assuming that the magnetic field drops off over the vertical extension of the interferometer one can set $b = 4 \mu\text{T}/\text{mm}$. This yields a phase shift between spin up and spin down components of

$$|\Delta\varphi_{\text{Mag},+} - \Delta\varphi_{\text{Mag},-}| = |\Delta 2\varphi_{\text{Mag},+}| = 1.6 \cdot 10^{-7}. \quad (5.76)$$

Presently, this contribution can be neglected as long as the gradient is not higher than the values measured during *Test-2455*.

5.6.3.5. Phase Shift due to Casimir Effect

A Casimir-Polder potential of a neutron due to its magnetic moment in front of an electrical conducting surface is proposed in Gebhart, Klatt and Buhmann (2016). It is given by

$$U_{\text{casimir, PF}} = \frac{\hbar^2}{64\pi y^3} \gamma^2 \mu_0 \quad (5.77)$$

with $\gamma = g_n e_0 / (2m)$, the g-factor of the neutron $g_n = -3.8$, and the vacuum permeability μ_0 . The phase shift in Lloyd's mirror due to this potential is calculated in appendix A.8.2 and is given in equation (A.137) as

$$\Delta\varphi_{\text{Casimir}} = \frac{m\gamma^2 \mu_0 L}{128\pi k} \left(\frac{a^3 + y^3}{a^2 y^2 (a^2 + y^2)} - \frac{1}{(y+a)y_{\text{min}}^2} \right) \quad (5.78)$$

$$\approx -\frac{m\gamma^2 \mu_0}{128\pi k} \frac{L}{(y+a)y_{\text{min}}^2}. \quad (5.79)$$

5. Theory

As the potential diverges for $y = 0$, a lower cutoff y_{\min} is introduced and is set to be $y_{\min} = \lambda_{\perp}/4$ with the perpendicular component $\lambda_{\perp} = 2\pi/k_{\perp}$ relative to the mirror's surface. This estimate cuts between first maximum of a wave and the mirror. k_{\perp} is estimated using the first zero of the single slit diffraction which is approximately the steepest angle under which a neutron can hit the mirror in the main interference region. This angle is discussed in section 5.5.2 and thus the lower limit is given as $y_{\min} \approx 2 \cdot 10^{-6}$ m. The resulting phase shift is rather small around

$$|\Delta\varphi_{\text{casimir}}| < 5 \cdot 10^{-6} \quad (5.80)$$

and highly dependent on the value of y_{\min} . Note, that a more refined calculation method is needed to assess the suitability of this phase shift as measurement quantity. The phase shift is calculated for $\lambda = 6.3$ nm and standard parameters. Additional to the potential for the perfect conducting surface also other models are proposed in Gebhart, Klatt and Buhmann (2016). In mind of a rough estimation, the perfect conducting surface potential is used as it offers the potential with the highest magnitude. Further models are not considered in this work.

5.6.4. Non-Standard Model Effects

Lloyd's mirror can be used as a probe for physics beyond the Standard Model. Several proposed models beyond the Standard Model of particle physics would lead to measurable effects. Three hypothetical models are introduced and their contributions will be discussed. The phase shift of a hypothetical chameleon field, a hypothetical axion and non-Newtonian gravity are discussed in the following.

5.6.4.1. The Chameleon Field

Section 2.4 introduced the hypothetical chameleon field that is proposed by Khoury and Weltman (2004) to resolve the cosmological dark energy problem. At the moment, the strictest limits are stated in Hamilton et al. (2015) using atom-interferometry. Selected previous limits were presented in Burrage, Copeland and Hinds (2015) reanalyzing atom-interferometry data, in Jaffe et al. (2017) deriving from recent cesium interferometer experiments, in H. Lemmel et al. (2015) for neutron-interferometry, and in Cronenberg (2015) for the current strictest limit deriving from a neutron experiment.

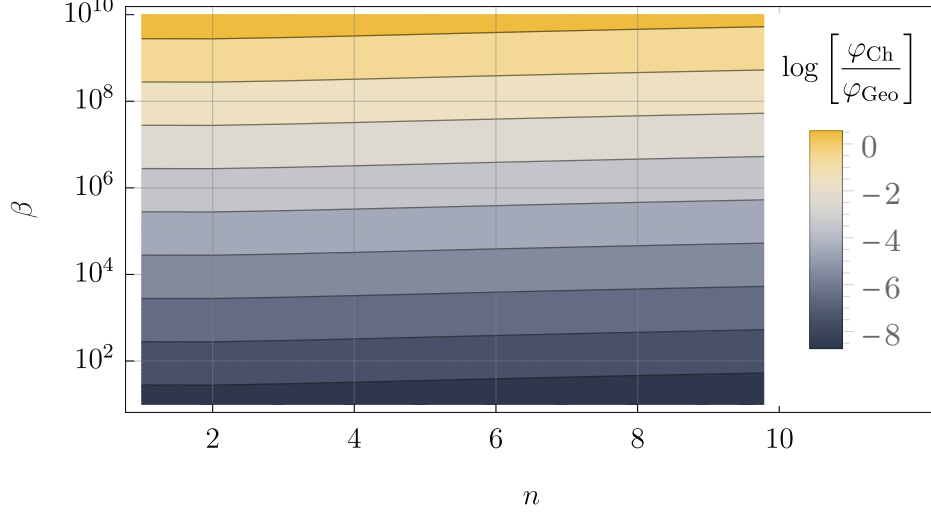


Figure 5.26.: The logarithm of the relative chameleon phase shift $\Delta\varphi_{\text{cham}}/\Delta\varphi_{\text{geo}}$ as a function of the relative interaction strength β and the Ratra-Peebles index n . The dependence on n is rather small as can also be seen in the depiction of the expected sensitivity in figure 5.27.

The phase shift due to a chameleon field in Lloyd's mirror is introduced in Pokotilovski (2013a). There the phase shift is given as

$$\Delta\varphi_{\text{cham}} = \frac{\gamma\beta}{\lambda_{\text{DE}}^{\alpha-1}\alpha} 2ay \frac{y^{\alpha-1} - a^{\alpha-1}}{y^2 - a^2} \quad (5.81)$$

with $\alpha = (4+n)/(2+n)$,

$$\gamma = \zeta \frac{mL}{k\hbar^2} \left(\frac{2+n}{\sqrt{2}} \right)^{\frac{2}{2+n}} \quad (5.82)$$

and the parameter $\zeta = 0.9 \cdot 10^{-21}$ eV with $\lambda_{\text{DE}} = \hbar c/\Lambda_{\text{scale}}$ and $\Lambda_{\text{scale}} = (\hbar^3 c^3 \rho_{\text{DE}})^{1/4} \approx 2.24$ meV the dark energy scale and $\rho_{\text{DE}} = (3.3 \pm 0.03)$ keV/cm³ the dark energy density as given in section 2.2. The chameleon field is parametrized by the interaction strength relative to gravity β and the Ratra-Peebles index n . Figure 5.26 shows the relative phase shift $\Delta\varphi_{\text{cham}}/\Delta\varphi_{\text{geo}}$ as a function of β and n . $\Delta\varphi_{\text{geo}}$ is defined in equation (5.36). Note that the predicted phase shift can be substantial, as first noted in Pokotilovski (2013a).

Assuming that the chameleon interaction is fully turned on and off in a measurement, equation (5.60) leads to a sensitivity to a chameleon field of

$$\delta\beta = \frac{1}{\sqrt{2N_{\text{max}}}} \frac{1}{\left. \frac{\partial}{\partial y} |\Psi_{\mathcal{L}}|^2 \right|_{y_s}} \left(\frac{\lambda_{\text{ch}}^{\alpha-1}}{\gamma} \frac{\alpha}{2ay_s} \frac{y_s^2 + a^2}{y_s^{\alpha-1} - a^{\alpha-1}} \right) \frac{2\pi}{\lambda_{\mathcal{L}}} \quad (5.83)$$

5. Theory

where $y_s = y_{\varphi=1/4\varphi(2n+1)}$, and $\Delta y_{\text{cham}} = \Delta\varphi_{\text{cham}} \frac{\lambda_{\mathcal{L}}}{2\pi}$ was used.

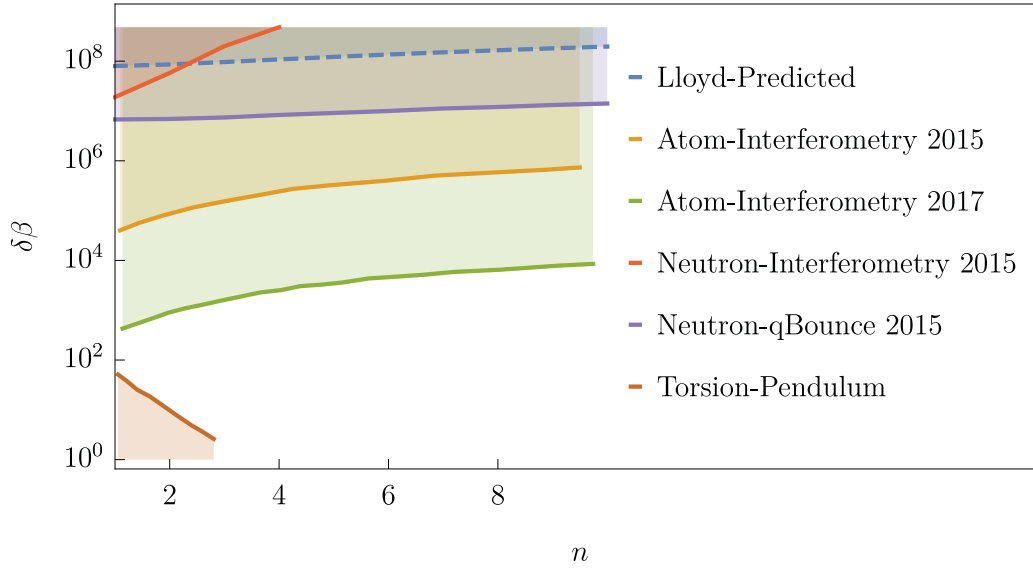


Figure 5.27.: The statistical sensitivity of Lloyd’s mirror for a chameleon field for standard parameters of the setup compared to current limits. The limits from neutron interferometry are taken from H. Lemmel et al. (2015), the limits from the qBounce experiment are taken from Cronenberg (2015) and limits from atom interferometry in 2015 as well as from torsion pendulum experiments are taken from Hamilton et al. (2015). The most recent limits deriving from atom interferometry are stated in Jaffe et al. (2017). The sensitivity is calculated using the intensity explained in equation (6.19) which is calculated for a $1.2\ \mu\text{m}$ wide scanning slit and an integration time of one week.

The sensitivity expected from different configurations of Lloyd’s mirror are shown in figure 5.27 together with current limits on the interactions given by different experiments. The recent limits given by atom interferometry already exclude the range that can be hoped to be tested with Lloyd’s mirror if the phase shift as given in Pokotilovski (2013a) is assumed. It is to be checked if this is still true, if recent progress in the formulation of the chameleon interaction, especially for table top experiments, are taken into account as discussed in H. Lemmel et al. (2015). For $n = 1$, at the slope point $y_s = y_{7/4\pi} = 42\ \mu\text{m}$, and for the intensity taken from equation (6.19), the sensitivity per time is given as

$$\delta\beta = 1.8 \cdot 10^8 \frac{1}{\sqrt{\text{days}}} \quad (5.84)$$

and for an increase of a factor six the sensitivity per day becomes

$$\delta\beta = 2.9 \cdot 10^7 \frac{1}{\sqrt{\text{days}}}. \quad (5.85)$$

5.6.4.2. The Axion

Using the Lloyd's mirror as a probe for a hypothetical axion particle is first proposed in Pokotilovski (2011) and the effect is introduced in section 2.4.

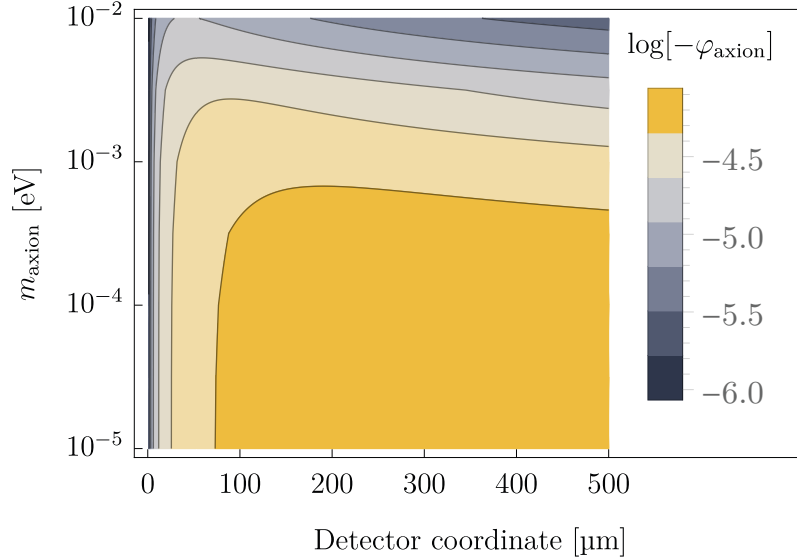


Figure 5.28.: Shown is the phase shift in Lloyd's mirror for standard parameters due with a coupling to a hypothetical axion.

The potential from an interaction of a neutron with the surface of the mirror is given in Pokotilovski (2013b) as

$$U_{\text{mon-dip}} = \pm g_s g_p \frac{\hbar^2 N \lambda}{4m} (e^{-y/\lambda_{\text{ax}}} - e^{-(y+d)/\lambda_{\text{ax}}}) \quad (5.86)$$

where $g_s g_p$ are the coupling constants for a monopole-dipole interaction, $\lambda_{\text{ax}} = \hbar/(m_{\text{ax}} c)$ is the interaction range, and m_{ax} is the mass of the axion.

The phase shift is calculated in Pokotilovski (2011) to be

$$\Delta\varphi_{\text{axion}} = \frac{2g_s g_p \gamma \lambda_{\text{ax}}}{y^2 - a^2} (a(1 - e^{-y/\lambda_{\text{ax}}}) - y(1 - e^{-a/\lambda_{\text{ax}}})) \quad (5.87)$$

with $\gamma = N\lambda_{\text{ax}}\lambda L/(8\pi)$ and is shown in figure 5.28 for different m_a , as a function of y , and for $g_s g_p = 10^{-18}$. Again the sensitivity of Lloyd's mirror to an axion interaction is

5. Theory

calculated by assuming a scanning slit measurement. This leads to an adaptation of the equation (5.60) for $\xi = g_s g_p$ as follows

$$\delta g_s g_p \approx \frac{1}{\sqrt{2N_{\max}}} \frac{2\pi}{\lambda_{\mathcal{L}}} \left(\frac{\partial}{\partial y} P(y, 0) \Big|_{y_s} \right)^{-1} \frac{1}{2\gamma\lambda_{\text{ax}}} \frac{y^2 - a^2}{a(1 - e^{-y/\lambda_{\text{ax}}}) - y(1 - e^{-a/\lambda_{\text{ax}}})}. \quad (5.88)$$

The resulting sensitivity is shown in figure 5.29 as a function of the axion mass.

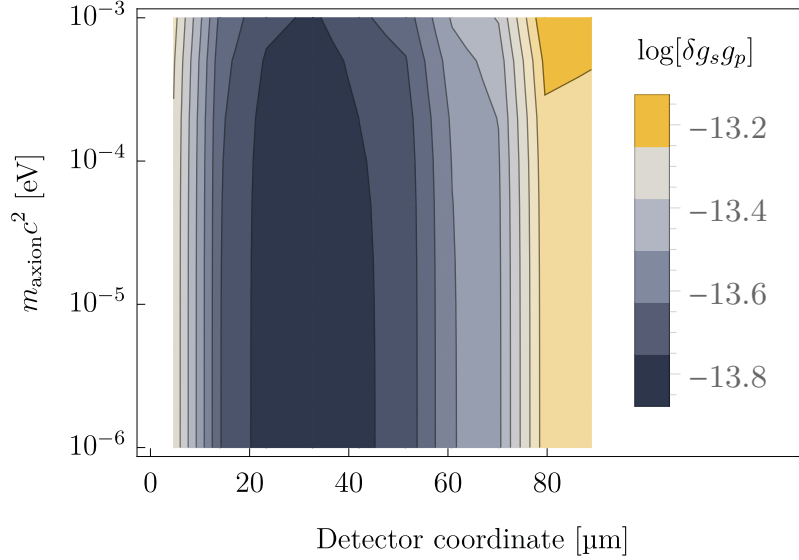


Figure 5.29.: Shown is the sensitivity of Lloyd's mirror for standard parameters to the coupling strength $g_s g_p$ and for a measurement period of one week assuming the neutron intensity extrapolated in section 7.1.4.

The best sensitivity is found for an implementation with standard parameters at $n = 3$ for $y_s = y_{\pi 1/4(2n+1)} \approx 33 \mu\text{m}$ and for $m_{\text{ax}} c^2 \sim 10^{-6} \text{ eV}$ with

$$\delta g_s g_p \approx 1.3 \cdot 10^{-14} \frac{1}{\sqrt{\text{days}}} \quad (5.89)$$

for a wide range of m_{ax} and at neutron wavelength of $\lambda = 6.3 \text{ nm}$. In the case of an increase of the intensity by a factor of forty in neutron intensity this becomes

$$\delta g_s g_p \approx 7.9 \cdot 10^{-16} \frac{1}{\sqrt{\text{days}}}. \quad (5.90)$$

In Afach et al. (2015) strict limits to the coupling strength $g_s g_p$ are given for an axion mass range of $10^{-1} \text{ eV} > m_{\text{ax}} c^2 > 10^{-5} \text{ eV}$ determined by laboratory experiments. Note that this mass range corresponds to an interaction range of $0.02 \text{ m} > \lambda_{\text{ax}} > 0.2 \cdot 10^{-6} \text{ m}$.

These and other limits together with the expected sensitivity of Lloyd’s mirror are shown in figure 5.30. The sensitivity of Lloyd’s mirror is calculated for standard parameters and the neutron intensity determined in section 7.1.4.

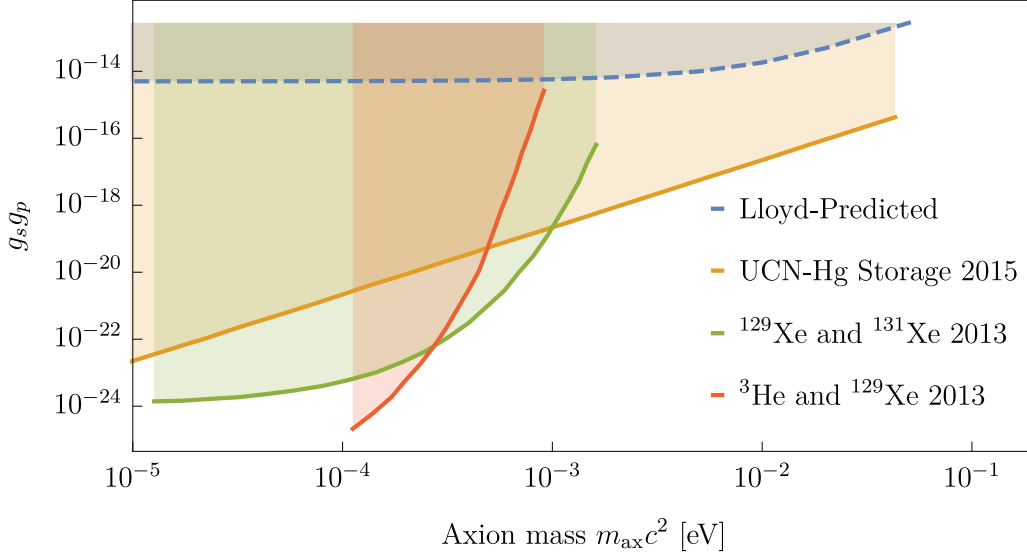


Figure 5.30.: Shown are current limits of the coupling strength $g_s g_p$ for different axion masses extracted from Afach et al. (2015). The limits for ^{129}Xe and ^{131}Xe 2013 are first presented in Bulatowicz et al. (2013) and for ^3He and ^{129}Xe 2013 are first presented in Allmendinger et al. (2013). Finally, the expected sensitivity of Lloyd’s mirror to a hypothetical axion using standard parameters is included. It is assumed that using Lloyd’s mirror the measurement is integrated over one week.

As in the case of the searches for a chameleon field, the sensitivity of Lloyd’s mirror implemented at the PF2 does not cover a not yet probed parameter space. This is even true if the neutron intensity can be enhanced by several orders of magnitude.

5.6.4.3. Gravitational Torsion

In Ivanov and Wellenzohen (2016) the connection between gravitational torsion in General Relativity and the phenomenon of dark energy is discussed. The hypothetical effect of gravitational torsion is also briefly sketched in section 2.4.

The phase shift due to gravitational torsion is stated in Ivanov (2016, priv. comm.) as

$$\Delta\varphi_{\text{torsion}} = \mathcal{B}_z \frac{mc}{2\hbar k} \frac{ay}{L}, \quad (5.91)$$

5. Theory

where \mathcal{B}_z is the axial component of the torsion tensor. An upper bound for \mathcal{B}_z is given in a recent summary of Lorentz violation searches in Kostelecký, Russell and Tasson (2008). The upper bound is given as

$$\mathcal{B}_z = 1.7 \cdot 10^{-14} \frac{1}{\text{m}}. \quad (5.92)$$

The induced phase shift would be on the order of $\Delta\varphi_{\text{torsion}} \sim 10^{-16}$ and thus be considerably smaller than most of the previously discussed effects in Lloyd's mirror. Thus, a measurement of this hypothetical effect in the scope of an implementation of Lloyd's mirror at the PF2 is not realistic.

5.7. Summary

Recapitulating this chapter, relevant standard theoretical tools of diffraction experiments are discussed and applied to Lloyd's mirror. In particular the theoretical foundation for Lloyd's mirror is reproduced and extended upon to model the expected interferogram in an ideal setup. Especially the wave function for the ideal setup with an infinite mirror $\Psi_{\mathcal{L},\text{st}}$ and an approximation of the wave function for the finite mirror $\Psi_{\mathcal{L},F}$ are presented. Extended calculations are referenced to and explained in detail in appendix A, for example the time-dependent solution which is used to justify the approximation of a setup with a finite mirror. Following these deliberations, the phase shifts caused by different effects are given and the sensitivity to small disturbances is calculated. Most phase shifts are taken from literature i.e. from Helmut Rauch and Samuel A. Werner (2015) and from Pokotilovski (2013a). The calculation for the phase shift of the Casimir-effect are presented in appendix A.8.2.

After introducing standard tools of diffraction theory, two standard examples, the single-slit and the straight edge are discussed. Both, model diffraction at a thin object which is well in the scope of the Kirchhoff-diffraction formula. This is not the case for Lloyd's mirror as the mirror extends along the propagation axis. To solve this problem one can use Green's identity which relates the solution of a differential equation in a volume to its derivative on the surface of the same volume. Using basic symmetries of the system, Green's identity is applied to Lloyd's mirror and the solution is compared to the plane wave solution of Lloyd's mirror in section 5.5.2 and the tangential phenomenon of the straight edge in section 5.5.2.5. The solutions for the infinite and finite mirror setups are shown in figure 5.13.

In conclusion, this provides several important results: The solution $\Psi_{\mathcal{L},st}$ given in equation (5.44) which derives from using Green's identity, correctly reproduces the single-slit diffraction near the slit and in addition produces a pattern with a period corresponding to $\lambda_{\mathcal{L}}$ near the mirror for sufficient distance to the slit. For $\Psi_{\mathcal{L},st}$ the period of the interferogram is not a constant anymore and diverges from $\lambda_{\mathcal{L}}$ with growing distance from the vertical mirror. For the case of an observation of the pattern with a distance between mirror and detector which is discussed in section 5.5.2.1 the resulting solution $\Psi_{\mathcal{L},F}$ has a period that closely resembles the behavior of $\Psi_{\mathcal{L},st}$. As expected, the pattern of $\Psi_{\mathcal{L},F}$ has a slightly lower contrast and a propagation of the first maximum into the region behind the mirror with growing distance from the slit in the propagation direction. As a verification of the validity of the theoretical calculation in section 5.5.2.3, Lloyd's mirror is implemented using a laser optical setup at a wavelength of $\lambda = (653 \pm 0.3)$ nm. Indeed, the measured pattern can be closely modeled using $\Psi_{\mathcal{L},F\beta}$ which models a finite mirror with an additional propagation region and non-normal incident of the beam on the entrance slit. Only at an intermediate point of the pattern a significant deviation is visible which is probably due to the extension of the entrance slit in the direction of propagation. Finally, the detector contribution is estimated based on the reflectivity of the surface facing the neutron beam. The reflectivity of the used boron coating is negligible at $R < 10^{-5}$ as discussed in section 5.5.2.4 and thus also the detector contribution can be neglected if the finite mirror model is used. In section 5.6 small phase shifts

Effect	$\Delta\varphi$ Magnitude	Measurement Scenario	Information
Reflection	$\sim 20 \cdot 10^{-3}$	Interferogram	Section 5.6.3.1
Gravity	$< 0.4 \cdot 10^{-3}$	Comparison (Rotation)	Section 5.6.3.2
Gravity (v. drop)	$< 50 \cdot 10^{-6}$	Comparison (Rotation)	Section 5.6.3.2
Sagnac	$15 \cdot 10^{-3}$	Interferogram	Section 5.6.3.3
Magnetic	$< 10^{-7}$	Comparison (External field)	Section 5.6.3.4

Table 5.5.: Summary of phase shifting effects which are present in an experimental realization. All phase shift magnitudes are given for standard parameters as given in table A.3. The measurement scenario describes a method to change the effect magnitude and discern it from other effects.

due to additional potentials present in the interferometer region are considered. Many effects are already considered in Helmut Rauch and Samuel A. Werner (2015) and are adapted as Lloyd's mirror is topologically analogous to a two-path interferometer. The relevance of these effects is considered with respect to a measurement. Further, hypothetical non-Standard Model effects, as for example the shift due to a chameleon field,

5. Theory

are introduced in Pokotilovski (2013a). Here the expected sensitivity to selected effects of Lloyd’s mirror at the PF2 is calculated. Table 5.5 summarizes the discussed phase shifting effects and gives the sensitivities per day. Note that the sensitivity depends on the intensity \mathcal{I} which can be calculated from equation (6.19) at the detector plane and thus is dependent on the specific experimental implementation. The used beam intensity is the expected intensity due to the already realized beam preparation as is discussed in chapter 7 which fulfills the resulting constraints to a realization in chapter 6.

Distinguishing two measurement goals, different priorities can be given to these effects. While the Sagnac effect and gravitational effects can be neglected for a first verification of Lloyd’s mirror with neutrons, the homogeneity of the magnetic field in the interferometer region needs to be controlled. If the experiment is to reach the realm of a high precision measurement instrument, also the previously neglected effects are to be addressed. For example, in the case of gravity this means independent measurements of the local acceleration, an accurately vertically aligned mirror and, in case the of the magnetic field, an accurate monitoring of the magnetic field is necessary.

A summary of these effects is shown in table 5.5. In table 5.6 the sensitivities due to different hypothetical scenarios are listed. In summary, it has to be stated that the here

Effect	Sensitivity \mathcal{I}_{\max}	Sensitivity \mathcal{I}_2	Measurement Scenario
Chameleon ($\delta\beta$)	$1.8 \cdot 10^8 \frac{1}{\sqrt{\text{day}}}$	$2.9 \cdot 10^7 \frac{1}{\sqrt{\text{day}}}$	Pressure Variation
Axion ($\delta g_s g_p$)	$1.3 \cdot 10^{-14} \frac{1}{\sqrt{\text{days}}}$	$7.9 \cdot 10^{-16} \frac{1}{\sqrt{\text{days}}}$	—
Effect	$\Delta\varphi$ Magnitude		Measurement Scenario
Casimir	$> -5 \cdot 10^{-6}$		Interferogram
Torsion	Expected effect too small to be measured in Lloyd’s mirror.		

Table 5.6.: Summary of phase shifting effects due to hypothetical effects. All phase shift magnitudes are given for standard parameters as defined in table A.3. \mathcal{I}_{\max} is the neutron intensity measured and extrapolated in section 7.1.4 and section 6.2.4 while $\mathcal{I}_2 = 40\mathcal{I}_{\max}$.

discussed hypothetical effects are outside the scope of Lloyd’s mirror implemented at the PF2 considering the already excluded parameter space. Further, it is clear that in order to capture the interferogram of Lloyd’s mirror, several expected effects need to be considered and even decreased. This is true for temporal and spatial variations of the magnetic field, and effects due to gravitation.

6. Dimensioning and Simulation

For an implementation of Lloyd’s mirror with matter waves the calculations in the previous chapter are adapted to account for realistic beam characteristics. For example, a finite spectral width $\Delta\lambda/\lambda$ and a finite detector resolution are considered in section 6.3. Although, as will be seen in section 6.4, it is in principle possible to produce an interference pattern at the available wavelength with all geometrical constraints in mind, a limited very-cold neutron flux at the entrance slit \mathcal{F}_{S1} could easily push the needed measurement time into an infeasible domain. Thus, before analyzing constraining parameters the measurement procedure needs to be defined. Figure 6.1 gives an overview over the planned general setup and its most relevant features for this section.

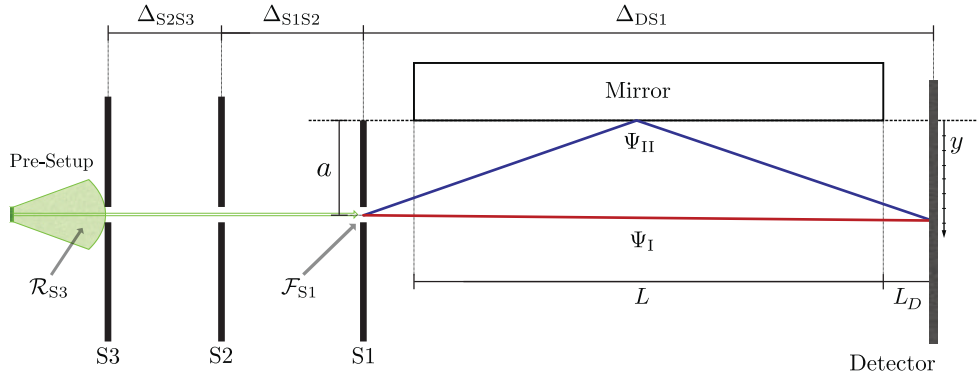


Figure 6.1.: Relevant components and quantities for the simulation. The y -axis is synonymously called ‘detector-coordinate’. \mathcal{F}_{S1} is the flux at the plane of slit S1 and \mathcal{R}_{S3} is the radiance at the plane of slit S3.

First measurement procedures are discussed in the following section and then in section 6.2 practical constraints are considered. Finally, a simulation of the interferometer is presented in section 6.3.

6.1. Measurement Procedure

In chapter 5 the basic wave functions for various configurations of Lloyd's mirror are presented and phase shifts due to external perturbations (gravity, Sagnac effect, ...) are calculated. These calculations are now used to define specific measurement scenarios. As for example to check the validity of the calculation for the static wave function for an infinitely long mirror and the model for a finite mirror as presented in section 5.5.2. Besides verification of the theoretical framework for Lloyd's mirror it is of special interest to investigate use-cases. These are for example possible searches for hypothetical fifth forces and particles beyond the Standard Model of particle physics or verifications of quantum mechanics and gravity which jointly act in Lloyd's mirror. For practical purposes the neutron energy is restricted to the range of very-cold neutrons which can be treated analog to standard optics as is discussed in Eder et al. (1989) and section 3.2. The wavelength range of interest is thus (1 → 50) nm. An incomplete overview of available neutron beams is shown in appendix A.2.

6.1.1. Theoretical Framework Verification

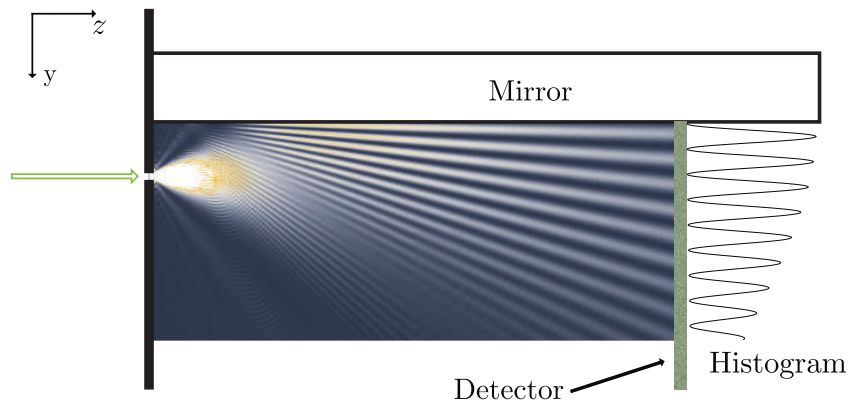


Figure 6.2.: Measurement scheme for full interferogram detection. The detector can be a spatially sensitive detector or a scanning slit/grid setup.

If the interference pattern is of sufficient size, a spatially sensitive detector can be employed to directly capture the interferogram as shown in figure 6.2.

It can be estimated that for a very-cold neutron beam with mean wavelength $\lambda = 6$ nm, a reasonable interferometer size of $L = 1$ m and a mirror-slit distance of $a = 50$ μm the period of the interference pattern is $\lambda_{\mathcal{L}} = 60$ μm as given by equation (5.39). Figure 6.3 shows $\lambda_{\mathcal{L}} = \lambda L / (2a)$ as function of L and λ . A recurring quantity is the angle $\beta = L/a$

which is useful as a characteristic of the interferometer. More implementation examples are shown in table 6.1 for different instruments. As is shown in section 5.5.2.1 the pattern will expand while still adhering to equation (5.39). In addition to the mirror length also the available flight path will be included in table 6.1.

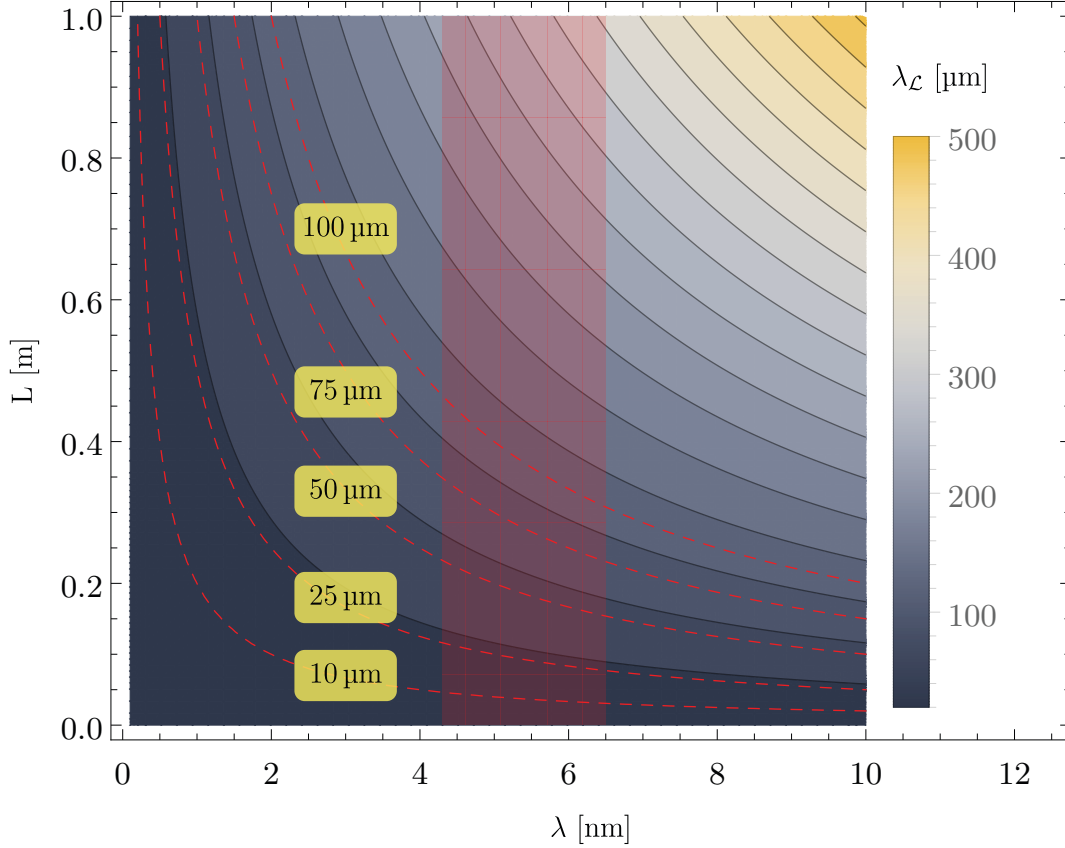


Figure 6.3.: The period of the interference pattern λ_C as a function of the mirror length L and wavelength λ . The distance between slit and mirror surface a is taken to be constant at $a = 1 \mu\text{m}$. The red square marks the region accessible at the PF2 very-cold neutron source at the ILL. See section 3.3 for the characteristics of the very-cold neutron beam at the PF2.

If the interferogram is to be captured directly behind the mirror, a detector with a spatial resolution of the order of a few micrometers is needed. For a detector that is placed at a distance L_D to the mirror, this can be slightly relaxed¹ as is shown in section 5.5.2.1. For the same parameters as above, but with an additional flight path of $L_D = 5 \text{ m}$, the period at the detection plane becomes $\lambda_C = 300 \mu\text{m}$.

¹Nevertheless, coherence and diffraction constraints need to be fulfilled independently. This is the topic of section 6.2.

6. Dimensioning and Simulation

Instrument	L [m]	λ [nm]	$\lambda_{\mathcal{L}}$ [μm] $a = 53 \mu\text{m}$	$\lambda_{\mathcal{L}}$ [μm] $a = 100 \mu\text{m}$
PF2-VCN	5	6.3	297	158
PF2-VCN	0.34	6.3	20	10.7
D11	34	3.5	1091	578
D11	0.34	3.5	11	5.78

Table 6.1.: Comparison of implementations of Lloyd’s mirror at the PF2 and D11 and different mirror lengths. The individual instrument characteristics are summarized in appendix A.2.

As detection mechanism for $\lambda_{\mathcal{L}} > 4 \mu\text{m}$, image plates based on a ^{10}B converter as described in Jenke et al. (2013) can be used². Depending on the post-measurement treatment the spatial resolution³ can be as low as $\zeta \approx 1 - 2 \mu\text{m}$.

Instead of measuring the full interferogram in one take, it can be advisable to scan the pattern with a small slit as it has been done in neutron double-slit experiments by Anton Zeilinger et al. (1988). For example, if $\lambda_{\mathcal{L}} \gg 4 \mu\text{m}$ such a scan removes the technical difficulty of a detector with micrometer resolution as a simple on-line detector would be sufficient. This is done at the expense of a reduced total neutron capture as the signal will be only partly be detected.

²Here the Nyquist-Shannon sampling criterion is used. It states that a periodic signal with frequency f_{signal} under optimal conditions can be reconstructed without aliasing, if sampled with doubled frequency $f_{\text{sample}} > 2f_{\text{signal}}$. Keep in mind that a measurement in the context of Lloyd’s mirror will not happen under optimal conditions and thus the distance between f_{sample} and f_{signal} has to be more than doubled. See Landau, Páez and Bordeianu (2008) for example applications of the Nyquist-Shannon sampling criterion.

³In the scope of this thesis a production process for these detectors and an analysis framework was developed. A detailed discussion follows in section 8.1.

6.1.2. Single-slit Scan with Varying Phase

If the basic features of the interferogram are known the measurement scheme can be simplified to allow for precise phase shift measurements. This scheme has already been discussed in section 5.6.2 where the sensitivity to a small phase shift is given. Instead of directly measuring the interferogram, a slit is used to capture only a small part of the pattern. Thus, figure 6.4 is the intensity plotted over the slit position. If the effect under investigation can be tuned or switched

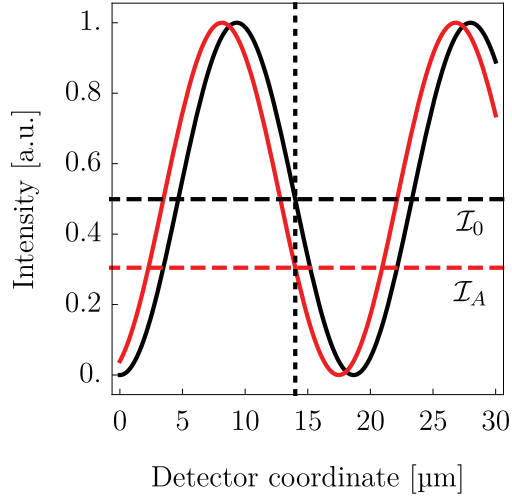


Figure 6.4.: Simplified measurement scenario for a varying phase shift. The black line corresponds to the intensity $\mathcal{I}(y, \Delta\varphi = 0) := \mathcal{I}_0$ and the red line to the intensity $\mathcal{I}(y, \Delta\varphi = \Delta\varphi_A) := \mathcal{I}_A$.

off, the measurement can be reduced to a measurement of the change in intensity while tuning. Note that the extension of the slit reduces the visibility of the probability density as shown in figure 6.5, as the probability density has to be convoluted with the slit transmission function \mathcal{T} . The transmission function can be assumed to be a rectangular function as used and defined in figure 6.5.

A switchable effect A which results in a phase shift $\Delta\varphi_A$ is assumed in the following. The setup needs to distinguish between unaffected intensity $\mathcal{I}(y, \Delta\varphi = 0) := \mathcal{I}_0$ and the shifted pattern $\mathcal{I}(y, \Delta\varphi = \Delta\varphi_A) := \mathcal{I}_A$. If only one detector dimension y_n is considered, the goal is to show a significant deviation of $\Delta\mathcal{I} = \mathcal{I}_0 - \mathcal{I}_A$. The uncertainty of $\Delta\mathcal{I}$ is given by

$$\delta(\Delta\mathcal{I}) = \sqrt{(\delta(\mathcal{I}_0))^2 + (\delta(\mathcal{I}_A))^2}, \quad (6.1)$$

and for a significant measurement $\Delta\mathcal{I} < \mathcal{S}\delta(\Delta\mathcal{I})$ with \mathcal{S} being the significance.

In addition to the reduced complexity this scheme is especially powerful, as systematic effects present in both measurements will cancel out and only leave statistical fluctuations and deviations caused by the switching of the effect itself. An example in the case of Lloyd's mirror is the search for a hypothetical chameleon field which strongly depends on the gas pressure in the interferometer arms as is shown in section 5.6.4.1. If a chameleon field is present the phase shift will translate into a shift of the interference

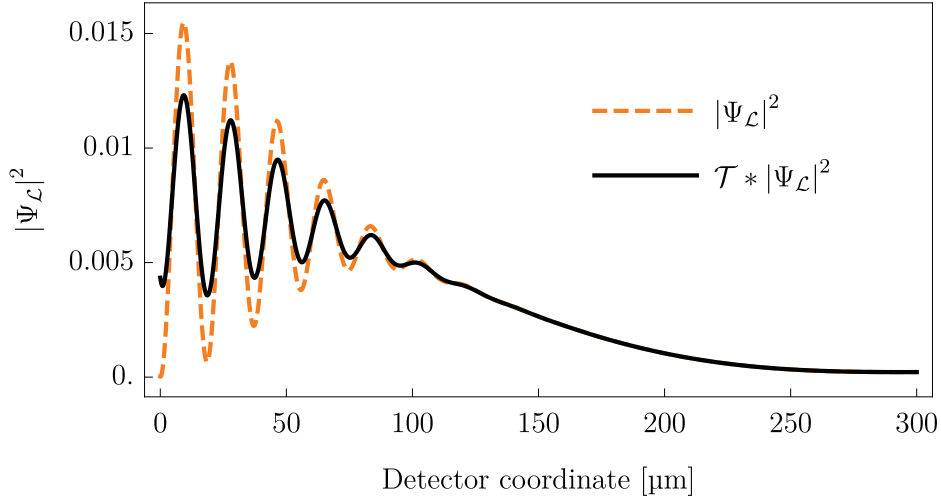


Figure 6.5.: Propability density of Lloyd’s mirror convoluted with the slits transmission function \mathcal{T} . It is calculated using the standard parameter as defined in appendix A.4 by $|\hat{\Psi}|^2 = |\Psi(y^*)|^2 * \mathcal{T}(y)$. Comparing the shown distribution to figure 5.13 one can note that the visibility even in the not convoluted case is still reduced. The reason is that by anticipating section 6.3.1.1 the measured wavelength bandwidth is already incorporated in $|\hat{\Psi}_L|^2$. The transmission function $\mathcal{T}(y)$ is assumed to be a rectangular opening with a width of $b_{\text{Scan}} = 10 \mu\text{m}$. Thus $\mathcal{T}(y) = 1$ if $|y| \leq |b_{\text{Scan}}|$ and $\mathcal{T}(y) = 0$ if $|y| > |b_{\text{Scan}}|$.

pattern and the previous scheme would be applicable. In section 6.2.4 the discussion of this scheme is continued and used to estimate the necessary measurement time for precision measurements.

6.2. Measurement Constraints

In the previous chapter different measurement scenarios were discussed to precisely define the experimental challenge. For the implementation of Lloyd’s Mirror requirements on the beam characteristics need to be set. Even at a very high flux neutron sources as at the Institut Laue-Langevin, the very-cold neutron density can be low, if certain beam constraints are to be fulfilled. Thus, the feasibility of an implementation highly depends on the required constraints and their strictness.

The following constraints are to be considered and will be discussed individually in sections 6.2.1 and 6.2.4:

— Angular Constraints

The incoming beam irradiating the entrance slit of the interferometer should be

as coherent as possible. Neutron sources produce incoherent beams, as the fundamental production mechanism is of statistical nature. Therefore, coherence can be achieved by restricting the angular spread i.e. the angular distribution. See for example Felber et al. (1998) for an educational overview of the phenomenon of coherence.

— Spatial Distribution

An inhomogeneous beam profile will lead to a distorted interferogram. If the 2-dimensional interferogram is to be captured, a reference image is needed to correct the pattern. In this setup, fluctuations in the vertical dimension can be neglected as they are integrated out during the binning process for the one-dimensional projection⁴. Additionally, note that for an inhomogeneous beam it can be time consuming to find the position of maximal intensity.

— Wavelength Distribution

If wavelengths are homogeneously and isotropically distributed and a small fraction is selected, $\Delta\lambda/\lambda$ and λ are sufficient measures for the wavelength distribution. This is not the case for the unprocessed beam of the very-cold neutron port at the PF2, as can be seen in section 7.1.1. For a monochromatized and collimated beam these two quantities are a sufficient approximation as will be shown in section 7.1.2 and section 7.1.3.

— Statistical Constraints

To gather enough statistics to resolve interference fringes on a reasonable time scale, the neutron beam needs to have a high enough brilliance \mathcal{B} while simultaneously fulfilling previous requirements.

6.2.1. Angular Constraints

The angular characteristics of a neutron beam play a major role in the realization of Lloyd's mirror. Foremost the prerequisite for the calculations in chapter 5 is an incoming coherent plane wave. It has to be shown that the beam can be prepared in a sufficient way. Further, it has to be checked if the condition for total reflectivity and the illumination of the mirror are fulfilled.

⁴See figure 6.15 for an example of an one-dimensional projection and figure 8.18 for an example of an two-dimensional map.

Wavefront Coherence Reactor neutrons are emitted from an extended volume, as for example a cold source (See section 3.3) inside the reactor, and they are fully incoherent because of their thermal origin⁵. Nevertheless, this kind of source coherence can be achieved by a propagation region and finite spatial selection. The basic idea is that free space propagation will blow up fluctuations and thus increase the volume where the phase relation is nearly constant. If an aperture cuts out this region, the result is a coherent beam. This concept is illustrated in figure 6.6 for a circular aperture. See Felber et al. (1998) for an educational introduction.

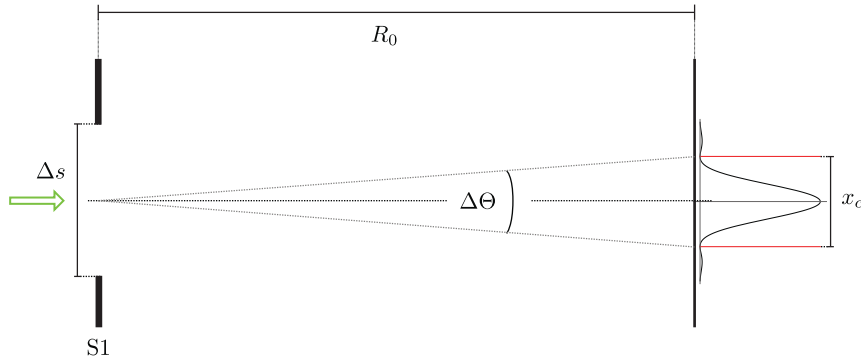


Figure 6.6.: Coherence patch x_c for a circular aperture S_1 with size Δs in a distance R_0 . See Mandel and Wolf (1995) for the popular double-slit deviation of the coherence patch.

The Van Cittert-Zernike theorem relates a source to the coherence at a specified downstream point as it is for example explained in Cowley (1995) and Mandel and Wolf (1995). There the case of interference in between two points in a screen that is irradiated by a finite incoherent circular source is analyzed. If the distance R_0 between the source and the screen is much higher than the object extension on the screen i.e. the far field requirement is fulfilled, visibility and coherence are equal and are given by

$$\gamma_{12} = \left(\mathcal{J}_1 \left(\frac{\pi \Delta s \Delta x}{R_0 \lambda} \right) \right) / \frac{\pi \Delta s \Delta x}{R_0 \lambda} \quad (6.2)$$

⁵For small angles $\theta < 1^\circ$ the angular distribution at neutron beams follows a $f(\theta) = \cos^2 \theta$ distribution. This has been shown for the very-cold neutron beam at the PF2 in the Thesis Heumesser (2016). Thus, the angular distribution does locally not deviate significantly from the expected distribution of neutrons emitted from a reactor and which are viewed from a certain solid angle.

Here, a is the source diameter, Δx is the point separation, R_0 is the source-screen distance and \mathcal{J}_1 is the first Bessel function. A coherent area called the coherent patch can then be approximated by the area between the first minima of \mathcal{J}_1 at

$$x_c = x_{1,2} = 1.22 \frac{\lambda R_0}{\Delta s} \quad (6.3)$$

$$\approx \frac{\lambda R_0}{\Delta s}. \quad (6.4)$$

Thus, the convenient relation for the coherent region of an incoherent source follows as

$$\lambda \geq \frac{\Delta s}{R_0} x_c \quad (6.5)$$

$$\geq \Delta\Theta x_c \quad (6.6)$$

with $\Delta\Theta = R_0/\Delta s$.

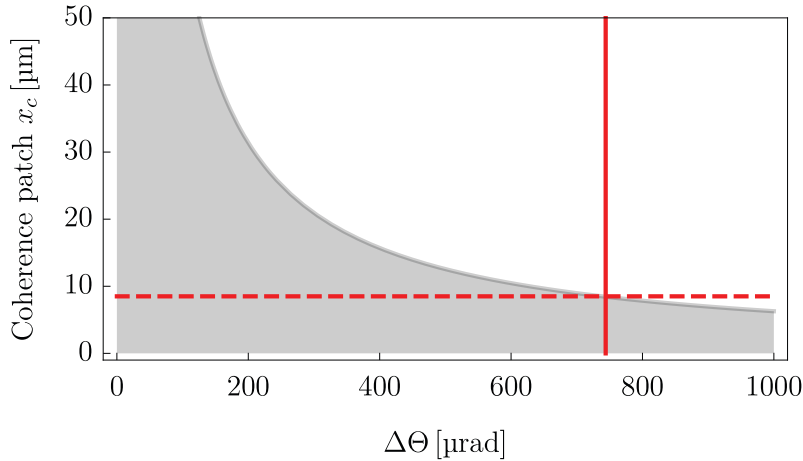


Figure 6.7.: Horizontal coherent region bound by x_c for different angles $\Delta\Theta$ and with a mean wavelength $\lambda = 6.3 \text{ nm}$. The horizontal dashed line is placed at the anticipated opening of the entrance slit $S1 = 8.5 \text{ μm}$ and the vertical red line is at the corresponding angular constraint.

If the entrance slit of the interferometer has a width of $x_c \geq S1 = 8.5 \text{ μm}$ and the mean wavelength is $\lambda = 6.3 \text{ nm}$, it follows that the angular distribution in front of the entrance slit has to be narrower as

$$\Delta\Theta \leq 0.74 \text{ mrad}. \quad (6.7)$$

Total Reflection Neutrons with a kinetic energy smaller than the optical potential of a barrier will reflect under every incident angle. See Golub, Lamoureux and Richardson (1991). The corresponding wavelength is called the critical wavelength and is given by

$$\lambda_{\text{crit}} = \sqrt{\frac{2\pi^2}{m} \hbar^2 V_{\text{opt}}^{-1}}. \quad (6.8)$$

For mirrors used in experiments with very-cold neutrons and ultra-cold neutrons several different materials are used. Here the incident surface is given by a thick coating of SiO₂ on top of a polished BK7 mirror⁶. The optical potential is thus given by $V_{\text{opt}} \approx 100$ neV and the critical wavelength evaluates to $\lambda_{\text{crit}} = 90.57$ nm. Neutrons faster than ultra-cold neutrons i.e. very-cold neutrons will totally reflect only if the incident angle is smaller than the critical angle α_{crit} which is given by

$$\alpha_{\text{crit}} = \arctan \left[\left(\left(\frac{E_{\text{kin}}}{V_{\text{opt}}} \right)^2 - 1 \right)^{-1/2} \right]. \quad (6.9)$$

Figure 6.8 shows the reflectivity for the relevant wavelength interval.

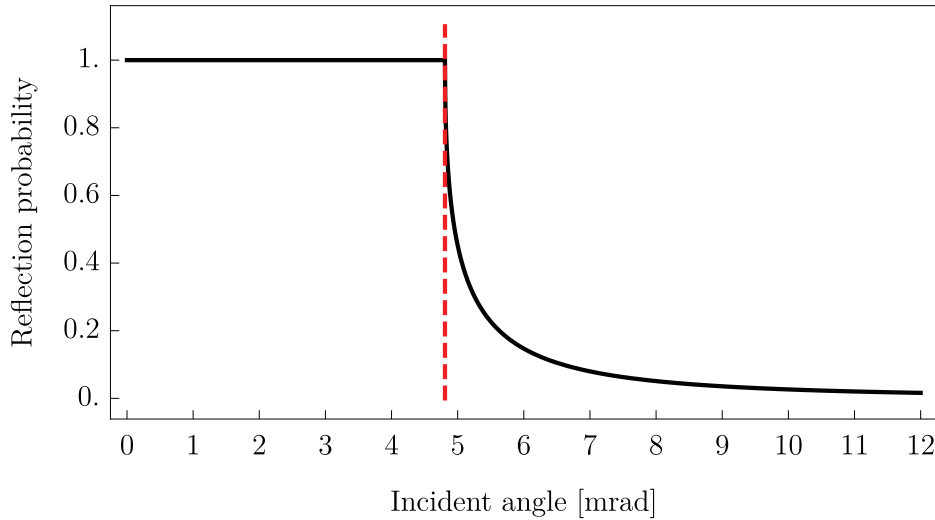


Figure 6.8.: Reflection at a thick SiO₂-surface plotted against the incident angle for neutrons with $\lambda = 6.28$ nm. The red line marks the angle of total reflection α_{crit} .

Shadow Region and Minimum Reflection Angle Previously in section 5.5.1 the geometrical shadow effect of a finite mirror is discussed without considering the entrance

⁶More information regarding the main mirror can be found in section 7.2.2. Additionally, the optical potential of different materials as used for this experiment is given in appendix A in table A.6.

slit. If the beam can only enter Lloyd's mirror at a specific height over the mirror a shadow region will form in which the incident beam does not illuminate the mirror. This can be seen in figure 5.12 where the incoming beam expands due to diffraction at the entrance slit until it reaches the mirror and reflects onto itself.

As the region where the beam is not yet reflected upwards can be described by single-slit diffraction, it is sufficient to consider equation (5.22) and its zeros

$$\beta_{\text{zero}} = \arcsin \left[\frac{\pm n\lambda}{D} \right] = \arctan \left(\frac{a}{L_n} \right), \quad (6.10)$$

where D is the slit width, n is the diffraction order and L_n is the mirror position of the n th zero. To produce a reasonable pattern, $\beta = \tan(a/L_I)$ should be smaller or equal to β_{zero} . In any case β_{zero} should be large enough so that the overall setup is reasonably small. Note that this feature is incorporated in $\Psi_{\mathcal{L},\text{st}}(\vec{r})$ given in equation (5.44) and thus can be quickly checked graphically.

6.2.2. Spatial Distribution

Neutrons which originate from the thermalization position i.e. the cold source should have a fairly homogeneous spatial distribution. If the position of extraction is placed far away from the thermalization position, local fluctuations will be washed out. Due to interactions a beam will gain structure again. For example, reflections can add fluctuations of the order of the size of the beam at the position of extraction, as it is seen at the very-cold neutron beam at the ILL. This will not interfere with a measurement in a practical way, as long as the chosen size of the extraction region is chosen much smaller than the fluctuations

$$\delta X_{\text{spatial}} \gg D. \quad (6.11)$$

D is the characteristic size of a beam component, e.g. a slit, which cuts out a small portion of the beam. The very-cold neutron beam at the PF2 is locally smooth $D_{\text{Horizontal}} \approx (10 - 100) \mu\text{m} \ll \delta X_{\text{Horizontal}} \sim (1 - 10) \text{mm}$ which can be seen in Heumesser (2016), where the angular and spatial distributions of the beam were studied. In the vertical direction this relation does not hold, as can be seen in figure 6.9. The beam profile was captured using the BiDim-26⁷, a two-dimensional wire-chamber. The projection on the vertical axis features a non-smooth distribution on the mm-scale, thus the fluctu-

⁷The BiDim-26 detector is a ³He wire-chamber with an active area of $A = (256 \times 256) \text{mm}$. More information can be found in appendix A.4 in table A.3.

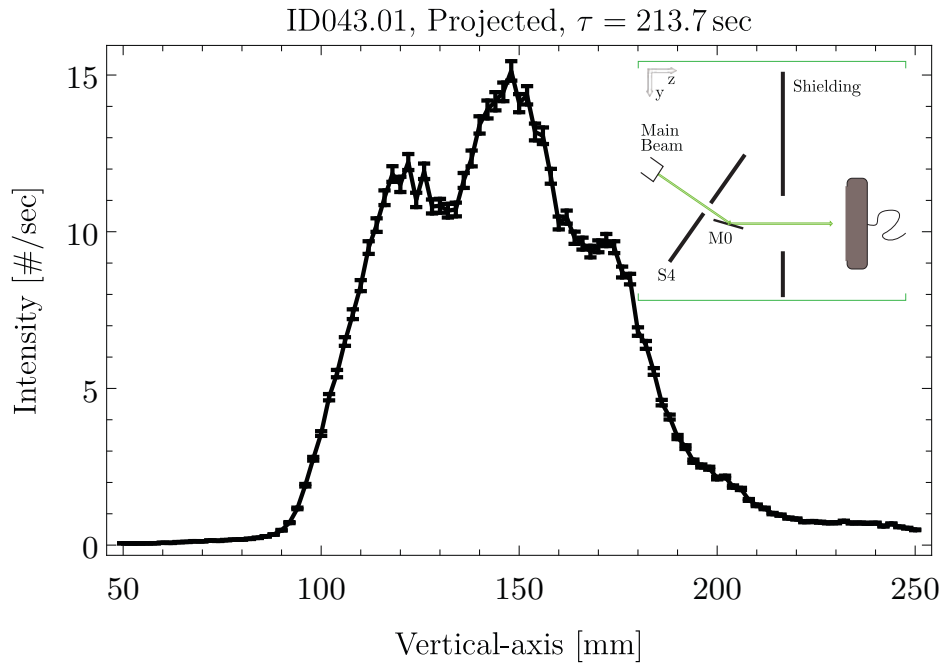


Figure 6.9.: Projection on the vertical axis of the spatial beam distribution of the very-cold neutron beam at the PF2. The projection is calculated from measurement ID0043 taken in beam-time *Test-2455* with the Bidim-26 detector. The detector resolution is given by the pixel size to be $\zeta_{\text{BiDim26}} = (2 \times 2)$ mm. The beam was aligned to the measurement cabin by a super mirror M0, which cleans up the beam together with slit S4. $d_{\text{M0}} = 76$ mm and $S4_{\text{Vertical}} \approx 120$ mm.

ations are smaller than the extension of the beam components in vertical direction with $D_{\text{Vertical}} \sim 100$ mm. As long as one can sum over the vertical axis the interferogram does not depend on the vertical coordinate and the vertical distribution will not alter the final interferogram.

6.2.3. Wavelength Distribution

The wavelength distribution of a realistic beam has a finite width. An example for the beam spectrum is shown in figure 7.5 and an example for a constrained spectrum is shown in figure 7.9. Each wavelength λ_k produces a slightly different pattern according to equation (5.39). As these patterns contribute incoherently, the resulting pattern for the distribution has a decreased visibility ν . Thus, to achieve an acceptable visibility, the wavelength distribution frequently has to be restricted. Figure 6.10 shows the visibility calculated using $\Psi_{\mathcal{L},st}$ from equation (5.44) convoluted⁸ with velocity distributions with different $\Delta\lambda/\lambda$. Figure 6.11 shows the number of interference maxima in a region of visibility $\nu \geq 30\%$. If at least four maxima are required to be in this region, the wavelength bandwidth cannot be greater than

$$\Delta\lambda/\lambda \approx 6.5\%. \quad (6.12)$$

6.2.4. Statistical Constraints

Here it is estimated, whether an interference pattern can be resolved in a practicable time-frame at the PF2 beam-port. This analysis is completed in section 6.3 where a simulation of an interferogram of Lloyd's mirror is presented. Here the prerequisites for the statistical analysis are given and the specific case of a two-point comparison is discussed.

Measurement Specification In section 6.1 different measurement procedures are discussed. The case in which a slit scans the pattern is presented in section 6.1.2, where the question of a significant deviation simplifies to a comparison of the difference of two measurement points $\Delta N_{n,m}$ to its uncertainty $\delta\Delta N_{n,m}$. In section 5.6.2 the sensitivity to a small phase shift is given for a linear approximation of the pattern. Instead of the

⁸See section 6.3 for an overview of the simulation of the interferogram which is used to calculate the visibility in dependence of the wavelength.

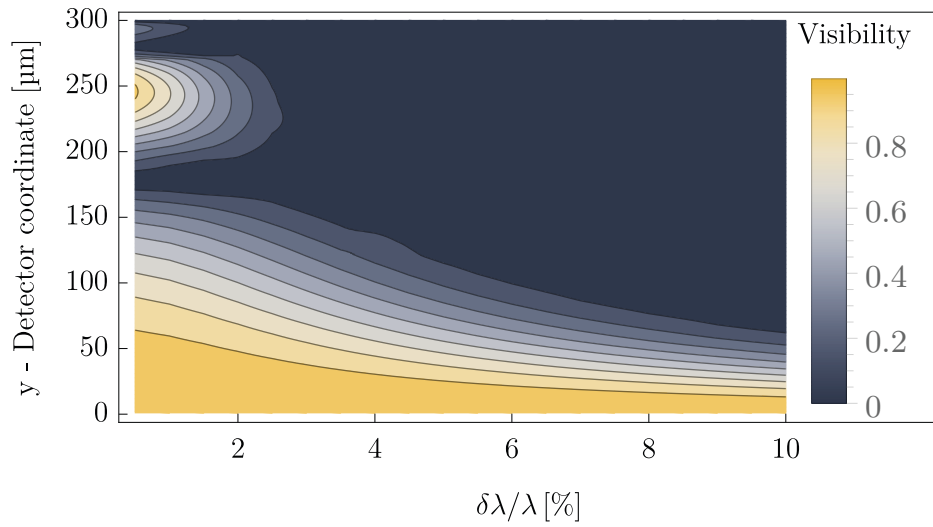


Figure 6.10.: Visibility reduction for a non-monochromatic beam. The visibility of the static solution of Lloyd's mirror is convoluted with a velocity distribution with $\Delta\lambda/\lambda = 1\% \rightarrow 10\%$ and $\lambda = 6.3 \text{ nm}$. Further, parameters are standard parameters as defined in appendix A.4.

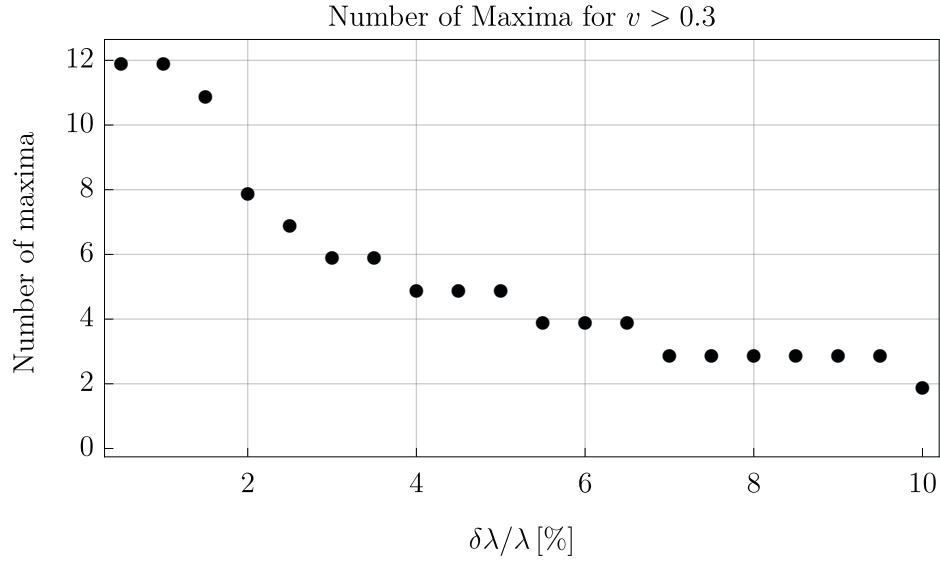


Figure 6.11.: Shown is the number of interference maxima which are contained in a region with a visibility of $\nu < 30\%$.

sensitivity to small variations, the needed measurement time with respect to features of the pattern and the intensity per bin at the detector can be calculated. Figure 6.12 gives a simple example of a two point measurement. The difference between N_n and N_m

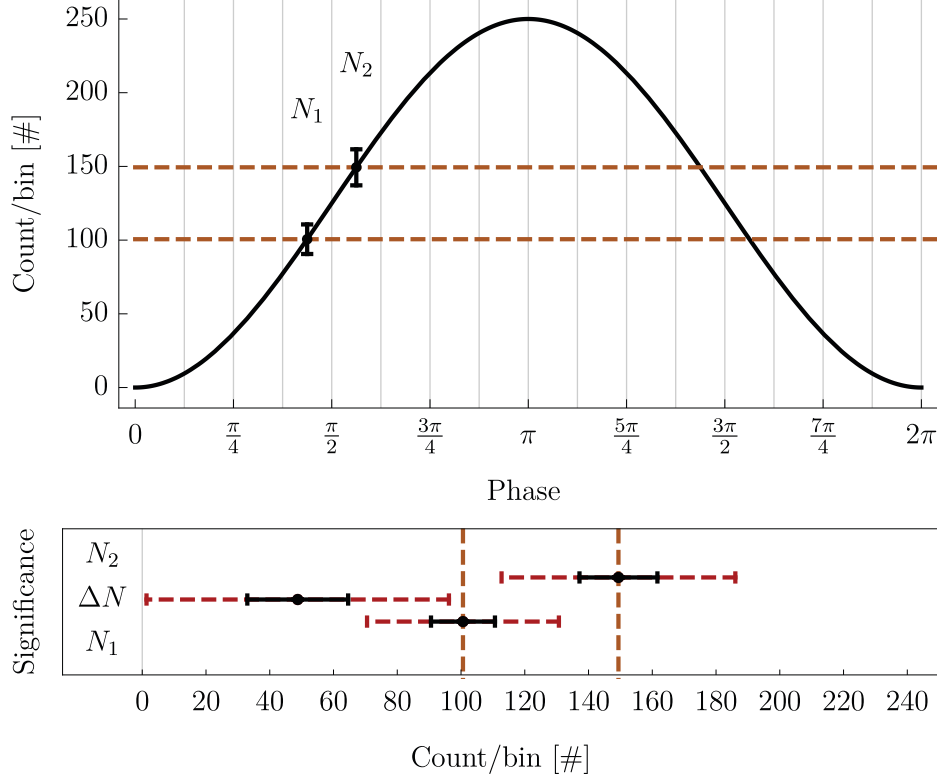


Figure 6.12.: Two-Point measurement scheme with binarized data. For a bin-count at the maximum of $\hat{N}_{\max} > 225$ the difference ΔN has accumulated enough counts so that zero is not within a three sigma region. The black bars indicate a one sigma deviation and the red dashed bars a three sigma deviation. The visibility is assumed to be $\nu = 1$, the phase difference is $\Delta\varphi = \pi/8$, and the bin size is also chosen to be $b = \pi/8$.

is significant if

$$\Delta N_{n,m} = N_n - N_m < \mathcal{S}_{stat} \delta \Delta N_{n,m} = \mathcal{S}_{stat} \sqrt{(\delta N_n)^2 + (\delta N_m)^2} \quad (6.13)$$

$$\Rightarrow \frac{N_n - N_m}{\sqrt{N_n + N_m}} < \mathcal{S}_{stat}. \quad (6.14)$$

Here counting statistics applies and thus the relation $\delta N = \sqrt{N}$ is used. \mathcal{S}_{stat} is the significance which can be set to $\mathcal{S}_{stat} = 3$ for a small scale experiment. For a measurement symmetric around the steepest slope the counts at that bin are given as $\hat{N}[\pi/2] =$

6. Dimensioning and Simulation

$\hat{N}_{\max} \cdot P[\pi/2]$, where $\Delta P = P[\pi/2 + \Delta\varphi] - P[\pi/2 - \Delta\varphi]$. With a small phase shift $\Delta\varphi$ the equation (6.14) can be rearranged by using $\hat{N}_{\max} = \hat{\mathcal{I}}_{\max} T$ to be

$$\hat{N}_{\max} \geq \left(\frac{\mathcal{S}}{\Delta P} \right)^2 \quad (6.15)$$

$$\hookrightarrow T \geq \frac{1}{\hat{\mathcal{I}}_{\max}} \left(\frac{\mathcal{S}}{\Delta P} \right)^2. \quad (6.16)$$

Here T is the integration time, $\hat{\mathcal{I}}_{\max}$ is the intensity per bin at the maximum, and P is the pattern at the detector. If the visibility is already included in the used model, only ΔP is needed, otherwise the visibility is to be included explicitly as ν . For example, for the plane wave solution given in equation (5.38), the difference is $\Delta f = \nu(P_{\text{pl}}(y_n) - P_{\text{pl}}(y_m)) = \nu\Delta P_{\text{pl}}$.

In order to specify a binning, the Nyquist-Shannon theorem is a convenient starting point. To fulfill the theorem, the binning has to be at least twice as narrow as the period $\lambda_{\mathcal{L}}$ to resolve the difference between maximum and minimum. Thus, the maximal bin size b_{\max} is set to be $b_{\max} = \lambda_{\mathcal{L}}/2$. If the pattern is to be resolved even better, the bin size has to be correspondingly smaller. I.e. to make efficient use of the point of the steepest slope, the bin width has to be $b < b_{\max}$. For example, for a bin width of $b_{\varphi} = \pi/8$, the non-linear contributions are smaller than 0.6% for the plane wave model. Thus, it is acceptable for the calculations in section 5.6.2 and the bin size is set to be $b_{\max} = \lambda_{\mathcal{L}}/16$.

Intensity Estimation The intensity per bin at the detector plane is given as

$$\hat{\mathcal{I}} = \int_{-b/2}^{b/2} |\Psi(y - y')|^2 dy', \quad (6.17)$$

where $\Psi(y)$ has to account for the finite wavelength distribution. $\Psi(y)$ is calculated by convoluting the wave function from equation (5.44) or equation (5.46) with the wavelength distribution measured in section 7.1.3. If the pattern is normalized to the maximum value, only the quantity $\hat{\mathcal{I}}(y_{\max})$ is needed to characterize the pattern intensity.

The intensity \mathcal{I} at the interferometer entrance slit S1 can be extrapolated for a specific beam-shaping region, if the radiance \mathcal{R} at the beam port or after the beam-shaping section is measured. Appendix A.2 gives an overview of different instruments and their beam radiance. Specifically chapter 7 states characteristics of the very-cold neutron port

Case	L [m]	λ [nm]	$\lambda_{\mathcal{L}}$ [μm]	b [μm]	$\hat{\mathcal{I}} \cdot 10^{-6}$ [# /s]
I	0.315	6.3	18.7	1.17	79 ± 4
II	0.315	6.3	18.7	9.4	648 ± 29
III	5.315	6.3	315	20	118 ± 5
IV	5.315	6.3	315	157	954 ± 38

Table 6.2.: Shown are the intensities in a bin at the maximum of the pattern for different setups. For each set of setup lengths L , two bin sizes are given. For each setup length the bin size is given for the comparison of maximum and minimum and a measurement of a small shift around the point of the steepest slope. Note that the pattern which describes the short setup $\Psi_{\mathcal{L},\text{st}}$ and the long setup $\Psi_{\mathcal{L},\text{F}}$ deviate significantly, as can be seen in section 6.3.

at the PF2 for the beam as it enters the very-cold neutron cabin and after it traversed the beam shaping section. Anticipating section 7.1.4 the radiance of the very-cold neutron beam at the PF2 with set up beam shaping is given in equation (7.17) as

$$\mathcal{R}_{\text{S1}}^* = (1.4 \pm 0.06) \cdot 10^3 \frac{\text{\# /s}}{\text{rad mm}}. \quad (6.18)$$

The mean wavelength is determined in section 7.1.3 to be $\lambda = (6.73 \pm 0.16)$ nm with a spectral bandwidth $\frac{\Delta\lambda}{\lambda} = (5.55 \pm 0.48)\%$ which satisfies the previous condition in equation (6.12). The height of the beam is approximately 80 mm. Assuming that the angular distribution is constrained to be no wider than $\Delta\alpha = 740$ μrad as discussed in equation (6.7) the intensity \mathcal{I} at the entrance slit is given as

$$\mathcal{I}_{\text{S1}} = (8.9 \pm 0.4) \cdot 10^{-3} \text{\# /s}. \quad (6.19)$$

Using this intensity at slit S1, the intensity at the maximum of the pattern for a specific bin/slit size at the detector can be calculated using equation (6.17). The results for a short and a long setup, as well as for two different bin sizes are summarized in table 6.2.

Conclusion Table 6.3 summarizes the minimal required measurement time for a significant detection T_{min} as specified in equation (6.16) for the cases specified in table 6.2. Due to the high measurement time that is required for a statistically significant result, a realization of a high precision measurement utilizing Lloyd's mirror does not seem feasible at the PF2. Even if the setup could make use of the full brilliance that is stated in section 7.1.1, which is higher compared to the brilliance of the monochromized beam, as stated in section 7.1.4, this would be still insufficient. The measurement time for case I drops by a factor of 40 and a single measurement would take at least one day using

6. Dimensioning and Simulation

Case	ΔP	$\Delta\varphi$	$\left(\frac{\mathcal{S}}{\Delta P}\right)^2$	T_{\min}	T_{\min}^*
I	0.188	$\pi/8$	254	(37 ± 2) days	(124 ± 19) days
II	0.96	π	9.8	(4.2 ± 0.2) h	(14 ± 2) h
III	0.119	$\pi/8$	636	(71 ± 3) days	(236 ± 38) days
IV	0.61	π	24	(7.0 ± 0.3) h	(23 ± 3) h

Table 6.3.: Comparisons of the necessary measurement time for very-cold neutron beam at the PF2. The second time T_{\min}^* is given for a detector efficiency of $\epsilon_{\text{CR39}} = 32\%$ instead of 100% as is assumed for T_{\min} . For ΔP either the solution from equation (5.44) or from equation (5.46) is used, while including a finite wavelength distribution. The significance goal is set to be $\mathcal{S} = 3$. $\Delta\varphi = \pi$ compares two neighboring extrema.

a detector with unit efficiency. Considering that a careful measurement needs several data points, adjustments, and a time consuming initial setup, this is not in the scope of a measurement at the PF2 either. The detection of the maxima of the interferogram on the other hand, can be realized in approximately half a day utilizing a CR39 detector even with \mathcal{I}_{S1} . Thus, between the strict requirement of a $\Delta\varphi = \pi/8$ -shift measurement⁹ and the most rudimentary detection of the periodic interferogram there exists space to resolve finer structures at the measured intensity.

It should be noted that if $\Delta\varphi = \pi$ and consequently the extrema are to be compared, it is implicitly assumed that the pattern can be approximated by a rectangle function with period $\lambda_{\mathcal{L}}$. This indicates that the value given for T_{\min} is an underestimate of the needed measurement time. Consequently, this estimate is not sufficient for an interferogram detection, as discussed in section 6.1.1. It is of special interest which parts of the interferogram will be significantly detectable through statistical noise and finite detector resolution. A more sophisticated way estimating the pattern is the direct simulation of the pattern. The following section presents such a simulation for a CR39-detector as described in chapter 8.

⁹The $\Delta\varphi = \pi/8$ -shift is considered as a reference. Additionally, in section 5.6.2 a small shift in $\mathcal{I}(y, \Delta\varphi)$ is considered by a linear approximation around $\mathcal{I}(y_s, 0)$. y_s is the point of the steepest slope. This is valid as long as non-linear deviations are relatively small. For $\Delta\varphi = \pi/8$ the deviation are below 1% at least for the first few maxima where the diffraction pattern is comparable to the plane wave solution.

6.3. Measurement Estimation

The goal of the following calculation is to simulate an interferogram of Lloyd's mirror at the very-cold neutron beam at the PF2. The subsequent subsections will take into account the wavelength distribution, the detector resolution, and slight misalignments of the detector. The contribution of the mirror roughness, slit imperfections, bending of the detector, and incomplete knowledge about the mirror position relative to the detector are briefly discussed or incorporated in the simulation.

6.3.1. Interferogram Simulation

In chapter 5 several different approximations to the probability density of Lloyd's mirror are given. Here the static solution $\Psi_{\mathcal{L},st}$ as given in equation (5.44) with a mirror length of $L = 0.315$ m is applied. Figure 6.13 shows the scheme which is used for the simulation. The individual modules are discussed in the following section 6.3.1.1, section 6.3.1.2, and the simulation is finalized in section 6.3.1.3.

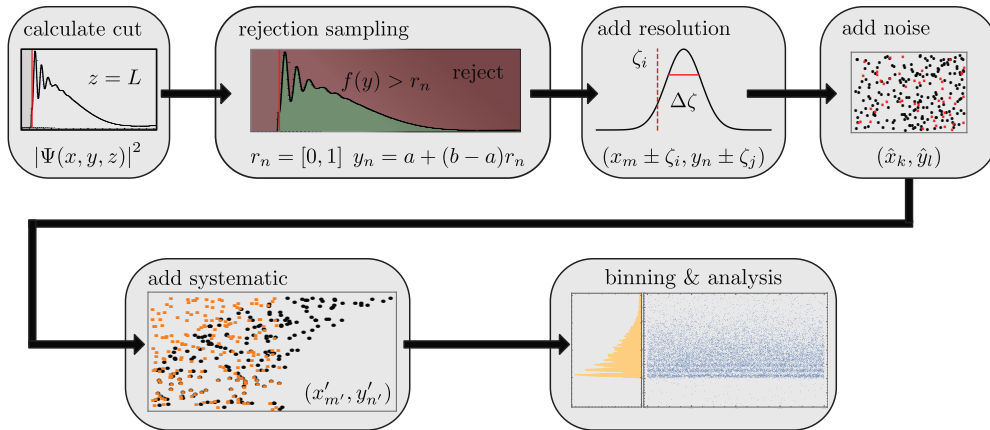


Figure 6.13.: Simulation scheme that is used to estimate the interferogram as it would be seen on a detector with resolution ζ_{det} . The technique of Monte-Carlo rejection sampling is presented as described in Lang and Pucker (2016).

6.3.1.1. Wavelength Distribution

The effect of a finite wavelength distribution has already been discussed in section 6.2.3, where figure 6.10 shows the visibility as a function of $\Delta\lambda/\lambda$. For a given wave function $\Psi(y, \lambda)$ the effect can be included by incoherently summing and weighting the individual patterns with the wavelength distribution of the beam. The integral is then given as

$$\Psi_I(y) = \int_{\lambda_{\min}}^{\lambda_{\max}} f(\lambda)\Psi(y, \lambda)d\lambda. \quad (6.20)$$

Figure 6.14 shows the effect of a Gaussian wavelength distribution with varying $\Delta\lambda/\lambda$ which features a strong drop in visibility. In section 6.2.3 the fact that the visibility drops significantly has already been discussed and a threshold for $\Delta\lambda/\lambda$ is defined. Utilizing these results, $\Psi_I(y)$ with $\lambda = 6.3$ nm and $\Delta\lambda/\lambda = 6.5\%$ is used at different sections of this thesis. See for example section 5.6 and section 6.2.4.

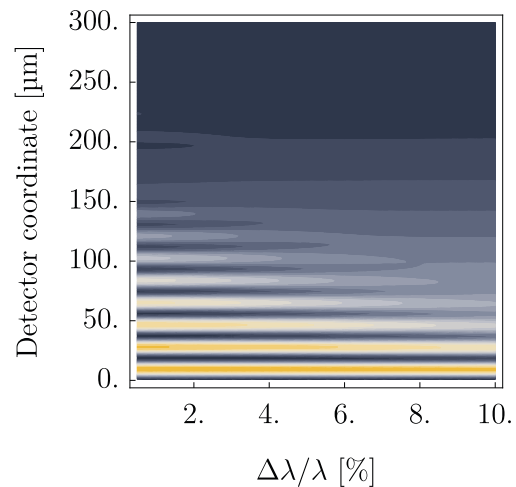


Figure 6.14.: Dependency of $\Psi_{\mathcal{L}}$ on the $\Delta\lambda/\lambda$.

6.3.1.2. Detector Effects

The interference pattern can be detected by employing a spatial resolving detector. Such a detector has a finite resolution ζ_{Det} . Because the expected interferogram period $\lambda_{\mathcal{L}}$ is rather small and can be of the same order of magnitude as the detector resolution, this has to be considered. If for example a neutron hits the detector at a position (x, y) , it is only possible to measure the position with an uncertainty corresponding to ζ_{Det} ¹⁰ and thus

$$(x, y) \rightarrow (x \pm \zeta, y \pm \zeta). \quad (6.21)$$

Further, several other effects will interfere with the spatial neutron detection. A detector can be misaligned relative to the interference pattern. For example, its surface can be rotated, bent, skewed, or a combination of all effects can interfere with the precise spatial detection. This is not limited to the process of exposing the detector to neutrons,

¹⁰Note that ζ_{Det} does not have to be isotropic.

Quantity	Value	Information
λ	6.3 nm	Center wavelength of the distribution shown in section 7.1.3.
$\frac{\Delta\lambda}{\lambda}$	6.5%	Width of the spectral distribution as measured in section 7.1.3. Conservatively the uncorrected value is used instead of the smaller corrected value.
ζ_{CR39}	2.4 μm	Estimated resolution of a boron-coated CR39 neutron detector.
d_{width}	15 mm	Width of the simulated region. y -coordinate region.
d_{height}	80 mm	Height of the simulated region. x -coordinate region.
b_{width}	3 μm	Bin width to produce a histogram from the simulated detector.
ϵ_{CR39}	32%	CR39 detector efficiency.

Table 6.4.: Parameters that are needed for the simulation of the Lloyd’s mirror interferogram.

but can also cover the optical readout mechanism of the detector and the reconstruction of the neutron distribution. In the case of a boron-based CR39 detector as discussed in chapter 8, the detector can be pressed tightly on the mirror’s edge and thus bending and skewing during neutron exposure can be neglected¹¹. By scanning a chemical preprocessed¹² detector using an optical microscope, several systematic effects are introduced. Detectors are fixed on the microscope stage and thus bent slightly; the microscope’s objective adds coordinate distortions as a function of the distance to the center point as is analyzed in Thalhammer (2018); misalignments of the focal plane relative to the detector plane add not uniform distributed noise; and finally dust that settles on the detector adds a uniform noise. In the context of this thesis only the most prominent effects are considered. This is the detector resolution, noise not distinguishable from neutron signals, and a slight bending of the detector. The simulation process first draws individual neutron incident positions (x, y) using the Monte-Carlo rejection technique and the probability density $\Psi_I(y)$ stated in equation (6.20). On each neutron a random noise drawn from a Gaussian distribution with ζ as width is added to simulate the detector resolution. Finally, a polynomial describing a y -deviation is added simulating a bending of the detector in y direction. The relevant parameters are given in table 6.4.

¹¹This is only true for the presented setup. In general CR39 detectors bent and their surface deviates from the detector plane. Depending on the needed resolution this is not necessarily problematic.

¹²See section 8.3 regarding the post-processing of the exposed CR39 detectors.

6.3.1.3. Finalization and Statistical Assessment

The finalized simulation is shown in figure 6.15 for two measurement times $\tau = 7$ days and $\tau = 21$ days. Here again the radiance from section 7.1.4 is taken

$$\mathcal{R}_{S1}^* = (941 \pm 44) \frac{\#/s}{\text{rad mm}}, \quad (6.22)$$

which is corrected for the CR39 detector efficiency $\zeta_{\text{CR39}} = 32\%$.

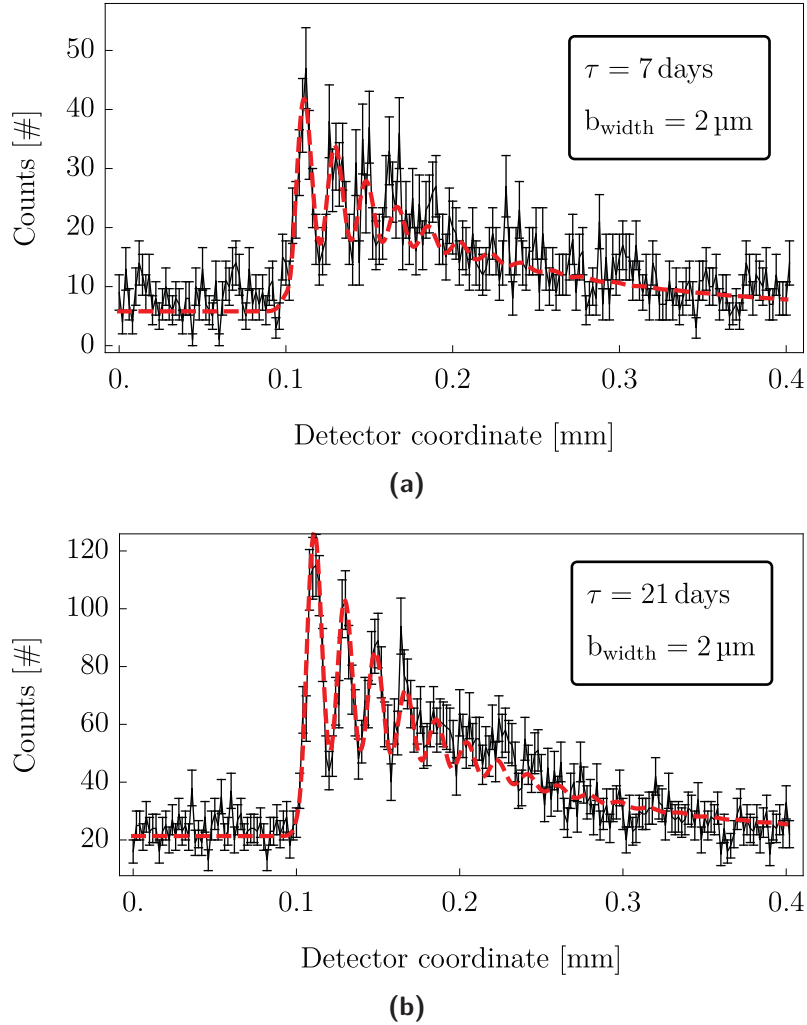


Figure 6.15.: Shown are simulations and fits of the interferogram of Lloyd’s mirror for standard parameters and for an integration times of $\tau = 7$ days in Figure (a) and for an integration time of $\tau = 21$ days in Figure (b). The important fit parameters are collected in table 6.5.

In the case of a seven day integration time the first three maxima and minima are clearly distinguishable from the background, while the rest of the pattern cannot be

resolved. The longer measurement with $\tau = 21$ days shows the interferogram with sufficient statistical data to distinguish at least four to five extrema.

This statement can be refined by comparing the significance of a fit and its parameters of each simulation. A simplified model consisting of five functional parts is used to fit to the data. A periodic part that models the interference pattern by Lloyd's Mirror and is given in section 5.5.1, an exponential $1/(1 + e^{\tau_1(y_0 - y)})$ that models the rising behavior near the mirror, an exponential $\kappa e^{-\tau_2 y}$ that approximates the visibility modulation, an exponential $e^{-\tau_3 y}$ that models the intensity decay of the overall pattern, and finally a constant background B . The compound function is given as

$$f(y) = \frac{1}{1 + e^{\tau_1(y_0 - y)}} \left(1 - \kappa \cdot e^{-\tau_2(y_0 - y)} \cos \left(\frac{3\pi}{2} + \frac{2\pi}{\lambda_{\mathcal{L}}} y \right) \right) e^{-\tau_3 y} + B. \quad (6.23)$$

The fit is calculated using Mathematica¹³ by Wolfram Research (2017). The resulting parameters are collected in table 6.5 and show that even for a seven day measurement, characteristics of the pattern can be extracted from the simulation data.

Mainly the first maxima can be cleanly modeled while deviations exist in the decaying slope. The adjusted¹⁴ $R_7^{*,2} = 0.9$ and $R_{21}^{*,2} = 0.97$ and thus sufficient agreement¹⁵ of the simplified model and the data exist to extract $\lambda_{\mathcal{L}}$. This is in accordance with the conclusion of section 6.2.4.

Despite the very low intensity and the various constraints the signal can still be distinguished from the background with sufficient visibility and in a practical time frame. Especially the fact that the first three maxima are well resolved is important for tests of hypothetical interactions and particles. The potentials introduced have a strong dependency on the detector coordinate as for example discussed in section 5.6.4.1 and section 5.6.4.2. Thus, the point of highest sensitivity to these effects is at the second or third flank. For a $\tau = 21$ days measurement these points of the interferogram should indeed be resolvable after accounting for systematic effects. Additionally, the simulation is able to assess the statistical situation in between the extreme cases of section 6.2.4.

¹³In particular the function `NonlinearModelFit[Data, Model, Parameter, y, Options]` is used. The options that were supplied for the "NonlinearModelFit" are `Weights -> (1/(#)^2 & /@UncertaintyData, VarianceEstimatorFunction -> (1 &),` and `Method -> "LevenbergMarquardt"`.

¹⁴ $R^{*,2} = 1 - \frac{n-1}{n-p} (1 - R^2)$, n is the length of the dataset, p is the number of parameters, $R^2 = \left(\sum_i^n (f_i - \sum_j^n g_j) \right)^2 / \left(\sum_i^n (g_i - f_i)^2 \right)$, and g_i is a datapoint at position y_i . The definition is taken from Wolfram Research (2017).

¹⁵See figure A.2 and figure A.3 for the residuals of each fit for further verification.

6. Dimensioning and Simulation

Quantity	Value	Information
7 Day Simulation		
$\lambda_{\mathcal{L}}$	$(18.7 \pm 0.3) \mu\text{m}$	Estimated plane wave period of Lloyd's Mirror.
κ	(0.64 ± 0.13)	Visibility of the pattern for the first maxima.
y_0	$(101.8 \pm 0.6) \mu\text{m}$	Mirror surface position.
B	$(5.8 \pm 0.3) \#/(s \cdot \text{bin})$	Background in the region $0 \text{ mm} < y < 0.1 \text{ mm}$.
21 Day Simulation		
$\lambda_{\mathcal{L}}$	$(18.7 \pm 0.2) \mu\text{m}$	Estimated plane wave period of Lloyd's Mirror.
κ	(0.64 ± 0.07)	Visibility of the pattern for the first maxima.
y_0	$(101.9 \pm 0.3) \mu\text{m}$	Mirror surface position.
B	$(21.3 \pm 0.6) \#/(s \cdot \text{bin})$	Background in the region $0 \text{ mm} < y < 0.1 \text{ mm}$.
Initial Simulation Parameters		
$\lambda_{\mathcal{L}}$	$18.7 \mu\text{m}$	Plane wave period of the Lloyd's Mirror.
κ	0.84	Visibility of the pattern for the first maxima.
y_0	$100 \mu\text{m}$	Mirror surface position.
B_7	$8.0 \#/(s \cdot \text{bin})$	Intensity in a non-signal region of size $A = 8 \text{ mm}^2$
B_{21}	$23.8 \#/(s \cdot \text{bin})$	with a bin size of $\text{bin}_y = 2 \mu\text{m}$ and integration time of 7 and 21 days.

Table 6.5.: Result of a fit on the simulation of Lloyd's Mirror. An additional parameter table is given in appendix A.4 in table A.7 which includes decay and rise parameters.

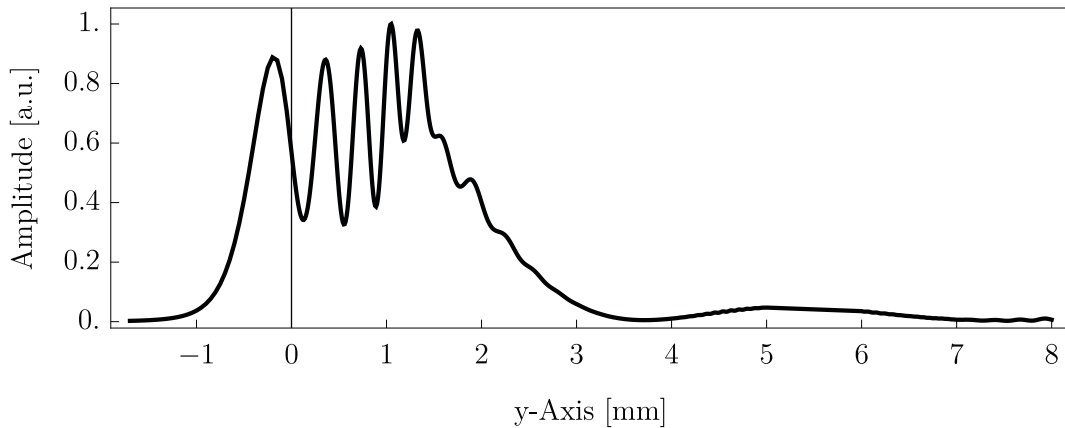


Figure 6.16.: Shown is the interference pattern $|\Psi_{\mathcal{L},F}|^2$ of a setup where the main mirror is followed by a $L_D = 5 \text{ m}$ propagation region which will stretch out the pattern. As for the situation presented in figure 6.15 the finite width of the wavelength spectrum is considered.

Looking at a more general setup with an additional flight path behind the mirror as is described by $\Psi_{\mathcal{L},F}$ and is given in equation (5.46), a stretched out interference pattern is detected. See figure 6.16 which shows the simulated probability density captured using a CR39 at a position $L_D = 5$ m behind the mirror. The pattern spans several millimeters and from the point of view of the size of the pattern, it should be easily resolvable by a scanning slit setup. However, such a setup is not feasible, as it would be impossible to distinguish the interference signal from the background. The background intensity per area at the detector can be expected to be more or less constant for a position further beam downwards, and thus the value calculated in section 7.2.4 is used for a comparison. In this case, the signal magnitude given by equation (7.16) is diluted to be

$$\mathcal{F} = \mathcal{I}/A \approx 44 \cdot 10^{-6} \frac{\#/s}{\text{mm}^2} \quad (6.24)$$

and therefore does not elevate above the detector background flux of $\mathcal{F} = (83 \pm 8) \cdot 10^{-6} \frac{\#/s}{\text{mm}^2}$ as given in equation (7.19). Only with a detector that features a lower background flux, a measurement with an added propagation region of the order of L_D is realizable at the PF2.

6.3.2. Additional Systematic Effects

Besides the already discussed systematic effects the contribution of additional ones need to be estimated. What will for example happen, if the slit is not well aligned or the mirror is not perfectly flat or even rough?

6.3.2.1. Misaligned Slit

Consider a slit consisting of two absorbing blades $S1_a$ and $S1_c$ which are misaligned in the x-axis relative to the mirror as shown in figure 6.17. For the perfectly aligned system one can sum over the pattern along the x-axis because no relevant structure is expected besides intrinsic beam fluctu-

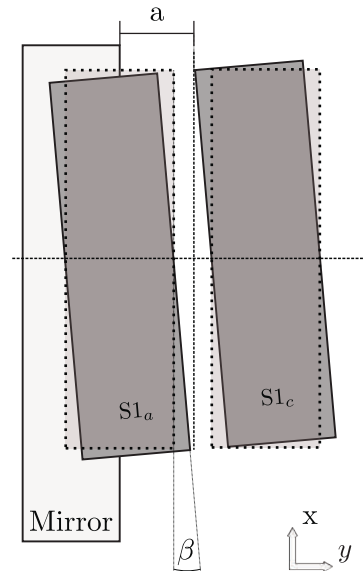


Figure 6.17.: Geometry of a misaligned entrance slit in front of the main mirror. The slit is composed of three regions. Two beam blocking components $S1_a$ and $S1_c$, and a transmissive region $S1_b$.

6. Dimensioning and Simulation

ations as discussed in section 6.2.2. Recalling the interference pattern period given in equation (5.39), a deviation Δa leads to

$$\lambda_{\mathcal{L}, \Delta a} = \frac{L\lambda}{2(a + \Delta a)}. \quad (6.25)$$

For a misalignment of $\beta = 10 \mu\text{rad}$, a vertical extension of the slit of $S1_{\text{vert}} \approx 100 \text{ mm}$, and $a \approx 53 \mu\text{m}$ leads to a maximal change of $\Delta a \approx \beta S1_{\text{vert}} = 1 \mu\text{m}$ and

$$\frac{\lambda_{\mathcal{L}, \Delta a} - \lambda_{\mathcal{L}}}{\lambda_{\mathcal{L}}} = 1 - \frac{a}{(a + \Delta a)} \approx 1.8\%. \quad (6.26)$$

Summing along the x-axis the visibility of the pattern will be reduced as is shown in figure 6.18, where the drop in visibility is given as a function of β and y . In order to conserve a high visibility the angle β needs to be below $\beta < 2 \mu\text{rad}$ for the chosen value of a . Dependent on the achievable β in a specific implementation of Lloyd's mirror, a is constrained. For example, if alignment can only be achieved to a level of $\beta \approx 20 \mu\text{rad}$, one would need to choose $a > 530 \mu\text{m}$ respectively larger.

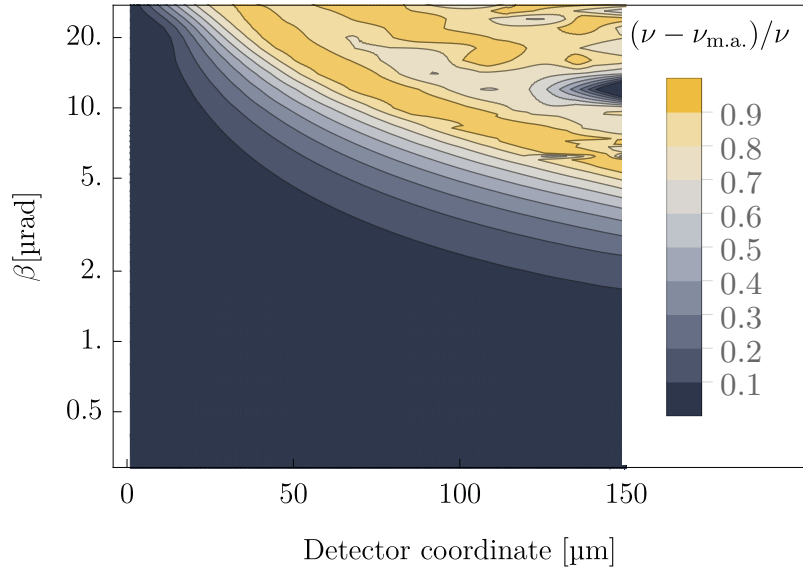


Figure 6.18.: Shown is the visibility drop $(\nu - \nu_{\text{m.a.}})/\nu$ for a misaligned slit with a visibility $\nu_{\text{m.a.}}$. To calculate the visibility the probability density in equation (5.44) is used. The slit is divided in $N = 20$ vertical sections which are shifted as indicated in figure 6.17 by β and for which the interference pattern is calculated individually. Summing over the individual sections and calculating the visibility of the resulting pattern leads to the shown result. The structure on the upper right corner is partly caused by numerical artifacts, because the calculated visibility in this region is very close to zero. Interesting is the low loss at $\beta = 10 \mu\text{rad}$ and $y = 150 \text{ mm}$ which is explainable as the original pattern and the disturbed pattern are very similar. Thus, this low loss region does not indicate a usable parameter set, because of the low absolute visibility at this point.

6.3.2.2. Rough Slit

The inner surfaces of the blades shaping the slit will have some roughness. Here it is assumed that the deviations of the inner surfaces between different points n follow a Gaussian distribution with

$$f(n) \sim \frac{1}{\sigma\sqrt{2\pi}} e^{-\frac{1}{2}\frac{x-a}{\sigma}^2} \quad (6.27)$$

and σ the roughness of the surface. This is similar to varying the slit width $S1$ and the slit mirror distance a for different points along the x-axis. The model is shown in figure 6.19 where the slit is divided into N subsections with individual a_n and $S1_n$. Summing and weighting over the set of patterns gives the interference pattern with reduced visibility¹⁶. The resulting visibility drop compared to the pattern formed by a perfect slit is shown in figure 6.20. In order to conserve the visibility of the pattern, the roughness should be smaller than $\sigma < 1 \mu\text{m}$ for the standard parameter defined in table A.3.

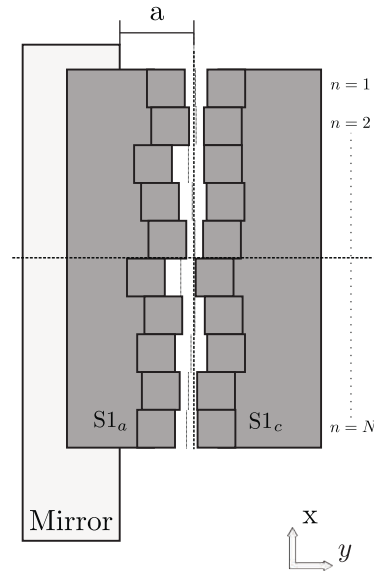


Figure 6.19.: Geometry of rough entrance slit surfaces in front of the main mirror. The slit is formed by two opaque components $S1_a$ and $S1_c$. In the setup as presented in section 7.2.1 boron-steel is used for these components.

In order to conserve the visibility of the pattern, the roughness should be smaller than $\sigma < 1 \mu\text{m}$ for the standard parameter defined in table A.3.

6.3.2.3. Main Mirror Imperfections

As the slit, the mirror surface will also deviate from a perfect plane. In section 7.2.2 the profile function $f(x) = a(x - c)^2 + b$ is calculated from fitting a parable at an optical measurement of the profile of the used mirror. The parameter a is determined to be $a = -11.1 \cdot 10^{-6} \mu\text{m}$. Over the extension of the mirror a height change of $\pm 0.4 \mu\text{m}$ can be observed. Additionally, the mirror roughness is measured using a needle roughness tester to be $r_a \approx (0.007 \pm 0.001) \mu\text{m}$. While in general both the roughness as well as the overall shape of the mirror will contribute to the interferogram, both effects are neglected. In case of the overall shape or waviness this can be a particularly bad approximation and has to be addressed in future considerations.

¹⁶Note that the the neutron beam is not coherent in the vertical direction/x-direction.

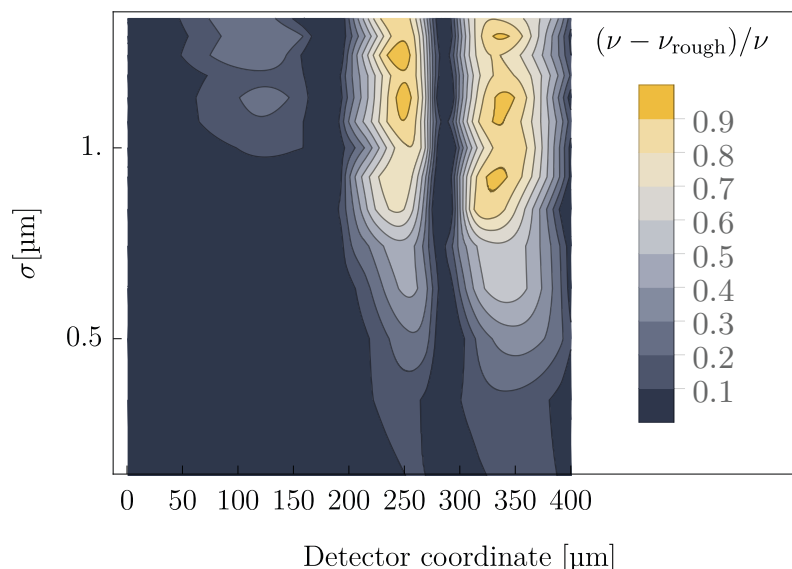


Figure 6.20.: Shown is the visibility drop $(\nu - \nu_{\text{rough}})/\nu$ for a rough slit with a visibility ν_{rough} . To calculate the visibility the probability density in equation (5.44) is used. The slit is divided in $N = 30$ vertical sections which are shifted as indicated in figure 6.19 by β and for which the interference pattern is calculated individually. Summing over the individual sections and calculating the visibility of the resulting pattern gives the shown result. The structure along the detector coordinate is due to the periodic revival of the pattern.

6.4. Summary

In this chapter experimental constraints of an implementation of Lloyd's mirror are discussed and analyzed with respect to the very-cold neutron beam at the PF2 at the Institut Laue-Langevin. To achieve an acceptable visibility of the interferogram both the angular and the spectral width of the beam need to be constrained as is shown in section 6.2.1. Using standard parameters for the setup dimensions the divergence has to be

$$\theta < 740 \mu\text{rad} \quad (6.28)$$

in order to have a coherent wavefront over the extension of the entrance slit. In section 6.2.2 it is shown that the spectral width has to be constrained to be around

$$\frac{\Delta\lambda}{\lambda} = 6.5\% \quad (6.29)$$

in order to achieve a visibility of $v > 30\%$ up to the fourth maxima. Both constraints, if implemented by cutting in phase-space tightly, limit the available intensity at the entrance slit \mathcal{I}_{S1} . This is discussed in section 6.2.4. Therefore a measurement which

6. Dimensioning and Simulation

compares two points in the interferogram around the point of the steepest slope, the needed measurement time for a specific significance \mathcal{S} is estimated. Due to the very low expected intensity at the entrance slit of the interferometer, it is not possible to resolve phase shifts of the order of $\Delta\varphi = \pi/8$. The measurement time that is needed to distinguish two points with a significance of $\mathcal{S} \geq 3$ for such a shift is estimated to be higher than $T_{\min} \geq (37 \pm 2)$ days for a detector with unit detection efficiency. It has to be noted that a loss in brilliance by a factor of forty is not accounted for over the monochromatization stage as discussed in section 7.1.4. The most probable cause is a not optimal beam positioning which would be possible to be compensated in principle. For a successful compensated loss, the necessary measurement time would reduce to $T_{\min} \geq (0.9 \pm 0.001)$ days which is still feasible but does not constitute a high precision measurement. Anticipating the results of this section, the simulated pattern is already used in the sensitivity estimation in section 5.6. There the achievable sensitivity with the given interferogram and beam intensity is discussed for various phase shifting effects. Despite these constraints it is shown that the interferogram itself can certainly be resolved with high significance as the minimal measurement time for a peak to peak detection is just about $T_{\min} \geq (14 \pm 2)$ hours for a measurement employing a CR39 detector. This is consistent with the result of the full simulation shown in figure 6.15 where the interferogram is distinguishable from the measured background as presented in section 7.2.4.

The entrance slit of the interferometer is discussed more closely in section 6.3.2.1 and section 6.3.2.2. There a misalignment and the roughness of the entrance slit is considered which will both reduce the visibility of the pattern. The constraints on the specific material properties as for example a roughness below $\sigma < 1 \mu\text{m}$, are followed up on in section 7.2.2 which is embedded in part III. The following chapter 7 presents a not yet finished experimental implementation of Lloyd's mirror and the intensity measurements which were referenced throughout this part of the thesis.

Part III.

Selected Experiments

7. Experimental Setup and First Measurements

This section gives an overview of an experimental setup to realize Lloyd’s mirror at the PF2’s very-cold neutron beam at the Institut Laue-Langevin. A basic scheme for a successful implementation of the setup as described in chapter 6 depends on three prerequisites.

First, the wavelength distribution needs to be as narrow as specified in section 6.2.3. Second, the coherence condition has to be met as shown in section 6.2.1 and third, the intensity has to be high enough to make a measurement practical. Together these constrain the minimal radiance needed over the horizontal divergence angle \mathcal{R}/γ . The mean brilliance \mathcal{B} of different beam ports is summarized in table 7.1 together with the available wavelength range of selected very-cold neutron beams at the ILL¹.

Instrument	λ [nm]	\mathcal{B} [$\frac{\#/s}{\text{cm}^2 \text{sterad nm}}$]
D11	0.45 – 4	$2 \cdot 10^{11}$
D33	0.45 – 25	$\sim 2 \cdot 10^{11}$
H18	1.5 – 3.0	$1.3 \cdot 10^8$
PF2-VCN	2 – 400	–

Table 7.1.: Brilliance and wavelength range of different neutron beams at the ILL. The values for D11, D33, and H18 are taken from the flux distribution plot on page 8 in Laue-Langevin (2008) which is reproduced in appendix A as figure A.12.

Note that for the very-cold neutron beam at the PF2 no value for the mean brilliance is available. Extrapolating for a wavelength of $\lambda = 60$ nm from figure A.12 yields a wide value range of $\mathcal{B} \sim (2 \cdot 10^5 - 2.5 \cdot 10^7)$ [$\frac{\#/s}{\text{cm}^2 \text{sterad nm}}$], which is not reliable as an estimate for a specific beam port as the brilliance strongly depends on the implemented extraction

¹For a general description of the very-cold neutron source at the Institute Laue-Langevin see section 3.3 and figure 3.4.

7. Experimental Setup and First Measurements

mechanism. The flux per wavelength at the neutron vertical guide exit port is stated in Laue-Langevin (2008) and measured in Steyerl et al. (1986) as

$$\mathcal{R} \approx 40 \cdot 10^3 \frac{\#/\text{s}}{\text{cm}^2 \text{ \AA}} \quad (7.1)$$

around a wavelength of $\lambda \approx 10$ nm. This value is problematic to use for estimates as no angular information about the beam at the cabin entrance is provided. Thus, an experimental determination is necessary for further calculations.

Nevertheless, the very-cold neutron beam at the PF2 is expected to have the lowest mean brilliance compared to the other mentioned beams because of its higher mean wavelength and the overall cold source wavelength distribution. Conversely, this beam is favorable in respect to its wavelength's distribution of up to $\lambda \sim 10$ nm and that it offers relatively long experimental-periods of a couple of weeks. Both points are especially relevant in respect to searches for fifth-forces and dark matter as indicated in section 5.6.

In the following section an implementation of a beam preparation stage (section II) for the interferometer obeying the beam constraints is presented together with relevant brilliance measurements. The brilliance measurements are compared to the characteristics of the H18 beam², which has been used for similar free-space interferometry as presented in Anton Zeilinger et al. (1988). Finally, the proposed interferometer setup (section I) and its components are presented as they have been prepared in beam-time *Test-2455*.

7.1. Experimental Implementation

The figure 7.1 shows a proposed setup that fulfills the restrictions explained in chapter 6. The overall setup at the very-cold neutron port at the PF2 is situated on a vibrationally isolated optical table which is equipped with two spring-mass systems to damp vibrations. Further, the table can be placed on air cushions to damp vibrations.

Neutron optical components are placed on 25.4 mm diameter thick rods in order to avoid enhancing the residual vibration magnitude. The setup in section II consists of three neutron optical mirrors and three slits. The alignment of these components in relation to the neutron beam is accomplished using a multi in-line laser system and a sequential build-up of the setup. Each mirror has a motorized rotational degree of freedom and each, slit a motorized translational degree of freedom perpendicular to the neutron beam.

²Currently, the beam is permanently used for the D17 instrument and is not available for full setup experiments.

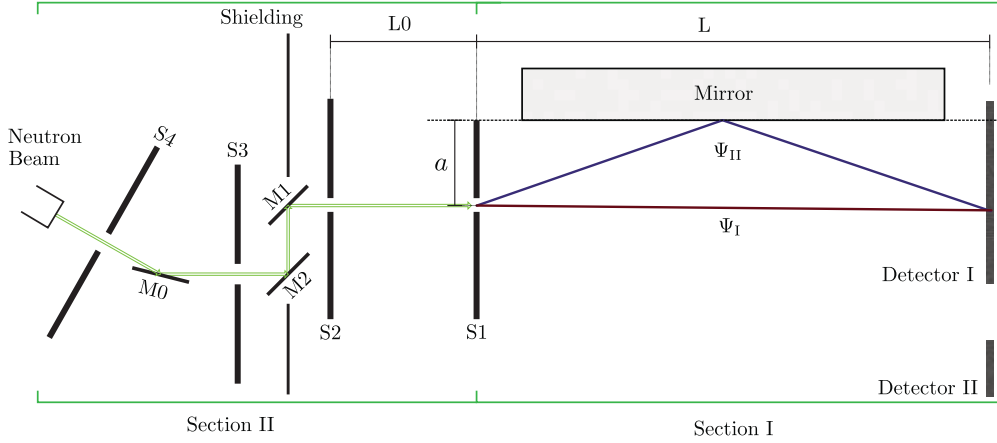


Figure 7.1.: Full schematic of the setup of Lloyd’s mirror at the PF2 at the ILL. Section II composes the beam preparation region and section I the interferometer region.

The overall motorization of the setup is discussed in Heumesser (2016). The laser beams and the neutron beam are aligned relative to each other by employing an in-line silicon mirror that is transmissive for neutrons. An on-line detector is placed beam downwards from section I for alignments that require a neutron beam. This detector is a Bidim-26 wire chamber detector with a pressurized ^3He gas filling and an efficiency of roughly $\epsilon_{\text{Bidim26}} = (68.3 \pm 1)\%$.

The beam enters the setup at the left in section II and mirror M0 aligns the very-cold neutron beam to the experimental chamber. The slits S4 and S3 form the first beam shaping stage. There the beam collimation is reduced to be compatible with the monochromatization stage. Monochromatization is achieved with Ni-Ti multilayer mirrors³ with a spacing $d = 4.3 \text{ nm}$ and a variation of the spacing of $\Delta d/d \approx 5\%$ ⁴. Finally, slit S2 and S1 prepare a coherent region in front of the mirror. This concludes the beam preparation and the beam enters section I through slit S1. After transversing the region forming Lloyd’s mirror, the beam hits the detector plane. The main detector I captures the signal and detector II captures a background signal. Over every part of the setup shielding is added. In particular heavy shielding is present at each mirror to capture transmitted neutrons and stray neutrons. By this a very low neutron background of $\mathcal{F}_{\text{Background}} \approx 0.3 \text{ \#}/(\text{mm}^2\text{h})$ is achieved at the detector plane, as will be presented in section 7.2.4.

³These mirrors were graciously supplied to us by Hino Masahiro and Tatsuro Oda from Kyoto University. They are also used in other experiments as for example M. Hino et al. (2003).

⁴As discussed in section 7.1.3 the resulting expected spectral bandwidth is $\Delta\lambda/\lambda = (5.75 \pm 0.01)\%$ as given in equation (7.11).

7. Experimental Setup and First Measurements

Beam Preparation Section II of the setup shown in figure 7.1 has been realized and tested at the PF2 during the beam-time *Test-2455* in 2015 and *3-14-343* in 2014⁵. Specific modules are presented and discussed in Bricher (2015) and in Heumesser (2016). Especially in the following, the slit and the mirror motion and measurement control system are presented.

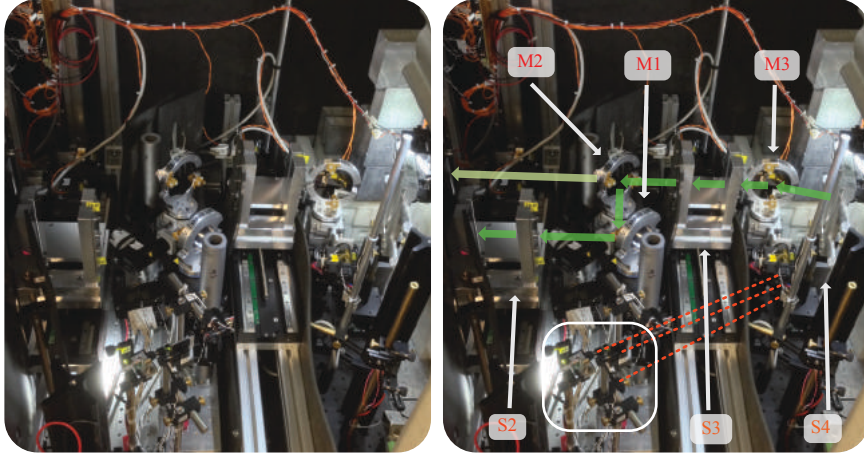


Figure 7.2.: Implementation of the beam-shaping section. M0 is the first neutron super-mirror with $m = 2$ which deflects the very-cold neutron beam in the direction of the experimental chamber. The slits S4 & S3 are used to collimate the beam for the wavelength selection which is realized using Ni-Ti-super mirrors M1 & M2. Beam downwards, slit S2 prepares a wavefront together with S1 through which the wavefront enters the interferometer region.

The implemented beam preparation is shown in figure 7.2 as built up during beam-time *Test-2455*. The setup closely follows the setup shown in figure 7.1, where a system of slits is applied to collimate the beam and mirrors used to restrict the wavelength. At the position of M0 a neutron $m = 2$ super-mirror deflects the very-cold neutron beam in the direction of the experimental chamber. The slits S4 and S3 are used to collimate the beam to achieve a narrow wavelength distribution at the monochromatization stage. The wavelength selection itself is realized using the Ni-Ti-super mirrors M1 & M2. Beam downwards, slit S2 prepares a wavefront together with S1 which marks the entrance to the interferometer region.

Each component can be moved through an unified control system based on LabView. Measurement scripts then allow for time intensive measurements as for example narrow slit scans of the beam. Slits are placed on translation stages⁶ and mirrors are placed

⁵Due to an unforeseen reactor shutdown further testing and measurements were not possible. This is particular true for the spectral selection which is here presented as constructed in beam-time *3-14-343*.

⁶The translation stages are various stages produced by Physik Instrumente. Examples are the M-403.1DG which offers a travel range of 25 mm and a minimal step size of 0.2 μm .

on rotational stages⁷ as well as on translation stages. Angular alignment is guaranteed by using the optical table as common reference and a laser alignment system which allows for easy alignment of slits and mirrors relative to the beam axis. The subfigure on the right in figure 7.2 shows this system consisting of three $\lambda = 670$ nm lasers that are reflected by an in-line neutron-transmissive silicon mirror. Each laser beam crosses at a slightly different height to cover the vertical extension of each slit. Thus, the optical beams can closely follow the neutron beams path.

7.1.1. Very-Cold Neutron Beam at the PF2

The size of the very-cold neutron beam at the PF2 is half the size of the neutron guide leading to the turbine. Thus, the beam cross-section has a size of about $A \approx (70 \times 34)$ mm as already noted in section 3.3. In beam-time 3-14-343 the full beam was captured directly behind the beam port without any additional beam components using a ³He-filled wire chamber. The measured total intensity⁸ is

$$\mathcal{I} = (2 \pm 0.044) \cdot 10^6 \text{ \#}/\text{s} \quad (7.2)$$

and thus gives a flux of

$$\mathcal{F} = (0.84 \pm 0.02) \cdot 10^3 \frac{\text{\#}/\text{s}}{\text{mm}^2} \quad (7.3)$$

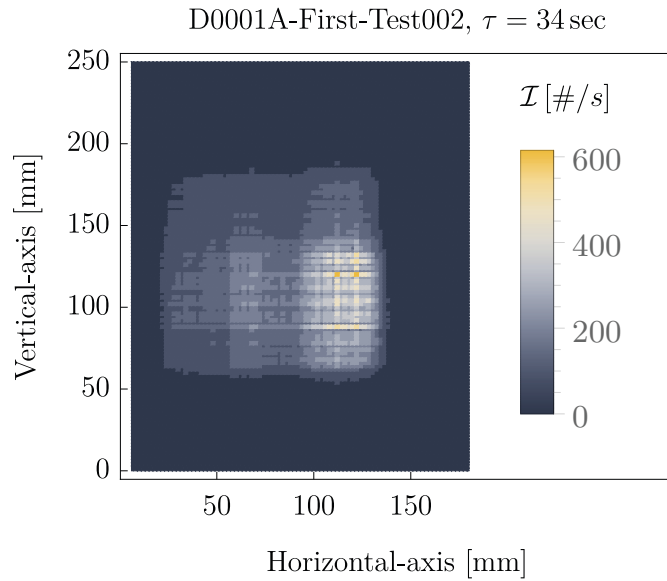


Figure 7.3.: Spatial distribution before M0 measured without any additional beam shaping components. It was measured in beam-time 3-14-343. The main part of the beam is restricted to a square of $A \approx (4.2 \times 8.4)$ cm² at the detector with a fraction of the beam carrying an upward and a leftward component.

⁷The rotational stages are Physik Instrumente M-61.DG which can turn through 360° with a resolution of 1.2 μrad

⁸This value captured in measurement ID0001H using the Bidim-26 detector, is corrected for the detector efficiency of $\epsilon_{\text{Bidim26}}$. The measurement shows non-uniform efficiency on the level of 60% in a limited number of rows. This is probably due to the saturation of singular wires, as this effect is not visible in measurements with lower intensity. Additionally, measurements directly after the beam port had significant dead time because of the high neutron intensity. The distance between detector and beam port was $d = 1145$ mm.

7. Experimental Setup and First Measurements

through the beam port. The spectral width of the raw beam is $\text{FWHM} \approx (10.8 \pm 0.5) \text{ nm}$ ⁹ around the maximum at $\lambda \approx 4 \text{ nm}$ and thus, the flux per wavelength at the beam port follows as

$$\mathcal{R} = (78 \pm 4) \frac{\#/\text{s}}{\text{mm}^2 \text{ nm}} = (0.78 \pm 0.04) \cdot 10^3 \frac{\#/\text{s}}{\text{cm}^2 \text{ \AA}}. \quad (7.4)$$

Comparing this value to the one given by the ILL in equation (7.1) a discrepancy of a factor of approximately 51 becomes apparent. Note that this comparison is not valid as both values should differ due to the following effects.

— Measurement Position:

The value given in Steyerl et al. (1986) is measured at the end of the vertical neutron guide coming from the cold source before the ultra-cold neutron turbine. In contrast to this beam extraction position the here presented value is taken after the turbine at the very-cold neutron cabin entrance. Losses are expected due to scattering at the guides and non-guiding components (shutter and joints), as well as general absorption in the section separating foil.

— Quantity:

The presented value is the peak flux at the specified wavelength. The radiance given in equation (7.4) is the mean over the full beam and does not respect inhomogeneities and the anisotropy of the beam. Later measurements are performed on small sections of the beam, thus enhancing the accuracy of the homogenous approximation.

— Detector:

The measurement is corrected for the detector efficiency, and air absorption is negligibly small. But the detector is saturated at some parts due to the high intensity, as can be seen in figure 7.3. For measurements beam downward this effect is not problematic.

While a lower value for the measured radiance at the cabin entrance is expected, the magnitude is still surprising and should be further investigated. This is especially important as this experiment is heavily restricted by the intensity at hand and losses between the turbine entrance and the very-cold neutron cabin can in principle be reduced, if present.

⁹This value has been graciously supplied by Geltenbort (2013, priv. comm.).

7.1.1.1. Time of Flight

In order to measure the spectral distribution, a Time of Flight measurement¹⁰ is implemented. The setup consists of a neutron super-mirror M0¹¹ to deflect the beam, a chopper, and a synchronized detector. As the beam enters the cabin under a small angle, the super-mirror is needed to realign the beam. This effectively truncates the beam and only selects an area of $A = (12 \times 76)$ mm. The logarithm of the spatial distribution of the central part of the beam after transversing M0 is shown in figure 7.4. The central peak in the figure is wider as the

mirror cross-section of roughly 12 mm due to the divergence of the beam. The selected central beam is the most bright part of the beam and it is important to emphasize that no other stronger or comparable maximum is visible in the full beam. Figure 7.5 gives the wavelength distribution for the same beam and shows a broad peak with $\Delta\lambda/\lambda \sim 70\%$ around $\lambda = 6.5$ nm. With mirror M0 a wavelength cutoff is introduced. For the incident angle of 9.1° the cutoff is at $\lambda_{\text{cutoff}} = 4.53$ nm. The flux at the deflecting mirror can be calculated¹² to be

$$\mathcal{F} = (21 \pm 1) \frac{\#/\text{s}}{\text{mm}^2} \quad (7.5)$$

which carries a high uncertainty as the mirror is approximated by a rectangular aperture.

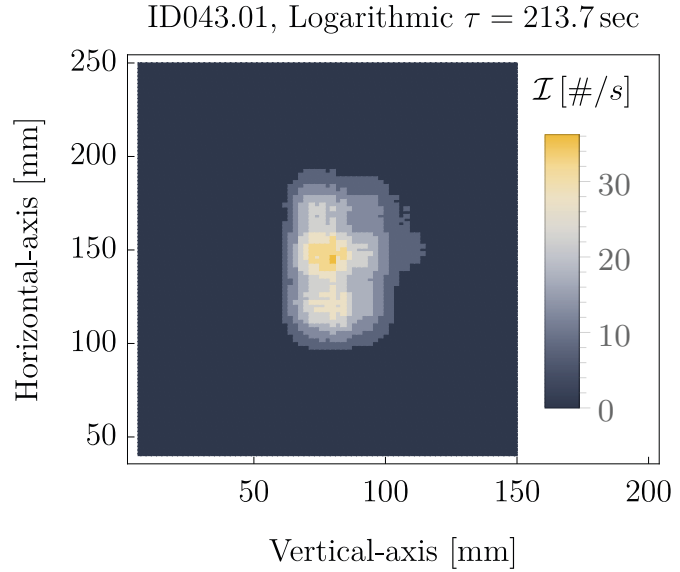


Figure 7.4.: Spatial distribution after M0. The plateau on the right side after the main peak is due to the high beam divergence.

¹⁰S4 has been opened for ID0043.

¹¹ $M = 2$, non-polarizing, Ni-Ti-super mirror, produced by Hino Masahiro, Kyoto University

¹²Measured is the intensity without chopper. With the chopper the beam is truncated by a two by two centimeter aperture. Note that this value is not used further in this thesis.

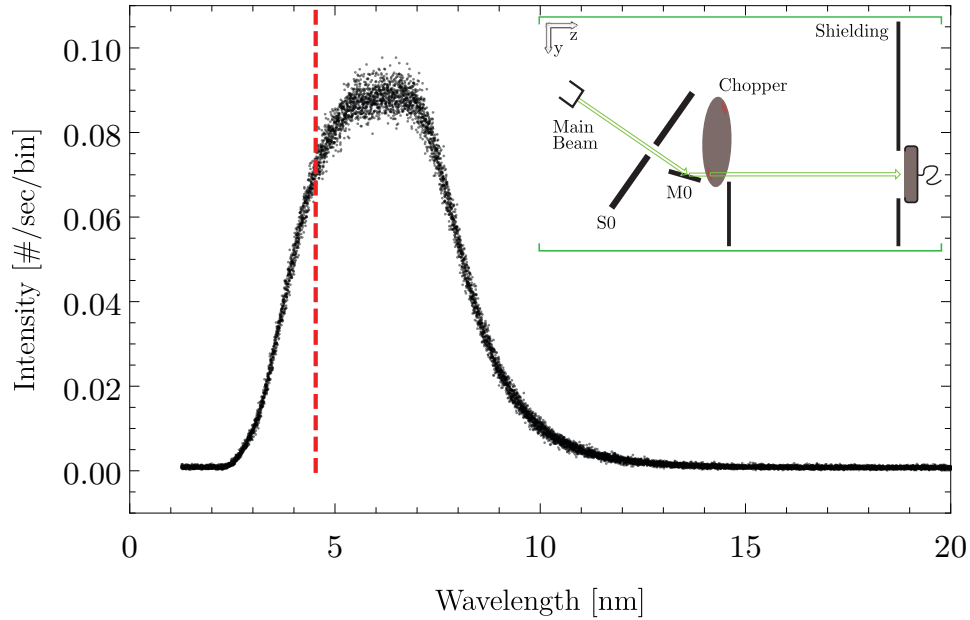


Figure 7.5.: Shown is the wavelength distribution of the center beam measured at ID0038 during beam-time 3-14-343. The offset between the physical opening and the trigger signal has been determined to be $\Delta T = (10.03 \pm 0.1)$ ms and is corrected analogously to Bricher (2015). The divergence of the beam is only restricted by a super-mirror (M0) which cuts out a roughly (12×76) mm portion of the beam and is placed 443 mm after the beam port. The chopper opening function was not corrected as it only contributes marginally. The wavelength cutoff due to M0 is drawn in dashed-red $\lambda_{\text{cutoff}} = 4.53$ nm. The wavelength at the maximum can be determined to be $\lambda_{\text{max}} \approx 6.5$ nm with a relative width of $\Delta\lambda/\lambda \sim 70\%$. In the upper right corner the setup for this measurement is shown. The chopper window has a size of (20×20) mm, and the distance between chopper and detector is $\Delta_{\text{Chop.},\text{Det.}} = 1.161$ mm, between beam port and M0 $\Delta_{\text{Port.},M0} = 390$ mm, and between M0 and chopper $\Delta_{M0,\text{Chop.}} = 291$ mm. See Bricher (2015) for an extensive analysis of TOF-measurements at the PF2 very-cold neutron beam. Only every fifth data point is shown. The total intensity in this measurement is $\mathcal{I} = (1267.8 \pm 0.3)$ #/s.

7.1.1.2. Angular Dependence

Finally, using two aligned slits, angular information can be extracted. Figure 7.7 shows the integrated beam intensity \mathcal{I} after a two-slit setup consisting of S3 and S2. Slit S2 horizontally moves over the beam profile shaped by slit S3 as shown in figure 7.6. For a slit position of $S3_{\text{pos}} = 43.5 \text{ mm}$ the flux through slit S2 is $\mathcal{F} = (26.3 \pm 0.3) \frac{\#/\text{s}}{\text{mm}^2}$ and with the maximal divergence angle of $\gamma_{\text{horizontal}} = 6.6 \text{ mrad}$ ¹³ and $\gamma_{\text{vertical}} = 87 \text{ mrad}$ this gives

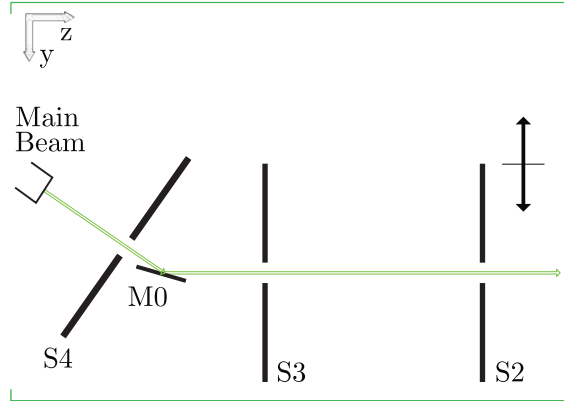


Figure 7.6.: Measurement scheme to determine the angular characteristic of this section of the beam. Slit S2 is moved perpendicularly to the beam while S3 is kept fixed.

$$\mathcal{R} = (45.9 \pm 0.4) \cdot 10^3 \frac{\#/\text{s}}{\text{mm}^2 \text{ sterad}}. \quad (7.6)$$

Slit S3 has been set to a horizontal width of 1.024 mm and a vertical width of 100 mm, while Slit S2 has been set to a horizontal width of 0.511 mm.

7.1.1.3. Summary

Combining the previous numbers and correcting for the detector efficiency of $\epsilon_D = 67\%$ the brilliance of the selected part of the beam can be approximated by

$$\mathcal{B} \approx \mathcal{R}/\Delta\lambda = (1.6 \pm 0.3) \cdot 10^3 \frac{\#/\text{s}}{\text{mm}^2 \text{ sterad } \text{\AA}}. \quad (7.7)$$

This underestimates by a few percent as the mirror M0 is approximated by a rectangular aperture, but it is useful to compare beam downwards brilliance values and check for losses in that sections.

¹³As measured by Heumesser (2016).

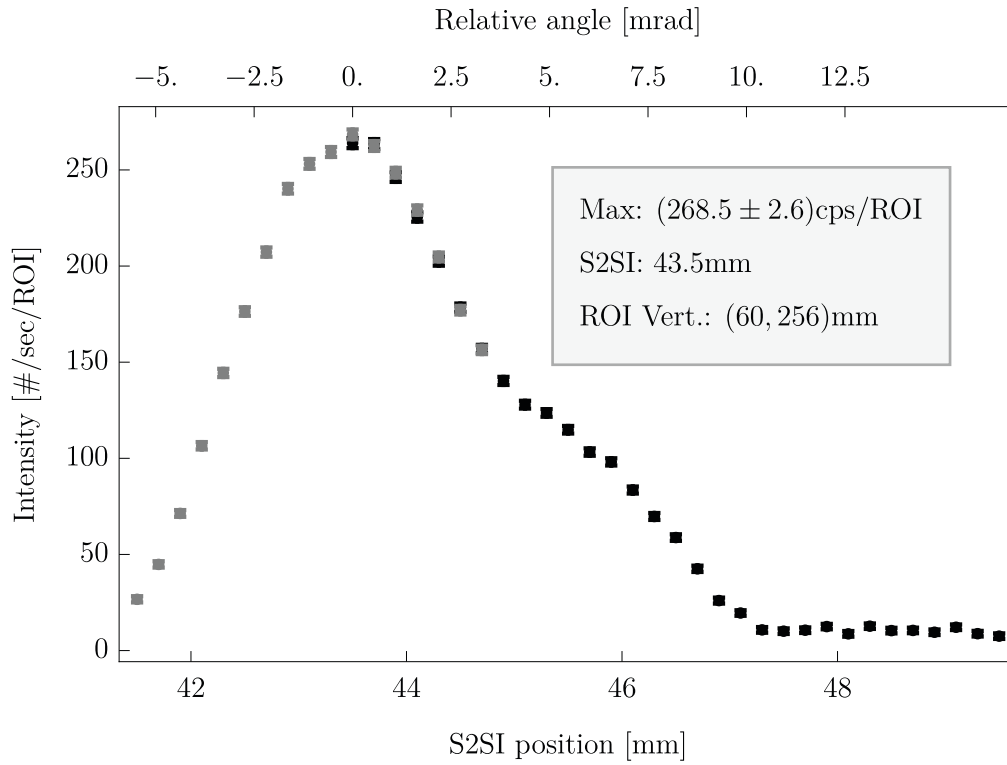


Figure 7.7.: Flux of the integrated beam after a two-slit setup where the second slits moves over the beam in horizontal direction. (Grey, black) represent the two measurements (ID0059, ID0061) that were combined for this plot and were taken during beam-time *Test-2455*. The experimental setup has a horizontal angular width (grey) of $\gamma_{\text{horizontal}} = 6.6$ mrad and a maximal vertical divergence angle of $\gamma_{\text{vertical}} = 87$ mrad. The maximum on the right side (black) is the reflection of the beam at the inner surface of slit S3. The beam is constrained horizontally by the second slit with $S2 = 0.511$ mm and vertically by an aperture with $S3 \approx 20$ mm. The distance between S3 and S2 is given as $\Delta_{S2,S3} \approx 384$ mm. The ROI is chosen to capture the full beam at the detector. See Heumesser (2016) for an in-depth analysis of this dataset and in particular for the measurement of the angular width.

7.1.2. Angular Preparation

At several positions in the setup a constrained angular distribution is needed. Firstly, restricting the beam in a controlled manner reduces stray neutrons at the detector plane beam downwards. Secondly, the monochromatization stage accepts neutrons for a given beam incident angle around the central wavelength, if their individual incident angle slightly deviates from the beam axis. Thirdly, the interferometer needs a constrained distribution to fulfill the coherence requirement. The maximal possible angle to the beam axis of a trajectory is given by size and placement of two spatially constraining components (S2, S1). This maximal angle is called divergence angle of the beam γ_D .

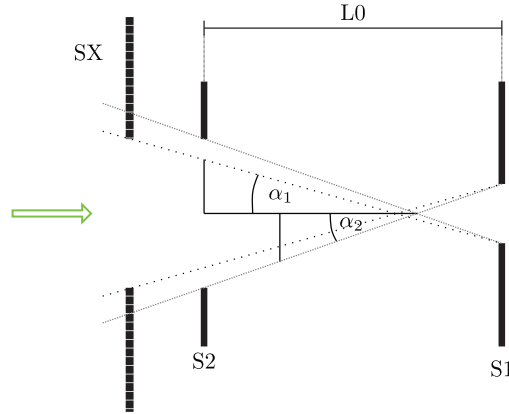


Figure 7.8.: Slit S1 and Slit S2 restrict maximal angles from the beam axis. Thus, the beam divergence is restricted to $\gamma_D = 2\alpha_2$. An additional smaller component SX defines a smaller divergence angle $\gamma_D = 2\alpha_1$.

The angular dependency of the beam has been thoroughly investigated in Heumesser (2016). An important result is that the measured angular width in front of the monochromatizing mirrors and the angular width behind the mirrors do not differ significantly. Thus, as is already stated in Heumesser (2016), the mirrors M1 and M2 do not add significant divergence to the beam. Consequently, the angular characteristic of the mirrors are not a significant loss contribution. In table 7.2 angular characteristics at different positions of the setup are collected. Finally, to match the coherence restriction

Position	Horizontal FWHM	Slit Width	Distance from Port
Behind S3	(6.51 ± 0.01) mrad*	(1 ± 0.005) mm	(653 ± 0.5) mm
Before S2	(6.6 ± 0.2) mrad	(0.511 ± 0.001) mm	(1183 ± 0.5) mm
Expected at S1	~ 0.74 mrad	$8.5 \mu\text{m}$	1873 mm

Table 7.2.: Geometrical parameters and achieved beam collimation at different beam positions during beam-time *Test-2455*. The values for S2 and S3 are taken from Heumesser (2016). (*) The distribution after S3 shows two peaks where the main peak has the stated width and the secondary peak was identified as a reflection on the inside of S3. The secondary peak is not accepted by the two mirrors due to its divergence from the central beam.

7. Experimental Setup and First Measurements

in section 6.2.1, the position of S1 for $S1 = 8.5 \mu\text{m}$ has to be chosen as

$$L_0 \geq \frac{S1 + S2}{\lambda S1} \approx 690 \text{ mm.} \quad (7.8)$$

beam downwards from S2.

7.1.3. Wavelength Selection

Out of the Maxwell-Boltzmann distribution that is emitted by the vertical cold source only the front most part is cut by the guide leading to the experimental area as discussed in section 3.3. The center wavelength that will reach the guide port is selected around $\lambda_{VCN} = 6.5 \text{ nm}$, as defined by the guides length and curvature which is discussed in section 3.3.

The wide wavelength spectrum shown in figure 7.5 does indeed feature prominently neutrons with λ_{VCN} . Important to note is that smaller wavelengths (below the cutoff) are only present before M0. In fact, it exists a rather broad peak around $\lambda \approx 4 \text{ nm}$ in the beam which is regarded as unwanted background. The composition of the distribution varies strongly on the extraction position. This is partly due to gravity and reflections on the inner guide wall. In particular a small cut-out of the beam can have a thinner distribution with a width of $\Delta\lambda/\lambda \sim 15\%$. In general it will be still too wide to not reduce the visibility of Lloyd's mirror substantially as discussed in section 6.2.3.

To achieve the necessary spectral width two monochromatic neutron Ni-Ti multilayer mirrors are used. The mirrors M1 and M2¹⁴ have a $d = 4.8 \text{ nm}$ and a $\Delta d/d \approx 5\%$. Thus, with a collimated beam the selected wavelength for $\theta = (41.4 \pm 0.01)^\circ$ is given by

$$n\lambda = 2d \sin(\theta) \approx 6.3 \text{ nm.} \quad (7.9)$$

Further, the width of the selected distribution is given in Majkrzak (1984) by

$$\frac{\Delta\lambda}{\lambda} = \cot(\theta)\Delta\theta + \frac{\Delta d}{d} \quad (7.10)$$

Slit S4 and S3 collimate the beam to have a divergence of $\Delta\theta = (6.51 \pm 0.01) \text{ mrad}$ as is given in table 7.2. The expected spectral width is thus

$$\frac{\Delta\lambda}{\lambda} = (5.75 \pm 0.01)\%. \quad (7.11)$$

¹⁴The used Ni-Ti mirrors as well as the initial super mirror are manufactured in Kyoto, Japan by Masahiro Hino and were graciously lend to us for the duration of the project.

The selected distribution for this configuration is shown in figure 7.9. Selected wavelength distributions of beam-time 3-14-343 and specifically their width are discussed in more detail in the thesis Bricher (2015).

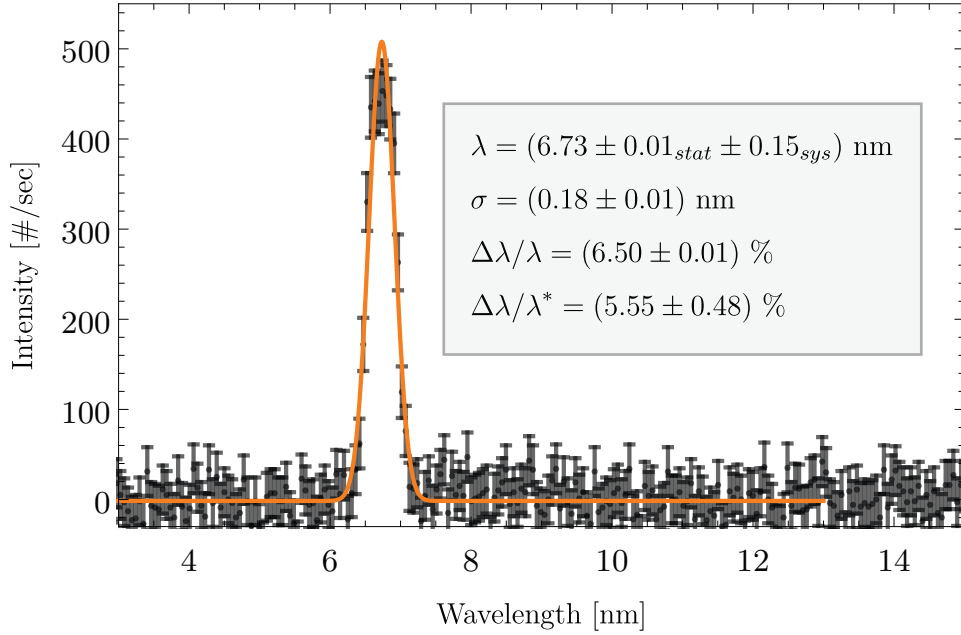


Figure 7.9.: Time of Flight setup that was used to measure the wavelength distribution of the center beam. The distance between chopper and detector is 1.303 mm. The center wavelength has two uncertainties, first, the statistical uncertainty originating from counting statistics, and second, a systematic uncertainty originating from uncertainties of the conversion parameters (distance, time offset). Two values for $\Delta\lambda/\lambda$ are given. The first is calculated from the FWHM of the shown distribution and the second (starred) corresponds to the width if the chopper opening-function is corrected.

The resulting spectral characteristics of the beam are summarized and compared to other experiments in table 7.3. With a measured spectral width of

Beam	Wavelength [nm]	Bandwidth [%]
PF2/VCN*	6.3 ± 0.001	5.3 ± 0.001
PF2/VCN	$6.73 \pm 0.01_{stat} \pm 0.15_{sys}$	$5.55 \pm 0.48_{sys}$
H18	$1.929 \pm 2 \cdot 10^{-3}$	3.6

Table 7.3.: Comparison of very-cold neutron wavelength and frequently used bandwidths $\Delta\lambda/\lambda$ at selected beams at the ILL. The value for PF2/VCN* is calculated for an incident angle of $\theta = (41.4 \pm 0.01)^\circ$ and according to Bragg's law. The values for the PF2 very-cold neutron beam are taken from measurements in beam-time 3-14-343 and *Test-2455*. The values for the H18 beam are extracted in appendix A.3 from Anton Zeilinger et al. (1988).

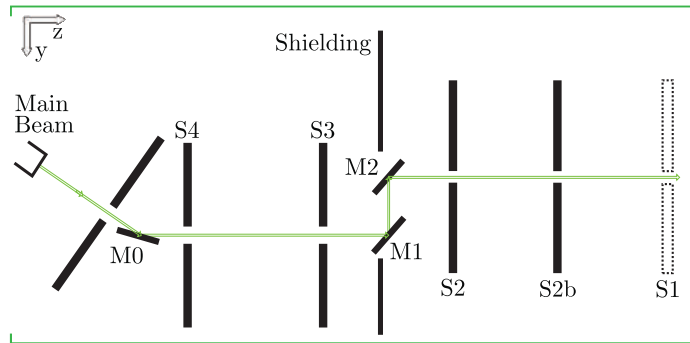
7. Experimental Setup and First Measurements

$$\frac{\Delta\lambda}{\lambda} = (5.6 \pm 0.5)\% \quad (7.12)$$

the spectral constraint is indeed fulfilled sufficiently. Note that both the uncertainty of the width and also for the center wavelength is rather large and both values differ from Bricher (2015). The first is due to a rough estimation of the chopper opening function which is approximated by a simple unit hat function. The second is due to a correction on the chopper time offset due to a modification on the original chopper setup.

7.1.4. Expected Intensity in Front of S1

The expected intensity after the beam preparation which is transmitted through S1 is the most important quantity to estimate the practicability of Lloyd's mirror and is estimated in this subsection. The corresponding setup is shown in figure 7.10.



In measurement ID0091.008 in beam-time *Test-2455* collimation, monochromatization, and Lloyd's mirror are present and

Figure 7.10.: Setup that is used to calculate the expected intensity at slit S1. Slit S1 is not present in this setup as indicated by the dashed of the component.

the measured and background corrected intensity at detector position I is $\mathcal{I} = (0.33 \pm 0.01) \text{ \#}/\text{s}$. Table 7.4 summarizes experimental parameters that are used to calculate the brilliance of the very-cold neutron beam. Correcting for air absorption¹⁵ and detector efficiency gives the neutron intensity at the detector plane as

$$\mathcal{I} = (0.93 \pm 0.04) \text{ \#}/\text{s}. \quad (7.13)$$

¹⁵This implies a compensation of air absorption in the final setup. For this, helium-filled tubes at atmospheric pressure with thin AlMg3 foils are prepared. This is studied in Scheicher (2015), where the foils with a thickness of $d = 15 \mu\text{m}$ are prepared. The minimal beam path of $L > 2.7 \text{ mm}$ is required for an absorption compensating effect and for reducing the absorption below 1%.

Quantity	Value	Uncertainty	Info
ϵ_D	67%	1%	The efficiency is extrapolated from Manzin (2011).
T_{air}	53.8%	1%	The transmission is calculated for standard conditions. $T = 298.15$ K and $p = 1013.25$ mbar.
S2b _h	0.3 mm	0.01 mm	Horizontal beam constraint at S2b. The slit consists of two boron-steel sheets with a natural boron content of roughly 1.74%. The inner surface of the slits are polished with a roughness of below $ra = (0.06 \pm 0.02)$ μm .
S2 _h	511 μm	1 μm	The slit is build up analog to S2b.
S2b _v	76 mm	0.1 mm	Vertical beam constraint at S2b. The slit is constrained by mirror M1 directly in front of S2.
$\Delta_{\text{S2,S2b}}$	300 mm	0.5 mm	Given is the direct optical path as measured using a laser distance meter with an accuracy of $\delta d = \pm 0.5$ mm.
$\Delta_{\text{Port,S2b}}$	1487 mm	0.5 mm	
γ_h	2.7 mrad	0.1 mrad	The angle then is given as
γ_v	107 mrad	1 mrad	$\gamma = (SA + SB)/R$. SA and SB are the constraining slit widths and R is the distance between them.
$\Delta\lambda_{\text{FWHM}}$	0.37 nm	0.03 nm	See section 7.1.3 for more details.

Table 7.4.: Parameters that are needed for the estimation of the brilliance of the very-cold neutron beam at the PF2 and for the estimation of the intensity in Lloyd’s mirror.

The last slit present in the system is S2b, an intermediate slit between S1 and S2. All relevant beam parameters are provided in table 7.4. The flux at S2b is given as

$$\mathcal{F} = \frac{\mathcal{I}}{\text{S2b}_h \text{S2b}_v} = (40.7 \pm 1.8) \cdot 10^{-3} \frac{\#/\text{s}}{\text{mm}^2}. \quad (7.14)$$

Considering maximal angular restrictions between S2 and S2b as also wavelength restrictions as given in section 7.1.3 the brilliance can be calculated as

$$\mathcal{B} = \frac{\mathcal{F}}{\gamma_h \gamma_v \cdot \Delta\lambda_{\text{FWHM}}} = (4.14 \pm 0.18) \cdot 10^3 \frac{\#/\text{s}}{\text{cm}^2 \text{ sterad } \text{\AA}}. \quad (7.15)$$

Note that the brilliance is only valid for areas and a solid angle comparable to the prepared system in measurement ID0091.008.

7. Experimental Setup and First Measurements

Continuing from the brilliance, the intensity which would be transmitted through S1 can be extrapolated by using the values given in table 7.5.

Quantity	Value
S1 _h	8.5 μm
S1 _v	100 mm
Δ _{S2,S1}	690 mm
γ _h	0.75 mrad
γ _v	90 mrad

Table 7.5.: Parameter that are used to estimate the intensity that is transmitted through the slit S1 in the interferometer region section I.

The extrapolated intensity at slit S1 is thus given by

$$\mathcal{I}_{S1} = (8.9 \pm 0.4) \cdot 10^{-3} \text{ \# / s.} \quad (7.16)$$

Additionally, the partial radiance \mathcal{R}^* at the slit S1 is given as

$$\mathcal{R}_{S1}^* = (1.4 \pm 0.06) \cdot 10^3 \frac{\text{\# / s}}{\text{rad mm}} \quad (7.17)$$

which is useful to calculate the intensity for different slit sizes. Table 7.6 shows a comparison of the estimated brilliance for section II, to the brilliance without monochromatization stage, the brilliance given for the H18 beam, and the brilliance at the D11 instrument.

Beam	Brilliance [$\frac{\text{\# / s}}{\text{cm}^2 \text{ strad \AA}}$]	Source
PF2/VCN	$(1.6 \pm 0.3) \cdot 10^5$	Equation (7.7)
PF2/VCN _{mono}	$(4.14 \pm 0.18) \cdot 10^3$	Equation (7.15)
H18 _{mono}	$(1.33 \pm 0.01) \cdot 10^9$	Anton Zeilinger et al. (1988) & appendix A.3
H18 _{Exp}	$1.3 \cdot 10^9$	Laue-Langevin (2008)

Table 7.6.: Comparison of the PF2 very-cold neutron beam's brilliance measured before and after monochromatization and the brilliance of the H18 beam. The value for the brilliance of the H18 beam is calculated from Anton Zeilinger et al. (1988) and is shown in appendix A.3. Additionally, the value for H18_{Exp} is the expected value taken from Laue-Langevin (2008). The brilliance that is given for PF2/VCN is taken from measurement ID0059 and ID0061 in beam-time *Test-2455* and is discussed in more detail in Heumesser (2016). The value for PF2/VCN_{mono} is taken from measurement ID0094.008 in beam-time *Test-2455* with an added monochromatization stage as discussed in section 7.1.3.

It is apparent that the brilliance at the raw beam at the PF2 is rather low but it is in agreement with a rough extrapolation from the overall flux distribution in figure A.4. In contrast, the brilliance after monochromatization does drop by a factor of ~ 40 . This could indicate that only 15% of the beam is reflected on each mirror, which is in disagreement with the reflectivity of 80 – 90% per mirror as specified in Masahiro Hino (2015). More realistic is that both values are not very well comparable for two reasons. Firstly, the value before monochromatization is a mean over a bigger solid angle and it cannot be expected, that a small cut from this solid angle is similar to the overall mean. Secondly, the selected region of the beam with a high probability is not identical in the two measurements, as they are taken during two different beam-times. Nevertheless, this mismatch indicates that by readjusting the setup an increase of the local intensity is possible.

7.2. Lloyd's Interferometer

Section I as shown in figure 7.1 houses the interferometer, detectors, and monitoring probes and begins at the entrance slit S1. A possible implementation for this section is shown in figure 7.11. The prepared neutron beam enters the interferometer region from the left through the entrance slit S1. Interference is accomplished by a superposition of a path where the neutron is reflected at a vertically aligned glass mirror and a path where the neutron directly travels to the viewing screen. The capture of the interference pattern can be realized by adding a CR39 detector either directly behind the mirror or further away.

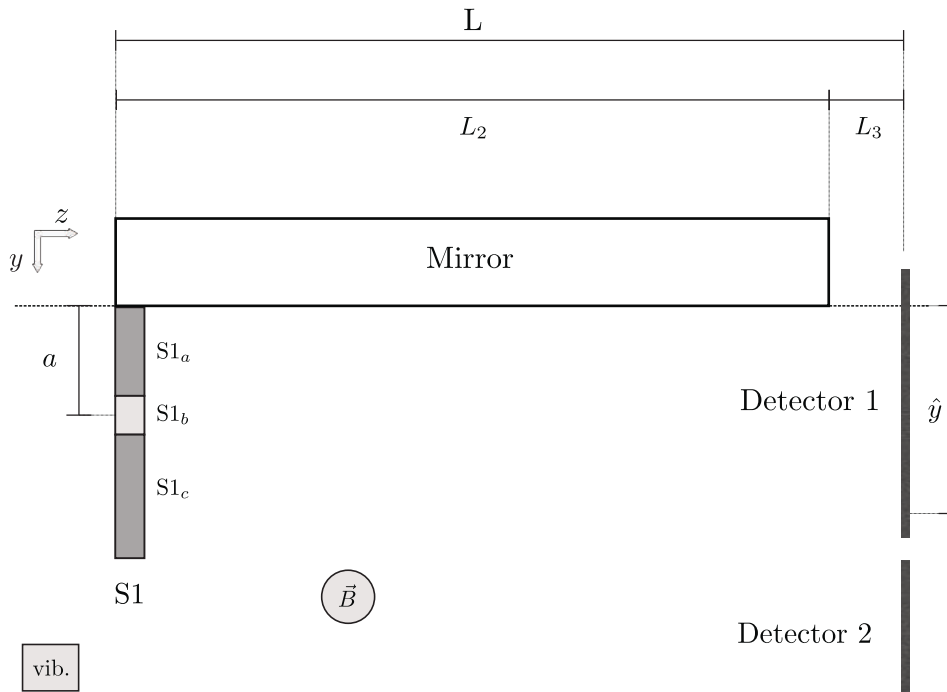


Figure 7.11.: Proposed scheme of the interferometer region. The entrance slit is composed of a small mirror $S1_c$ that is pressed on two metallic spacers on the main mirror. Thus, the layer $S1_b$ is transmissive and the layers $S1_c$ and $S1_a$ are absorptive. The rectangle on the bottom labeled vib. is a vibration sensor on the mirror and the disk labeled with \vec{B} which is a precision magnetic field sensor.

This section presents the proposed setup, the intended characteristics, and individual setup components.

7.2.1. Entrance Slit

The entrance slit and its alignment to the main mirror is a rather complicated issue. The vertical extension of the slit is of the order of the beam diameter to not discard usable flux. Thus, at the very-cold neutron beam at the PF2 the vertical opening is chosen to be $S1_{\text{ver}} \sim 100$ mm. As the pattern is integrated over the vertical extension of the slit, non-parallelity α between the S1 and the mirror will reduce the contrast of the integrated pattern as shown in section 6.3.2.1. The alignment of a free standing slit would be particularly difficult. Thus, here a stack of a small mirror, a transmissive (aluminum) and an absorptive (high-brass) layer on top of the main mirror is used. The thickness of each layer determines the interferometer geometry, while the width specifies the transmission of the neutron beam through each layer. As is shown in table 7.7, the

Component	Material	Thickness	Width	Transmission
S1 _a	High-brass*	53 μm	10 mm	< 0.14%
S1 _b	Aluminum	8.5 μm	10 mm	57.9%
S1 _b	Carbon	8.5 μm	12 μm	99.92%
S1 _c	BK7	20 mm	20 mm	$\ll 10^{-10}\%$

Table 7.7.: Entrance slit neutron transmission characteristics. The transmission given is determined by the width of the specific layer into section I and denotes the fraction of not absorbed and not scattered neutrons. The edge of the high-brass* spacer is coated with a $d > 200$ nm thick boron-10 layer to further reduce transmission. For the layer S1_b two possibilities exist where the carbon layer consists of two thin threads or neutron transmissive aluminum. The uncertainty of the aluminum, high-brass, and carbon thread thickness was measured to be below $\delta d < 1\%$.

fraction of undisturbed neutrons passing through the transmissive layer is higher than $T > 57\%$ in the case of an aluminum stripe and higher than $T > 99.9\%$ in the case of two carbon threads. The aluminum case is easily adjustable but produces a incoherent background signal of scattered neutrons of around 5%. In the carbon thread case two threads are used as spacers between mirror and brass spacers, which is hard to adjust correctly but is superior in terms of signal influences. Finally, the maximal misalignment of the slit S1 to the mirror's surface is determined by the variation in thickness of each layer foil. Each foil is checked using a high accuracy thickness gauge and only foils with a variation below $\Delta d < 0.1 \mu\text{m}$. Thus, the maximal misalignment angle under optimal

7. Experimental Setup and First Measurements

conditions¹⁶ is $\beta \approx 1 \mu\text{rad}$ and therefore is compatible with the constraint of $\beta < 2 \mu\text{rad}$ stated in section 6.3.2.1.

7.2.2. Main Mirror

The main mirror is a boron silicon glass block with a thickness of 30 mm, a vertical extension of 100 mm, and an available length of $L = 315 \text{ mm}$ due to the entrance slit assembly. Both sides of the mirror are polished to have a roughness of less than $r_a \approx (0.007 \pm 0.001) \mu\text{m}$, which satisfies the constraint derived in section 6.3.2.2. The surface profile of the mirror¹⁷ in the direction of the neutron flight path can be roughly approximated by a paraboloid

$$f(x) = a(x - c)^2 + b \quad (7.18)$$

with

$$a = (-11.1 \pm 0.5) \cdot 10^{-6} \frac{\mu\text{m}}{\text{mm}^2}$$

$$b = (0.372 \pm 0.006) \mu\text{m}$$

$$c = (179.6 \pm 2) \text{ mm}.$$

Thus, the maximal deviation relative to the mirror's edge of about $\Delta f \approx 0.37 \mu\text{m}$ is found in the middle of the mirror.

Both surfaces are coated with an optical layer $\sim 10^2 \text{ nm}$ of aluminum and a thin protective layer of silicon oxide. The glass block is held in place by an aluminum holder shown in figure 7.12. It offers two rotational degrees of freedom with which the mirror

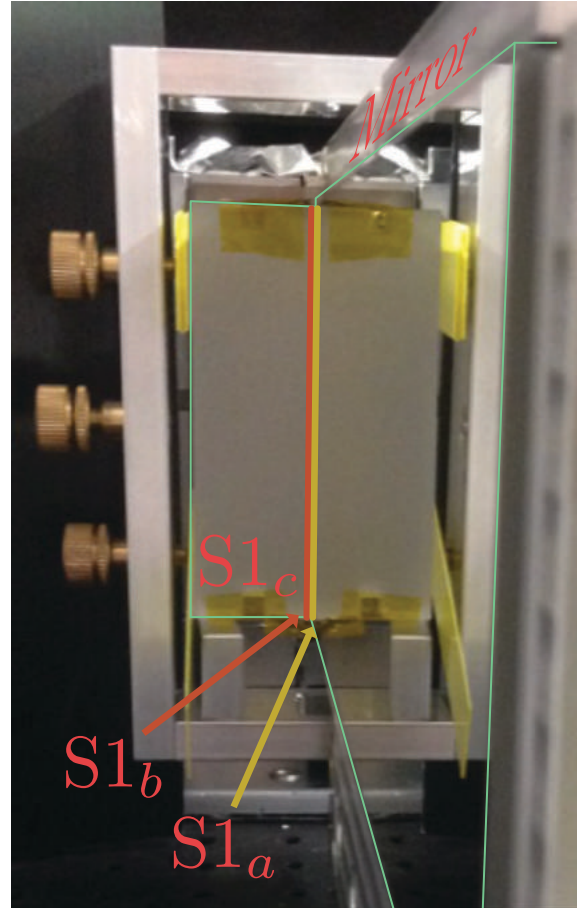


Figure 7.12.: Shown is the main mirror entrance slit setup viewed from the perspective of the detector. The main mirror is enclosed in an aluminum holder on the right side. The small mirror $S1_c$ is uniformly pressed on the main mirror using μm -screws.

¹⁶A clean working environment is a crucial necessary condition, as a single dust particle has the potential to seriously inhibit the formation of a high contrast interferogram.

¹⁷The profile has been measured by S-DH Sputter-Duenschichttechnik GmbH by laser optical means. The profile is measured along the middle axis of the mirror. The perpendicular axis shows a similar behavior with a deviation of $\Delta f \approx 0.25 \mu\text{m}$ between the middle and the mirror's edge.

can be aligned relative to the incoming beam. They are controlled using two piezo actuators¹⁸ (I/II) with micrometer screws which are monitored using strain gauges. At the end of the mirror holder a fitting for a CR39 detector is designated which presses the detector close to the mirror to avoid bending effects during exposure. If no CR39 detector is used the beam propagates further and can be captured in a beam downwards placed detector.

7.2.3. Monitoring Scheme

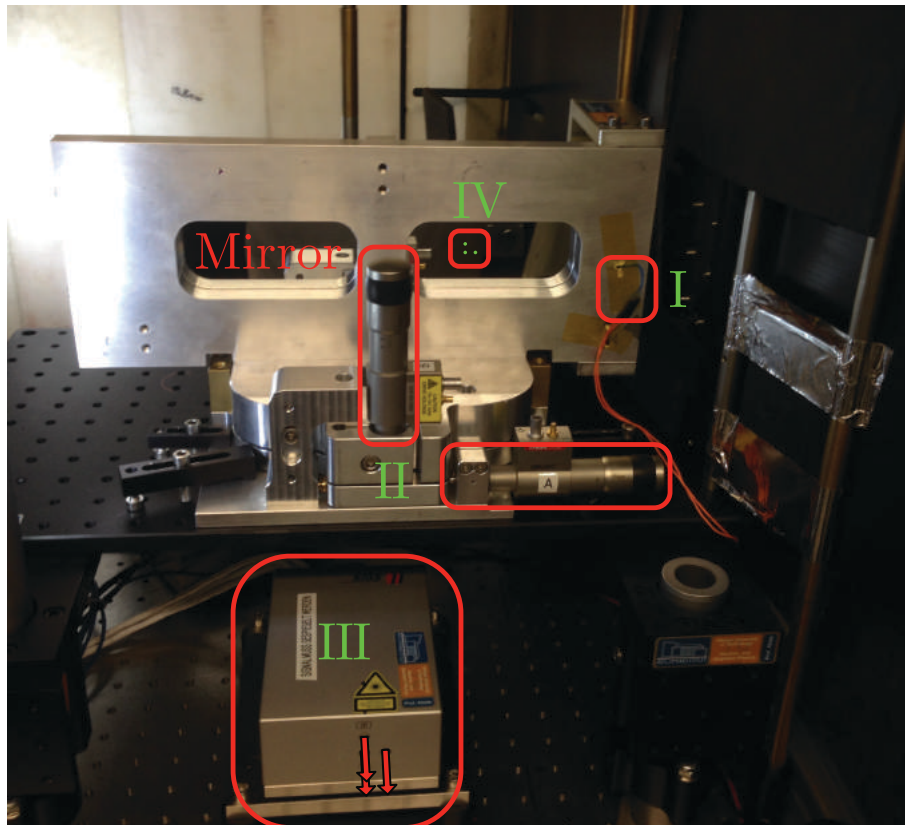


Figure 7.13.: Visible is the holder of the main mirror from the back showing several monitoring systems supporting the measurement. I is the temperature sensor attached to the mirror holder, II are the positions of the piezo controlling roll and yaw angle of the mirror, III is a three-beam laser interferometer which hits the mirror at position IV.

¹⁸The piezo actuators are Thorlabs DRV517 with a travel range of $30\ \mu\text{m}$ for the actuator and $12.7\ \text{mm}$ for the micrometer screw. The accuracy of the mirror system in respect to the piezo actuators is studied in Kappl (2016). There the yaw angle that is controlled by the lever, composed by the piezo and the mirror holder mechanics, can be calculated by using $k_\beta = (8.75 \pm 0.06) \frac{\mu\text{rad}}{\mu\text{m}}$. For the roll angle lever this is determined to be $k_\beta = (7.89 \pm 0.06) \frac{\mu\text{rad}}{\mu\text{m}}$.

7. Experimental Setup and First Measurements

The setup is monitored in several aspects as shown in figure 7.13. The temperature is monitored using NTC-resistors¹⁹ placed at various components. For example, at position I in figure 7.13 the temperature stability of the mirror holder is monitored as well as each moving stage in section II is equipped with a temperature sensor to detect stage malfunctions early. At position I/II the movement of the mirror is monitored by strain gauges which are incorporated in the piezo actuators.

Quantity	Variability	Time Scale and Information
Magnetic field variation	$\pm 0.5 \mu\text{T}$	Between min and hourly variations. Mostly stray fields by neighboring experiments. The phase shift due to magnetic field fluctuations is discussed in section 5.6.3.4.
Table tilt	$\sim 10 \mu\text{rad}$	Unidirectional tilt drift in both directions over a period of five days. The tilt of the table affects foremost the orientation relative to gravity and thus induces a phase shift as discussed in section 5.6.3.2. Note that due to the small magnitude this effect can be neglected.
Table tilt measurement systematic	$\pm 5 \mu\text{rad}$	The used electrolytic tilt sensor is susceptible to temperature variations, thus a false tilt variation following the day-night cycle is introduced.
Ambient/table temperature	$\pm 0.125 \text{ K}$	Main contributions are sinusoidal variations with low amplitude and a period 12 h. This is expected for the day-night cycle in a stabilized environment.
Mirror holder temperature variation	$\pm 0.1 \text{ K}$	The temperature of the holder is strongly dominated by the day-night cycle. In the present measurement the temperature varied around $T = (25.09 \pm 0.06) \text{ K}$ without significant drift.

Table 7.8.: During beam-time *Test-2455* environmental quantities were monitored. Exemplary a long measurement (ID96 & ID97) spanning five days is used. During that time the neutron beam ran almost continuously and the setup has been checked only once a day. The very-cold neutron cabin is insulated against thermal and vibrational disturbance but has no active stabilization.

¹⁹The electronic back-end has been implemented and tested in Bloch (2016) during beam-time *Test-2455*.

Additionally, as a reference, a three-beam laser interferometer²⁰ at position III, monitors the relative movement of the mirror’s rear side at position IV. Not visible in the picture is a magnetic field probe²¹ that is drawn in figure 7.1 as a circle labeled with \vec{B} . Vibrations of the setup are monitored using an electrolytic tilt sensor²² attached to the surface of the optical table. The summary of the measured variations during a longer measurement period are collected in table 7.8. The effects of a residual magnetic field or time variations of the field are discussed in section 5.6.3.4. There it is argued that shielding of the interferometer region is needed and can be implemented with the same Mu-metal sheets that are used for the qBounce experiment.

7.2.4. Background Intensity

Name	Value	Unit
Threshold	0.173	a.u.
Training Set	ID2017.02	—
Training #	3021	Tracks
Track Area	30	pixel
Class	N. Prior Probability	
Neutron_Point	0.22	
Neutron_Inclined	0.09	
Neutron_Faint	0.09	
Neutron_Extreme	0.01	
Candidate_Faint	0.09	
Candidate_Extreme	0.01	
Systematic_Noise	0.13	
Systematic_Crack	0.22	
Systematic_Dust	0.13	

Table 7.9.: Table of the relevant parameters that are used for the classification of tracks for the detector IDL001 and measurement ID0098 in beam-time *Test-2455*. The used classifier is an earlier version which can handle low neutron density but features no cluster examples.

During beam-time *Test-2455* a CR39-based spatial resolving detector is placed at detector position II as seen in figure 7.1. This position is just outside of the main beam

²⁰The used device is a SIOS™ SR 2000 which operates on a HeNe-laser at $\lambda = 633$ nm.

²¹The magnetic field has been measured using a FLC3-70 magnetic field sensor from Stefan Mayer Instruments. It offers a measurement range of ± 90 μ T.

²²The used sensor is the IRIS™ model of “Applied Geomechanics”. It can measure tilts on two axes in a range of $\pm 25^\circ$ with a resolution of 0.012° .

7. Experimental Setup and First Measurements

and is as heavily shielded as the position of the main interferogram measurement. The detector has been exposed for $T = 539882 \text{ s} \approx 6 \text{ days}$ at this position and then optically scanned at nine different positions over an area of $A = 1.56 \text{ mm}^2$ each. In total 4219 tracks were found on this detector of which (629 ± 25) were identified as neutron tracks. The neutron irradiance is thus given as

$$\mathcal{F}_{\text{Background}} = (83 \pm 8) \cdot 10^{-6} \frac{\#/\text{s}}{\text{mm}^2}. \quad (7.19)$$

The procedure for the classification of the tracks is presented in section 8.3.3 and the relevant parameters are given in table 7.9.

7.3. Summary

This chapter summarizes the results of the two beam-times *3-14-343* and *Test-2455*. An additional beam-time *3-14-320* in 2013 was mainly used to gather information on the beam-port, rough characteristics, present equipment, and the dimensioning of the future setup. First section II which shapes the beam is discussed in section 7.1. The beam is roughly characterized in section 7.1.1 and the characterization of the implementation of section II is presented in the subsequent Subsection:

Section 7.1 for the angular preparation, section 7.1.3 for the wavelength preparation, and section 7.1.4 for the estimation of the transmitted intensity. Second section I, which encompasses the planned interferometer setup, the monitoring scheme, and example environmental measurements are presented in section 7.2.

The built up time of section II is optimized to be as short as $T \approx 10 \text{ days}$ to make efficient use of a full reactor cycle at the ILL of about 50 days. This is especially important as individual measurements periods are estimated in chapter 6 to be of the order of several days. The spectral characteristics of the very-cold neutron beam are determined to be

$$\frac{\Delta\lambda}{\lambda} = (5.6 \pm 0.5)\% \quad (7.20)$$

at a wavelength of

$$\lambda = 6.73 \text{ nm}. \quad (7.21)$$

The brilliance \mathcal{B} after section II has been determined to be

$$\mathcal{B} = (3.7 \pm 0.4) \frac{\#/\text{s}}{\text{cm}^2 \text{ sterad } \text{\AA}} \quad (7.22)$$

and thus the expected radiance over the horizontal dimension is \mathcal{R}^* at S1 followed as

$$\mathcal{R}_{S1}^* = (941 \pm 44) \frac{\#/s}{\text{rad nm}}. \quad (7.23)$$

In this way, the radiance is extrapolated by only assuming the extension of the proposed entrance slit S1 and is thus no major inaccuracies are to be expected.

The geometrical constraints which are given by the proposed setup in section 7.2 are already used for the predefinition of the standard parameter as given in appendix A.4 and thus the presented intensity is acceptable as a bases for the calculations in the previous chapters.

A first attempt on the full interferometer setup is made in beam-time *Test-2455*. In section 7.2.1 an implementation of the entrance slit is proposed, that fulfills the constraints calculated in section 6.3 and subsequently the main mirror is presented. Important environmental parameters which were measured during this beam-time are presented in section 7.2.3. Temperature variations and vibrations are already on a low level during these measurements. Additional magnetic shielding should not be necessary but magnetic components in the interferometer region were avoided. Prominently, the background neutron intensity at detector position II is determined in section 7.2.4 to be

$$\mathcal{F}_{\text{Background}} = (83 \pm 8) \cdot 10^{-6} \frac{\#/s}{\text{mm}^2}. \quad (7.24)$$

during active beam and full shielding of section I.

8. Spatial Neutron Detection

8.1. Spatial Resolving Neutron Detection

To capture the interference pattern as discussed in section 6.1.1 CR39 plate detectors are a convenient candidate. They offer a spatial resolution of $\zeta \sim 2 \mu\text{m}$ and are discussed in detail in Rueß (2002) and in Nesvizhevsky, Börner and Gagarski (2000) for the measurement of quantum neutron states over a horizontal mirror. In the scope of the qBounce experiment a simplified version of these detectors on CR39 basis with a boron coating¹ is presented in Nahrwold (2005) and refined in Jenke et al. (2013). The production at the Atominstitut has been realized in the scope of this thesis. Together with a machine learning supported analysis this detector concept is applicable for Lloyd’s mirror. In this section basic concepts are introduced as for example a short overview of the developed production procedure in section 8.1.2. This is followed up by some considerations on the exposure of CR39 detectors in section 8.2. Finally, in section 8.3 the machine vision aided neutron track detection is presented.

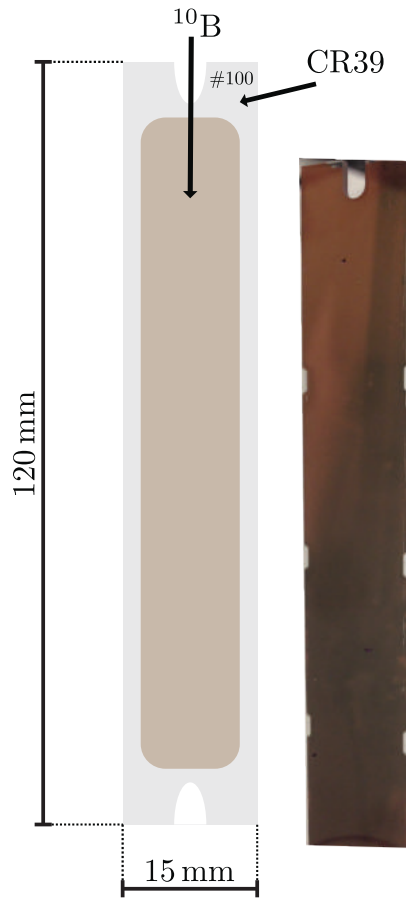


Figure 8.1.: On the left: CR39, ¹⁰B detector dimensions. On the right: Photo of a CR39 plate detector with ¹⁰B coating.

¹An alternative design of the CR39-based detector is presented in Krantz (2006). Instead of an boron coating an uranium 235 is used in this implementation.

8.1.1. CR39-based Detector Design

The overall design of CR39² plate detectors that were used in this experiment has a three layer structure, as presented in Jenke et al. (2013) which is a refined design from Nahrwold (2005). CR39 serves as substrate and as imaging layer which stores the spatial information, copper as post-processing layer, and boron-10 as neutron converting layer. Figure 8.2 provides a schematic overview and table 8.1 gives relevant information for each layer.

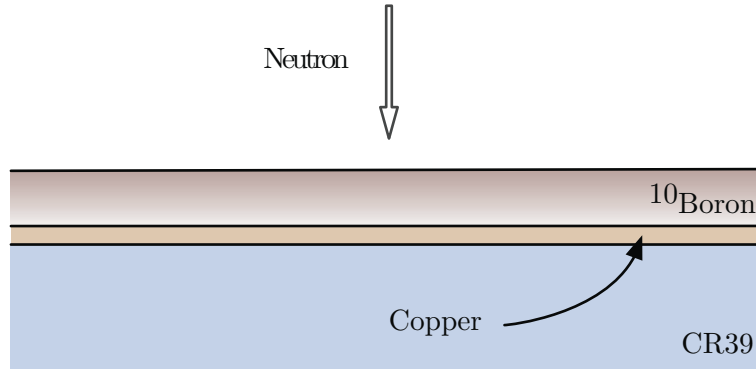
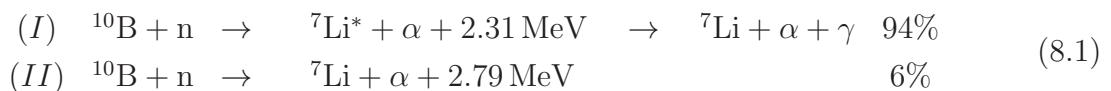


Figure 8.2.: Three layer structure of CR39-based detectors used in this project. This detector design is presented in Jenke et al. (2013) which is refined design from Nahrwold (2005).

Layer function	Compound	Thickness	Density
Neutron converter	¹⁰ Boron	220 nm	2.46 g/cm ³
Post-processing	Copper	< 50 nm	8.92 g/cm ³
Substrate & imaging layer	CR39	1.5 mm	1.32 g/cm ³

Table 8.1.: Information for each layer that together built up a spatial-resolving CR39-based plate detector. This detector design is presented in Jenke et al. (2013). It is a refined design from an earlier version presented in Nahrwold (2005).

Neutron converting Layer Neutrons that impinge on the ¹⁰B layer trigger a nuclear reaction as described in Knoll (2010) and studied in M. O. Klein (2000). This reaction leaves a Li-ion and an α -particle in 6% of the cases in the ground state (case *I*) and otherwise in an excited state (case *II*) as shown in equation (8.1).



²Using the CR39 holopolymer as a nuclear track detector for heavy ions is first proposed in Cassou and Benton (1978).

The reaction products leave the place of the reaction back to back and one strikes the CR39 layer as shown in figure 8.3. There Li or α -particle disconnect chemical bounds

Branch	Occurrence	$E_{\text{kin}}(^7\text{Li})$ ^7Li	$E_{\text{kin}}(\alpha)$ α	Material	R_{max} [μm] ^7Li	R_{max} [μm] α
I	94%	0.84 MeV	1.47 MeV	CR39	3.2 ± 0.2	6.1 ± 0.2
II	6%	1.02 MeV	1.77 MeV	CR39	3.6 ± 0.2	7.4 ± 0.1
I				Boron	1.8 ± 0.1	3.5 ± 0.1
II				Boron	$2. \pm 0.1$	4.4 ± 0.1

Table 8.2.: Given are theoretical kinetic energy of daughter particles in the two possible branches (I,II) for a $^{10}\text{B} + \text{n}$ nuclear reaction. Additionally, the maximal range R_{max} of these ions in CR39 and boron is given. Due to the thinness of the boron and copper layer, these do not significantly contribute to the range in CR39 and are neglected in the calculation of the stopping range in CR39. The shown range values were extracted from a simulation using the SRIM by Ziegler (2013).

on its way through the holopolymer³, until its energy is dispensed in the material. The ions stop at a range between $5 \mu\text{m}$ and $10 \mu\text{m}$ in the CR39 layer, which is simulated using Ziegler (2013). The specific energy per branch and particle and the stopping range is shown in table 8.2.

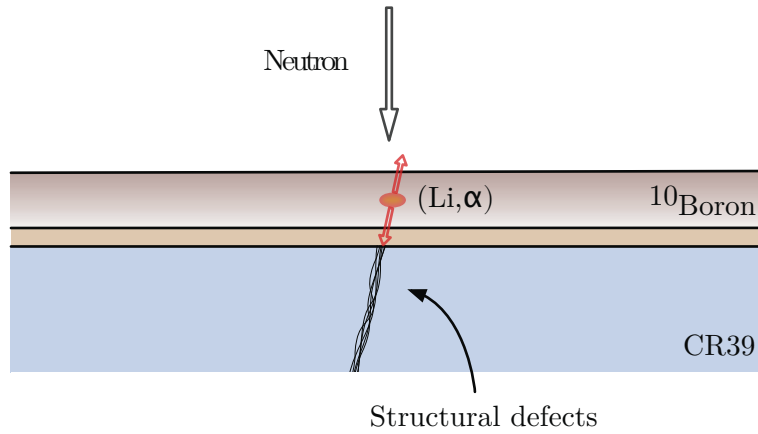


Figure 8.3.: CR39-based detector is hit by a nuclear fragment (lithium-ion or α -particle) and enters the CR39 layer where it loses its energy through the production of structural defects.

If the boron and the copper layers are removed and the CR39 is etched with a sodium hydroxide solution, the upper most layer of the CR39 is removed. Because the etching velocity is enhanced in the areas where reaction products penetrated the CR39 and

³An holopolymer is produced by polymerization of the CR39 monomere. This process makes CR39 highly resistant to most chemicals and environmental effects as presented in PPG-Industries (2006).

8. Spatial Neutron Detection

destroyed internal bounds, the nuclear tracks are enlarged over time. For a 25% sodium hydroxide solution at 42° and an etching time of $\tau = 5$ h the average track diameter reaches $d_{\text{track}} \sim 1 \mu\text{m}$. Figure 8.4 shows a post processed CR39 with a high neutron count.

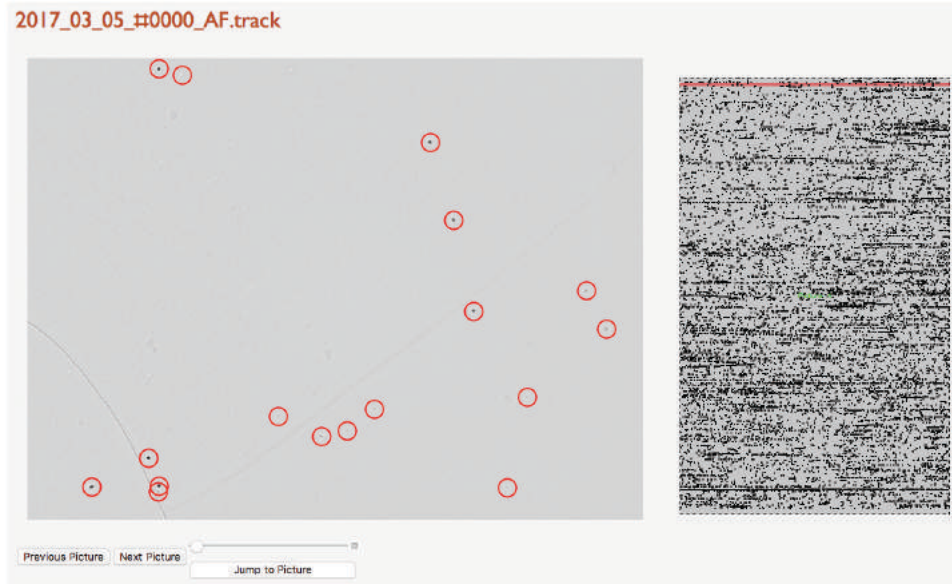


Figure 8.4.: On the left: Example image of an exposed and chemically treated CR39 as seen after $50\times$ magnification with an optical microscope. Candidates for nuclear tracks that got enlarged by chemical etching are selected with a grey scale threshold and are marked with a red circle. On the right: Map of a scan of a detector. Each dot is a nuclear track candidate. Depending on the chosen threshold the map can be dominated by several effects. The scan used is #057_Mittig_1_225x1 of CR39 IDL003.

The chemically etched CR39 with enlarged nuclear tracks is scanned with an optical microscope. By means of manual or automatic feature detection, a map of these tracks is produced and an example map is shown on the right side of figure 8.4.

Detector Resolution and Efficiency Resolution and efficiency are directly related to the thickness of the neutron converting layer. The attenuation of an homogeneous neutron beam transversing matter is given by the Beer-Lambert equation (5.3) in section 5.1. For a $d = 220$ nm thick⁴ absorptive boron layer⁵ $\epsilon_{\text{Ideal}} = 35\%$ of the neutrons with a wavelength of $\lambda = 6.3$ nm will trigger a nuclear reaction. Not all ionizing fragments will reach the CR39 layer. A few will be absorbed due to the finite range in the boron layer.

⁴For Lloyd's Mirror a thicker layer is advisable but a technical challenge. This has to be addressed in the future.

⁵See table A.5 in appendix A for the macroscopic absorption cross-section of the boron coating of the used detector. The coating is not pure ^{10}B but a compound of approximately 95% ^{10}B and 5% ^{11}B .

This can be accounted for as shown in Stadler (2009) which is based on M. O. Klein (2000). There the efficiency for an ionizing fragment originating from the boron layer and reaching the CR39 layer is given by

$$\epsilon_{\text{CR39}} = 0.94(\epsilon[\alpha, \text{I}] + \epsilon[\alpha, \text{II}]) + 0.06(\epsilon[\text{Li}, \text{I}] + \epsilon[\text{Li}, \text{II}]). \quad (8.2)$$

If $z \leq R_{\text{max}}$ and by using the calculated ranges of the ions in matter in table 8.2, the efficiency for each reaction branch can be calculated with

$$\epsilon[\text{Particle}, \text{Branch}] = \frac{1}{2\kappa_B \frac{v_0}{v} R_{\text{max}}} \left(1 + \kappa_B \frac{v_0}{v} (R_{\text{max}} - z) - (1 + \kappa_B \frac{v_0}{v} R_{\text{max}}) e^{-\kappa_B \frac{v_0}{v} z} \right). \quad (8.3)$$

R_{max} is the range in boron, v is the velocity of the neutron, $v_0 = 2200$ m/s, $\kappa_B = \sigma N$, σ is the absorption cross-section at v_0 , and N is the number density. The resulting reduced efficiency is only slightly smaller with a value of

$$\epsilon_{\text{CR39}} = 32.4\%. \quad (8.4)$$

The point of the nuclear reaction in the boron layer is on the order of 100 nm away from the entrance point of the reaction product in the CR39 layer. Additionally, the etching process removes the surface of the CR39. Thus, the projected position (x, y) of the track in the CR39 layer does not exactly coincide with the reaction position (x_r, y_r) . The equation for the reduced resolution is given in Stadler (2009) by

$$\zeta_{\text{CR39}} = \sqrt{\zeta_{\text{Geo}}^2 + \zeta_{\text{Trace}}^2} = 1.77 \mu\text{m}. \quad (8.5)$$

While $\zeta_{\text{Trace}} \approx 0.77 \mu\text{m}$ considers the uncertainty due to the finite track diameter,

$$\zeta_{\text{Geo}} = \left(d - \frac{\int_0^d dz \epsilon[p, b](z) \cdot z}{\int_0^d dz \epsilon[p, b](z)} + d_{\text{etched}} \right) \tan[\theta_C] \quad (8.6)$$

considers the uncertainty of the track mapping between CR39 layer and reaction position. $d_{\text{etched}} \approx 0.6 \mu\text{m}$ is the thickness of the CR39 layer that is removed in the chemical post processing and $\theta_C \approx 67^\circ$ is the critical angle for the angle between surface normal and track direction. Tracks with $\theta > \theta_C$ will be very faint after etching and will be at best tracks with enlarged size but shallow depth. Finally, systematic effects of the detector reduce the achievable resolution further. For discussions of the efficiency and resolution see Nahrwold (2005), Filter (2009), Stadler (2009) and Jenke et al. (2013). Especially

8. Spatial Neutron Detection

in Jenke (2011) the experimental resolution is measured to be $\zeta_{\text{CR39}} < 2.1 \mu\text{m}$ for $\sim 8 \text{ m/s}$ neutrons compared to a theoretical resolution of $\zeta_{\text{CR39}} = 1.8 \mu\text{m}$. The resolution ζ_{CR39} and detector efficiency ϵ_{CR39} for a wavelength of $\lambda = 6.3 \text{ nm}$ is plotted against the thickness of the converting layer in figure 8.5.

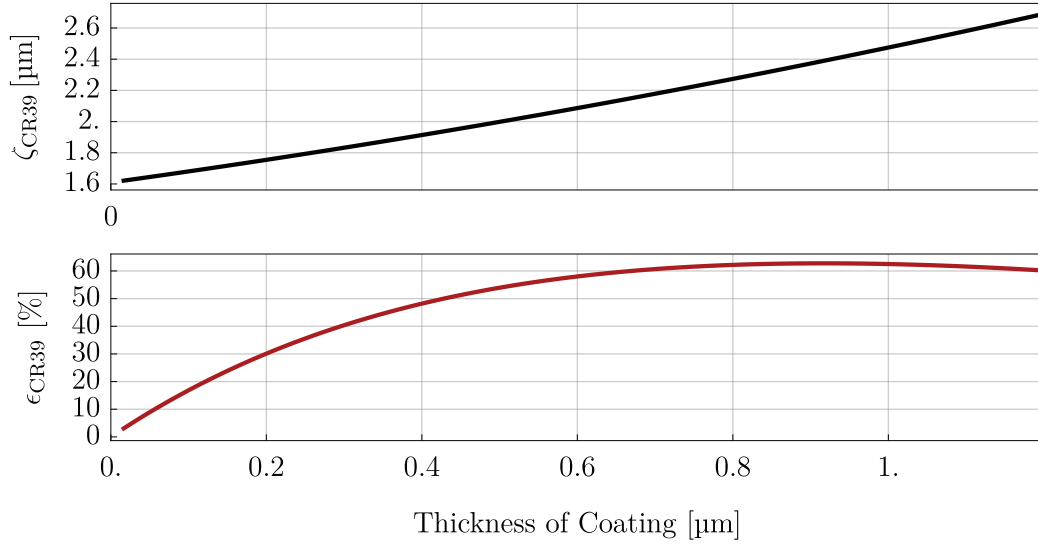


Figure 8.5.: The upper plot shows the resolution ζ_{CR39} of boron-coated CR39-based neutron detectors over the thickness of a boron coating. The second plot shows the efficiency ϵ_{CR39} of the same detectors over the same thickness range. The neutron wavelength is set to be $\lambda = 6.3 \text{ nm}$. The top plot is calculated using equation (8.5) and the bottom plot is calculated using equation (8.3).

8.1.2. Detector Production and New Developments

Continuing the work in Rueß (2002), Nesvizhevsky, Börner and Gagarski (2000), Westphal (2001), Nahrwold (2005), Krantz (2006), Filter (2009), Stadler (2009), Jenke (2011) and most recently Jenke et al. (2013), several aspects of the detection using CR39 were reviewed in the scope of this thesis. As part of this thesis a thin film coating facility at the Atominstitut was put in operation and the thin film coating procedures were developed. The cleaning procedure was refined and track detection was enhanced to make use of current machine learning methods. The latter is discussed extensively in section 8.3. Here the production procedure will only be sketched in order to provide a context. It centers around a vacuum electron beam coating facility at the Atominstitut which is sketched in figure 8.6.

The basic concept is based on heating the material to be evaporated with an electron beam which is guided by magnetic fields from a filament onto the material. The heated

material emits atoms of which some are able to reach the substrate that is to be coated on ballistic trajectories.

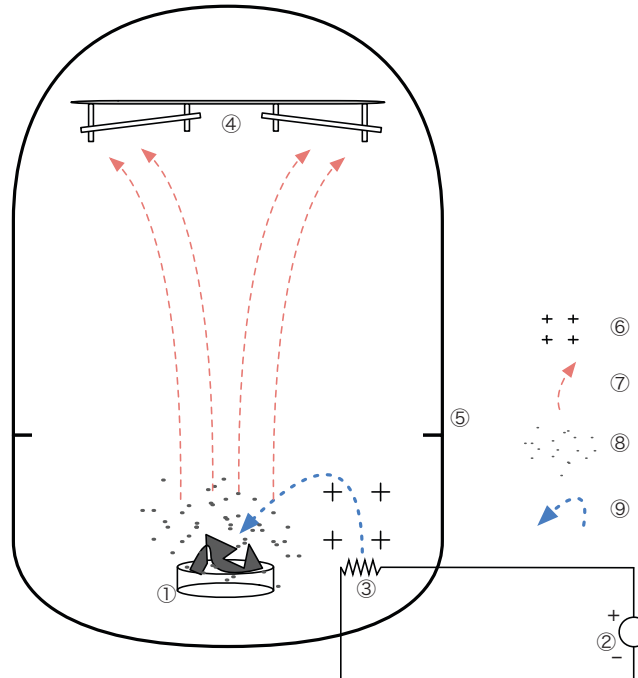


Figure 8.6.: Basic principle of the thin film coating setup at the Atominstitut. (1) is the crucible containing the material to be evaporated. (2) is a 10 kV High-voltage supply (3) is the filament which produces the electron beam. (4) is the substrate holder which carries the substrate face downwards. (5) the setup is arranged in a vacuum chamber. The electron beam (9) is guided by a static magnetic field (6). The heated material emits atoms (8) and a fraction of these have trajectories (7) that are able to reach the substrate. The graphic is taken from Filter (2009).

To achieve a homogeneous and intact coating, the amount of heat that is deposit and the maximal heat transfer gradient need to be tightly controlled. This was realized at the Atominstitut to achieve a sufficiently homogeneous coating as shown in figure 8.7. This figure shows microscope images of pre-2012 detectors as described in Jenke et al. (2013), an early Vienna prototype with considerable inhomogeneities, and the latest result of the coating process in Vienna. In particular, cracks of the coating layer were reduced over the extension of the area of the detector, which eliminates local resolution uncertainty due to partial coating detachment around the cracks.

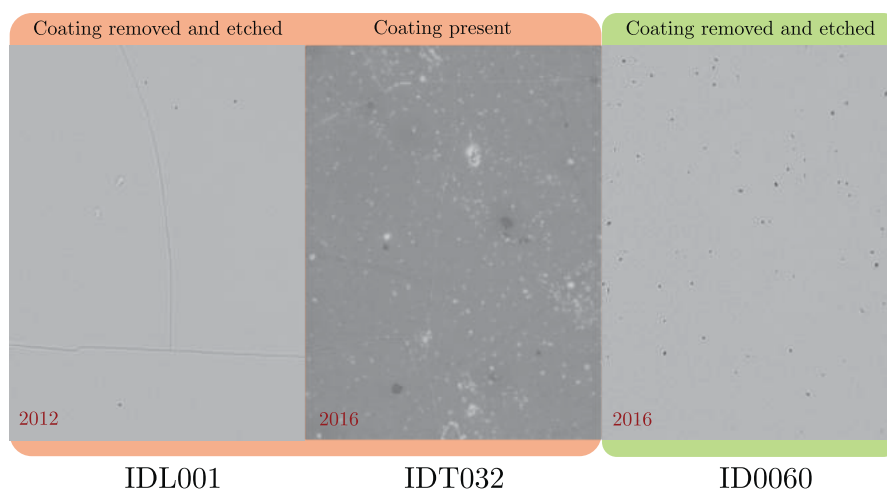


Figure 8.7.: Shown are three exemplary boron 10 coated CR39 detectors imaged using optical microscope at $50\times$ magnification. On the left, the detector IDL001 is shown that is exposed to neutrons and etched. In the middle, the detector IDT0036 is shown that belongs to an early test batch of the coating process in Vienna and is not etched. On the right, an example of the coating development in Vienna namely detector ID0060 is shown. The middle image shows early problems of the coating process in Vienna, namely deep cracks in the coating and substrate, partial detachment of the coating from the substrate in the vicinity of cracks, and small point-like defects from boron squirts. On the right side, the improved coating process does not produce cracks over major parts of the detector and no further non-noise is visible.

8.2. Radiating CR39 Detectors with Neutrons

If the neutron intensity is high enough nuclear tracks in the CR39 layer may overlap. This can be taken as a natural upper limit for the neutron exposure of CR39 plate detectors as the track identification is considerably more difficult for overlapping tracks. Further, the false positive density and neutron background give a lower limit for the exposure.

8.2.1. Lower Limit for Neutron Exposure

The lower exposure limit for CR39-based detectors is constrained by several effects:

— **Very-cold neutron background:**

Neutrons that do not coherently contribute to the observed signal. For example, scattered very-cold neutrons.

— **Thermal neutron background:**

The beam-guide leading to the PF2 turbine is a source for scattered neutrons. Most slow neutrons with low energy do not penetrate the very-cold neutron cabins casing but especially thermal neutrons could reach the detector and react with a boron-10 nucleus. Only $P = 1\%$ of the thermal neutrons which hit the detector react with the boron layer. This contribution is neglected as no significant thermal neutron flux at the beam position has been detected.

— **Other ionizing Radiation:**

γ -rays that originate from the reactor or are from secondary γ -ray producing processes in the radiation shielding.

— **Post processing:**

The production of a map of neutrons on a detector is accompanied by adding artifacts and dust which are falsely classified as neutron tracks.

Most of these contributions can be determined by placing a CR39-based detector close to the measurement position during a measurement but outside the direct beam. Figure 7.1 shows the Lloyd's mirror setup with CR39 positions marked as 'Detector I' and 'Detector II'. Position I corresponds to the interferogram and position II to a background estimation. Such a background measurement has been done⁶ and resulted in

⁶The relevant CR39 has the IDL001 and has been exposed during beam-time *Test-2455* 2015. Section 7.2.4 discusses this result in more detail.

8. Spatial Neutron Detection

$\mathcal{F}_{\text{Background}} = (83 \pm 8) \cdot 10^{-6} \frac{\#/\text{s}}{\text{mm}^2}$. The estimate for the minimal exposure is then given by the amount of neutrons that are needed to produce a signal that can be distinguished from the overall background. The difference between \mathcal{F}_B and \mathcal{F}_S is significant with $\mathcal{S} = 3$ if

$$\sqrt{\frac{\mathcal{F}_S - \mathcal{F}_B}{\mathcal{S}} - (\delta\mathcal{F}_B)^2} < \delta\mathcal{F}_S. \quad (8.7)$$

8.2.2. Upper Limit for Neutron Exposure:

The upper limit for the exposure is given through the ability to distinguish between tracks and the accuracy of the coordinate mapping even if tracks overlap. If there is no possibility to distinguish between single tracks and overlapping tracks, a very conservative limit is appropriate. For example, by setting the limit to the amount of cases for which two tracks overlap to be below 1% of the overall neutron count.

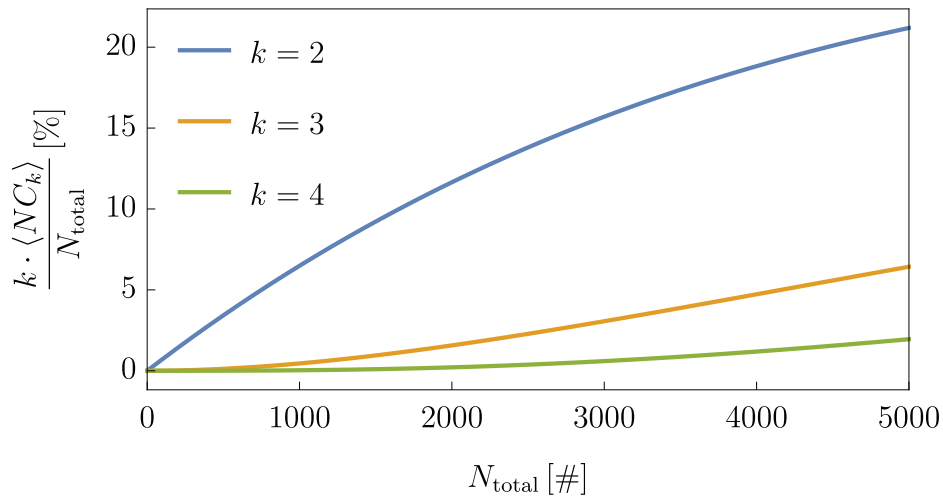


Figure 8.8.: Shown is the average number of tracks normalized to single tracks for a k -track cluster for different k and the sum as function of the number of tracks per microscope picture. A microscope picture covers an area of 0.06 mm^2 . The consistency of this calculation has been verified by checking $N_{\text{total}} = \sum_{k=1}^{\infty} k \cdot \langle NC_k \rangle$.

If k tracks overlap in certain region this is called in the following a k -constituent cluster $\langle NC_k \rangle$. The ratio between the average number of tracks in k -constituent cluster and the number of tracks N_{total} should thus be

$$\frac{\langle NC_k \rangle}{N_{\text{total}}} = n_k \cdot k \leq 1\% \quad (8.8)$$

where n_k is the average relative number of k -constituent clusters. In Quintanilla and Torquato (1996) it is shown that

$$n_k = \frac{p_1(1 - p_1)^{k-1}}{k} \quad (8.9)$$

is a good approximation for n_k , if the area covered by tracks is small compared to the total area. Here $p_1 = e^{-4\hat{N}V_1}$ is the probability to find a single track with an area $V_1 = \pi(d_{\text{track}}/2)^2$ for a number density of $\hat{N} = N_{\text{total}}/A$. Solving the right side of the equation (8.8) for N for a specific area A gives the maximal number of tracks N_k^{limit} for which clustering is insignificant. In figure 8.8 the average relative number of tracks in a specific cluster is shown.

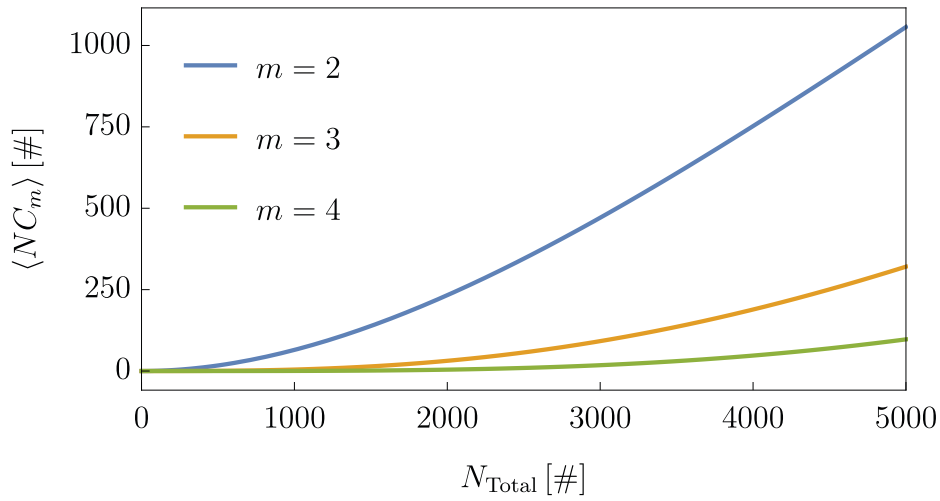


Figure 8.9.: Average number of tracks in k -track clusters with $k \geq 1$.

For a microscope image with an area of $A = 0.06 \text{ mm}^2$ and an average track diameter of $d_{\text{track}} = 1.2 \mu\text{m}$ an uniformly exposed picture can have an average of $N_2^{\text{limit}} = 140$ tracks before more than 1% of the tracks form a 2-constituent cluster. If it is possible to do

cluster size	$N_k^{\text{limit}} [\#]$	$\frac{N_k^{\text{limit}}}{A} [\frac{\#}{\text{mm}^2}]$
$k = 2$	140	2244.4
$k = 3$	1545	24705.9

Table 8.3.: Values for the maximal track number per microscope image N_k^{limit} , which satisfy equation (8.8), if the number of tracks in k -clusters is below 1%. It is assumed that the detector is uniformly exposed to neutrons.

both, distinguish the elements of a 2-constituent and determine the position to sufficient

precision, one can limit the amount of 3-constituent clusters. Again a threshold of 1% allows on average for $N_3^{\text{limit}} = 1545$ tracks per picture. These values are collected in table 8.3 together with the corresponding density limits.

In low intensity measurements the total number of tracks per picture is well below N_2^{limit} and thus only single tracks need to be considered. For measurements with intensities above the given limit, clusters with $k > 1$ constituents need to be included in the classification and analysis.

8.3. Post-Processing of a CR39 Detector

8.3.1. Chemical Treatment

The residual defects that are left behind by impinging ionizing particles in the poly-matrix can be etched away with a base, for example NaOH. These residual defects following the flight path of the impinging particle are called *track* in the following. The procedure of etching can be seen as a region of interest for particle type and energy. The phenomenology of track formation is extensively studied in Fleisher, Price and Walker (1975) for various substrates.

After production, the detectors are exposed to several different types of radiation. This covers electromagnetic radiation as for example γ -rays and x-rays, secondary radiation from fast and thermal neutron radiation, and other kinds of ionizing radiation. Most of these produce tracks but of varying size and depth. By etching a specific time and with a specific strength, tracks produced by low energy background are etched away leaving only the wanted neutron tracks to be enlarged in the chemical process. For the specific energies of the produced Li and α ions the detectors are etched with 25% – NaOH at $T = 42^\circ$ for $\tau = 5$ h. The basic procedure has been developed and is presented in Nahrwold (2005).

8.3.2. Image Capture and Image Processing

The chemically treated detectors are scanned with an optical microscope and a sufficiently accurate 2D-stage⁷. The result is a set of pictures, taken at 50× magnification. A single picture has a size of $A_{\text{image}} = (288.8 \times 216.6) \mu\text{m}^2$. Additional parameters related

⁷As is shown in the dissertation of Thalhammer (2018) the camera and lens system used to capture individual pictures does not preserve the coordinate system but introduces distortions. This can be corrected by using a map which transforms into the not distorted frame. The resulting uncertainty is on the order of $0.3 \mu\text{m}$ and is neglected in the scope of this thesis.

to these pictures are summarized in table 8.4. To detect neutron tracks on these pictures

Picture Parameter	x-Axis	y-Axis	Unit
Size in μm	288.83	216.63	μm
Size in Pixel	1376	1032	pixel
Conversion	0.20991	0.20991	$\mu\text{m}/\text{pixel}$

Table 8.4.: Shown are important values for pictures produced with an optical microscope at the Atominstitut. The values are supplied in private communication in Thalhammer (2018).

and build a track-map, one needs to perform several image processing steps before an automated algorithm is able to yield a meaningful result. Most importantly, this is the normalization of all pictures of one set to a joint intensity baseline. Alternatively, for small scanned areas it is possible to detect the tracks by manual selection⁸, as etched neutron tracks have a unique appearance. See figure 8.13 for a non-complete sample set of neutron tracks.

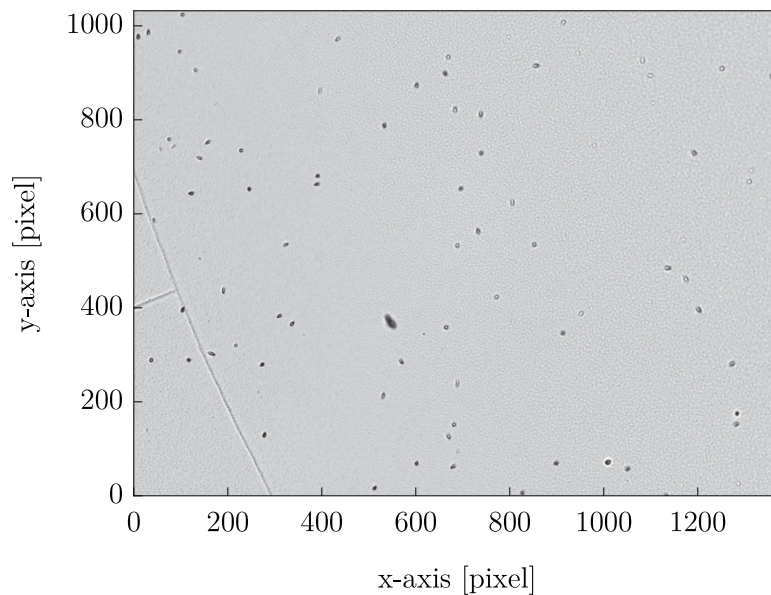


Figure 8.10.: Image 552 taken from CR39 ID0067, Scan 2016_06_28_4x429_Normalised before post-processing. For visual clarity the intensity scale of the image is normalized to values between $I = (0 - 1)$. Visible is a crack originating from the boron layer which propagated to the CR39 surface and was subsequently etched. In the middle a big black spot is a dust particle on the detector. The small black points are nuclear tracks that are formed by etching up regions weakened due to the impact of ionizing radiation.

⁸Additionally, to a solely manual selection a combined algorithm can be employed. There the human interaction is reduced to removing wrong tracks and adding missed tracks to the pool of neutron tracks.

8.3.2.1. Image Normalization

Image normalization is necessary as the image capturing process does not produce image sets with equal intensity distributions. Additionally, the normalization allows to comparing tracks from different scans and detectors, which is necessary to build a classifier which then can be used on all detectors. The distribution depends on the picture content and on the distance of the focal plane to the detector plane.

Here each image is normalized to its background intensity. Figure 8.10 shows a representative image of a single scan of detector IDL001. From such an image N pixel samples with size $A = (30 \times 30)$ pixel² are selected randomly and the mean as well as the standard-deviation of their intensity distribution is calculated. This yields a distribution $\hat{\mathcal{B}}$ as shown in figure 8.11. From this distribution only samples which are close to the mean are selected (red dots) in order to remove samples that are sampled randomly from non-background areas. The selected tracks build up the distribution \mathcal{B} .

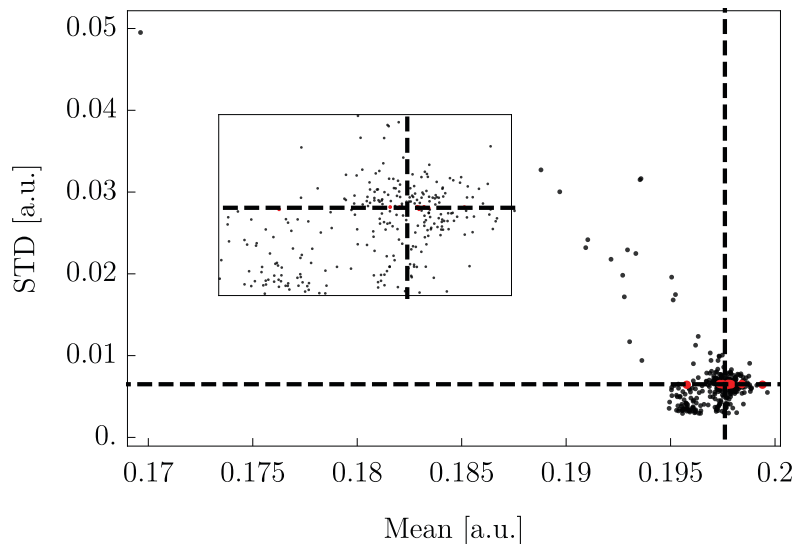


Figure 8.11.: Shown is the sample distribution \mathcal{B} of randomly selected samples from a single image. For each sample area the mean and the standard deviation are calculated. Each black dot represents one sample and each red dot represents one accepted sample which is used to calculate the mean background intensity. The image 552 is taken from CR39 ID0067, Scan 2016_06_28_4x429_Normalised.

The mean of \mathcal{B} is taken as the approximate image background value. This is valid if the background covers a major part of the image.

If the background is not the dominant feature, for a small subset m of images the standard deviation of \mathcal{B}_m is bigger compared to the set of all \mathcal{B}_m . By defining a threshold

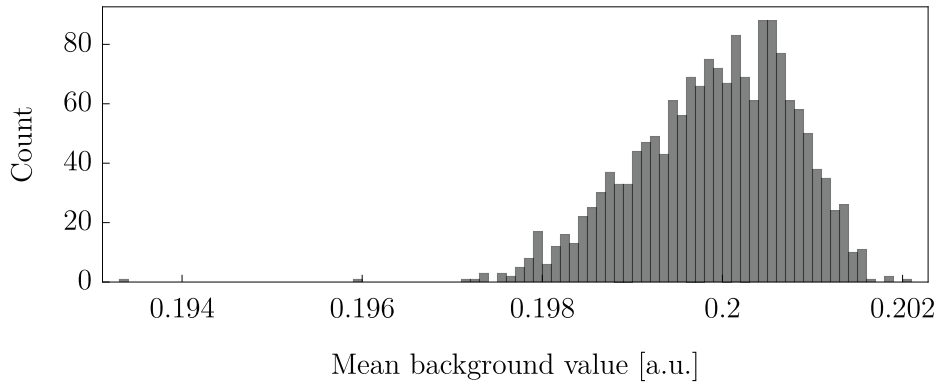


Figure 8.12.: Mean background values which are used to normalize individual pictures. The shown distribution is calculated for CR39 ID0067, Scan 2016_06_28_4x429_Normalised with a total of 1716 pictures. The broad distribution is due to imperfect focusing of images.

for the standard deviation, images without accurate background estimation are identified and an extrapolation from neighboring images is used for the background value.

Figure 8.12 shows the distribution of calculated mean background values for an example dataset with 1716 images. The visible width is mostly due to imprecisions in the image focusing procedure. For 40% of the images it was necessary to repeat the random sample drawings and for 20% of the images the mean value had to be extrapolated from a neighbor image. For the present scan this can be explained by the neutron intensity at the peak of the neutron distribution where no background is visible anymore. A classification of this detector is shown in figure 8.19. For regular neutron densities the number of images where extrapolation is needed are zero or below 0.1%.

8.3.3. Track detection

After image capture and normalization the next step is the determination of the position of nuclear tracks. Therefore, a threshold for the intensity value range is defined, which selects all pixels over that threshold and determines the size of clusters of the selected pixel.

With a defined region of interest for the cluster size one yields a dataset of candidates for nuclear tracks. Figure 8.13 shows a set of candidate tracks that were selected for an example image. The delicate problem thus is to determine which of the candidate tracks are nuclear tracks and which are not. In past experiments in the qBounce project this selection was done by hand⁹. First it is identified, which of the tracks originate from

⁹See appendix A.1.4 for an overview of the front-end of the software. Figures A.5 and A.6 show the manual classification front-end as used in the early scope of this thesis.

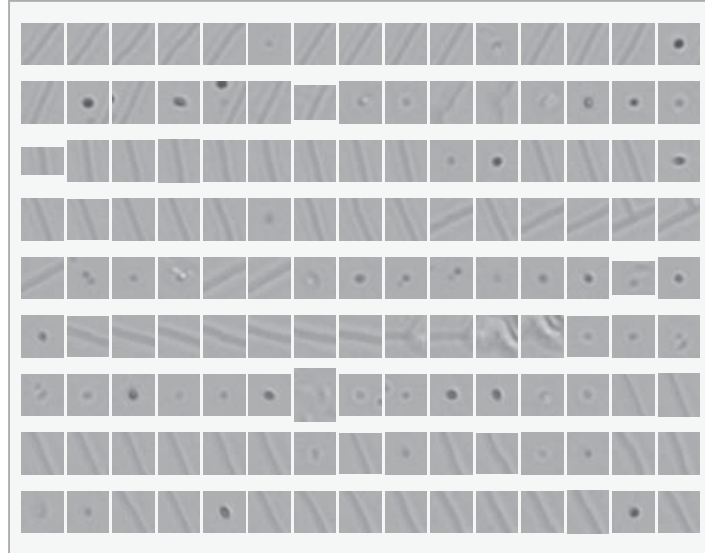


Figure 8.13.: Shown are example candidates which were selected by a grey-scale and size threshold. Both thresholds were slightly relaxed to reduce a False-Negatives bias. The size of the track image varies if the track is located near the border of a picture. Especially cracks are selected which is not an issue for detectors produced at the Atominstitut but earlier versions.

neutron exposure and their possible peculiarities as for example in Nahrwold (2005) or in Stadler (2009). Then scans of parts of a detector with highlighted candidates are time-consumingly¹⁰ classified by hand. Due to these practical restrictions the neutron detection is limited to small areas and low counts. In past qBounce experiments the expected pattern did not exceed the dimension of one image slice of the detector of $A_{\text{Slice}} = 289 \mu\text{m} \times b \cdot 217 \mu\text{m}$, where b is the number of images to be stitched¹¹. Thus, in this case manual selection is still practicable. This is not necessary the case for Lloyd's mirror. Due to the expectedly low beam intensity it might be necessary to search a big area of a detector. As this is not possible by hand, an automated method of classification was developed.

8.3.4. Machine Vision Based Detection

Machine vision algorithms were extended and hardened extensively over the past decade and even ported to popular and accessible computer algebra systems as for ex-

¹⁰A well trained researcher only needs a few seconds per candidate track to judge and note the choice with computer assistance. For past scans full classification would need on the order of days for one detector slice of $A_{\text{Full, Slice}} \approx (289 \mu\text{m} \times 80 \text{mm})$, if it is taken into account that one scan has to be judged by several researchers to estimate systematic effects.

¹¹Figure A.7 shows an example of a stitched track map.

ample Wolfram Research. Making use of these developments the problem of classification is significantly hardened against human bias, increases the reproducibility, and decreases the time necessary for the analysis. In the following, an application of machine vision techniques to the problem of track identification is presented¹².

8.3.4.1. Classification

In the scope of this thesis the implementation of the Random Forest algorithm by Mathematica¹³ is used to classify found tracks in one of several classes. A feature of the random forest is that it is efficient and especially able to identify a dominant class. As here the goal is to discriminate tracks of secondary neutron radiation against dust, cracks, and background, this algorithm is chosen.

Class Definition Foremost every track which can be attributed to a neutron triggering, a nuclear reaction in the boron layer should be classified as **neutron**. As the lithium and helium ions enter the CR39 layer under different angles, point-like and inclined shapes can be expected. Also as the ions lose energy in the bulk faint tracks for ions with a short path are expected but with a significant lower probability. Further, dependent on the neutron density each of these tracks can be in close proximity and form different sized clusters, as explained in section 8.2. Thus, to capture the expected variety at least five classes are needed.

{Neutron_Point , Neutron_Inclined , Neutron_Faint ,
Neutron_Double , Neutron_Tripplet }

It is to be noted, that 2-clusters are not frequent and 3-clusters can normally be neglected, as stated in section 8.2. The faint neutron category is vulnerable to other kind of damages which are also etched away by the chemical treatment procedure. Therefore, a buffer category **Candidate** is introduced to reduce the false positive rate in the neutron category.

{Candidate_Faint , Candidate_Extreme }

Finally, dust, cracks in the initial coating, and other non-nuclear tracks are merged in the **Systematic** category.

{Systematic_Artifact , Systematic_Dust , Systematic_Crack }

¹²See appendix A.1.4 for an overview of the developed front-end of the software.

¹³The Mathematica implementation is based on the implementation by Breiman (2001). Dependent on the specific detector at hand the program can switch to a different algorithm for the classification.

8. Spatial Neutron Detection

As some tracks will not be recognizable easily, additional sub-classes are added to catch these during manual classification but are then dropped in the actual training set. An example of manually classified tracks is shown in figure 8.14.

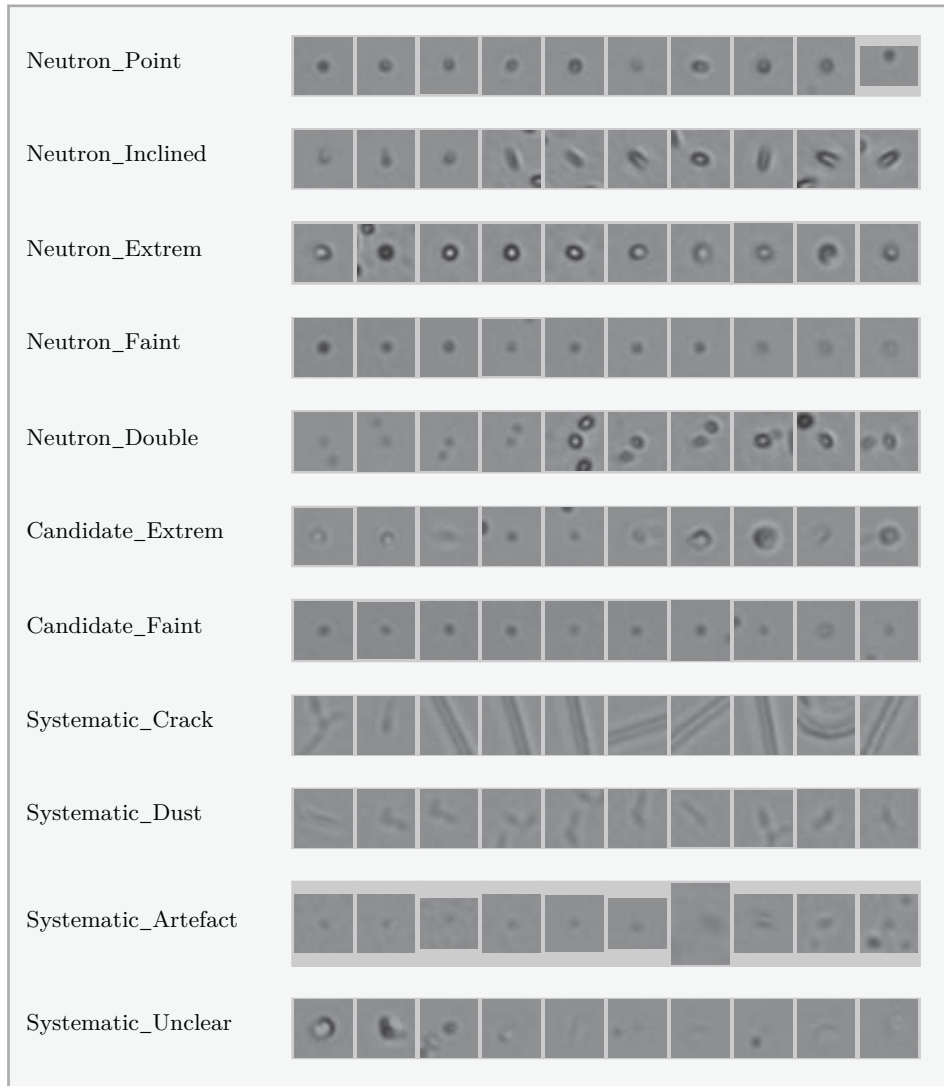


Figure 8.14.: Manually classified nuclear track candidates. Shown are classifications for the classes Neutron, Candidate, and Systematic as they would be chosen in past manual track classification. The sub-classification is introduced to yield more robust classifiers. Some pictures slightly vary in size when a track is found close to the border of the image.

Training Tracks To train the classifier a large set of training tracks is manually classified¹⁴ using the classes and sub-classes introduced in the previous paragraph. These training tracks should originate from a set which is distinct from the set of measurements to be classified. For this purpose scans without relevant information are used to extract examples¹⁵. In general, this is no problem for a Random Forest algorithm, as long as the training set is big enough.

Table 8.5 summarizes the detectors and scans used and the total of training tracks on each scan. A specific training set is assigned an identifier which for the present case is ID2017.04 and has a total of $N = 3983$ training tracks.

Detector	Scan	Prominent Classes	Count
ID0036	Scan_1_Normalised	Neutron	339
ID0060	2016_02_16_#017_MIII_Normalised	Neutron & Candidate	442
ID0084	#054_ID0084_40x20_Normalised	Neutron	991
IDL001	2015_07_12_Normalised	Artifacts	235
IDL001	2016_02_22_#018_MII_Normalised	Crack & Dust	202
IDL001	2016_02_22_#018_MIII_Normalised	Crack & Dust	327
IDL003	#057_Mittig+1_225x1_Normalised	Crack	630
IDL012	2016_09_09_7x215_#047_Normalised	Crack	828

Table 8.5.: Detectors and scans which were used to extract training examples. Only scans which are excluded from further analysis are used to avoid trivial classification.

Using the training set, the classifier is set up as depicted in figure 8.15.

Out of the training set a subset is selected randomly which is used to build up a decision tree as is described in Wolfram Research (2017). This implementation¹⁶ selects at an individual branch, a random feature subset out of the 900 pixel per sample region¹⁷ to calculate a test case. The size of the subsets is optimized while building the classifiers by internal cross-correlation. The tree is applied by testing each candidate track at each branch and applying the label at the leaf (end point). A track that is to be classified is tested at each branch until an end point is reached and a class per tree is assigned. This procedure is repeated to build up a forest of decision trees, each built up with a random

¹⁴See appendix A.1.4 for an overview of the front-end of the software. Especially figure A.10 which depicts the training front-end.

¹⁵ID0084 and IDL001 are classified with an earlier version of the classifier which does not include training tracks from the same detector. If these detectors were to be reclassified, it would be advisable to exclude the respective examples, even if in the case of ID0084 only 3% of the neutron tracks are used.

¹⁶The used implementation is a bootstrap aggregating algorithm by Breiman (2001).

¹⁷For each track a region of $A = (30 \times 30)$ pixel² is cut around the center of the track.

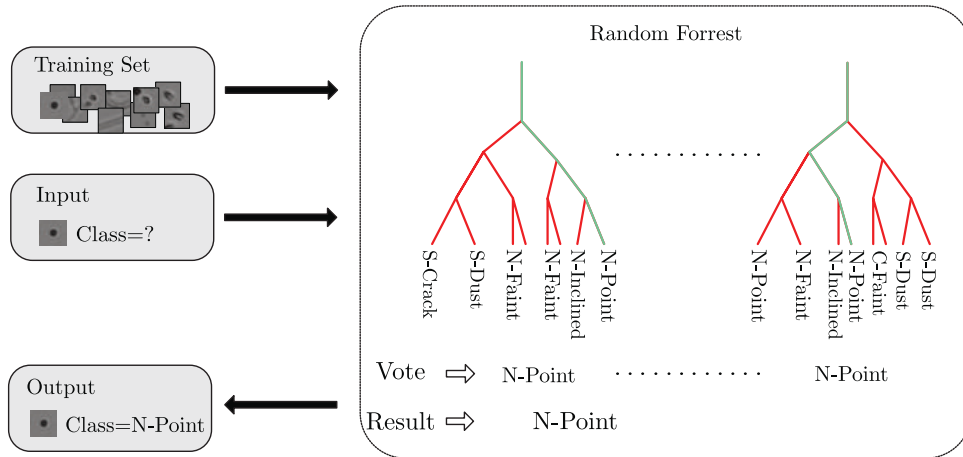


Figure 8.15.: Random Forest algorithm illustration.

subset of the training data and as big as the maximal training time allows. Finally, the mean over all trees is taken and the mean class is returned as the result.

To optimize the accuracy of the algorithm, the prior probability¹⁸ of each class is adjusted instead of using equal prior probability. If the intensity at the detector is known, the relative abundance of (Neutrons, Neutron_Doublets, Neutron_Triplet) are calculated in section 8.2. The abundance of systematic effects is dependent on several external factors and in general not known. It thus has to be estimated for each detector. Because the classification is repeatable, the prior probabilities can be tuned until optimal parameters are found. In the present case the false positive rate is minimized in the neutron category or, for datasets with several thousands tracks, the homogeneity of the background is used as a test quantity. See table 8.6 for an example for prior probabilities and the resulting classification.

8.3.4.2. Example Classification

To illustrate the classification process the detector IDL001 is used. During beam-time *Test-2455* it has been placed near the detector position II to capture the signal background. See figure 7.1 for a depiction of detector position I and II. The training result of the Random Forest with ID2017.04 which is used to classify the tracks found on scan 2016-02-22-#018-UIII-Normalised produces the maps shown in figure 8.16. Sub-figure (a) shows all tracks that are detected as described in section 8.3.3. subfigures (c)

¹⁸See appendix A.1.4 for an overview of the front-end of the software. Especially figure A.9 which shows an example definition of the prior probabilities.

and subfigures (d) show first tracks classified as **Neutron** and second tracks classified as **Not-Neutron**. Where **Not-Neutron** joins the **Candidate** and the **Systematic** class. The corresponding parameters and numerical results are summarized in table 8.6. As expected, for a detector which is not directly exposed, neutrons are randomly distributed. In contrast, systematic tracks like cracks and dust are more likely to be found in clusters¹⁹ which is in agreement with the visible distribution. Long curves correspond to cracks and the cluster on the right side in the middle corresponds to a dust particle which produced multiple track candidates. In appendix A figure A.4 shows the full scan with the images stitched together. For this classification the parameters, training data, prior probability for each class, the count of classified tracks, and the false positive count are given in table 8.6. Only one case of false positive detection exists in the **Neutron**

Name	Value	Unit		
Threshold	0.173	a.u.		
Training Set	ID2017.04	—		
Training #	3923	Tracks		
Track Area	30	pixel		
Neutron Accuracy	≈ 99	%		
Overall Accuracy	≈ 77	%		
Class	N. Examples	Prior Probability	Classified	FP
Neutron_Point	723	0.12	14	
Neutron_Inclined	499	0.15	18	
Neutron_Faint	383	0.12	16	
Neutron_Extreme	76	< 0.02	0	1
Neutron_Doublet	101	< 0.02	0	
Neutron_Triplet	35	0.00	0	
Candidate_Faint	407	0.12	19	
Candidate_Extreme	25	< 0.02	0	0
Systematic_Noise	312	< 0.02	0	
Systematic_Crack	1020	0.30	370	—
Systematic_Dust	314	0.15	191	—

Table 8.6.: Classification parameters and results for the detector CR39 IDL001, Scan '2016–02–22–#018–UIII–Normalised'. The detector was exposed during beam-time *Test-2455* and should not show neutron structure. Examples are used to train and verify the classification. The prior probability is an estimate of the probability of a track belonging to a class. FP are **false positives** where a track is wrongly classified in the given class. Note that a buffer category for unrecognized particles is not shown.

¹⁹A very big object with texture will be broken up in smaller pieces by the binarizing threshold.

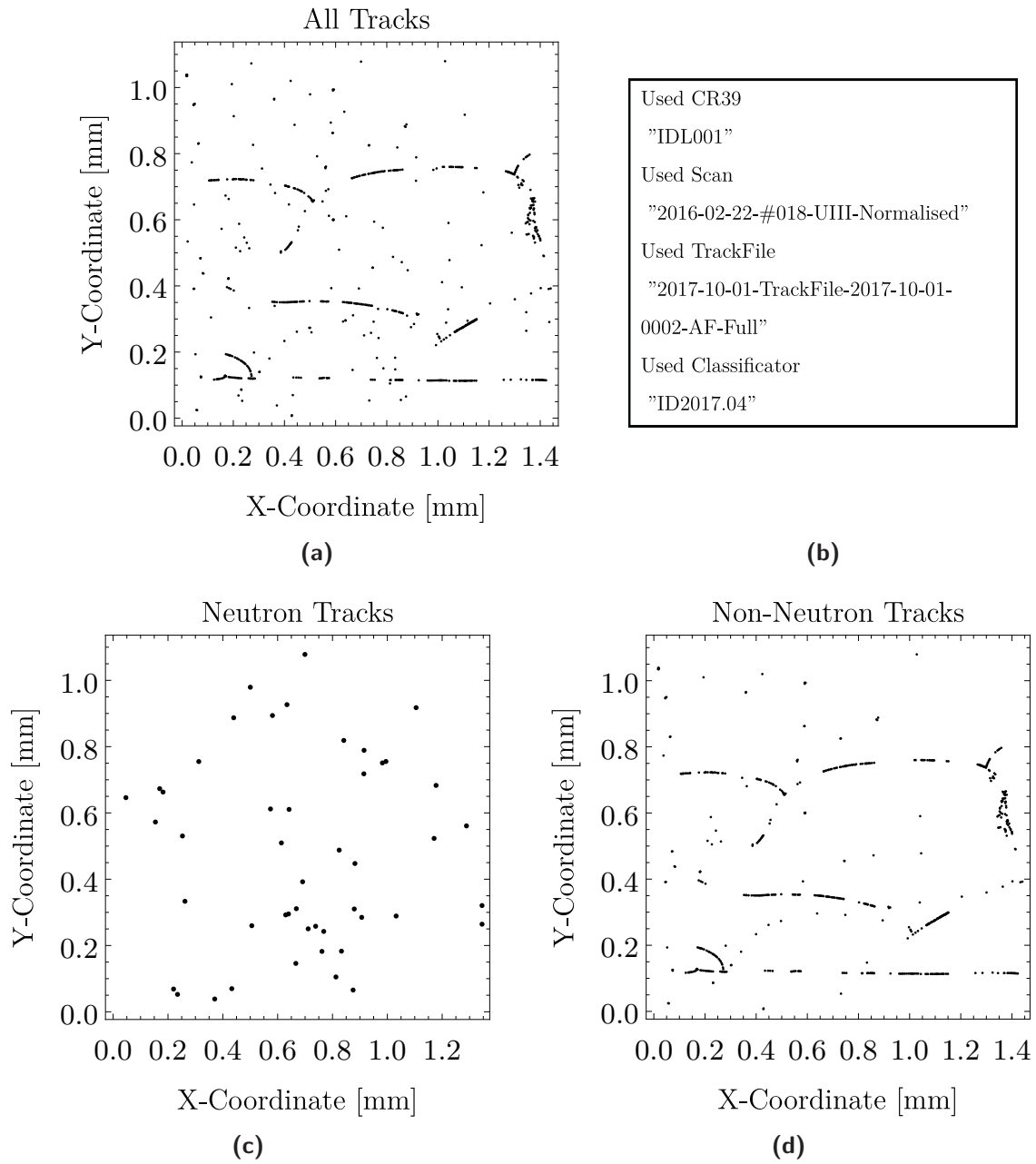


Figure 8.16.: Figure (a) shows the raw input of the classification which consists of a list of coordinates and properties of an identified track. Figure (b) shows tracks which are classified as of neutron origin and Figure (c) show objects which are classified as not being of neutron origin.

class which in this case was checked manually. The low neutron count means that the false positive rate is below 2%. Between sub-classes the false positive rate is higher as for example between Neutron_Point \leftrightarrow Neutron_Inclined. These classes are merged later and thus this is not of importance for neutron detection.

Finally, the questions about the accuracy of the classifier on a more diverse set and about its stability under frequent repetition for a given set of prior probabilities have to be addressed.

8.3.4.3. Classification Accuracy

The accuracy of a classification is measured by the fraction of correctly classified objects and is stated in Powers (2011) as

$$ac = (TP + TN)/N. \quad (8.10)$$

Here N is the total number of objects to be classified and TP and TN are defined as:

— **TP , True Positives**

A track is correctly classified as a member of class \mathcal{A} .

— **FP , False Positives**

A track is in-correctly classified as a member of class \mathcal{A} .

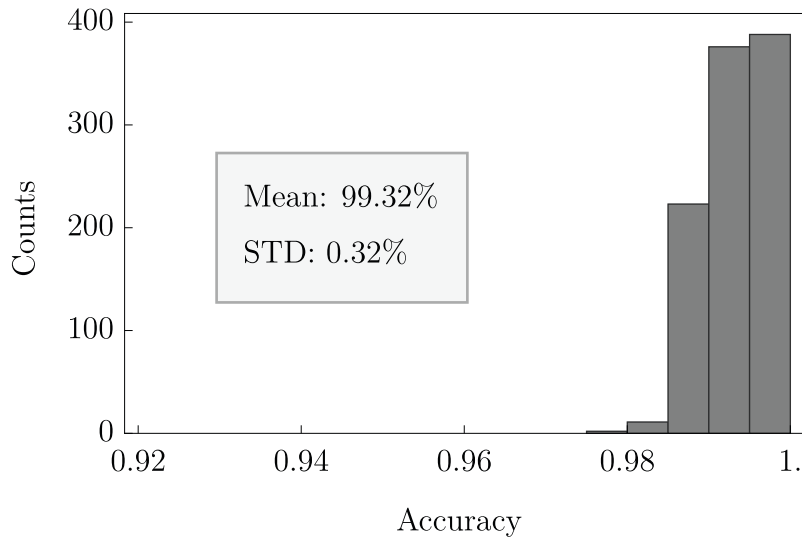
— **TN , True Negatives**

A track is correctly classified as to be not a member of class \mathcal{A} .

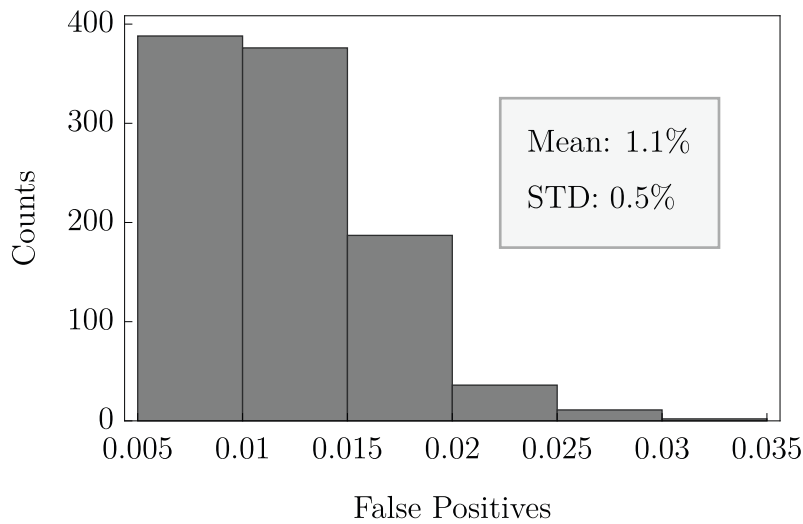
— **FN , False Negatives**

A track is in-correctly classified as not to be a member of class \mathcal{A} .

For the present problem it is important to note that **false positives** and **false negatives** are not equally problematic. **False positives** need to be avoided as much practically possible. If a fraction of neutron tracks is rejected uncorrelated to their position, only a fraction of the beam intensity is lost. If, on the other hand, tracks which are not neutron tracks (dust, cracks, ...) are classified as neutrons, an incoherent background is added to the signal. This in turn reduces the significance of the signal. Thus, the goal is to reduce **false positives** as much as possible while maintaining a reasonable level of **true positives**. The central benefits of automated detection are the straightforward implementation of reproducible accuracy estimations and the fast processing of a single track classification.



(a)



(b)

Figure 8.17.: Figure (a) gives the accuracy of the classification for the neutron category. The classifier was calculated in $N = 1000$ runs while the prior probabilities were taken to be constant. Figure (b) shows the fraction of cases which were falsely classified as neutrons. Note that neither mean nor standard deviation are good estimates for the moments of the data distribution and are only added as rough approximation.

The classification of one track takes on average $\tau_{\text{Classification}} = (14 \pm 2)$ ms while the most time consuming process is the training of the classifier which takes $\tau_{\text{Training}} \approx (42 \pm 1)$ s on average for the roughly $N_{\text{Examples}} \approx 4000$ training examples. Thus, it is possible to repeat classification and training a sufficient number of times to estimate the stability of characteristics of the classifier. This was done for the classification on the example dataset from detector IDL001 for which $N = 1000$ distinct classifiers are trained. The resulting distributions of the accuracy and false positive cases are shown in figure 8.17. Indeed, the neutron accuracy is stable at 99% and the neutron false positive cases are stable at 1%. This is important as in practice not the classifier but only the training set is saved and classifiers are calculated as needed and as a prediction for new classifications.

8.4. Summary

The presented classification procedure succeeds in selecting nuclear tracks in noisy microscope images automatically and to sufficient accuracy by applying machine vision algorithms. In section 8.3.4.3 it is shown that the classification can classify reproducible to accuracy up to $\sim 99\%$ without having an overlap between training data and classification data. The manual labour that is necessary is reduced substantially and a classification can be easily assessed in respect to its accuracy and in particular to its false positives rate. Figure 8.18 and Figure 8.19 show two distinct measurements of other experiments where CR39-based detectors were used and the presented procedure is applied. The first example features an example classification of a detector that was exposed during beam-time 3-14-331. It shows the quantum mechanical probability density of ultra-cold neutron gravitational bound over a horizontal mirror. The result indeed features the heavy neutron band in the middle with a visible sub-structure which can be attributed to the phenomenon of the quantum bouncing ball²⁰ as discussed in Thalhammer (2018). Also the background neutron noise shows the expected structure as the bottom of the detector was covered by a mirror and has a lower neutron density. Here an exciting result is the increased neutron count compared to the traditional manual selection. Traditionally only neutron tracks with clear shape and intensity are selected to reduce the false positive rate as much as possible. This leaves out a quite substantial amount of neutron tracks which are classified in the category Neutron-Faint.

²⁰The quantum bouncer is a phenomenon where a quantum mechanical state propagates on top of a hard boundary condition in a gravitational field. The problem can be solved using Airy functions. It is for example discussed in Gibbs (1975), in Langhoff (1971), and in Gea-Banacloche (1999) and in the case of ultra-cold neutrons in Luschikov and Frank (1978).

8. Spatial Neutron Detection

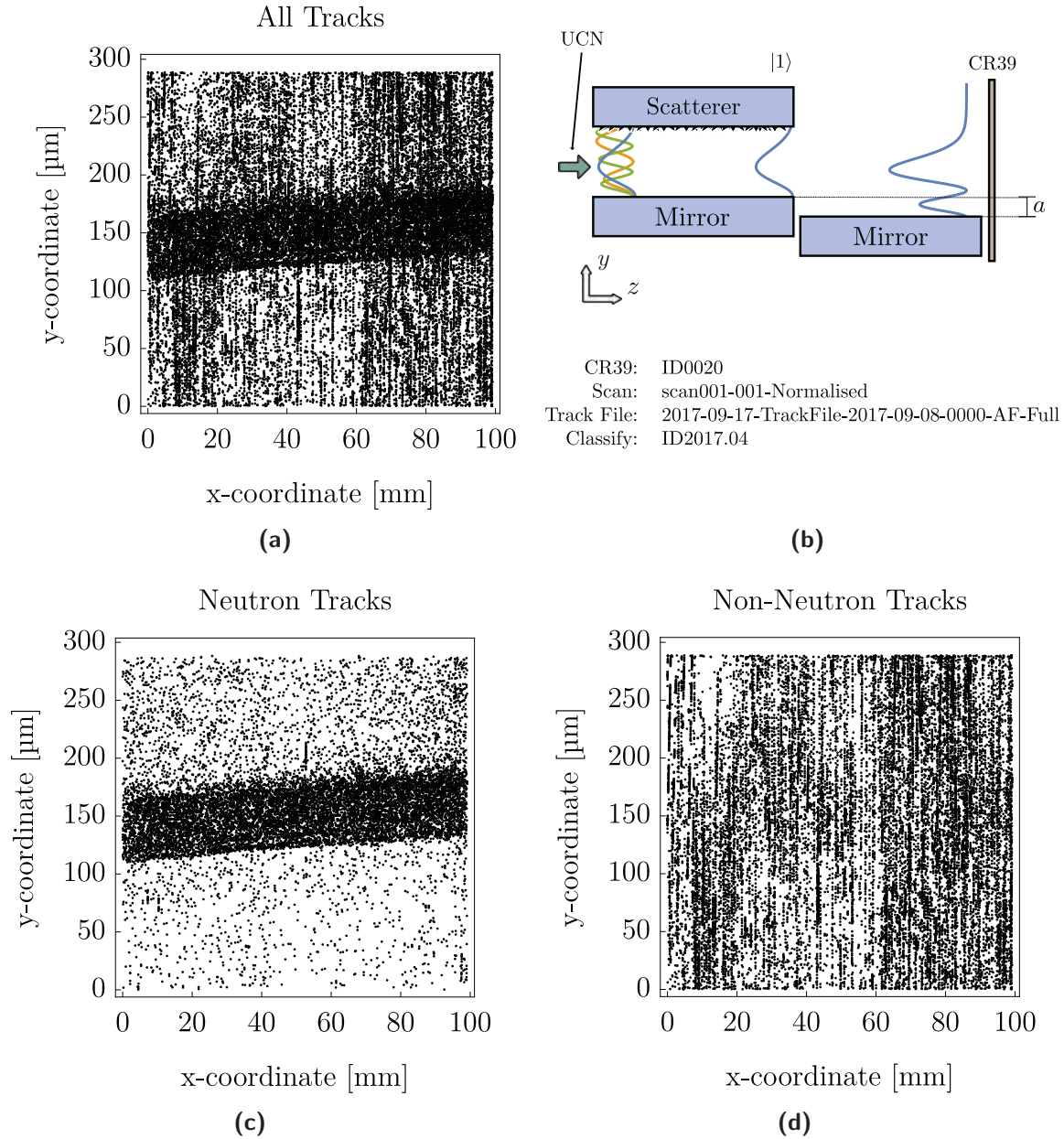


Figure 8.18.: Shown is the classification result of CR39 ID0020 which was exposed during the qBounce beam-time *3-14-331*. Further analysis and information can be found in Thalhammer (2018) who is the principle investigator of the experiment. A detector was placed at the edge of a mirror on which neutrons formed bound state. The bottom of the detector is covered by the mirror and is not directly exposed. Subfigure (a) shows all tracks which are found by setting a gray value threshold. Subfigure (b) shows the setup of the experiment where ultra-cold neutrons propagate from left to right. The prepared state $|1\rangle$ falls down at the step between both mirrors which generates a quantum bouncer that is to be observed. The embedded table collects the file information for this particular dataset. Subfigure (c) shows the selected neutron tracks (note that quantum mechanical structure is already visible as faint horizontal stripes) and finally Subfigure (d) depicts the subtracted systematic. The classified neutrons are checked for false positive cases. 63 false positive cases are found for all neutron classes.

If automatic classification is used, not only shape and intensity can be used as parameters but also the resulting distribution of neutron tracks as well as systematic tracks²¹. If the systematic map shows a clear neutron signal the classifier priors are adjusted to better distinguish between these categories. Thus, a category of faint tracks is classified robustly as neutrons which have been missed before.

The second example features the spatial neutron distribution inside a single crystal silicon interferometer that was heavily exposed to the point of multiple track overlap. This complicates the detection significantly as single tracks cannot be identified anymore. The stripe on the left is the beam that is transmitted by the first plate and the right stripe corresponds to the first diffraction order. As no sub-structure is expected due to the setup geometry, the classification is sufficient as the overall beam shape can still be recovered even in this extreme case.

²¹If for example it is known that parts of the detector are covered by neutron absorbing material, the fact that now neutrons can reach this area can be used to refine the class priors.

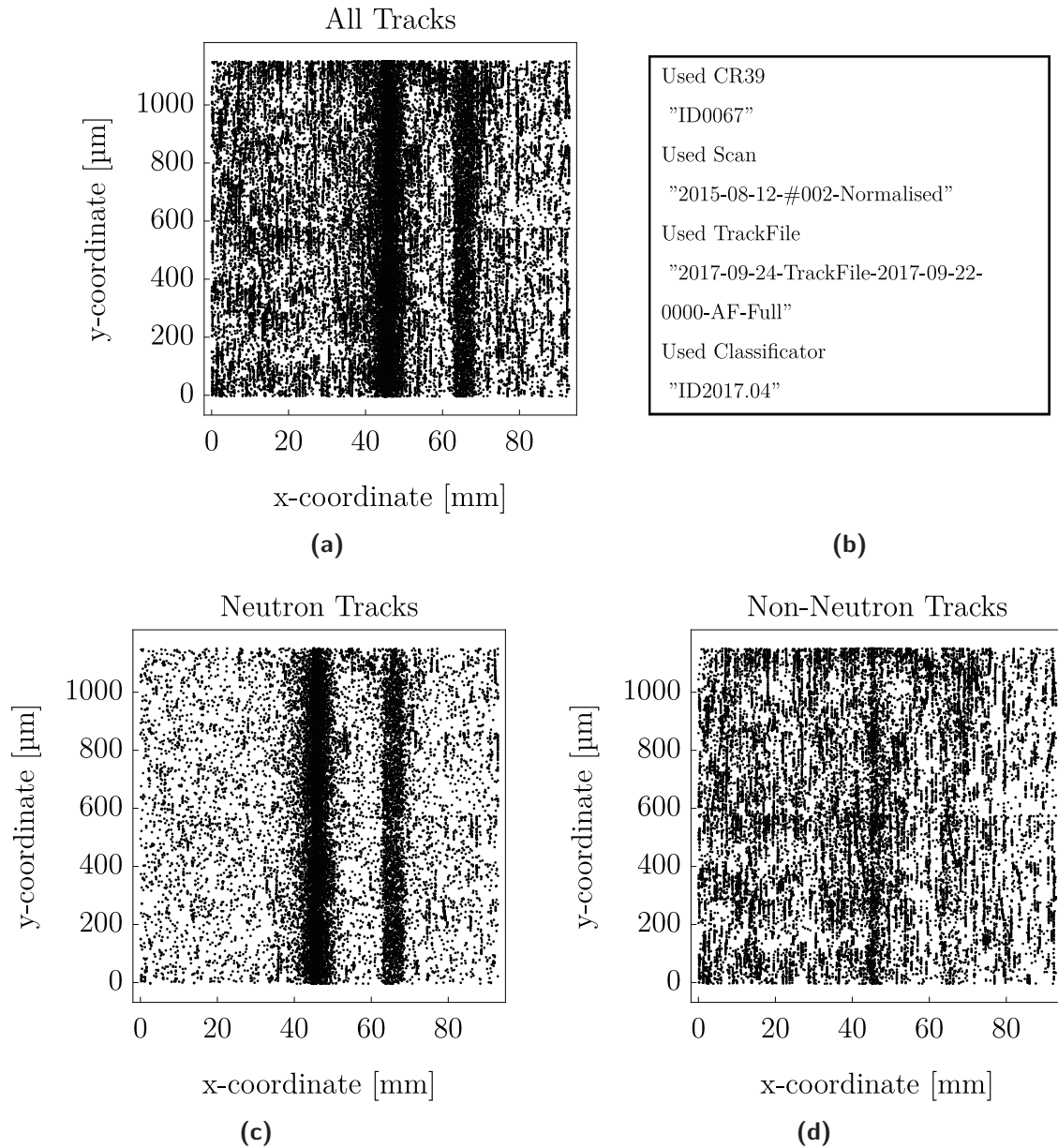


Figure 8.19.: Subfigure (a) shows tracks which are classified as neutrons. The visible distribution is the spatial distribution inside of a single crystal silicon interferometer of the LLL type taken in 2013 at the S18 instrument at the ILL. The detector has been placed directly in front of the second plate. The dominant stripe is the transmitted beam and the faint stripe on the side is the refracted beam. Subfigure (b) gives data information and Subfigure (c) shows the classified neutron tracks. Subfigure (d) shows tracks which are not classified as neutrons for the same measurement. Especially on the transmitted beam clearly neutron tracks are wrongly discarded. In the here presented measurement the neutron density at the peak reached the threshold where no single neutron tracks are present. To offer a high accuracy also at the peak, binarizing, cutting at a threshold, and a rectangular image cut out is not sufficient to characterize tracks of interest.

Part IV.

Prospects and Conclusion

9. Future Prospects

Part II of this thesis discusses and analyzes the prospect of Lloyd’s mirror. Chapter 5 gives the theoretical foundations in the form of the wave function of an idealized setup. Chapter 6 discusses a simulation of the interference pattern, and part III chapter 7 presents a not yet finalized implementation of Lloyd’s mirror.

Chapters 6 and 7 present realizations of the above considerations in a specific setup at the PF2 at the Institut Laue-Langevin. It might be worth reflecting whether a different part of the parameter space would offer a more favorable realization environment. Further, it is shown in chapter 5 that the search for a chameleon field and an axion particle does not seem to be competitively realizable with Lloyd’s mirror. This suggests that a new search area for a novel physical effect where Lloyd’s mirror can perform competitively is needed.

Apart from these two theoretical questions especially in chapter 7 and in chapter 8 concrete experimental methods are presented. As central characteristics of the interferometer are restricted by the chosen implementation, it is sensible to ask whether different experimental methods could lower the complexity and difficulty of a realization or even enlarge the accessible parameter space. The following section sketches possible paths to continue the work performed in the individual chapters.

9.1. Proposed Implementation at the PF2

The implementation of Lloyd’s mirror as proposed in this thesis and the characterized beam preparation setup does indeed offer a feasible prospect of a realization of the interferometer. This is the conclusion made in chapter 6 on the basis of an intensity measurement at the PF2 and a simulation of the interference pattern. Nevertheless, the low intensity as measured in section 7.1.4 hampers precision measurements under the constriction of a practical time frame. The next logical step is to analyze the setup for further potential intensity gains and adapt the setup accordingly. Three aspects are already mentioned in this thesis and are sketched in the following:

— **Divergence losses**

Only the path between S4 and S3 as well as the path between S2 and S1 restrict the angular distribution of the beam and losses in these sections cannot be avoided. Losses in the remaining section could be reduced by employing beam guides which reflect neutrons back into the beam. This conserves the brilliance of the beam between the end points of the beam guides. Since most distances between neutron optical components vary strongly, additional beam guides would need to be fitted to each path. For example, rectangular beam guides consisting of four ^{58}Ni coated mirrors should be sufficient.

— **Air absorption**

The current setup is realized in an air atmosphere with an option to add a helium atmosphere or a rough vacuum. As already discussed in Scheicher (2015), losses due to scattering or absorption can be avoided by using either beam guides which are kept at a low pressure or in a helium atmosphere.

— **Wavelength Selection**

If the propagation region behind the mirror is chosen to be $L_3 \sim 2$ m or bigger, a smaller wavelength could be selected which in turn yields a higher intensity. See figure 6.16 for a simulated pattern with an extended propagation region after the mirror. Note that ultimately a cold neutron beam could be considered.

— **Monochromatic Mirrors**

The graciously loaned disk shaped super mirrors (M1 and M2) with a diameter of $d = 76$ mm could be increased in size in the vertical direction to make full use of the beam (70 – 85) mm.

See figure 9.1 for the proposed additions to the current setup. This figure shows areas where beam guides with helium atmosphere can be added in orange. In general the full beam path should transverse a helium atmosphere to reduce air absorption. Finally, in section I a low pressure region should be added to make measurements that depend on pressure variation possible.

Further, the overall alignment system as used during the last beam-time *Test-2455* would be more robust, if adaptations made during the beam-time were included in a revised version. Up until now alignment has been achieved by a three-beam laser guiding system sufficient for the beam shaping setup and initial alignment of Lloyd's mirror. Adding on-line detection by a CCD camera, photo diodes, and alignment routines, the laser

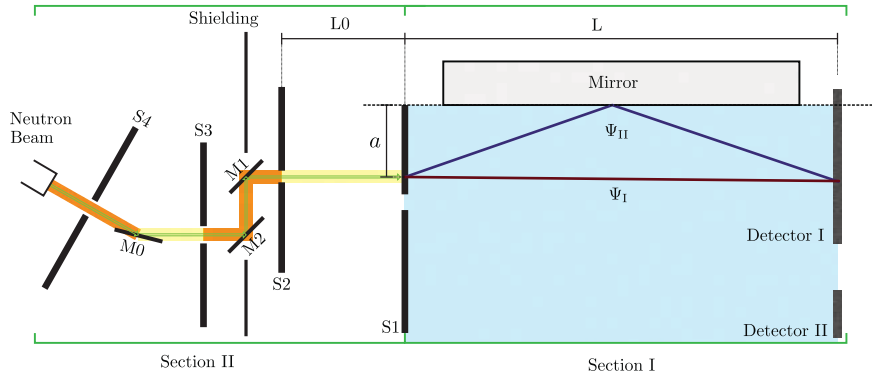


Figure 9.1.: Possible additions to the current setup of Lloyd's mirror with very-cold neutron at the PF2. The light blue Section I should be kept at a low pressure to make measurements that depend on pressure variation possible. In orange beam regions an approximately rectangular beam guide with a helium atmosphere can be added. In yellow beam regions the beam is shaped by slits and losses are necessary to yield constricted distributions. Nevertheless, these regions should have a helium atmosphere to reduce absorption and scattering.

guided alignment would be more comprehensible. This is especially important at the interferometer stage where one can make use of the optical analogue of Lloyd's mirror as presented in section 5.5.2.3.

9.2. Refined Theoretical Model for Lloyd's Mirror

In chapter 5 wave functions for specific cases of Lloyd's mirror as well as phase shift calculations due to various effects are presented. These are essential for future measurements as all deviations from the plane wave approach would have been considered to be systematic effects without a deeper theoretical understanding. Despite now having necessary theoretical tools these calculations can be further enhanced and adapted, especially in respect to the finite mirror length or systematic deviation of the mirror's surface from the perfect plane. Both cases should be thoroughly modeled. This can be accomplished with finite element methods or by employing the path integral formalism. While the phase shift estimations of several phenomena in section 5.6 are sufficient for the estimation of systematic effects and the initial estimation of the sensitivity to specific phase shifting effects, it does neglect peculiarities of the wave function of the system. For example, if a future measurement is used to test a hypothetical model beyond the Standard Model, it is necessary to calculate the probability density including the hypothetical effect. As high accuracy is needed in this endeavors, one has to go beyond

the plane wave approach as used in section 5.6 and directly calculate the wave function or an estimate. Also in the case of a possible Casimir-Polder interaction this has to be implemented as the current model is highly sensitive to a artificially introduced cut-off parameter that is necessary to avoid the divergence of the integral.

9.3. Probing Physics beyond the Standard Model of Particle Physics

An important motivation to implement Lloyd's mirror with very-cold neutrons is given in Pokotilovski (2013b) where it is discussed as a tool to probe the hypothetical chameleon field. In section 5.6 it is shown that as of 2015 the chameleon parameter space accessible by Lloyd's mirror is mostly excluded by strong limits derived from atom interferometry most notably presented in Hamilton et al. (2015). The same is true for the hypothetical axion particle for which strict limits were published in Afach et al. (2015) and already exclude the parameter space accessible by Lloyd's mirror. An alternative measurement subject can be the hypothetical symmetron field, which is proposed in Hinterbichler and Khoury (2010) to address the phenomenon of dark energy. In the scope of this thesis the symmetron field is not examined.

Further, general searches of deviation from Earth's linearized gravity would be a possibility. The highest sensitivity to a gravity-like phenomenon can be achieved, if the effect in question acts normal to the mirror's surface similar to gravity as discussed in section 5.6.3.2. This case is analogous to the mirror oriented horizontally in Earth's gravitational field¹ where the introduced phase shift is bigger than the geometrical phase shift. For the vertical case the sensitivity is reduced to a point that not even Earth's gravity would be detectable with reasonable statistical significance at a very-cold neutron beam.

9.4. Future Developments

In the scope of this thesis several technologies were developed and extended. In each case it is advisable to develop these further to allow for more general applications, enhance accuracy, or enhance efficiency.

¹Parallel alignment between the surface normal to the mirror and the gravitational vector.

9.4.1. CR39-based Detection

In chapter 8 a process to detect very-cold neutrons with a spatially high resolution based on established technologies is presented. The focus is put on the track identification after optical scanning of exposed detectors. While succeeding in adding objective tools to detect particles even for high intensities or large exposed areas, the scanning procedure itself was not enhanced. The present system allows scanning detectors with several magnifications, but only for high magnification as for example $50\times$ track identification will succeed. Thus, the detector has to be scanned in $A = (289 \times 217) \mu\text{m}$ steps. For macroscopic areas exposed to neutrons several thousand pictures have to be taken and processed. At the moment, especially the image capture process relies on human interaction to put each picture into focus. This is not only time consuming but also introduces human subjectivity and thus possible human bias. Applying state-of-the-art software (Microscope Programming) and hardware (absolute distance measurements) a system could be envisioned which automatically and reliably scans detectors for neutron tracks.

Further, the presented machine vision based classification can surely be further enhanced. In this thesis, the definition of different classes was not chosen by its strength to be distinguish between each other but by functional considerations. Differentiating between functional classes (Neutron-Points, Neutron-Inclined, Cracks, Dust, ...) offers a simple way to interpret the result after the classification. An interesting prospect would be to investigate whether other parameter/feature composition are more suitable for robust classification. Thus, reducing the dependency on tuned prior probabilities. Also the classifier presented in this thesis only uses a single classification layer. Adding additional classification steps after the presented would further reduce the false positive rate and thus enhance the accuracy.

9.4.2. Detector Coating

At the moment, the implemented coating facility is mainly used for sophisticated boron coatings for CR39-based detectors and gas counters for ultra-cold neutron and very-cold neutron detection. The developed process produces reliable clean coating but due to the heat intake at the substrate limits the maximal coating time for CR39 and thus the thickness of the coating. Especially to gain flexibility on detector efficiency this should be addressed. For example, an active cooling/heating system at the substrate could offer

9. Future Prospects

exactly this advantage but would be rather complex due to vacuum conditions and the fact that the substrate needs to be rotating to be homogeneously deposited on.

Also the beam/coating instrumentation could be substantially enhanced by additional and more flexible sensors in and outside of the setup. The documentation process for each deposition only captures rough characteristics of the process and most essential details that are needed for a successful coating cannot be captured.

10. Conclusion

In this thesis several aspects of the implementation of Lloyd’s mirror are discussed and analyzed. The goal is to investigate the feasibility of Lloyd’s mirror especially in respect to its application to fundamental questions of physics. In chapter 5 the theoretical foundations of high precision measurements in the form of a quantum mechanical description of the diffraction phenomenon is presented. Namely the static solution $\Psi_{\mathcal{L},st}(\vec{r})$ and an approximation $\Psi_{\mathcal{L},F}(y, z)$ to the time-dependent solution. Both describe a quantum mechanical particle passing an entrance slit and then transverse along a horizontal mirror. The validity of these calculations is checked through the implementation of an optical analogue.

Further, in section 5.6 several phase shifting effects are investigated. Firstly, it is investigated what contributions can be expected from systematic effects like fluctuations in the magnetic field, the reflection at a surface, or the gravitational field. It is concluded that most effects can be suppressed sufficiently, or due to their time behavior can be neglected. Secondly, in section 5.6.4 possible measurement subjects for example those beyond the Standard Model of particle physics are discussed. In particular the sensitivities to different phase shifting effects for a specific implementation of Lloyd’s mirror is calculated. Such effects are for example the chameleon field, axion particle, and gravitational torsion which can be connected to dark matter or dark energy scenarios as well as a neutron Casimir-Polder interaction. Limits set by other experiments, exclude the accessible parameter space for the first two effects. While a small phase shift is predicted in the last case, the semi classical approach maybe insufficient to estimate the effect of a Casimir-Polder interaction and more elaborate means are advisable.

In chapter 6 the solutions presented in chapter 5 are used to estimate constraints and to simulate the interferogram of Lloyd’s mirror for an implementation at the very-cold neutron port at the PF2 at the Institut Laue-Langevin as shown in figure 10.1. The interferogram is simulated for a set of parameters as defined in table A.3 in appendix A.4 and is presented in section 6.3.1.3.

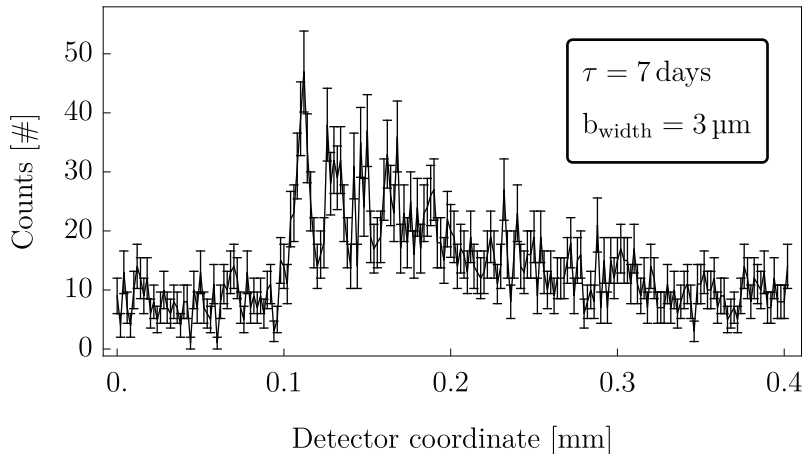


Figure 10.1.: Shown is a simulation of the interferogram of Lloyd’s mirror for integration time of $\tau = 7$ day. The wavelength is set to be $\lambda = 6.3$ nm, the mirror length $L = 0.315$ m, and the distance between mirror and slit $a = 53$ μm .

Following the considerations in chapter 6, the feasibility of an implementation at the PF2 can be positively assessed. This is strongly constrained by an expectedly low neutron flux and, consequently, a comparably long measurement time for a single interferogram on the order of several days.

In chapter 7 the raw beam parameters are discussed as well as an implementation of a beam preparation setup to collimate and monochromize the beam as specified in chapter 6. The presented measurements were performed during beam-time *Test-2455* and *3-14-343* at the very-cold neutron beam at the PF2. The achieved beam spectral bandwidth is $\frac{\Delta\lambda}{\lambda} = (5.6 \pm 0.5)\%$ at 6.7 nm while the divergence of the beam is constrained to be $\gamma < (2.7 \pm 0.1)$ mrad. Extrapolating the beam intensity after the beam preparation section to the next component, which is the entrance slit S1 of the interferometer, while satisfying the coherence constraint gives an intensity of

$$\mathcal{I}_{S1} = (8.9 \pm 0.4) \cdot 10^{-3} \text{ \#}/\text{s}. \quad (10.1)$$

This result is used at several points in this thesis, as for example for simulating the interferogram and estimating the necessary measurement time. Further, it is used for the estimate of the sensitivity of Lloyd’s mirror to effects beyond the Standard Model of particle physics. To check whether the measured intensity represents an optimal beam usage, the beam is traced throughout chapter 7 from the beam port beam downwards to the last slit in front of the detector. In the scope of the beam shaping region a possible

drop in the overall brilliance of the beam over the preparation setup is measured¹. This indicates that it the neutron intensity maybe increased as discussed in section 9.1.

Following the presentation of the beam preparation stage in section 7.2 characteristics of the interferometer stage are presented. This includes a proposal for a robust implementation at the PF2. It addresses the problems of the alignment of slit S1 relative to the mirror’s surface and the environmental stability at the interferometer position. For example, the magnetic field variations over several days are measured. The conclusion is that additional magnetic shielding is not required in a future implementation because of the size of the induced phase shift but magnetic components should be avoided. Also, in section 7.2.4 the background intensity at detector position II is captured using a CR39-based detector. This measurement is used as an estimate for the background intensity in a future experiment. It is determined to be

$$\mathcal{F}_{\text{Background}} = (83 \pm 8) \cdot 10^{-6} \frac{\#/\text{s}}{\text{mm}^2} \quad (10.2)$$

which is an order of magnitude lower than the expected signal and thus does not inhibit future measurements.

Finally, in chapter 8 a selected technology necessary to capture the full interferogram is presented. In order to capture the interferogram ¹⁰B-coated CR39-based spatially resolving detectors are used. In this thesis the focus is put on the development of a system to accurately classify possible nuclear tracks which are visible after chemical treatment and optical scanning of these detectors. In the scope of this thesis, a system is implemented that automatically classifies “neutron” tracks to a high accuracy. This is demonstrated with two examples as discussed in section 8.4. Furthermore, future prospects in the development of CR39 detectors are discussed in chapter 9.

In conclusion, a measurement scenario with a feasible prospect to be realized at the PF2 is developed cumulating in the simulation presented in chapter 6 section 6.3 and a first experimental progress is presented in chapter 7. These arguments are based on a theoretical description which is developed in chapter 5. Thus, Lloyd’s mirror does represent a feasible prospects as a neutron optical instrument and a device which works on the intersection between quantum mechanics and gravity.

New prospects to test novel hypothetical models are imaginable if the intensity at the entrance slit of the interferometer can be further enhanced through measures as are suggested and discussed in chapter 9.

¹It is also possible that the drop is an artifact of the initial beam selection as explained in section 7.1.4.

Appendices

A. Supplemental Information

A.1. Collected Figures

A.1.1. Optical Lloyd's Mirror

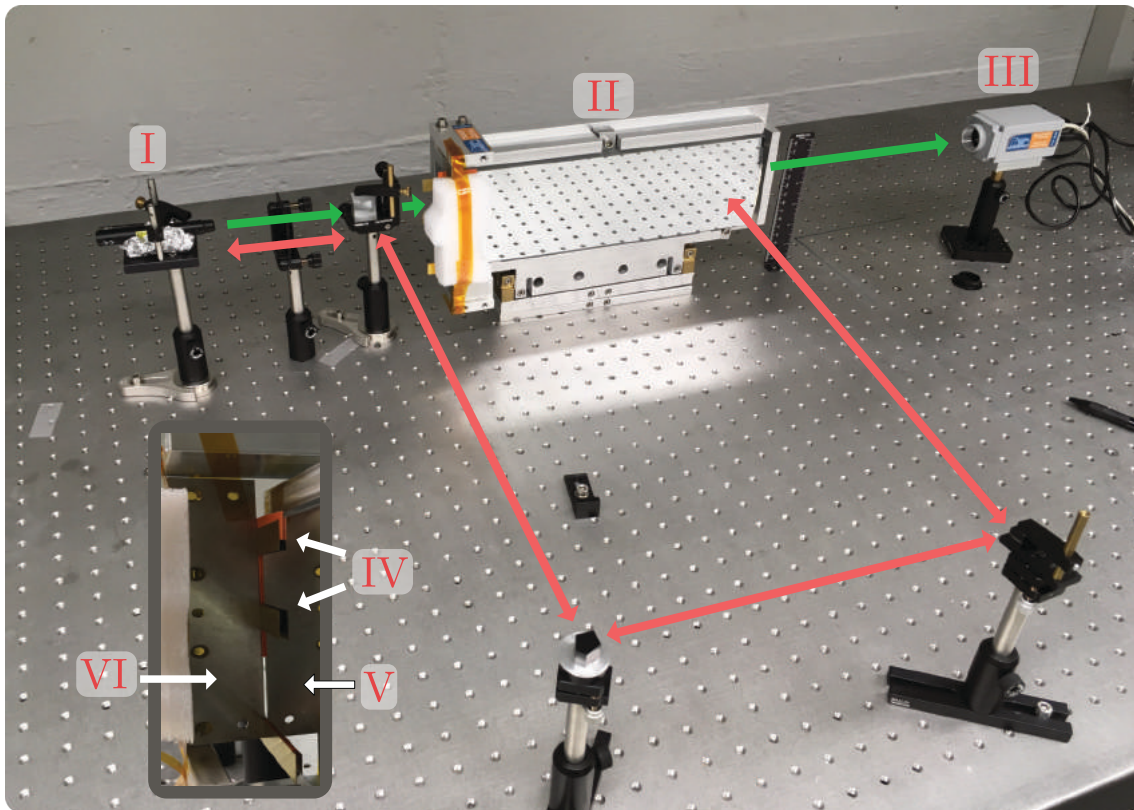


Figure A.1.: Shown is the setup of the optical Lloyd's mirror as implemented at the Atominstitut. As a light source a laser pointer with $\lambda = (653 \pm 0.3)$ nm is used. The green line is the beam path for the interferometer and the red line is an alignment path using pentaprism. *I* is the laser pointer, *II* is the main mirror, *III* is the CMOS camera, *IV* are $d = (155 \pm 0.1)$ μm spacers, *V* is the main mirror, and *VI* is the boron-steel sheet which builds up the slit on top of the mirror. The small picture on the left side is the view from the CMOS camera onto the slit.

A.1.2. Simulation Fit Residuals

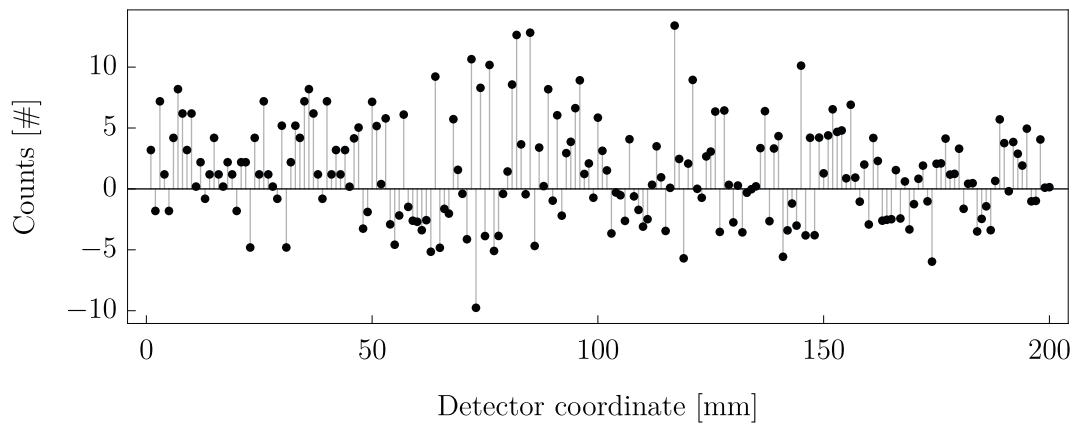


Figure A.2.: Shown are the residuals of the fit shown in figure 6.15 for the 7 day measurement.

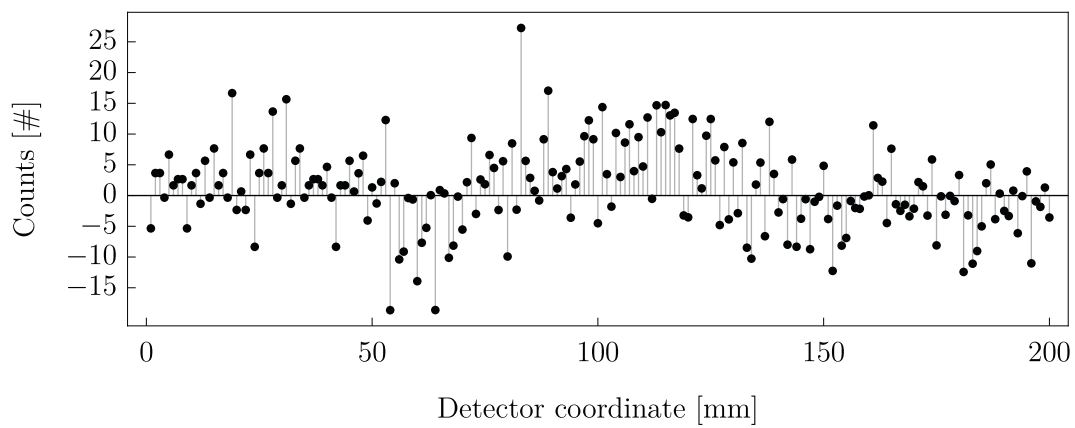


Figure A.3.: Shown are the residuals of the fit shown in figure 6.15 for the 21 day measurement. Especially in the middle of the image systematic deviations between data and fit model are visible. In this region the residuals are not normal distributed around zero.

A.1.3. CR39 Example

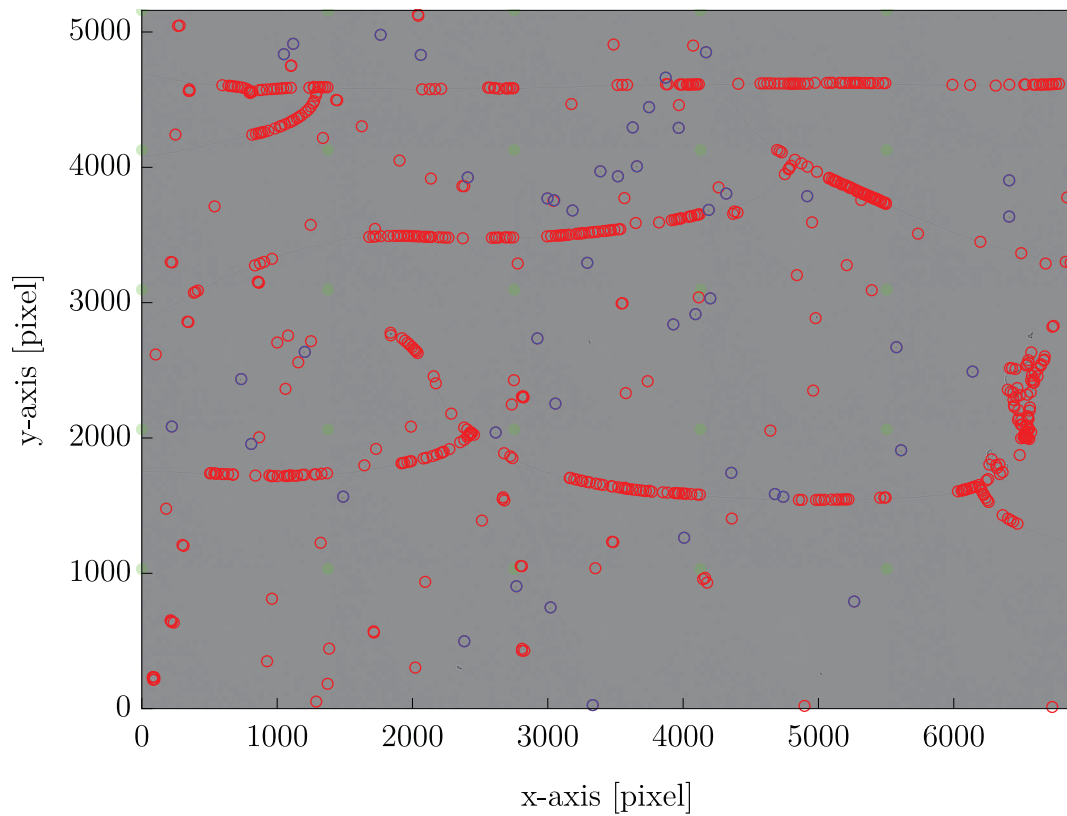


Figure A.4.: Stitched scan consisting of 25 single images for ID001. The green points that form a grid are the coordinate reference points for each single picture. The red circles are tracks classified as **Systematic**-tracks and thus are either cracks in the original coating, dust, or other noise. The blue circles depict tracks classified as **Neutrons**-tracks.

A.1.4. CR39Analyse.m

Shown are examples of the developed Mathematica package for the detection, classification, and the analysis of CR39 imaging plates.

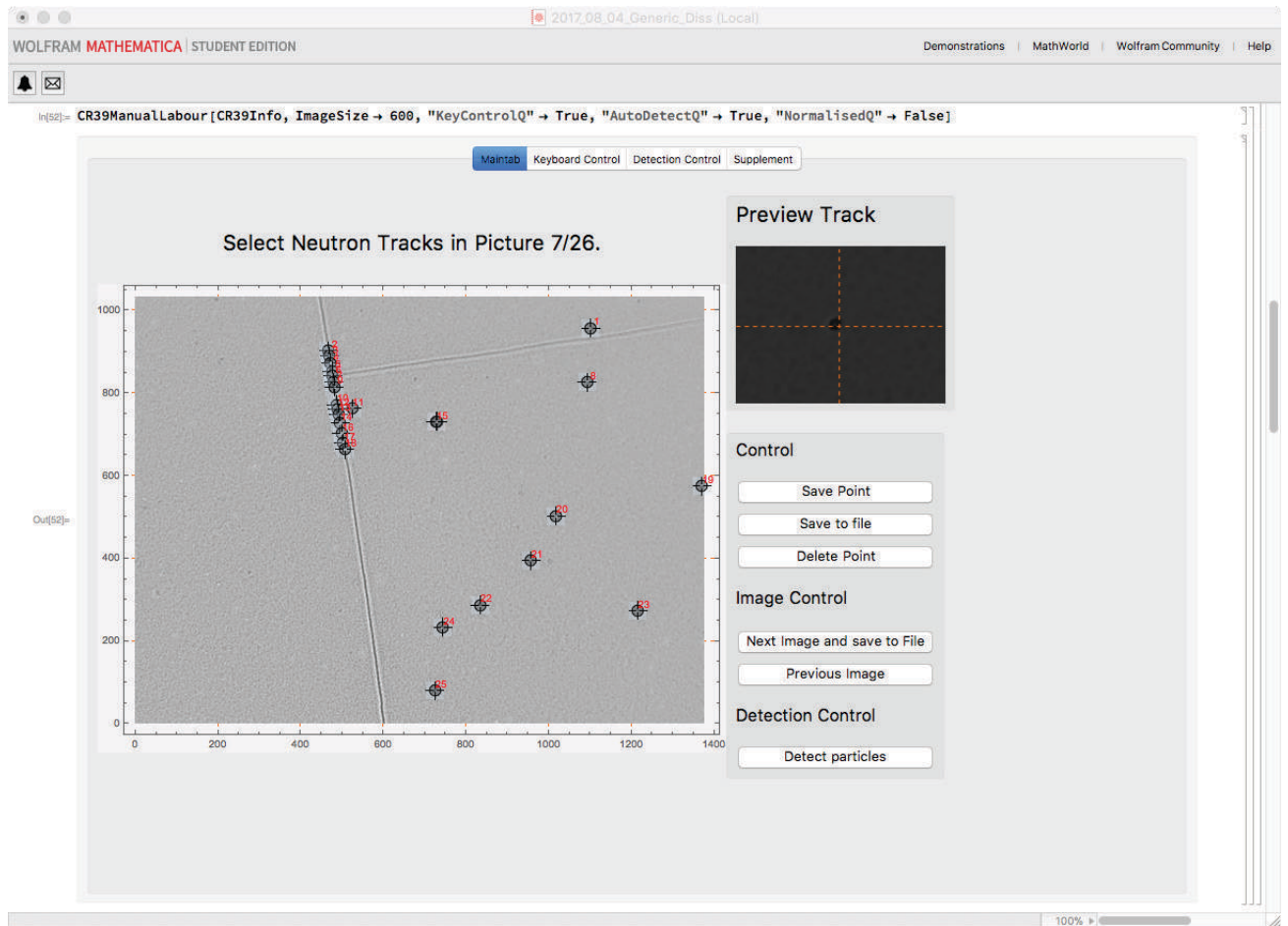


Figure A.5.: Front-end that is used for the detection of tracks on an etched neutron detector. Images of the detector are loaded to either manually select tracks or to run an automated script to detect tracks.

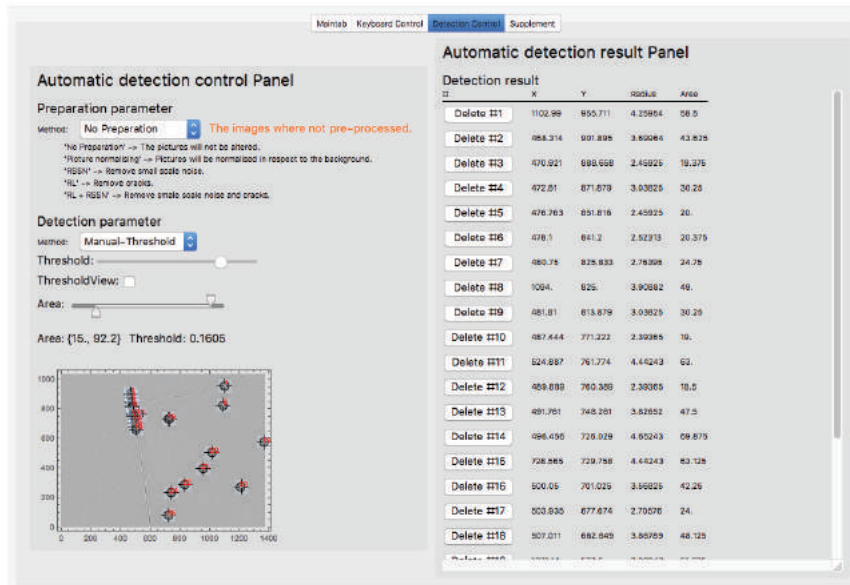


Figure A.6.: The necessary threshold for the gray value scale and the tracks size ROI, which are used to select tracks automatically can directly be investigated.

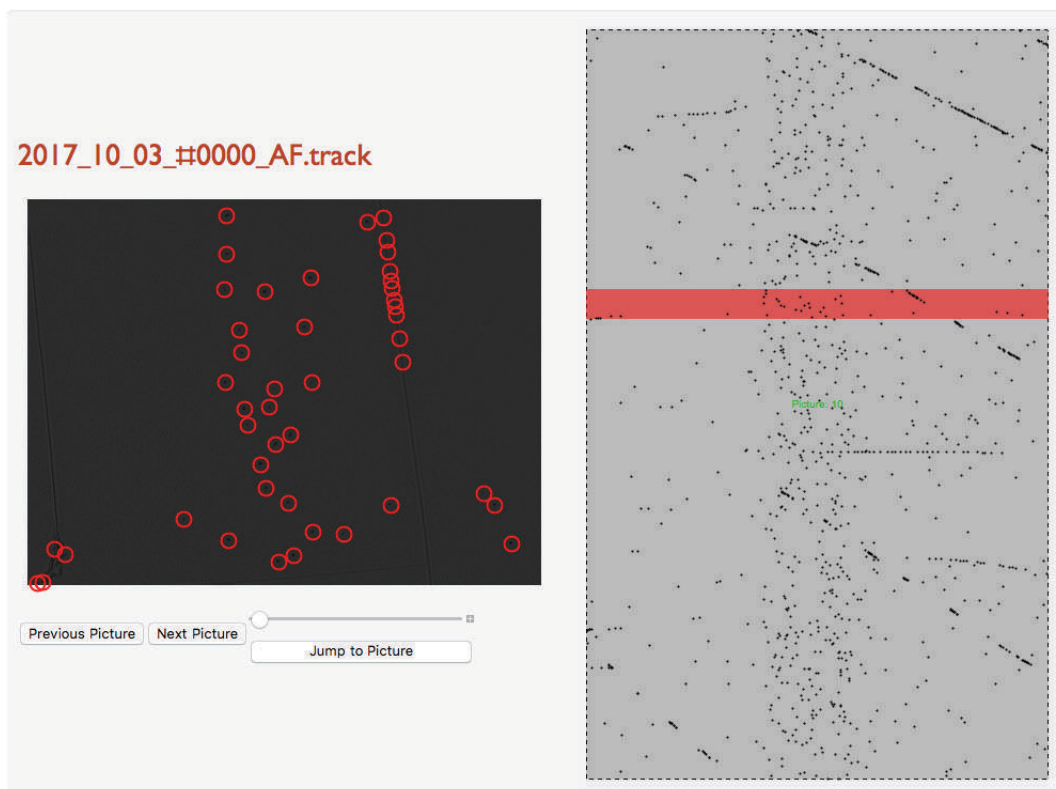


Figure A.7.: Selected tracks are saved together with their properties in a human readable text file. Several function exist to view and analyze the track files.

A. Supplemental Information

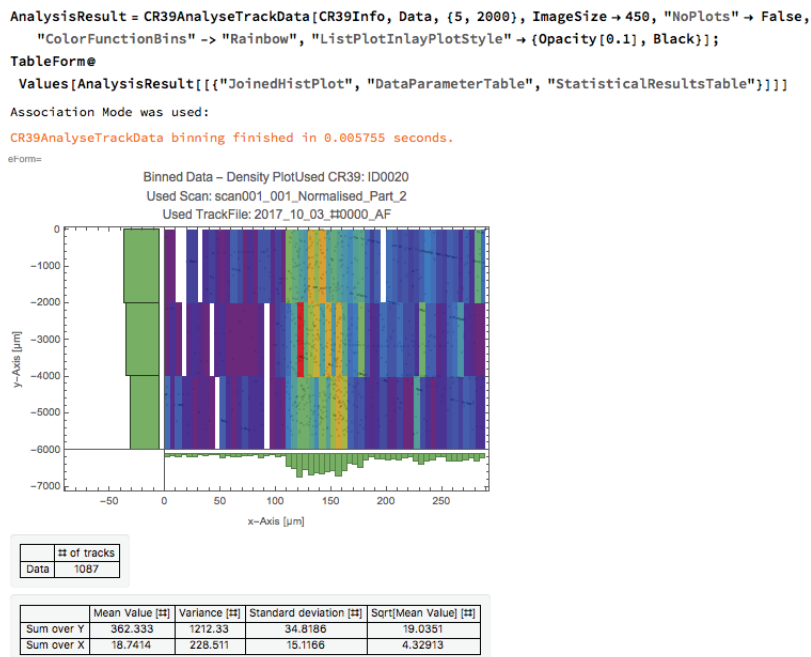


Figure A.8.: The most important low level analysis is binning and projection of the data.

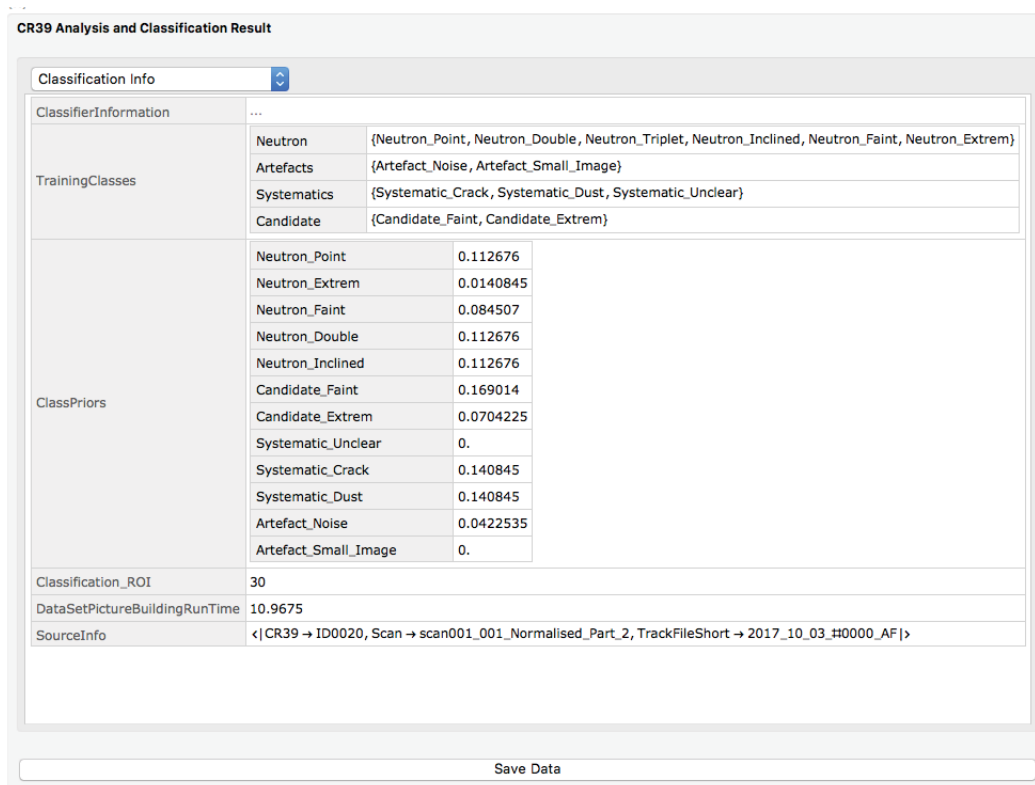


Figure A.9.: The machine learning sub-package handles the classification of tracks according to pre defined classes and prior probabilities.

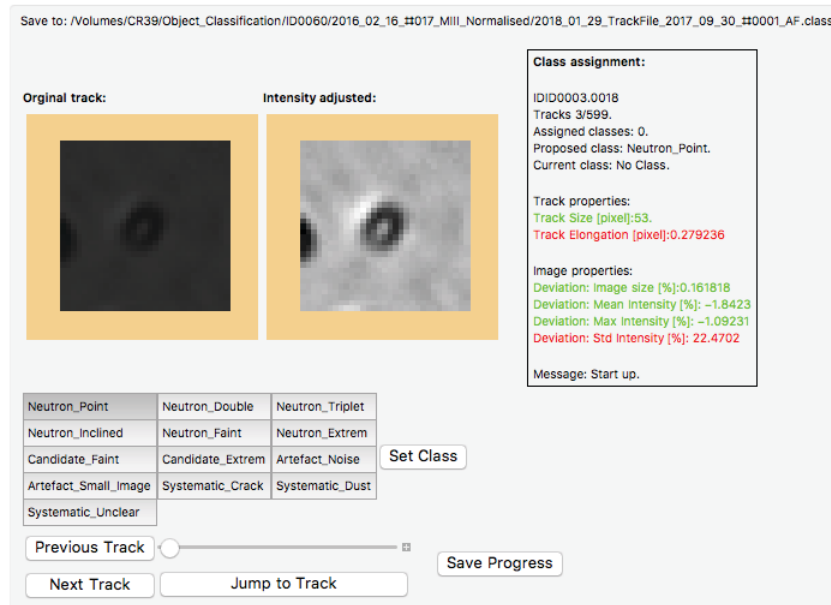


Figure A.10.: The necessary training tracks are assigned pre defined classes in this front-end for example images and are saved to a class file.

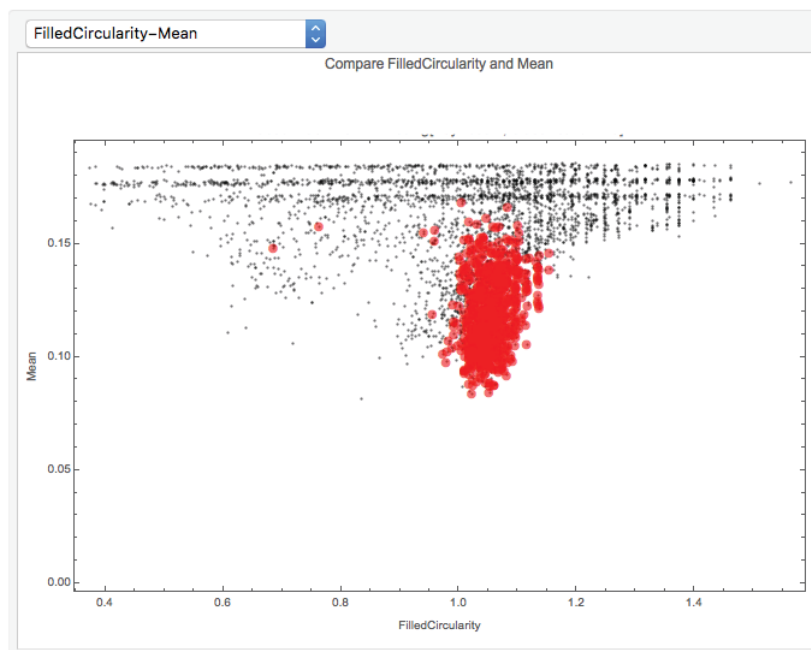


Figure A.11.: The track properties of all pre defined examples can be probed according to the initially saved track properties. In red are Neutron-Points and in black all other tracks and are plotted for their FilledCircularity vs. the Mean intensity. Note that different CR39 detectors and measurements are put together and thus a single title cannot be assigned.

A.2. Neutron Energy Availability

This section gives a short summary of available neutron beams which complements the section 3.3 for Very-cold neutron at the PF2 at the Institut Laue-Langevin.

Instrument	λ [nm]	\mathcal{F} [$\frac{\#}{\text{cm}^2\text{s}}$]	$\delta\lambda/\lambda$	Source
D11@ILL	0.45 – 4	$7 \cdot 10^7$	9%	Laue-Langevin (2008)
D33@ILL	0.45 – 25	10^8	10%	Laue-Langevin (2008)
PF2-VCN@ILL	2 – 400	$4 \cdot 10^5/\text{nm}$	– – –	Laue-Langevin (2008) & Geltenbort (2013, priv. comm.)
H18@ILL	1.5 – 3.0	– – –	– – –	Laue-Langevin (1986)
CG2@ORNL	0.4 – 2.5	$2 \cdot 10^7$	14%	DeBeer-Schmitt, He and Littrell (2017)

Table A.1.: Availability of Neutron energies and characteristic of sources and instruments. The flux \mathcal{F} is given at the sample position. If ‘Full’ is specified then the full beam without monochromatization is captured. In the case of the PF2 beam, the wavelength differential is given.

Instrument	Length	A [mm ²]	\mathcal{B} [$\frac{\#/\text{s}}{\text{cm}^2\text{nm sterad}}$]	Source
D11@ILL	39 m	40×55	$2 \cdot 10^{11}$	Laue-Langevin (2008)
D33@ILL	40 m	40×55	$\sim 2 \cdot 10^{11}$	Laue-Langevin (2008)
PF2@ILL	7.6 m	45×70		Laue-Langevin (2008) & Geltenbort (2013, priv. comm.)
H18@ILL	12 m		$1.3 \cdot 10^{10}$	Laue-Langevin (2008) & See appendix A.3
CG2@ORNL	20 m			DeBeer-Schmitt, He and Littrell (2017)

Table A.2.: Corresponding length scales to table A.1.

A.3. The H18 Beam at the Institut Laue-Langevin

The beam port H18 is now permanently taken by the instrument D17. Before this usage the beam has been used for various free-space interferometer experiments as for example Anton Zeilinger et al. (1988). The brilliance \mathcal{B} is extracted from this publication and is compared to the brilliance taken from figure A.12 which is taken from Laue-Langevin (2008).

Integrating over the single-slit interference pattern gives the intensity that is going through their object slit of $\Delta x = 0.09 \text{ mm}$ and the beam diameter $\Delta y \approx 60 \text{ mm}$.

$$\mathcal{I} = 5.08 \text{ Neutrons/s} \quad (\text{A.1})$$

Considering the width of the slit it can be concluded that the flux is

$$\mathcal{F}_{(\Delta x, \Delta y)} = (0.942 \pm 0.004) \frac{\text{Neutrons}}{\text{mm}^2 \text{ s}} \quad (\text{A.2})$$

. Further, the upstream setup allows for a maximal divergence of $\Delta\alpha = \pm 11 \mu\text{rad}$. Assuming an isotope angular distribution it follows that the radiance is

$$\mathcal{F}_{(\Delta x, \Delta y, \Delta\alpha)} = (2.96 \pm 0.09) \cdot 10^{-5} \frac{\text{Neutrons}}{\text{mm}^2 \mu\text{rad s}} \quad (\text{A.3})$$

Considering $\frac{\Delta\lambda}{\lambda} \approx 3.6\%$ at $\lambda = (1.929 \pm 0.002) \text{ nm}$ yields a brilliance \mathcal{F}^* of

$$\mathcal{F}^* = \frac{\mathcal{F}_{(\Delta x, \Delta y, \Delta\alpha)}}{\Delta\lambda} = (7.0 \pm 0.2) \cdot 10^{-5} \frac{\text{Neutrons}}{\text{mm}^2 \mu\text{rad s nm}}. \quad (\text{A.4})$$

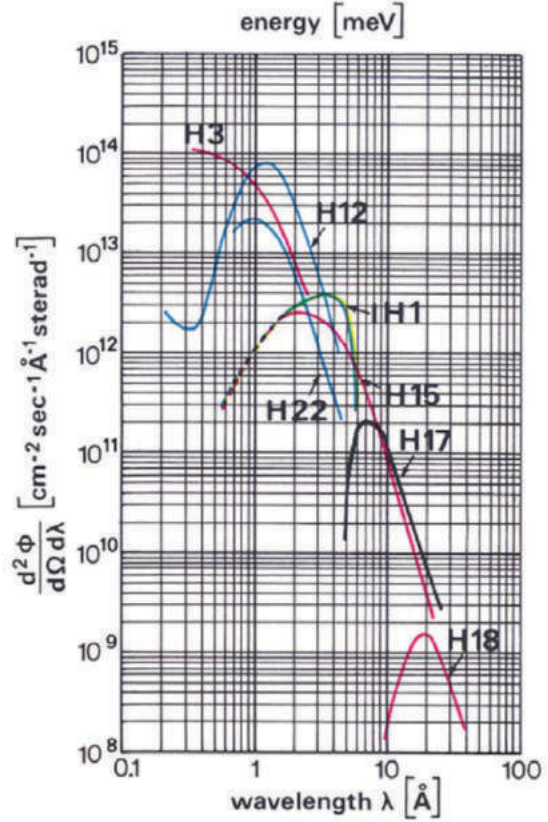


Figure A.12.: Brilliance as a function of Neutron energy for different beam-ports at the Institut Laue-Langevin. The plot is taken from Laue-Langevin (2008).

A. Supplemental Information

Estimating the vertical divergence constrained to be 4.6 mrad and thus overestimating gives

$$\mathcal{B} = 2.6 \cdot 10^9 \frac{\text{Neutrons}}{\text{cm}^2 \text{ sterad s } \text{\AA}} \quad (\text{A.5})$$

which is slightly bigger but of the same order as the brilliance given in figure A.12

$$\mathcal{B} = 1.3 \cdot 10^9 \frac{\text{Neutrons}}{\text{cm}^2 \text{ sterad s, } \text{\AA}}. \quad (\text{A.6})$$

A.4. Constants and Calculation Parameter

Calculations in this thesis were done with the parameter values in table A.3 if not specified otherwise. Table A.4 collects used natural constants and their corresponding sources.

Name	Value	Information
$\epsilon_{\text{BiDim26}}$	$(68.3 \pm 1)\%$	Efficiency of the BiDim-26 detector at λ_{mean} . Value is linearly extrapolated from source to cover the relevant range. The detector uses a gas mixture of 500 mbar ^3He + 1.5 bar CF_4 . See Manzin (2011).
ζ_{BiDim26}	(2×2) mm	Pixel size of the BiDim-26 detector. See Manzin (2011).
S1	8.5 μm	Opening of Slit S1
S2	500 μm	Opening of Slit S2
$\Delta_{\text{S1,S2}}$	0.35 m	Distance between S1 and S2
L	0.315 m	Length of the main mirror.
a	53 μm	Distance between slit middle axis and mirror.
v_{mean}	(62.6 ± 0.9) m/s	Mean of a Gaussian velocity distribution that is used in simulating the interference pattern. Based on the beam-time 2014, see Bricher (2015).
λ_{mean}	(6.32 ± 0.4) nm	Corresponding wavelength to the previously stated value. See Bricher (2015).
$\frac{\Delta\lambda}{\lambda}$	6.7%	Width of the Faussian velocity distribution. See Bricher (2015)

Table A.3.: Standard calculation parameter table. If not specified otherwise, these values were used for calculations in this thesis.

Name	Value	Unit	Uncertainty	Source/Information
m_u	$1.66053904 \cdot 10^{-27}$	kg	$2 \cdot 10^{-35}$	Unified atom mass
m_n	$1.674927471 \cdot 10^{-27}$	kg	$2.1 \cdot 10^{-35}$	Neutron mass
m_p	$1.672621898 \cdot 10^{-27}$	kg	$2.1 \cdot 10^{-35}$	Proton mass
$\mu_N = \frac{e\hbar}{2m_p}$	$5.050783699 \cdot 10^{-27}$	J/T	$3.1 \cdot 10^{-36}$	Nuclear magneton
$\frac{\mu_n}{\mu_N}$	-1.91304272	—	$4.5 \cdot 10^{-7}$	Ratio neutron and nuclear magnetic moment
c	299792458	m/s	exact	Speed of Light
h	$6.626070040 \cdot 10^{-34}$	J · s	$8.1 \cdot 10^{-42}$	Planck Constant
$\hbar = \frac{h}{2\pi}$	$1.054571800 \cdot 10^{-34}$	J · s	$1.3 \cdot 10^{-42}$	Reduced Planck Constant
e	$1.6021766208 \cdot 10^{-19}$	C	$9.8 \cdot 10^{-28}$	Elementary Charge
k_B	$1.38064852 \cdot 10^{-23}$	J/K	$5.7 \cdot 10^{-30}$	Boltzmann Constant
N_A	$6.022140857 \cdot 10^{23}$	1/mol	$1.2 \cdot 10^{15}$	Avogadro Constant
μ_0	$4\pi \cdot 10^{-7}$	N/A ²	exact	Vacuum permeability

Table A.4.: These constants were used for calculations in this thesis. All quantities are taken from Mohr, Newell and Taylor (2015) and from Patrignani (2016) for particle properties.

Name	Density	Atom Mass	N. Absorption Cross-Section
Copper	$8.96 \frac{\text{g}}{\text{cm}^3}$	63.55 u	3.78(2) barn
¹⁰ Boron	$2.35 \frac{\text{g}}{\text{cm}^3}$	10 u	3835.0(9.0) barn
Boron	$2.35 \frac{\text{g}}{\text{cm}^3}$	10.81 u	767.0(8.0) barn
Boron detector coating	$2.35 \frac{\text{g}}{\text{cm}^3}$	—	3661.8 barn
Silicon	$2.33 \frac{\text{g}}{\text{cm}^3}$	28.085 u	0.171(3) barn
Oxygen	—	15.999 u	0.00019(2) barn
N – BK7	$2.51 \frac{\text{g}}{\text{cm}^3}$	—	—
Aluminum	$2.6989 \frac{\text{g}}{\text{cm}^3}$	26.982 u	0.231(3) barn
Gold	$19.30 \frac{\text{g}}{\text{cm}^3}$	196.967 u	98.65(9) barn

Table A.5.: Relevant quantities for elements and compounds which were used in this thesis at standard conditions. The neutron velocity is set to be 2200 m/s. Data is taken from Bruckner (1999)&Dianoux (2003). The value for “Boron detector coating” is calculated for a mixture of 95 % ¹⁰B and 5 % ¹¹B using the NeutronsAndMatter Mathematica package. The density of BK7 is given in AG (2016).

A. Supplemental Information

Name	N [$\frac{1}{\text{cm}^3}$]	V [neV]	Information
BK7	$2.16 \cdot 10^{22}$	97.9	Calculated using the NeutronAnd-Matter Mathematica package.
Aluminum	$6.02 \cdot 10^{22}$	54	Taken from Golub, Lamoureaux and Richardson (1991).
Aluminumoxid	$2.33 \cdot 10^{22}$	147.33	Calculated using the NeutronAnd-Matter Mathematica package.
Silicondioxid	$2.43 \cdot 10^{22}$	99.75	Calculated using the NeutronAnd-Matter Mathematica package.
Berylliumoxide	$7.25 \cdot 10^{22}$	256.56	Calculated using the NeutronAnd-Matter Mathematica package.
CR39 Coating	$14.73 \cdot 10^{22}$	5.5	Calculated using the Neutron-AndMatter Mathematica package. 95% ^{10}B and 5% ^{11}B as is used for the CR39 detector.
Titanium	$5.6 \cdot 10^{22}$	-49.75	Taken from Golub, Lamoureaux and Richardson (1991).
Carbon	$10 \cdot 10^{22}$	180	Taken from Golub, Lamoureaux and Richardson (1991).

Table A.6.: Optical potentials for frequently used materials calculated using values from Dianoux (2003) and using the NeutronAndMatter package. For the calculation $V = \frac{2\pi\hbar^2}{m} \hat{N}a$ is used, as stated in Golub, Lamoureaux and Richardson (1991). a is the positive scattering length, \hat{N} is the number density, and V is the optical potential..

Quantity	Value	Information
7 Day Simulation		
$\lambda_{\mathcal{L}}$	$(18.7 \pm 0.3) \mu\text{m}$	Estimated plane wave period of Lloyd's Mirror.
κ	(0.64 ± 0.13)	Visibility of the pattern for the first maxima.
y_0	$(101.8 \pm 0.6) \mu\text{m}$	Mirror surface position.
B	$(5.8 \pm 0.3) \#/(s \cdot \text{bin})$	Background in the region $0 \text{ mm} < y < 0.1 \text{ mm}$.
A	$(59.8 \pm 6.2) \#/(s \cdot \text{bin})$	Amplitude of the pattern.
τ_1	$(583 \pm 234) 1/\mu\text{m}$	Rise parameter of the pattern.
τ_2	$(17 \pm 6) 1/\mu\text{m}$	Visibility modulation.
τ_3	$(8.5 \pm 0.6) 1/\mu\text{m}$	Overall intensity decay of the pattern.
21 Day Simulation		
$\lambda_{\mathcal{L}}$	$(18.7 \pm 0.2) \mu\text{m}$	Estimated plane wave period of Lloyd's Mirror.
κ	(0.64 ± 0.07)	Visibility of the pattern for the first maxima.
y_0	$(101.9 \pm 0.3) \mu\text{m}$	Mirror surface position.
B	$(21.3 \pm 0.6) \#/(s \cdot \text{bin})$	Background in the region $0 \text{ mm} < y < 0.1 \text{ mm}$.
A	$(194 \pm 14) \#/(s \cdot \text{bin})$	Amplitude of the pattern.
τ_1	$(828 \pm 325) 1/\mu\text{m}$	Rise parameter of the pattern.
τ_2	$(12 \pm 3) 1/\mu\text{m}$	Visibility modulation.
τ_3	$(9.6 \pm 0.5) 1/\mu\text{m}$	Overall intensity decay of the pattern.

Table A.7.: Result of a fit on the simulation of Lloyd's Mirror. This table completes the information in table 6.5. The parameter τ_1 has an expected high uncertainty. This does not interfere with the fit as this part of the equation is only used as a cutoff. The shape is not as important as the position which is defined by y_0 .

A.5. Beam Parameter Definition

The definition of beam characterizing parameters in this thesis can slightly differ from these in specific literature as beam parameters are frequently adapted to take specific properties of a research field into account. Note that the following quantities are only exact if they are local and not averaged over the beam. If macroscopic parts of the beam are used as for example for the bandwidth then it is assumed that the beam can be approximated by a homogeneous beam, which does not have to be a good approximation. For a similar definition see Hakamata (2006).

A. Supplemental Information

Intensity Intensity is the number of something [#] (i.e. particle) per unit time with $[\mathcal{I}] = \#/ \text{time}$.

Flux Flux describes the rate of transport of something through a surface. The unit is $[\mathcal{F}] = \#/ \text{time} / \text{area}$. Keep in mind that this quantity is directional and thus builds up a vector field.

Radiance Radiance incorporates the angular dependency and has a unit of $[\mathcal{R}] = \#/ \text{time} / \text{projected area} / \text{solid angle}$.

Brilliance Brilliance incorporates the angular dependency and the bandwidth of the beam. It has a unit of $[\mathcal{B}] = \#/ \text{time} / \text{projected area} / \text{solid angle} / \text{bandwidth}$.

Bandwidth The spectral bandwidth is here defined as the full width at the half maximum value. The unit is given as $[\text{FWHM}] = \text{wavelength}$.

A.6. Function Definition

This section gives relations that are used in this thesis and their sources.

Collected Relations The integral

$$\int_{-\infty}^{\infty} e^{iku^2} du = \sqrt{\frac{\pi}{2|k|}} (1 + i \operatorname{sgn}(k)) \quad (\text{A.7})$$

for $k \in \mathbb{R}$ and with the sign function $\operatorname{sgn}(x) = x/|x|$.

Fresnel Integrals In Arfken and Weber (2013) the Fresnel-integrals are given as follows

$$\int_0^t \cos u^2 du = \frac{\pi}{2} \mathcal{F}\mathcal{C} \left[\frac{\pi}{2} t \right] \quad (\text{A.8})$$

$$\int_0^t \sin u^2 du = \frac{\pi}{2} \mathcal{F}\mathcal{S} \left[\frac{\pi}{2} t \right]. \quad (\text{A.9})$$

$\mathcal{C}(u)$ and $\mathcal{S}(u)$ both have the same limit for $u \rightarrow \infty$

$$\lim_{u \rightarrow \infty} \mathcal{FC}(u) = \lim_{u \rightarrow \infty} \mathcal{FS}(u) = \frac{1}{2}. \quad (\text{A.10})$$

Further, the following integral is of interest

$$\int_0^{\infty} e^{i\eta(x-x')^2} dx' = \left(\frac{1}{2} + \frac{i}{2}\right) \sqrt{\frac{\pi}{2\eta}} \left(1 + (1-i)\mathcal{FC}\left[\sqrt{\frac{2\eta}{\pi}}x\right] + (1+i)\mathcal{FS}\left[\sqrt{\frac{2\eta}{\pi}}x\right]\right). \quad (\text{A.11})$$

Hankel-Functions The Hankel-functions which are used in this thesis are shown in their integral representation

$$\int_{-\infty}^{\infty} \frac{e^{i\kappa(\xi+\eta^2)}}{(\xi+\eta^2)^{1/2}} d\eta = i\frac{\pi}{2} e^{i\frac{\kappa}{2}\xi} \mathcal{H}_0^{(1)}\left[\frac{\kappa}{2}\xi\right] \quad (\text{A.12})$$

with $\xi > 0$ and $\kappa > 0$. See Wolfram Research for source.

A useful integral representation for two-dimensional problems is given in Schwinger et al. (1998) as

$$\int_{-\infty}^{\infty} \frac{e^{ik(\xi^2+\eta^2)^{1/2}}}{(\xi^2+\eta^2)^{1/2}} d\eta = i\pi \mathcal{H}_0^{(1)}[k\xi] \quad (\text{A.13})$$

if $\xi \geq 0$ and $k \geq 0$.

Additionally, several relations for Hankel-functions can be found in the standard literature

$$2\frac{d\mathcal{H}_n^{(P)}[x]}{dx} = \mathcal{H}_{n-1}^{(P)}[x] - \mathcal{H}_{n+1}^{(P)}[x] \quad (\text{A.14})$$

$$\frac{2n}{x}\mathcal{H}_n^{(P)}[x] = \mathcal{H}_{n-1}^{(P)}[x] + \mathcal{H}_{n+1}^{(P)}[x] \quad (\text{A.15})$$

for $n = 1, 2, 3, \dots$ and together

$$\frac{d\mathcal{H}_n^{(P)}[x]}{dx} = \frac{n\mathcal{H}_n^{(P)}[x]}{x} - \mathcal{H}_{n+1}^{(P)}[x]. \quad (\text{A.16})$$

To calculate $|\Psi|^2 = |\Psi^*\Psi|$ the complex conjugate of the Hankel-function. Note that the Hankel-function are defined as linear combinations of the Bessel-functions

$$\mathcal{H}_n^{(1)}(x) = \mathcal{J}_n(x) + i\mathcal{Y}_n(x) \quad (\text{A.17})$$

$$\mathcal{H}_n^{(2)}(x) = \mathcal{J}_n(x) - i\mathcal{Y}_n(x) \quad (\text{A.18})$$

thus it follows that

$$(\mathcal{H}_n^{(1)}(x^*))^* = \mathcal{H}_n^{(2)}(x). \quad (\text{A.19})$$

For negative n the following relations hold

$$\mathcal{H}_{-n}^{(1)}(x) = e^{n\pi i} \mathcal{H}_n^{(1)}(x) \quad (\text{A.20})$$

$$\mathcal{H}_{-n}^{(2)}(x) = e^{-n\pi i} \mathcal{H}_n^{(2)}(x). \quad (\text{A.21})$$

A.7. Wave Function of Lloyd's Mirror in Green's Formalism

In the following section a calculation of the wave function of Lloyd's mirror using Green's function is presented. The result is used in section 5.5.2 and the following thesis. The basic arguments presented here follow closely Morse and Feshbach (1953), partly Brukner and Anton Zeilinger (1997) and Economou (2013).

Time-Independent Schrödinger-Equation For a time-independent problem the potential force-free stationary Schrödinger equation

$$-\frac{\hbar^2}{2m} \nabla^2 \psi(\vec{r}) - \frac{\hbar^2}{2m} k^2 \psi(\vec{r}) = 0 \quad (\text{A.22})$$

can be solved with $\psi(\vec{r}) = Ae^{i\vec{k}\vec{r}}$ and that the time depended solution is given by $\Psi(\vec{r}, t) = \psi(\vec{r})e^{-i\omega t}$. If a source term is added equation (A.22) becomes the inhomogeneous Helmholtz equation

$$\nabla^2 \psi(\vec{r}) + k^2 \psi(\vec{r}) = -4\pi\rho(\vec{r}). \quad (\text{A.23})$$

If only a point source is considered $\rho(\vec{r}) = \delta(\vec{r}, \vec{r}')$ equation (A.23) can be solved by a Green's function $G(\vec{r}, \vec{r}')$ if boundary conditions and initial values are given

$$\nabla^2 G(\vec{r}, \vec{r}') + k^2 G(\vec{r}, \vec{r}') = -4\pi\delta(\vec{r}, \vec{r}'). \quad (\text{A.24})$$

Time-Dependent Schrödinger-Equation If boundary conditions or potentials are time-dependent the previous static approach is not sufficient. The time-dependent potential force-free Schrödinger-equation is given as

$$\frac{\hbar^2}{2m} \nabla^2 \psi(\vec{r}, t) + i\hbar \frac{\partial}{\partial t} \psi(\vec{r}, t) = 0. \quad (\text{A.25})$$

Again a source term $q(\vec{r}, t)$ is added and thus

$$\frac{\hbar^2}{2m} \nabla^2 \psi(\vec{r}, t) + i\hbar \frac{\partial}{\partial t} \psi(\vec{r}, t) = -4\pi q(\vec{r}, t) \quad (\text{A.26})$$

which can be solved by using a Green's function $G_0(\vec{r}, \vec{r}', t, t')$ which satisfies

$$\frac{\hbar^2}{2m} \nabla^2 G(\vec{r}, \vec{r}', t, t') + i\hbar \frac{\partial}{\partial t} G(\vec{r}, \vec{r}', t, t') = -4\pi\delta(\vec{r}, \vec{r}')\delta(t, t'). \quad (\text{A.27})$$

Force-Free Particles Green's Function If the goal is to describe particles as it is here it is convenient to solve first the problem of a force-free particle without boundary. Technically the boundary can be set at $\vec{r} \rightarrow \infty$ where it is required that $G(\vec{r}, \vec{r}')$ vanishes. Then the Green's function becomes

$$G(\vec{r}, \vec{r}') = G_0(\vec{r}, \vec{r}') = \chi \frac{e^{i|\vec{k}||\vec{r}-\vec{r}'|}}{|\vec{r}-\vec{r}'|} \quad (\text{A.28})$$

with $|\vec{r}-\vec{r}'| = \sqrt{(x-x')^2 + (y-y')^2 + (z-z')^2}$, as stated in Morse and Feshbach (1953). For the time-dependent problem the Green's function is given in Economou (2013) by¹

$$G_0(\vec{r}, \vec{r}', t, t') = \chi_0 [d] \left(\frac{1}{t-t'} \right)^{d/2} e^{i\frac{m}{2\hbar} \frac{|\vec{r}-\vec{r}'|^2}{t-t'}} \quad (\text{A.29})$$

¹It is used that $\vec{v} = \frac{\vec{r}-\vec{r}'}{t-t'}$. Note that G_0 treats the propagation of a single particle in space. The particle starts at \vec{r}' at time t' and will reach the point \vec{r} at time t , thus this definition of \vec{v} in this case is justified. See Brukner and Anton Zeilinger (1997).

A. Supplemental Information

for $t > t' > 0$, using $\vec{p} = \hbar\vec{k}$ and $E = \hbar\omega = \frac{\hbar^2}{2m}k^2$, with d the dimensionality of the problem, and $\chi_0[d] = -\frac{i}{\hbar}\left(\frac{m}{2\pi i\hbar}\right)^{d/2}$. The normalization constant χ is given as

$$\chi_{3D} = -\frac{i}{\hbar}\left(\frac{m}{2\pi i\hbar(t-t')}\right)^{3/2}. \quad (\text{A.30})$$

Wave Function Calculation — Static Case To calculate the wave function equation (A.23) and equation (A.24) are subtracted after they are multiplied by $G(\vec{r}, \vec{r}')$ and $\Psi(\vec{r})$ respectively

$$\frac{1}{4\pi} (G(\vec{r}, \vec{r}')\nabla'^2\Psi(\vec{r}') - \Psi(\vec{r}')\nabla'^2G(\vec{r}, \vec{r}')) = \Psi(\vec{r}')\delta(\vec{r} - \vec{r}') - G(\vec{r}, \vec{r}')\rho(\vec{r}'). \quad (\text{A.31})$$

By integrating over the volume V and note that $\iiint \Psi(\vec{r}')\delta(\vec{r} - \vec{r}')d^3r' = \Psi(\vec{r})$ if \vec{r} is restricted to V , we get

$$\Psi(\vec{r}) = \int_V d^3r' G(\vec{r}, \vec{r}')\rho(\vec{r}') \quad (\text{A.32})$$

$$+ \frac{1}{4\pi} \int_V d^3r' [G(\vec{r}, \vec{r}')\nabla'^2\Psi(\vec{r}') - \Psi(\vec{r}')\nabla'^2G(\vec{r}, \vec{r}')]. \quad (\text{A.33})$$

To yield a solution $\Psi(\vec{r})$ that is compatible with the Schrödinger equation we set $\rho(\vec{r}') = 0$ and thus Term A.32 vanishes. Using greens theorem² to express the volume integral as a surface integral in Term A.33 we finally get

$$\Psi(\vec{r}) = \frac{1}{4\pi} \oint_{\vec{S}} [G(\vec{r}, \vec{r}')\nabla'\Psi(\vec{r}') - \Psi(\vec{r}')\nabla'G(\vec{r}, \vec{r}')] d\vec{S}'. \quad (\text{A.34})$$

²Application of Gauss Theorem $\iiint [U(\vec{r})\nabla^2V(\vec{r}) - V(\vec{r})\nabla^2U(\vec{r})] d^3r = \oint [U(\vec{r})\nabla V(\vec{r}) - V(\vec{r})\nabla U(\vec{r})] d\vec{S}$ where $U(\vec{r})$ and $V(\vec{r})$ a scalar function, d^3r is the volume element, and $d\vec{S}$ is an element of the boundary surface of the volume considered. See for example Morse and Feshbach (1953).

Wave Function Calculation — Time-Dependent Case The treatment of the time dependent case is more lengthy and can be seen rigorously in Morse and Feshbach (1953). There the wave function is given as

$$\begin{aligned}
\Psi(\vec{r}, t) &= \int_0^{t^+} \oint_{\vec{S}} q(\vec{r}', t') G(\vec{r}, \vec{r}', t, t') \\
&+ \frac{1}{4\pi} \frac{\hbar^2}{2m} \int_0^{t^+} dt' \oint_{\vec{S}} [G(\vec{r}, \vec{r}', t, t') \nabla' \Psi(\vec{r}', t') \\
&- \Psi(\vec{r}', t') \nabla' G(\vec{r}, \vec{r}', t, t')] d\vec{S}' \\
&+ \frac{i\hbar}{4\pi} \int_V d^3r [\Psi(\vec{r}', t') G(\vec{r}, \vec{r}', t, t')]_{t'=0}. \tag{A.35}
\end{aligned}$$

Again $q(\vec{r}', t')$ is set to be zero to recover the physical solution that is only dependent on initial conditions and boundary conditions

$$\begin{aligned}
\Psi(\vec{r}, t) &= \frac{1}{4\pi} \frac{\hbar^2}{2m} \int_0^{t^+} dt' \\
&\times \oint_{\vec{S}} [G(\vec{r}, \vec{r}', t, t') \nabla' \Psi(\vec{r}', t') - \Psi(\vec{r}', t') \nabla' G(\vec{r}, \vec{r}', t, t')] d\vec{S}' \\
&+ \frac{i\hbar}{4\pi} \int_V d^3r \Psi(\vec{r}', 0) G(\vec{r}, \vec{r}', t, 0) \tag{A.36}
\end{aligned}$$

where $G(\vec{r}, \vec{r}', t, t') = 0$ for $t < 0$.

Boundary Conditions For different boundary conditions a solution can be built up as a sum between solution $G_0(\vec{r}, \vec{r}', t, t')$ and a term $F(\vec{r}, \vec{r}', t, t')$ covering the boundary effects and we get

$$G(\vec{r}, \vec{r}', t, t') = G_0(\vec{r}, \vec{r}', t, t') + F(\vec{r}, \vec{r}', t, t'). \tag{A.37}$$

The same relation holds for the static case.

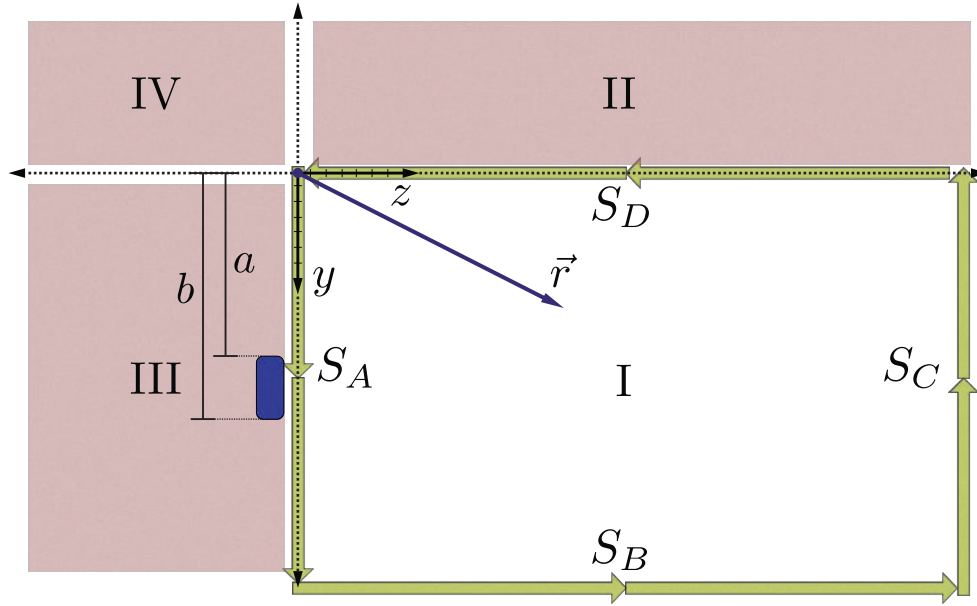


Figure A.13.: Surface integration for a corner geometry. The thick dashed line is the reflecting surface, the blue region is the position of the entrance slit, the red region will not be considered, and the green arrows follows the integration path.

A.7.1. Slit and Reflecting Half-Plane — Static

To model Lloyd's mirror geometry we start by modeling the mirror region as shown in figure A.13. To find the relevant Green's function we make use of the method of images³ and find

$$\begin{aligned}
G_{\mathcal{L}}(r, r') = G_0 & - \underbrace{G_0(|x - x'|, |y + y'|, |z - z'|)}_{G_{\text{I}}} \\
& - \underbrace{G_0(|x - x'|, |y - y'|, |z + z'|)}_{G_{\text{II}}} \\
& + \underbrace{G_0(|x - x'|, |y + y'|, |z + z'|)}_{G_{\text{III}}}
\end{aligned} \tag{A.38}$$

which does satisfy the boundary condition given by

$$G_{\mathcal{L}}(\vec{r}, \vec{r}') = \begin{cases} 0 & \text{for } z = 0 \text{ or } y = 0 \\ 0 & \text{for } z \rightarrow \infty \text{ or } y \rightarrow \infty. \end{cases} \tag{A.39}$$

³As described for acoustic waves in Y. A. Melnikov and M. Y. Melnikov (2012) and for time-dependent matter waves in Brukner and Anton Zeilinger (1997)

Thus, we assume perfect reflection at S_D and S_A . From the given Green's function the wave function can be calculated using

$$\Psi(\vec{r}) = +\frac{1}{4\pi} \oint d\vec{S}' \cdot [G(\vec{r}, \vec{r}') \text{grad}' \Psi(\vec{r}') - \Psi(\vec{r}') \text{grad}' G(\vec{r}, \vec{r}')]. \quad (\text{A.40})$$

where Term A.40 describes the effect of the boundary and as was chosen $G_{\mathcal{L}}(\vec{r}, \vec{r}')|_{\vec{r} \in S} = 0$ the first part vanishes. $\Psi(\vec{r})$ is then given by

$$\Psi(\vec{r}) = -\frac{1}{4\pi} \oint d\vec{S}' \cdot \Psi(\vec{r}') \text{grad}' G_{\mathcal{L}}(\vec{r}, \vec{r}'). \quad (\text{A.41})$$

Following the boundary surface in figure A.13 the closed surface integral becomes

$$\Psi(\vec{r}) = \frac{1}{4\pi} \int_0^\infty dy' \int_{-\infty}^\infty dx' \left[\Psi(\vec{r}') \frac{\partial}{\partial z'} G_{\mathcal{L}}(\vec{r}, \vec{r}') \right]_{\vec{r}' \in S_A} \quad (\text{A.42})$$

$$- \frac{1}{4\pi} \int_0^\infty dz' \int_{-\infty}^\infty dx' \left[\Psi(\vec{r}') \frac{\partial}{\partial y'} G_{\mathcal{L}}(\vec{r}, \vec{r}') \right]_{\vec{r}' \in S_B} \quad (\text{A.43})$$

$$- \frac{1}{4\pi} \int_{-\infty}^0 dy' \int_{-\infty}^\infty dx' \left[\Psi(\vec{r}') \frac{\partial}{\partial z'} G_{\mathcal{L}}(\vec{r}, \vec{r}') \right]_{\vec{r}' \in S_C} \quad (\text{A.44})$$

$$+ \frac{1}{4\pi} \int_{-\infty}^0 dz' \int_{-\infty}^\infty dx' \left[\Psi(\vec{r}') \frac{\partial}{\partial y'} G_{\mathcal{L}}(\vec{r}, \vec{r}') \right]_{\vec{r}' \in S_D}. \quad (\text{A.45})$$

If we presuppose that the mirror and the defining slit screen have an infinitely high potential the wave function should then vanish on S_A and S_D except at the entrance slit

$$\Psi(\vec{r}) = \begin{cases} 0 & \text{for } \vec{r} \in S_D \wedge \vec{r} \in S_B \wedge \vec{r} \in S_C \\ 0 & \text{for } \vec{r} \in S_A \wedge b < y < a \\ 1 & \text{for } \vec{r} \in S_A \wedge b > y > a \end{cases} \quad (\text{A.46})$$

thus only Term A.42 is non-zero

$$\Psi(\vec{r}) = \frac{1}{4\pi} \int_a^b dy' \int_{-\infty}^\infty dx' \left[\frac{\partial}{\partial z'} G_{\mathcal{L}}(\vec{r}, \vec{r}') \right]_{z'=0}. \quad (\text{A.47})$$

A. Supplemental Information

Substituting $z^- = z - z'$ and $z^+ = z + z'$ we get

$$\begin{aligned}
\left[\frac{\partial}{\partial z'} G_{\mathcal{L}}(|\vec{r} - \vec{r}'|)\right]_{z'=0} &= \left[\frac{\partial}{\partial z'} G_0 - G_{\text{I}} - G_{\text{II}} + G_{\text{III}}\right]_{z'=0} \\
&= \frac{\partial}{\partial z} [-G_0(|x - x'|, |y - y'|, |z^-|)]_{z^-=z} \\
&\quad + [G_0(|x - x'|, |y + y'|, |z^-|)]_{z^-=z} \\
&\quad - [G_0(|x - x'|, |y - y'|, |z^+|)]_{z^+=z} \\
&\quad + [G_0(|x - x'|, |y + y'|, |z^+|)]_{z^+=z} \\
&= 2\frac{\partial}{\partial z} [G_0(|x - x'|, |y + y'|, |z|)] \\
&\quad - G_0(|x - x'|, |y - y'|, |z|).
\end{aligned} \tag{A.48}$$

and can state that $\Psi(\vec{r})$ is given by the integral

$$\Psi(\vec{r}) = \underbrace{\frac{1}{2\pi} \int_a^b dy' \frac{\partial}{\partial z} \int_{-\infty}^{\infty} dx' G_0 \left(\sqrt{(x - x')^2 + (y + y')^2 + z^2} \right)}_{\Psi_{\text{I}}} \tag{A.49}$$

$$- \underbrace{\frac{1}{2\pi} \int_a^b dy' \frac{\partial}{\partial z} \int_{-\infty}^{\infty} dx' G_0 \left(\sqrt{(x - x')^2 + (y - y')^2 + z^2} \right)}_{\Psi_{\text{II}}}. \tag{A.50}$$

The part

$$\Psi_{\text{I}} = \frac{\chi}{2\pi} \int_a^b dy' \frac{\partial}{\partial z} \int_{-\infty}^{\infty} d\xi \frac{e^{i|\vec{k}|\sqrt{\xi^2 + (y + y')^2 + z^2}}}{\sqrt{\xi^2 + (y + y')^2 + z^2}}. \tag{A.51}$$

can be expressed with Hankel-function's by substituting $\xi = x - x'$, $\eta = \sqrt{(y + y')^2 + z^2}$, and using the definition in equation (A.13) in appendix A.6 as

$$\Psi_{\text{I}} = \frac{i\chi}{2} \int_a^b dy' \frac{\partial}{\partial z} \mathcal{H}_0^{(1)} \left[|\vec{k}| \sqrt{(y + y')^2 + z^2} \right] \tag{A.52}$$

Using Relation A.16 the derivative of the Hankel-function can be expressed as

$$\frac{d}{dz} \mathcal{H}_0^{(1)} \left[|\vec{k}| \sqrt{(y+y')^2 + z^2} \right] = -\mathcal{H}_1^{(1)} \left[|\vec{k}| \sqrt{(y+y')^2 + z^2} \right] \frac{|\vec{k}|z}{\sqrt{(y+y')^2 + z^2}}. \quad (\text{A.53})$$

As $\Psi_{\text{I}} = \Psi_{\text{II}}|_{y' \rightarrow -y'}$ the time-independent solution $\Psi(\vec{r})$ is given by

$$\Psi_{\mathcal{L}}(\vec{r}) = \Psi_{\text{I}} - \Psi_{\text{II}} \quad (\text{A.54})$$

$$\begin{aligned} &= \chi \frac{iz|\vec{k}|}{2} e^{i|\vec{k}|z} \int_a^b dy' \\ &\quad \times \left(\frac{\mathcal{H}_1^{(1)} \left[|\vec{k}| \sqrt{(y-y')^2 + z^2} \right]}{\sqrt{(y-y')^2 + z^2}} - \frac{\mathcal{H}_1^{(1)} \left[|\vec{k}| \sqrt{(y+y')^2 + z^2} \right]}{\sqrt{(y+y')^2 + z^2}} \right). \end{aligned} \quad (\text{A.55})$$

Alternatively, this can also be expressed as

$$\begin{aligned} \Psi_{\mathcal{L}}(\vec{r}) &= \chi \frac{iz}{4} |\vec{k}|^2 e^{i|\vec{k}|z} \int_a^b dy' \\ &\quad \times \left\{ \left(\mathcal{H}_0^{(1)} \left[|\vec{k}| \sqrt{(y-y')^2 + z^2} \right] + \mathcal{H}_2^{(1)} \left[|\vec{k}| \sqrt{(y-y')^2 + z^2} \right] \right) \right. \\ &\quad \left. - \left(\mathcal{H}_0^{(1)} \left[|\vec{k}| \sqrt{(y+y')^2 + z^2} \right] + \mathcal{H}_2^{(1)} \left[|\vec{k}| \sqrt{(y+y')^2 + z^2} \right] \right) \right\}. \end{aligned} \quad (\text{A.56})$$

A.7.1.1. Derivative for Static Solution

With the wave function of Lloyd's mirror given in equation (A.55) in the static case we can analyze its properties. A handy quantity is the derivative of the wave function in

A. Supplemental Information

respect to y . Only considering the first term in equation (A.55) $\Psi_{\mathcal{L},\text{I}}$, exchanging the derivative and the integral, and with equation (A.15) we get

$$\frac{\partial}{\partial y} \Psi_{\mathcal{L},\text{I}}(\vec{r}) = \chi \frac{iz}{4} |\vec{k}|^2 e^{i\vec{k}|z} \int_a^b dy' \frac{\partial}{\partial y} \frac{\mathcal{H}_1^{(1)} \left[|\vec{k}| \sqrt{(y-y')^2 + z^2} \right]}{\sqrt{(y-y')^2 + z^2}} \quad (\text{A.57})$$

$$\begin{aligned} &= \chi \frac{iz}{4} |\vec{k}|^2 e^{i\vec{k}|z} \int_a^b dy' \\ &\quad \times \left\{ -\mathcal{H}_1^{(1)} \left[|\vec{k}| \sqrt{\eta} \right] \frac{1}{\eta^{3/2}} (y-y') \right. \\ &\quad \left. + \frac{1}{2\sqrt{\eta}} \left(\mathcal{H}_0^{(1)} \left[|\vec{k}| \sqrt{\eta} \right] - \mathcal{H}_2^{(1)} \left[|\vec{k}| \sqrt{\eta} \right] \right) |\vec{k}| \frac{1}{\sqrt{\eta}} (y-y') \right\} \quad (\text{A.58}) \end{aligned}$$

$$\begin{aligned} &= \chi \frac{iz}{4} |\vec{k}|^2 e^{i\vec{k}|z} \int_a^b dy' \\ &\quad \times \left\{ -\mathcal{H}_1^{(1)} \left[|\vec{k}| \sqrt{\eta} \right] \frac{1}{\eta^{3/2}} (y-y') \right. \\ &\quad \left. + \frac{1}{\sqrt{\eta}} \left(\frac{\mathcal{H}_1^{(1)} \left[|\vec{k}| \sqrt{\eta} \right]}{|\vec{k}| \sqrt{\eta}} - \mathcal{H}_2^{(1)} \left[|\vec{k}| \sqrt{\eta} \right] \right) |\vec{k}| \frac{1}{\sqrt{\eta}} (y-y') \right\} \quad (\text{A.59}) \end{aligned}$$

$$= \chi \frac{iz}{4} |\vec{k}|^2 e^{i\vec{k}|z} \int_a^b dy' \mathcal{H}_2^{(1)} \left[|\vec{k}| \sqrt{\eta} \right] \frac{|\vec{k}|}{\eta} (y-y') \quad (\text{A.60})$$

$$= \chi \frac{iz}{4} |\vec{k}|^3 e^{i\vec{k}|z} \int_a^b dy' \mathcal{H}_2^{(1)} \left[|\vec{k}| \sqrt{(y-y')^2 + z^2} \right] \frac{(y-y')}{(y-y')^2 + z^2} \quad (\text{A.61})$$

where $\eta = (y-y')^2 + z^2$ and $\mathcal{H}_0^{(1)}(f) = \frac{2\mathcal{H}_1^{(1)}(f)}{f} - \mathcal{H}_2^{(1)}(f)$ was used. Using Mathematica the previous equation can be integrated and we get

$$\frac{\partial}{\partial y} \Psi_{\mathcal{L},\text{I}}(\vec{r}) = \chi \frac{iz}{4} |\vec{k}|^3 e^{i\vec{k}|z} \left(\frac{1}{2|\vec{k}|} - \frac{\mathcal{H}_1^{(1)} \left[|\vec{k}| \sqrt{(y-y')^2 + z^2} \right]}{|\vec{k}|^2 \sqrt{(y-y')^2 + z^2}} \right) \Bigg|_a^b \quad (\text{A.62})$$

and

$$\frac{\partial}{\partial y} \Psi_{\mathcal{L},\text{II}}(\vec{r}) = \chi \frac{iz}{4} |\vec{k}|^3 e^{i|\vec{k}|z} \left(\frac{1}{2|\vec{k}|} - \frac{\mathcal{H}_1^{(1)} \left[|\vec{k}| \sqrt{(y+y')^2 + z^2} \right]}{|\vec{k}|^2 \sqrt{(y+y')^2 + z^2}} \right) \Bigg|_a^b \quad (\text{A.63})$$

where the constant term can be dropped as it will cancel if the definite integral is evaluated. For the probability density $|\Psi_{\mathcal{L}}|^2$ we can write by using equation (A.19)

$$\frac{\partial}{\partial y} |\Psi_{\mathcal{L}}|^2 = \frac{\partial}{\partial y} |\Psi_{\mathcal{L}}^* \Psi_{\mathcal{L}}| \quad (\text{A.64})$$

$$= \left| \Psi_{\mathcal{L}} \frac{\partial}{\partial y} \Psi_{\mathcal{L}}^* + \Psi_{\mathcal{L}}^* \frac{\partial}{\partial y} \Psi_{\mathcal{L}} \right| \quad (\text{A.65})$$

$$= \left| \left(\frac{\partial}{\partial y} \Psi_{\mathcal{L},\text{I}}(\vec{r}) + \frac{\partial}{\partial y} \Psi_{\mathcal{L},\text{II}}(\vec{r}) \right)^* \Psi_{\mathcal{L}} + \Psi_{\mathcal{L}}^* \left(\frac{\partial}{\partial y} \Psi_{\mathcal{L},\text{I}}(\vec{r}) + \frac{\partial}{\partial y} \Psi_{\mathcal{L},\text{II}}(\vec{r}) \right) \right| \quad (\text{A.66})$$

$$= \chi^2 \frac{z^2}{16} |\vec{k}|^2 \left| (H_-^2 + H_+^2) \hat{\Psi}_{\mathcal{L}} + (H_-^1 + H_+^1) \hat{\Psi}_{\mathcal{L}}^* \right| \quad (\text{A.67})$$

with

$$H_{\pm}^n = \frac{\mathcal{H}_1^{(n)} \left[|\vec{k}| \sqrt{(y \pm a)^2 + z^2} \right]}{|\vec{k}|^2 \sqrt{(y \pm a)^2 + z^2}} - \frac{\mathcal{H}_1^{(n)} \left[|\vec{k}| \sqrt{(y \pm b)^2 + z^2} \right]}{|\vec{k}|^2 \sqrt{(y \pm b)^2 + z^2}}. \quad (\text{A.68})$$

Figure A.14 shows the the static probability density and the corresponding derivative.

A.7.1.2. Asymptotic Solution

Starting with the asymptotic expression for large z and vanishing δ

$$\Psi_{\text{Asymptotic}} = \delta C z \sqrt{\frac{k}{2\pi}} e^{-i\pi/4} \left\{ \frac{e^{ik\sqrt{(a-y)^2 + z^2}}}{((a-y)^2 + z^2)^{3/4}} - \frac{e^{ik\sqrt{(a+y)^2 + z^2}}}{((a+y)^2 + z^2)^{3/4}} \right\}. \quad (\text{A.69})$$

As $(a-y) \ll z$ and $(a+y) \ll z$ the denominator can be approximated to be

$$((a-y)^2 + z^2)^{3/4} \approx z^{3/2} \quad (\text{A.70})$$

A. Supplemental Information

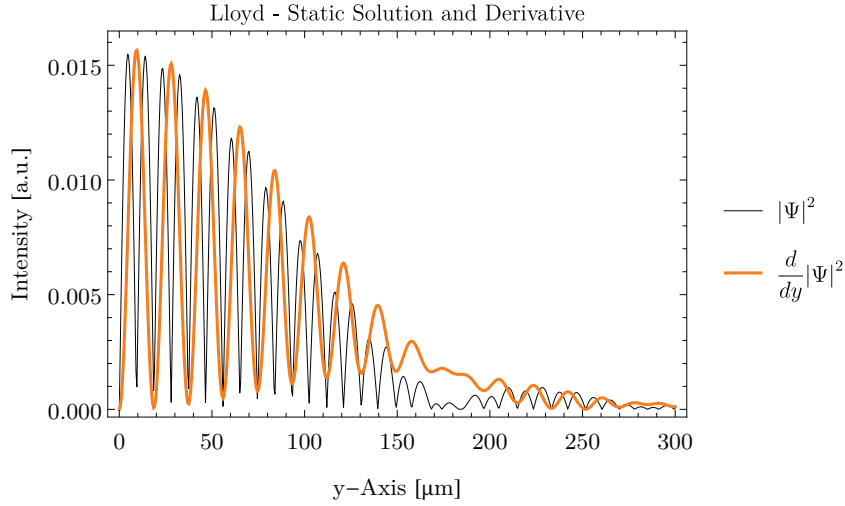


Figure A.14.: Probability density of Lloyd’s mirror for the static case with the derivative overlaid. The pattern was created for standard parameters with $L = 0.34$ m.

and the square root in the exponential gives in first order

$$\sqrt{(a \pm y)^2 + z^2} \approx \sqrt{a^2 + z^2} \pm \frac{ay}{\sqrt{a^2 + z^2}} + \mathcal{O}(2). \quad (\text{A.71})$$

Thus, the asymptotic wave function becomes

$$\Psi_{\text{Asymptotic}} = D \frac{1}{z^{1/2}} e^{ik\sqrt{a^2+z^2}} \left(e^{-ik\frac{ay}{\sqrt{a^2+z^2}}} - e^{ik\frac{ay}{\sqrt{a^2+z^2}}} \right) \quad (\text{A.72})$$

$$= -2i\hat{D} \sin \left(k \frac{ay}{\sqrt{a^2 + z^2}} \right) \approx -2i\hat{D} \sin \left(k \frac{ay}{z} \right) \quad (\text{A.73})$$

which exactly resembles the plane wave solution.

A.7.1.3. Non-Normal Incident

What happens if the incident plane wave hits the entrance slit under a slight angle? We use equation (A.50) and now use a plane wave in the slit of the following form

$$\Psi_0 = e^{ik_z z + ik_y (y-y')} \quad (\text{A.74})$$

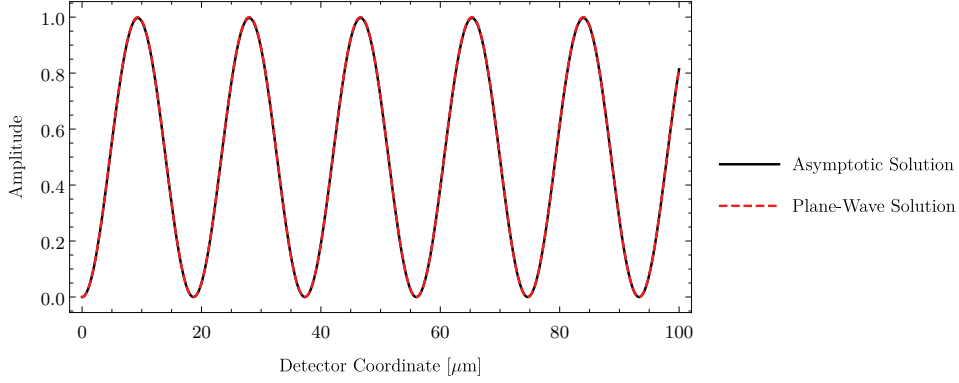


Figure A.15.: Asymptotic solution of Lloyd's mirror for $z \gg 1$ and $\delta \rightarrow 0$ compared to the plane wave solution.. The Asymptotic solution is plotted without the approximations in this section.

with $k_z = |\vec{k}| \cos(\beta)$ and $k_y = |\vec{k}| \sin(\beta)$ the wave vector components. For the wave function y and z lead only to a constant phase a can be dropped and thus only y' is of relevance

$$\begin{aligned} \Psi(\vec{r}) = & \underbrace{\frac{1}{2\pi} \int_a^b dy' \frac{\partial}{\partial z} \int_{-\infty}^{\infty} dx' e^{ik_y y'} G_0 \left(\sqrt{(x-x')^2 + (y+y')^2 + z^2} \right)}_{\Psi_I} \\ & - \underbrace{\frac{1}{2\pi} \int_a^b dy' \frac{\partial}{\partial z} \int_{-\infty}^{\infty} dx' e^{ik_y y'} G_0 \left(\sqrt{(x-x')^2 + (y-y')^2 + z^2} \right)}_{\Psi_{II}}. \end{aligned} \quad (\text{A.75})$$

Jumping ahead to the y' integration we get

$$\Psi_{\mathcal{L}}(\vec{r}) = \Psi_I + \Psi_{II} \quad (\text{A.76})$$

$$\begin{aligned} &= \chi \frac{iz}{4} |\vec{k}|^2 e^{i|\vec{k}|z} \int_a^b dy' e^{ik_y y'} \\ &\quad \times \left\{ \left(\mathcal{H}_0^{(1)} \left[|\vec{k}| \sqrt{(y-y')^2 + z^2} \right] + \mathcal{H}_2^{(1)} \left[|\vec{k}| \sqrt{(y-y')^2 + z^2} \right] \right) \right. \\ &\quad \left. - \left(\mathcal{H}_0^{(1)} \left[|\vec{k}| \sqrt{(y+y')^2 + z^2} \right] + \mathcal{H}_2^{(1)} \left[|\vec{k}| \sqrt{(y+y')^2 + z^2} \right] \right) \right\}. \end{aligned} \quad (\text{A.77})$$

A. Supplemental Information

The resulting interferogram $|\Psi|^2$ for normal incident and different angles are shown in figure A.16 for positive angles and in figure A.17 for negative angles

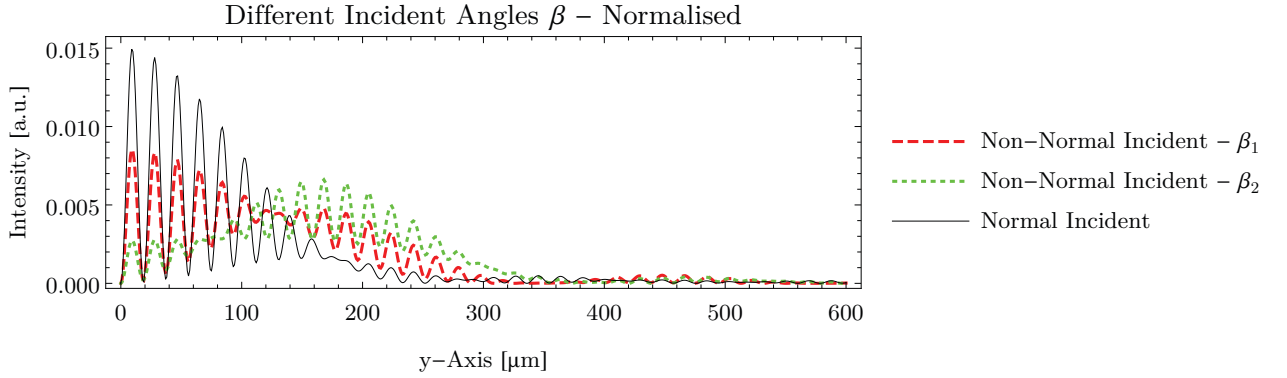


Figure A.16.: Lloyd's mirror probability density for non-normal incident wave for positive angles β . $\beta_1 = 156 \mu\text{rad}$ and $\beta_2 = 2\beta_1$

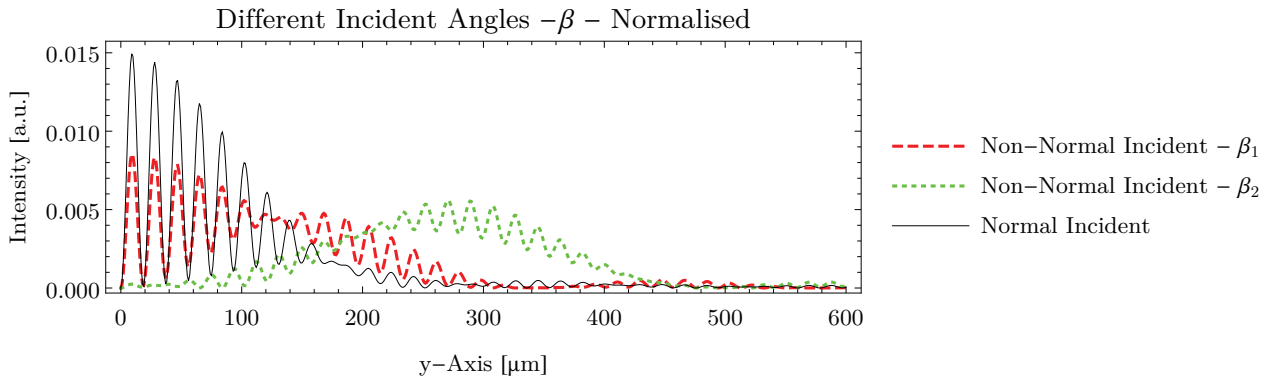


Figure A.17.: Lloyd's mirror probability density for non-normal incident wave for negative angles β . $\beta_1 = -468 \mu\text{rad}$ and $\beta_2 = 2\beta_1$

A.7.1.4. Finite Mirror Length

If equation (A.56) is evaluated at a plane $\mathcal{S}_{x,y,z=L}$ perpendicular to the mirror and direction of motion, the wave function is the result of reflections in both propagation directions. Thus, it is strictly only valid for the infinite plane. Despite this we use Huygen's principle to calculate the approximate behavior if the mirror has a finite size as seen in figure A.18. At the plane $\mathcal{S}_{x,y,z=L}$ every point is origin to a spherical wave and the resulting wavefront is evaluated at a later distance L_D .

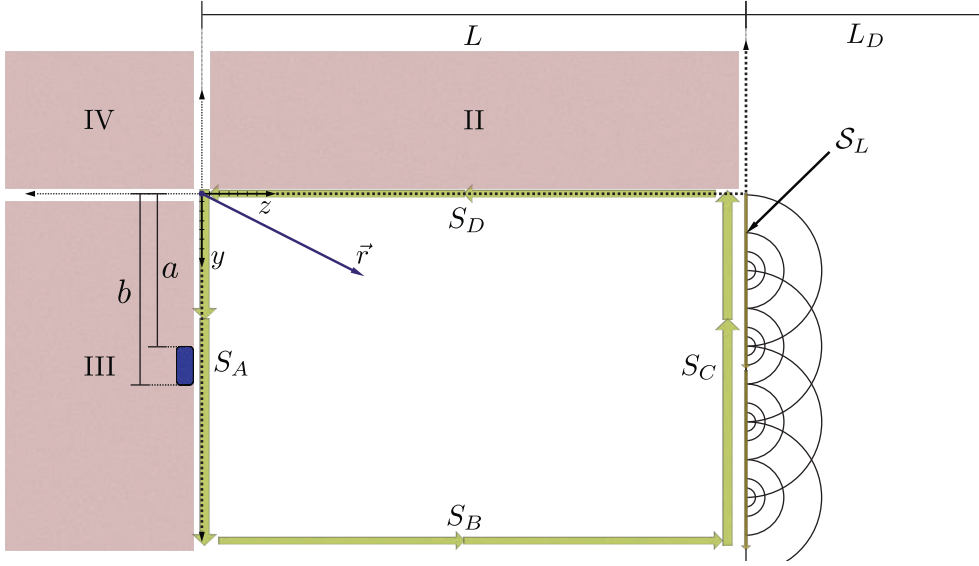


Figure A.18.: Derivation of the effect of a finite-mirror size far away from the mirror end plane $\mathcal{S}_{x,y,z=L}$.

$$\Psi_{\mathcal{L}}(y, z)|_{z < L} \approx \frac{k}{2\pi i} \int_0^{\infty} dy' \int_{-\infty}^{\infty} dx' \Psi_{\text{Green}}(\vec{r}')|_{S_L} \frac{e^{ik|\vec{r}|}}{|\vec{r}|} \quad (\text{A.78})$$

$$\begin{aligned} &\approx A \frac{ik^2 L}{4} \int_0^{\infty} dy' \mathcal{H}_1^{(0)} \left[k \sqrt{(y - y')^2 + (z - L)^2} \right] \\ &\times \left\{ \int_{y'+a}^{y'+b} dy'' \frac{\mathcal{H}_1^{(1)} \left[k \sqrt{y''^2 + L^2} \right]}{\sqrt{y''^2 + L^2}} - \int_{y'-a}^{y'-b} dy'' \frac{\mathcal{H}_1^{(1)} \left[k \sqrt{y''^2 + L^2} \right]}{\sqrt{y''^2 + L^2}} \right\}. \end{aligned} \quad (\text{A.79})$$

Figure A.19 shows a comparison between a wave function which was propagated by Huygen's principle after a mirror with length L and the static solution for Lloyd's mirror with a mirror of length $L_p = L + L_D$.

A.7.2. Slit and Reflecting Half-Plane — Time-Dependent

equation (A.55) does describes the diffraction integrated over all times. This makes it impossible to transition to a finite mirror length as every point at the mirror contributes to the wave function especially the points after a cut-off of the mirror. Thus, it is necessary to treat the problem time-dependent to discriminate reflection at t_1 and t_2 .

A. Supplemental Information

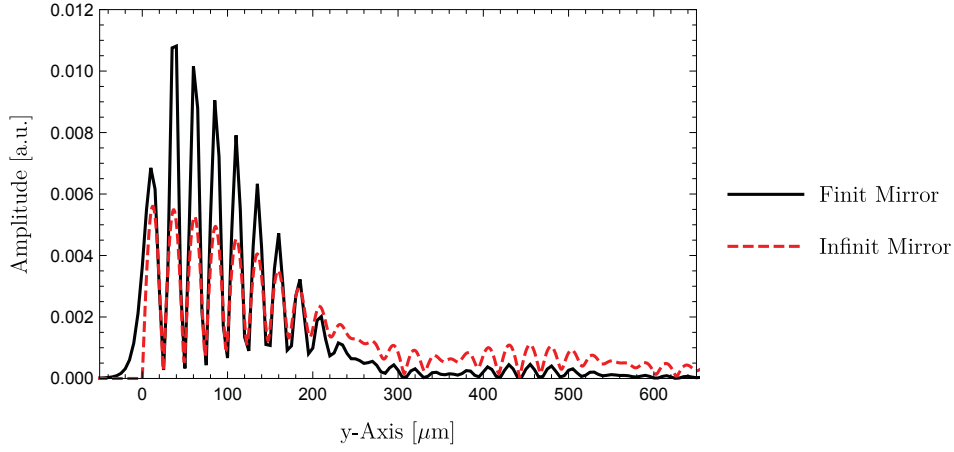


Figure A.19.: Cut through the diffraction pattern behind the mirror evolved through Huygen's principle. The probability of the finite mirror is given by the superposition of spherical waves at $L = 0.34$ m propagated over $L_D = 0.1$ m. The probability density for the plane wave case uses $L_p = L + L_D$.

Green's Function Construction Remembering the static Green's function $G_{\mathcal{L}}(|\vec{r} - \vec{r}'|)$ in equation (A.38) we switch from $G_0(|\vec{r} - \vec{r}'|)$ to $G_0(|\vec{r} - \vec{r}'|, |t - t'|)$ and get

$$\begin{aligned}
 G_{\mathcal{L}}(|r - r'|, |t - t'|) &= \underbrace{G_0(|x - x'|, |y - y'|, |z - z'|, |t - t'|)}_{G_0(|t-t'|)} \\
 &- \underbrace{G_0(|x - x'|, |y + y'|, |z - z'|, |t - t'|)}_{G_I(|t-t'|)} \\
 &- \underbrace{G_0(|x - x'|, |y - y'|, |z + z'|, |t - t'|)}_{G_{II}(|t-t'|)} \\
 &+ \underbrace{G_0(|x - x'|, |y + y'|, |z + z'|, |t - t'|)}_{G_{III}(|t-t'|)}.
 \end{aligned} \tag{A.80}$$

Boundary Condition As in the static case the Green's function satisfies the boundary condition given by

$$G_{\mathcal{L}}(\vec{r}, \vec{r}', t, t') = \begin{cases} 0 & \text{for } z = 0 \text{ or } y = 0 \\ 0 & \text{for } z \rightarrow \infty \text{ or } y \rightarrow \infty. \end{cases} \tag{A.81}$$

If we presuppose that the mirror and the defining slit screen have an infinitely high potential the wave function should then vanish on S_A and S_D except at the entrance slit

$$\Psi(\vec{r}, t) = \begin{cases} 0 & \text{for } \vec{r} \in S_D \wedge \vec{r} \in S_B \wedge \vec{r} \in S_C \\ 0 & \text{for } \vec{r} \in S_A \wedge b < y < a \\ e^{-i\omega_0 t} \Theta[t] & \text{for } \vec{r} \in S_A \wedge b > y > a \end{cases} \quad (\text{A.82})$$

where $\Theta[t]$ is the step function which is zero for $t \leq 0$. The step function will be in the following set to 1 as we restrict all calculation to $t > 0$.

Wave Function Construction By requiring that equation (A.36) satisfies the previous boundary equations we get

$$\begin{aligned} \Psi(\vec{r}, t) &= \frac{1}{4\pi} \frac{\hbar^2}{2m} \int_0^{t^+} dt' \oint_{\vec{S}} \Psi(\vec{r}', t') \nabla' G_{\mathcal{L}}(|\vec{r} - \vec{r}'|, |t - t'|) d\vec{S}' \\ &+ \frac{i\hbar}{4\pi} \int_V d^3r \Psi(\vec{r}', 0) G_{\mathcal{L}}(|\vec{r} - \vec{r}'|, |t - 0|). \end{aligned} \quad (\text{A.83})$$

Using Condition A.46 for $\Psi(\vec{r}, t)$ this reduces further to

$$\begin{aligned} \Psi(\vec{r}, t) &= \frac{1}{4\pi} \frac{\hbar^2}{2m} \int_0^{t^+} dt' \int_a^b dy' \int_{-\infty}^{\infty} dx' \left[\frac{\partial}{\partial z'} G_{\mathcal{L}}(|\vec{r} - \vec{r}'|, |t - t'|) \right]_{z'=0} \\ &+ \frac{i\hbar}{4\pi} \int_V d^3r \Psi(\vec{r}', 0) G_{\mathcal{L}}(|\vec{r} - \vec{r}'|, |t - 0|). \end{aligned} \quad (\text{A.84})$$

With equation (A.48) the derivative of $G_{\mathcal{L}}(\vec{r}, \vec{r}', t, t')$ in respect to z' gives

$$\begin{aligned} \left[\frac{\partial}{\partial z'} G_{\mathcal{L}}(|\vec{r} - \vec{r}'|, |t - t'|) \right]_{z'=0} &= 2 \frac{\partial}{\partial z} [G_0(|x - x'|, |y + y'|, |z|, |t - t'|)] \\ &- G_0(|x - x'|, |y - y'|, |z|, |t - t'|)]. \end{aligned} \quad (\text{A.85})$$

A. Supplemental Information

and get

$$\begin{aligned}\Psi_{\mathcal{L}}(\vec{r}, t) &= \frac{i\hbar}{2\pi} \underbrace{\int_V d^3r' \Psi(\vec{r}', 0) G_{\mathcal{L}}(|\vec{r} - \vec{r}'|, |t - 0|)}_{\hat{\Psi}_{\mathcal{L}, \text{Initial}}} \\ &\quad + \frac{\hbar^2}{4\pi m} \int_0^{t^+} dt' \int_a^b dy' \frac{\partial}{\partial z} \int_{-\infty}^{\infty} dx' [G_0(|x - x'|, |y - y'|, |z|, |t - t'|) \\ &\quad - G_0(|x - x'|, |y + y'|, |z|, |t - t'|)]\end{aligned}\tag{A.86}$$

$$= \hat{\Psi}_{\mathcal{L}, \text{Initial}} + \hat{\Psi}_{\mathcal{L}, \text{D}}.\tag{A.87}$$

First Summand — Initial Condition First we look at the term $\hat{\Psi}_{\mathcal{L}, \text{Initial}}$ which can be expressed by

$$\begin{aligned}\hat{\Psi}_{\mathcal{L}, \text{Initial}} &= \frac{i\hbar}{2\pi} \int_V d^3r' \Psi(\vec{r}', 0) G_{\mathcal{L}}(|\vec{r} - \vec{r}'|, |t - 0|) \\ &= \left(\frac{m}{2\pi i\hbar}\right)^{3/2} \frac{1}{4\pi} \frac{1}{t^{3/2}} \int_0^{\infty} dz' \int_0^{\infty} dy' \int_{-\infty}^{\infty} dx' \Psi(\vec{r}', 0) \\ &\quad \times \left\{ e^{i\frac{m}{2\hbar t}((x-x')^2 + (y-y')^2 + (z-z')^2)} - e^{i\frac{m}{2\hbar t}((x-x')^2 + (y+y')^2 + (z-z')^2)} \right. \\ &\quad \left. - e^{i\frac{m}{2\hbar t}((x-x')^2 + (y-y')^2 + (z+z')^2)} + e^{i\frac{m}{2\hbar t}((x-x')^2 + (y+y')^2 + (z+z')^2)} \right\}\end{aligned}\tag{A.89}$$

By separating the exponent and using equation (A.11)

$$\int_0^{\infty} e^{i\frac{m}{2\hbar} \frac{(\xi - \xi')^2}{t}} = \left(\frac{1}{2} + \frac{i}{2}\right) \sqrt{\frac{\pi\hbar}{m}} \left(1 + (1 - i)\mathcal{FC} \left[\sqrt{\frac{m}{\pi\hbar}}\xi\right] + (1 + i)\mathcal{FS} \left[\sqrt{\frac{m}{\pi\hbar}}\xi\right]\right)\tag{A.90}$$

and equation (A.7) this can be solved to be

$$\hat{\Psi}_{\mathcal{L},\text{Initial}} = \frac{1}{(2i)^{3/2}} \frac{1}{4\pi} (1+i) \left(\frac{1}{2} + \frac{i}{2} \right)^2 \quad (\text{A.91})$$

$$\begin{aligned} & \times \{ (1 + (1-i)\mathcal{F}\mathcal{C}_y + (1+i)\mathcal{F}\mathcal{S}_y) (1 + (1-i)\mathcal{F}\mathcal{C}_z + (1+i)\mathcal{F}\mathcal{S}_z) \\ & - (1 - (1-i)\mathcal{F}\mathcal{C}_y - (1+i)\mathcal{F}\mathcal{S}_y) (1 + (1-i)\mathcal{F}\mathcal{C}_z + (1+i)\mathcal{F}\mathcal{S}_z) \\ & - (1 + (1-i)\mathcal{F}\mathcal{C}_y + (1+i)\mathcal{F}\mathcal{S}_y) (1 - (1-i)\mathcal{F}\mathcal{C}_z - (1+i)\mathcal{F}\mathcal{S}_z) \\ & + (1 - (1-i)\mathcal{F}\mathcal{C}_y - (1+i)\mathcal{F}\mathcal{S}_y) (1 - (1-i)\mathcal{F}\mathcal{C}_z - (1+i)\mathcal{F}\mathcal{S}_z) \} \\ & = 2(1-i)\hbar \frac{\sqrt{\pi}}{\left(\frac{m}{\hbar t}\right)^{3/2}} (\mathcal{F}\mathcal{S}_y + i\mathcal{F}\mathcal{C}_y) (\mathcal{F}\mathcal{C}_z + i\mathcal{F}\mathcal{S}_z) \end{aligned} \quad (\text{A.92})$$

with $\mathcal{F}_\xi = \mathcal{F} \left[\sqrt{\frac{m}{\pi\hbar t}} \xi \right]$ and $\xi = \{y, z\}$.

Second Summand — Main Integration The second term $\hat{\Psi}_{\mathcal{L},\text{D}}$ can be expressed as

$$\begin{aligned} \hat{\Psi}_{\mathcal{L},\text{D}} &= -\chi \frac{i\hbar}{4\pi m} \left(\frac{m}{2\pi i\hbar} \right)^{3/2} \frac{\partial}{\partial z} \int_a^b dy' \int_0^{t^+} dt' \left(\frac{1}{t-t'} \right)^{3/2} \int_{-\infty}^{\infty} dx' \\ & \times \left(e^{i\frac{m}{2\hbar} \frac{(x-x')^2 + (y-y')^2 + z^2}{t-t'}} - e^{i\frac{m}{2\hbar} \frac{(x-x')^2 + (y+y')^2 + z^2}{t-t'}} \right) e^{-i\omega_0 t'}. \end{aligned} \quad (\text{A.93})$$

The x integration can be performed to be $\int_{-\infty}^{\infty} e^{i\frac{m}{2\hbar} \frac{(x-x')^2}{t-t'}} = (1+i) \sqrt{\frac{\pi}{2}} \sqrt{\frac{2\hbar(t-t')}{m}}$ and thus

$$\begin{aligned} \hat{\Psi}_{\mathcal{L},\text{D}} &= -\chi \frac{(1-i)}{(4\pi)^2} e^{-i\omega_0 t} \frac{\partial}{\partial z} \int_0^{t^+} dt' \frac{1}{t-t'} e^{i\omega_0(t-t')} \\ & \times \int_a^b dy' \left(e^{i\frac{m}{2\hbar} \frac{(y-y')^2 + z^2}{t-t'}} - e^{i\frac{m}{2\hbar} \frac{(y+y')^2 + z^2}{t-t'}} \right). \end{aligned} \quad (\text{A.94})$$

A. Supplemental Information

Integrating the term with $y - y'$ over y we get

$$\hat{\Psi}_{\mathcal{L},D}^- = -(-1)^{3/4} \chi \frac{(1-i)}{(4\pi)^2} \sqrt{\frac{\pi\hbar}{2m}} e^{-i\omega_0 t} \frac{\partial}{\partial z} \int_0^{t^+} dt' \frac{1}{t-t'} e^{i\omega_0(t-t')} e^{i\frac{m}{2\hbar} \frac{z^2}{t-t'}} \quad (\text{A.95})$$

$$\begin{aligned} & \times \sqrt{t-t'} \left(\text{Erfi} \left[\left(\frac{1}{2} + \frac{i}{2} \right) \sqrt{\frac{m}{\hbar}} \frac{a-y}{\sqrt{t-t'}} \right] - \text{Erfi} \left[\left(\frac{1}{2} + \frac{i}{2} \right) \sqrt{\frac{m}{\hbar}} \frac{b-y}{\sqrt{t-t'}} \right] \right) \\ & = -\frac{i\chi}{16\pi} \sqrt{\frac{\hbar}{\pi m}} e^{-i\omega_0 t} \frac{\partial}{\partial z} \int_0^{t^+} dt' \frac{1}{\sqrt{t-t'}} e^{i\omega_0(t-t')} e^{i\frac{m}{2\hbar} \frac{z^2}{t-t'}} \quad (\text{A.96}) \end{aligned}$$

$$\times \left(\text{Erfi} \left[\left(\frac{1}{2} + \frac{i}{2} \right) \sqrt{\frac{m}{\hbar}} \frac{a-y}{\sqrt{t-t'}} \right] - \text{Erfi} \left[\left(\frac{1}{2} + \frac{i}{2} \right) \sqrt{\frac{m}{\hbar}} \frac{b-y}{\sqrt{t-t'}} \right] \right).$$

Substituting $\xi = t - t'$, $d\xi = -dt'$, $\xi(0) = t$, and $\xi(t^+) = t - t^+$ which yields

$$\begin{aligned} \hat{\Psi}_{\mathcal{L},D}^- & = -\frac{i\chi}{16\pi} \sqrt{\frac{\hbar}{\pi m}} e^{-i\omega_0 t} \frac{\partial}{\partial z} \int_t^{t-t^+} d\xi \frac{1}{\sqrt{\xi}} e^{i\omega_0 \xi} e^{i\frac{m}{2\hbar} \frac{z^2}{\xi}} \\ & \times \left(\text{Erfi} \left[\left(\frac{1}{2} + \frac{i}{2} \right) \sqrt{\frac{m}{\hbar}} \frac{a-y}{\sqrt{\xi}} \right] - \text{Erfi} \left[\left(\frac{1}{2} + \frac{i}{2} \right) \sqrt{\frac{m}{\hbar}} \frac{b-y}{\sqrt{\xi}} \right] \right). \quad (\text{A.97}) \end{aligned}$$

In the limit of $t^+ \rightarrow t$, using the derivative in respect to z , and using $\omega = \frac{\hbar}{2m} k^2$ this becomes

$$\begin{aligned} \hat{\Psi}_{\mathcal{L},D}^- & = -\sqrt{\frac{m}{\pi\hbar}} \frac{z}{16\pi} e^{-i\omega_0 t} \int_0^t d\xi \frac{1}{\xi^{3/2}} e^{i\left(\frac{\hbar}{2m} k^2 \xi + \frac{m}{2\hbar} \frac{z^2}{\xi}\right)} \\ & \times \left(\text{Erfi} \left[\left(\frac{1}{2} + \frac{i}{2} \right) \sqrt{\frac{m}{\hbar}} \frac{a-y}{\sqrt{\xi}} \right] - \text{Erfi} \left[\left(\frac{1}{2} + \frac{i}{2} \right) \sqrt{\frac{m}{\hbar}} \frac{b-y}{\sqrt{\xi}} \right] \right) \quad (\text{A.98}) \end{aligned}$$

and the full solution is given as

$$\hat{\Psi}(t) = \hat{\Psi}_{\mathcal{L},\text{Initial}} + \hat{\Psi}_{\mathcal{L},D}^- - \hat{\Psi}_{\mathcal{L},D}^+. \quad (\text{A.99})$$

As $\hat{\Psi}_{\mathcal{L},\text{Initial}}$ is strongly suppressed⁴ in relation to $\hat{\Psi}_{\mathcal{L},D}^- - \hat{\Psi}_{\mathcal{L},D}^+$ and is dropped in future calculations.

⁴In the relevant parameter space for this experiment, this term is smaller by more than 50 orders of magnitude.

A.7.2.1. Time-Dependent — Time-Independent Transition

Using equation (A.93) we will now try to transition from the time-dependent case to the static case. The first question to answer is, does $\hat{\Psi}_{\mathcal{L},D}(t)$ settle if $t \rightarrow \infty$.

$$\begin{aligned} \hat{\Psi}_{\mathcal{L},D} &= -\chi \frac{i\hbar}{4\pi m} \left(\frac{m}{2\pi i\hbar} \right)^{3/2} \frac{\partial}{\partial z} \int_a^b dy' \int_{-\infty}^{\infty} dx' \\ &\quad \times \int_0^{t^+} dt' \left(\frac{1}{t-t'} \right)^{3/2} \left(e^{i\frac{m}{2\hbar} \frac{(\Delta x)^2 + (\Delta y)^2 + z^2}{t-t'}} - e^{i\frac{m}{2\hbar} \frac{\Delta x^2 + \Delta \hat{y}^2 + z^2}{t-t'}} \right) e^{-i\omega_0 t'} \end{aligned} \quad (\text{A.100})$$

with $\Delta x = x - x'$, $\Delta y = y - y'$, and $\Delta \hat{y} = y + y'$. Substituting while taking $t^+ \rightarrow t$ gives $\xi = t - t'$, $d\xi = -dt'$, $\xi(0) = t$, $\xi(t) = 0$, and thus

$$\begin{aligned} \hat{\Psi}_{\mathcal{L},D} &= \chi \frac{i\hbar}{4\pi m} \left(\frac{m}{2\pi i\hbar} \right)^{3/2} \frac{\partial}{\partial z} \int_a^b dy' \int_{-\infty}^{\infty} dx' e^{-i\omega_0 t} \\ &\quad \times \underbrace{\int_0^t d\xi \left(\frac{1}{\xi} \right)^{3/2} \left(e^{i\frac{m}{2\hbar} \frac{\Delta x^2 + \Delta y^2 + z^2}{\xi}} - e^{i\frac{m}{2\hbar} \frac{\Delta x^2 + \Delta \hat{y}^2 + z^2}{\xi}} \right) e^{i\omega_0 \xi}}_{\hat{\Psi}_\xi}. \end{aligned} \quad (\text{A.101})$$

Taking in addition the limit $t \rightarrow \infty$ of $\hat{\Psi}_\xi$ the integral becomes solvable and we get

$$\lim_{t \rightarrow \infty} \hat{\Psi}_\xi = \int_0^\infty d\xi \left(\frac{1}{\xi} \right)^{3/2} \left(e^{i\frac{m}{2\hbar} \frac{\Delta x^2 + \Delta y^2 + z^2}{\xi}} - e^{i\frac{m}{2\hbar} \frac{\Delta x^2 + \Delta \hat{y}^2 + z^2}{\xi}} \right) e^{i\omega_0 \xi} \quad (\text{A.102})$$

$$= (1+i) \sqrt{\frac{\hbar\pi}{m}} \left(\frac{e^{ik_0^2 \sqrt{\Delta x^2 + \Delta y^2 + z^2}}}{\sqrt{\Delta x^2 + \Delta y^2 + z^2}} - \frac{e^{ik_0^2 \sqrt{\Delta x^2 + \Delta \hat{y}^2 + z^2}}}{\sqrt{\Delta x^2 + \Delta \hat{y}^2 + z^2}} \right). \quad (\text{A.103})$$

A. Supplemental Information

Where $E = \hbar\omega_0 = \frac{\hbar}{2m}k_0^2$ is used to express the argument of the exponential. The full solution is given by

$$\begin{aligned} \lim_{t \rightarrow \infty} \hat{\Psi}_{\mathcal{L},D} &= \chi \frac{i\hbar}{4\pi m} \left(\frac{m}{2\pi i\hbar} \right)^{3/2} \lim_{t \rightarrow \infty} (e^{-i\omega_0 t}) \frac{\partial}{\partial z} \int_a^b dy' \int_{-\infty}^{\infty} dx' \\ &\times (1+i) \sqrt{\frac{\hbar\pi}{m}} \left(\frac{e^{ik_0^2 \sqrt{\Delta x^2 + \Delta y^2 + z^2}}}{\sqrt{\Delta x^2 + \Delta y^2 + z^2}} - \frac{e^{ik_0^2 \sqrt{\Delta x^2 + \Delta \hat{y}^2 + z^2}}}{\sqrt{\Delta x^2 + \Delta \hat{y}^2 + z^2}} \right) \end{aligned} \quad (\text{A.104})$$

$$\begin{aligned} &= \frac{\chi}{8\pi^2} \frac{\partial}{\partial z} \int_a^b dy' \int_{-\infty}^{\infty} dx' \\ &\times \left(\frac{e^{ik_0^2 \sqrt{\Delta x^2 + \Delta y^2 + z^2}}}{\sqrt{\Delta x^2 + \Delta y^2 + z^2}} - \frac{e^{ik_0^2 \sqrt{\Delta x^2 + \Delta \hat{y}^2 + z^2}}}{\sqrt{\Delta x^2 + \Delta \hat{y}^2 + z^2}} \right) \end{aligned} \quad (\text{A.105})$$

The term $\lim_{t \rightarrow \infty} (e^{-i\omega_0 t})$ is constant and can be joined in the normalization χ . The previous equation does indeed resemble the static case before spatial integration.

A.8. Calculation of the Phase Shifts in Lloyd's Mirror

In S. A. Werner (1994) the general formalism of quantum phase-shifts in a Mach-Zehnder type interferometer is used to calculate the phase shift for gravity, rotation and due to the topology in a perfect-silicon crystal neutron interferometer. The same formalism can be applied here as interference in Lloyd's mirror originates from the interference of two paths and thus is topological identical to a Mach-Zehnder type interferometer. Using this formalism the phase shift due to the Casimir–Polder interaction of the mirror coated with an electrical conducting material and the neutron is calculated.

A.8.1. General Phase Shift Calculation

Following S. A. Werner (1994) the phase shift $\varphi(\vec{r}, t)$ in a two-path interferometer in one path is given by the line integral in space-time as

$$\varphi(\vec{r}, t) = \frac{1}{\hbar} \int L dt' \quad (\text{A.106})$$

where $L = \vec{p} \cdot v - \hat{H}$ is the Lagrangian, \hat{H} the Hamiltonian of the system, \vec{p} the canonical momentum, and $\vec{v} = \frac{d\vec{s}}{dt}$ the classical group velocity.

The phase shift in both paths can be expressed as

$$\varphi_{I/II}(\vec{r}, t) = \frac{1}{\hbar} \int_{\vec{r}_0}^{\vec{r}} \vec{p}_{I/II} \cdot d\vec{s} - \frac{1}{\hbar} \int_{t_0}^t \hat{H}_{I/II} dt' \quad (\text{A.107})$$

The phase shift caused by a potential $U(\vec{r}, t)$ is given by the difference between the phase difference between an interferometer and the same interferometer without potential.

Thus, the phase shift is

$$\Delta\varphi_U = \varphi_I(\vec{r}, t) - \varphi_{II}(\vec{r}, t) - (\varphi_I(\vec{r}, t) - \varphi_{II}(\vec{r}, t))|_{U(\vec{r}, t)=0} \quad (\text{A.108})$$

$$\begin{aligned} &= \frac{1}{\hbar} \int_{\vec{r}_0}^{\vec{r}} \Delta\vec{p}_I \cdot d\vec{s} - \frac{1}{\hbar} \int_{t_0}^t \Delta\hat{H}_I dt' \\ &\quad - \frac{1}{\hbar} \int_{\vec{r}_0}^{\vec{r}} \Delta\vec{p}_{II} \cdot d\vec{s} + \frac{1}{\hbar} \int_{t_0}^t \Delta\hat{H}_{II} dt' \end{aligned} \quad (\text{A.109})$$

If the Hamiltonian \hat{H} is time-independent the time integration drops out and the phase shift due to the potential becomes the integral along the interferometer path through the potential region $\mathcal{R}(U)$

$$\Delta\varphi_U = \frac{1}{\hbar} \int_{\mathcal{R}(U)} \Delta\vec{p} \cdot d\vec{s} \quad (\text{A.110})$$

with the change of the kinetic momentum $\Delta\vec{p}$ in $\mathcal{R}(U)$.

A.8.2. Phase Shift due to the Casimir-Effect

Gebhart, Klatt and Buhmann (2016) propose a Casimir–Polder potential for a neutron in front of an electrical perfect conducting surface due to its magnetic moment. The proposed potential is

$$U_{\text{Casimir, PF}} = \frac{\hbar^2}{64\pi y^3} \gamma^2 \mu_0 \quad (\text{A.111})$$

$$= \xi_C \frac{1}{y^3} = \xi_C \mathcal{V}(y) \quad (\text{A.112})$$

A. Supplemental Information

with $\gamma = g_n e_0 / (2m)$, $\xi_C = \hbar^2 \gamma^2 \mu_0 / (64\pi)$, and the g-factor of the neutron g_n . An alternative to this potential the so called plasma model is given in the same publication but will not further discuss as justified in section 5.6.3.5.

The geometry of the problem is shown in figure A.20 where the Casimir–Polder potential expands from the mirror in the region transversed by the neutrons.

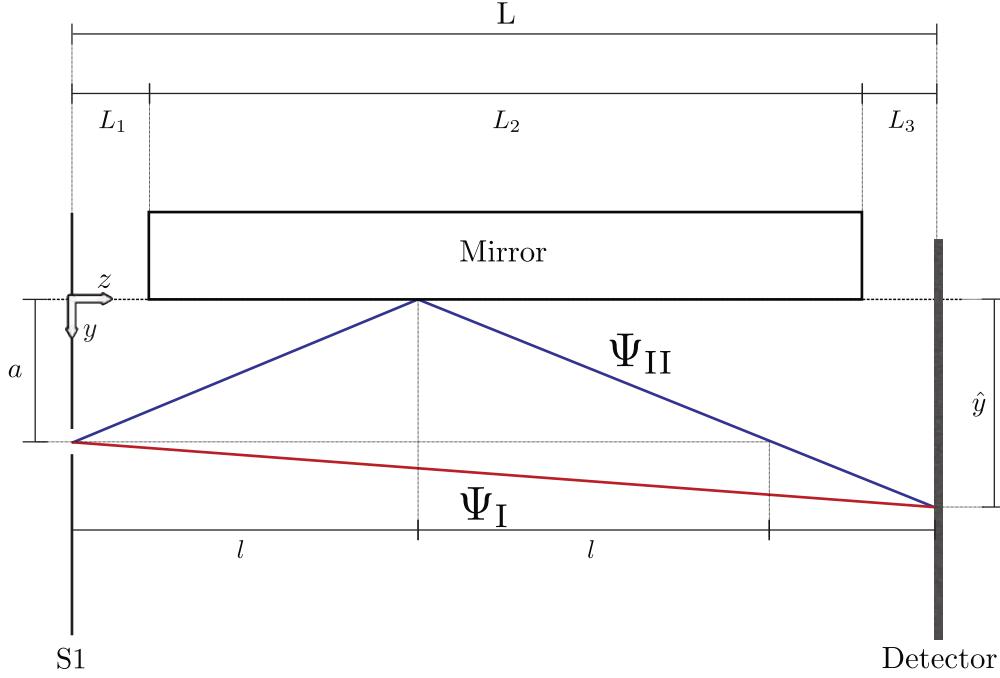


Figure A.20.: Definition of relevant quantities that are used for the calculation of phase shifts in Lloyd’s mirror as proposed in Ivanov (2016, priv. comm.).

As stated in appendix A.8.1 and following an analog calculation for the chameleon potential in Ivanov (2016, priv. comm.), the phase shift in Lloyd’s mirror due to the Casimir–Polder potential and the geometry is given by the closed line integral along the beam path. With $\vec{p} = \hbar \vec{k}$ and using Stokes integral theorem as given in Lang and Pucker (2016) equation (A.110) can be expressed as

$$\Delta\varphi_{\text{Casimir}} = \oint_{\text{I+II}} \vec{q}(\vec{r}) \cdot d\vec{r} = \iint_A \vec{n} \cdot (\nabla \times \vec{q}(\vec{r})) dA \quad (\text{A.113})$$

$$= \iint_{\mathcal{R}(U)} dz dy \left(\frac{\partial q_y(\vec{r})}{\partial z} - \frac{\partial q_z(\vec{r})}{\partial y} \right) \Big|_{x=0} \quad (\text{A.114})$$

where \vec{n} is the normal vector of area \mathcal{A} which is enclosed by path I and II. Due to energy conservation the momentum \vec{q} in the region of the potential $\mathcal{R}(U)$ is connected to the free-momentum \vec{k} by

$$\vec{k}^2 = \vec{q}^2 + \frac{2m}{\hbar^2} U_{\text{Casimir}}(\vec{r}). \quad (\text{A.115})$$

By rearranging for $|\vec{q}|$ and Taylor-expand around $U(\vec{r}) = 0$ one gets

$$|\vec{q}| = \sqrt{k^2 - \frac{2m}{\hbar^2} U_{\text{Casimir}}} = |\vec{k}| - \frac{m U_{\text{Casimir}}}{\hbar^2 |\vec{k}|} - \frac{m^2 U_{\text{Casimir}}^2}{2\hbar^4 |\vec{k}|^3} + \mathcal{O}(U_{\text{Casimir}}^3) \quad (\text{A.116})$$

$$\approx |\vec{k}| - \frac{m}{\hbar^2 |\vec{k}|} U_{\text{Casimir}} \quad (\text{A.117})$$

where terms of order $\mathcal{O}(U_{\text{Casimir}}^2)$ and higher can be neglected for $(\hbar \vec{k})^2 \gg m U_{\text{Casimir}}/2$. The change in kinetic momentum is then given by

$$\Delta q_x = 0 \quad (\text{A.118})$$

$$\Delta q_y = -\frac{m}{\hbar^2 |\vec{k}|} U_{\text{Casimir}}(y) \frac{k_y}{|\vec{k}|} \quad (\text{A.119})$$

$$\Delta q_z = -\frac{m}{\hbar^2 |\vec{k}|} U_{\text{Casimir}}(y) \frac{k_z}{|\vec{k}|} \quad (\text{A.120})$$

where the term $\frac{k_i}{|\vec{k}|}$ states the relative magnitude of the component and Δq_x as the potential cannot produce a change in momentum in x -dimension.

Thus, and by restricting the problem to the yz -plane equation (A.114) becomes

$$\Delta \varphi_{\text{Casimir}} = \iint_{\mathcal{R}(U)} dz dy \left(\frac{\partial q_y(\vec{r})}{\partial z} - \frac{\partial q_z(\vec{r})}{\partial y} \right) \Big|_{x=0} \quad (\text{A.121})$$

$$= -\frac{m}{\hbar^2 |\vec{k}|} \iint_{\mathcal{R}(U)} dz dy \underbrace{\left(\frac{\partial}{\partial z} U_{\text{Casimir}}(y) \frac{k_y}{|\vec{k}|} \right)}_{=0} \Big|_{x=0} \quad (\text{A.122})$$

$$+ \frac{m}{\hbar^2 |\vec{k}|} \iint_{\mathcal{R}(U)} dz dy \left(\frac{\partial}{\partial y} U_{\text{Casimir}}(y) \frac{k_z}{|\vec{k}|} \right) \Big|_{x=0} \\ = \frac{m}{\hbar^2 |\vec{k}|} \xi_C \iint_{\mathcal{R}(U)} dz dy \left(\frac{\partial \mathcal{V}(y)}{\partial y} \frac{k_z}{|\vec{k}|} \right) \Big|_{x=0} \quad (\text{A.123})$$

A. Supplemental Information

By canceling the y -derivative with the corresponding integral and evaluate the result at path I or path II and using equation (A.124) the previous equation becomes

$$\Delta\varphi_{\text{Casimir}} = \frac{m}{\hbar^2 k} \xi_C \int_0^L dz \left(\mathcal{V}(y) \frac{k_z}{k} \Big|_{\text{I}} - \mathcal{V}(y) \frac{k_z}{k} \Big|_{\text{II}} \right). \quad (\text{A.124})$$

where $k_z = k \cos(\alpha)$. To evaluate the integral one follows the contour of the area $\mathcal{R}(U)$ enclosed by the two interfering paths as shown in figure A.21.

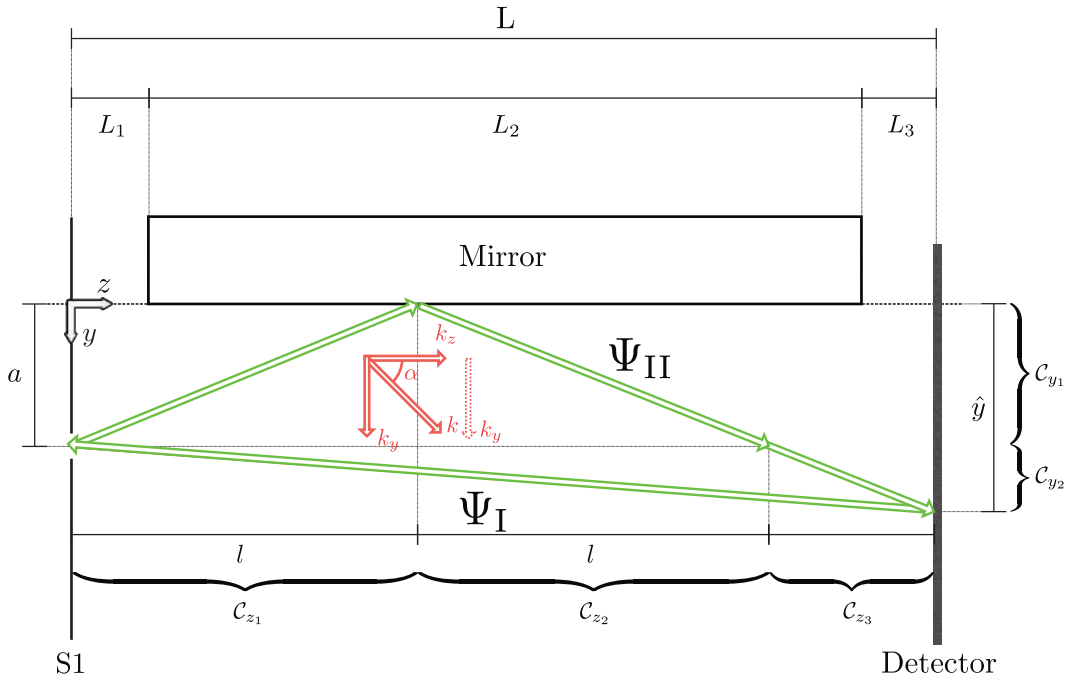


Figure A.21.: Contour that is used for the calculation of phase shifts in Lloyd's mirror as proposed in Ivanov (2016, priv. comm.).

In the enclosed area the integration along the mirror direction can be split in three parts. The parametrization for beam path I is

$$\left. \begin{aligned} y(z) &= a + \frac{\hat{y}-a}{L} z \\ dz &= \frac{L}{\hat{y}-a} dy \\ \cos(\alpha) &= \frac{L}{\sqrt{L^2 + (\hat{y}-a)^2}} \end{aligned} \right\} C_{z1} \ \& \ C_{z2} \ \& \ C_{z3} \quad (\text{A.125})$$

and for beam path II is

$$\left. \begin{aligned}
y(z) &= a - \frac{a+\hat{y}}{L}z \\
dz &= -\frac{L}{a+\hat{y}}dy \\
\cos(\alpha) &= \frac{L}{\sqrt{L^2+(\hat{y}+a)^2}}
\end{aligned} \right\} \mathcal{C}_{z1}$$

$$\left. \begin{aligned}
y(z) &= -a + \frac{a+\hat{y}}{L}z \\
dz &= \frac{L}{a+\hat{y}}dy \\
\cos(\alpha) &= \frac{L}{\sqrt{L^2+(\hat{y}+a)^2}}
\end{aligned} \right\} \mathcal{C}_{z2} \ \& \ \mathcal{C}_{z3}$$
(A.126)

and one yields for \mathcal{C}_{z1} , \mathcal{C}_{z2} and \mathcal{C}_{z3}

$$\frac{\hbar^2 k \Delta \varphi_{\text{Casimir}}}{m \xi_{\text{C}}} = \int_0^L dz \left(\mathcal{V}(y) \frac{k_z}{k} \Big|_{\text{I}} - \mathcal{V}(y) \frac{k_z}{k} \Big|_{\text{II}} \right) \quad (\text{A.127})$$

$$= \int_0^l dz \left(\mathcal{V}(y) \frac{k_z}{k} \Big|_{\text{I}} - \mathcal{V}(y) \frac{k_z}{k} \Big|_{\text{II}} \right) + \int_l^{2l} dz \left(\mathcal{V}(y) \frac{k_z}{k} \Big|_{\text{I}} - \mathcal{V}(y) \frac{k_z}{k} \Big|_{\text{II}} \right)$$

$$+ \int_{2l}^L dz \left(\mathcal{V}(y) \frac{k_z}{k} \Big|_{\text{I}} - \mathcal{V}(y) \frac{k_z}{k} \Big|_{\text{II}} \right) \quad (\text{A.128})$$

$$= \int_a^{a+\frac{\hat{y}-a}{L}l} dy \frac{L}{a-\hat{y}} \cos \alpha_{\text{I}} \mathcal{V}(y) + \int_a^{a-\frac{a+\hat{y}}{L}l} dy \frac{L}{a+\hat{y}} \cos \alpha_{\text{II}} \mathcal{V}(y) \quad (\text{A.129})$$

$$\int_{a-\frac{\hat{y}-a}{L}2l}^{a+\frac{\hat{y}-a}{L}2l} dy \frac{L}{a-\hat{y}} \cos \alpha_{\text{I}} \mathcal{V}(y) - \int_{-a+\frac{a+\hat{y}}{L}2l}^{-a+\frac{a+\hat{y}}{L}l} dy \frac{L}{a+\hat{y}} \cos \alpha_{\text{II}} \mathcal{V}(y) \quad (\text{A.130})$$

$$\int_{a+\frac{\hat{y}-a}{L}2l}^{\hat{y}} dy \frac{L}{a-\hat{y}} \cos \alpha_{\text{I}} \mathcal{V}(y) - \int_{-a+\frac{a+\hat{y}}{L}2l}^{\hat{y}} dy \frac{L}{a+\hat{y}} \cos \alpha_{\text{II}} \mathcal{V}(y). \quad (\text{A.131})$$

A. Supplemental Information

Connecting the integrands of Term A.129, Term A.130 and in Term A.131 and reformulated by using $l = La/(\hat{y} + a)$ yields

$$\begin{aligned} \frac{\hbar^2 k \Delta\varphi_{\text{Casimir}}}{m\xi_C} &= \int_a^{\hat{y}} dy \frac{L}{a - \hat{y}} \cos \alpha_I \mathcal{V}(y) + \int_a^{a - \frac{a + \hat{y}}{L} l} dy \frac{L}{a + \hat{y}} \cos \alpha_{II} \mathcal{V}(y) \\ &\quad - \int_{-a + \frac{a + \hat{y}}{L} l}^{\hat{y}} dy \frac{L}{a + \hat{y}} \cos \alpha_{II} \mathcal{V}(y) \end{aligned} \quad (\text{A.132})$$

$$\begin{aligned} &= \frac{\cos \alpha_I L}{a - \hat{y}} \int_a^{\hat{y}} dy \mathcal{V}(y) + \frac{\cos \alpha_{II} L}{a + \hat{y}} \int_a^0 dy \mathcal{V}(y) \\ &\quad - \frac{\cos \alpha_{II} L}{\hat{y} + a} \int_0^{\hat{y}} dy \mathcal{V}(y) \end{aligned} \quad (\text{A.133})$$

$$= \frac{\cos \alpha_I L}{\hat{y} - a} \int_a^{\hat{y}} dy \mathcal{V}(y) - \frac{\cos \alpha_{II} L}{\hat{y} + a} \left(\int_{y_{\min}}^a dy \mathcal{V}(y) + \int_{y_{\min}}^{\hat{y}} dy \mathcal{V}(y) \right). \quad (\text{A.134})$$

As the idealized potential diverges for $y = 0$, the lower integration limit has to be set at a small distance y_{\min} from the mirror. Then the integral can be solved as

$$\int_{y_-}^{y_+} \mathcal{V}(y) dy = \frac{1}{2} \left(\frac{1}{y_-^2} - \frac{1}{y_+^2} \right) \quad (\text{A.135})$$

and equation (A.134) becomes

$$\Delta\varphi_{\text{Casimir}} = L^2 \frac{m\xi_C}{\hbar^2 k} \left(\frac{a + \hat{y}}{a^2 \hat{y}^2 \sqrt{L^2 + (\hat{y} - a)^2}} - \frac{2 \frac{1}{y_{\min}^2} + \frac{1}{a^2} - \frac{1}{\hat{y}^2}}{(\hat{y} + a) \sqrt{L^2 + (a + \hat{y})^2}} \right). \quad (\text{A.136})$$

For $L \gg (a - \hat{y})$ and $L \gg (a + \hat{y})$ this can be simplified to

$$\Delta\varphi_{\text{Casimir}} = \frac{m\gamma^2 \mu_0 L}{128\pi k} \left(\frac{a^3 + \hat{y}^3}{a^2 \hat{y}^2 (a^2 + \hat{y}^2)} - \frac{1}{(\hat{y} + a) y_{\min}^2} \right). \quad (\text{A.137})$$

A.8.3. Phase Shift due to a Magnetic Field

In Helmut Rauch and Samuel A. Werner (2015) the potential energy of a neutron in an magnetic field \vec{B} is stated as

$$U_{\text{Mag}} = -\vec{\mu} \cdot \vec{B}(\vec{r}) \quad (\text{A.138})$$

with $\vec{\mu} = \vec{\sigma}\mu_n$, $\vec{\sigma}$ the Pauli matrices, and μ_n the magnetic moment of the neutron. Note that the phase shift due to an magnetic field in a two beam neutron interferometer as given in Helmut Rauch and Samuel A. Werner (2015) and presented in H. Rauch, Zeilinger et al. (1975) does describe a situation where the field acts only in one beam path. As the magnetic field is present in both paths in Lloyd's Mirror the previously sketched formalism is used to derive the phase shift due to a magnetic field.

Following the same argument as made in appendix A.8.2 the momentum can be expressed as

$$|\vec{q}| \approx |\vec{k}| - \frac{m}{\hbar^2 |\vec{k}|} U_{\text{Mag}} \quad (\text{A.139})$$

where terms of order $\mathcal{O}(U_{\text{Mag}}^2)$ and higher are neglected.

For $\frac{\partial}{\partial z}\vec{B} \neq 0 \vee \frac{\partial}{\partial y}\vec{B} \neq 0$: By construction, the interferometer area that is encompassed by the two beam paths is perpendicular to the x -dimension. Thus, the phase shift calculation is restricted to the yz -plane and the geometry is shown in figure A.21. By using equation (A.138) the equation (A.114) becomes

$$\Delta\varphi_{\text{Mag}} = \iint_{\mathcal{R}(U)} dzdy \left(\frac{\partial q_y(\vec{r})}{\partial z} - \frac{\partial q_z(\vec{r})}{\partial y} \right) \Big|_{x=0} \quad (\text{A.140})$$

$$\begin{aligned} &= -\frac{m}{\hbar^2 |\vec{k}|} \iint_{\mathcal{R}(U)} dzdy \left(\frac{\partial}{\partial z} U_{\text{Mag}} \frac{k_y}{|\vec{k}|} \right) \Big|_{x=0} \\ &\quad + \frac{m}{\hbar^2 |\vec{k}|} \iint_{\mathcal{R}(U)} dzdy \left(\frac{\partial}{\partial y} U_{\text{Mag}} \frac{k_z}{|\vec{k}|} \right) \Big|_{x=0} \end{aligned} \quad (\text{A.141})$$

Testing different magnetic fields in equation (A.141) it is clear for which fields a phase shift can be expect in this configuration. A phase shift is expected if

$$\Delta\varphi_{\text{Mag}} \begin{cases} = 0 & \text{for } \frac{\partial}{\partial z} U_{\text{Mag}} = 0 \wedge \frac{\partial}{\partial y} U_{\text{Mag}} = 0 \\ \neq 0 & \text{for } \frac{\partial}{\partial z} U_{\text{Mag}} \neq 0 \vee \frac{\partial}{\partial y} U_{\text{Mag}} \neq 0. \end{cases} \quad (\text{A.142})$$

A. Supplemental Information

This situation is analog to the case of gravity where no phase shift is expected if the beam path plane is perpendicular to gravitation. Only if a small angle between gravity and the x -dimension is present a phase shift is non-zero as shown in section 5.6.3.2. Further, if components of the setup are magnetic or neighboring experiments produce stray fields non-negligible inhomogeneous fields could be present.

It is assumed that indeed an inhomogeneous magnetic field

$$\vec{B} = \begin{pmatrix} B_x(y) \\ 0 \\ 0 \end{pmatrix} \quad (\text{A.143})$$

is present. The potential energy is given as

$$U_{\text{Mag},\pm} = \mp \mu_n B_x(y). \quad (\text{A.144})$$

The phase shift is then given by equation (A.113)

$$\Delta\varphi_{\text{Mag},\pm} = \iint_{\mathcal{R}(U)} dzdy \left(\frac{\partial q_y(\vec{r})}{\partial z} - \frac{\partial q_z(\vec{r})}{\partial y} \right) \Big|_{x=0} \quad (\text{A.145})$$

$$\begin{aligned} &= -\frac{m}{\hbar^2|\vec{k}|} \iint_{\mathcal{R}(U)} dzdy \underbrace{\left(\frac{\partial}{\partial z} U_{\text{Mag},\pm}(y) \frac{k_y}{|\vec{k}|} \right)}_{=0} \Big|_{x=0} \\ &+ \frac{m}{\hbar^2|\vec{k}|} \iint_{\mathcal{R}(U)} dzdy \left(\frac{\partial}{\partial y} U_{\text{Mag},\pm}(y) \frac{k_z}{|\vec{k}|} \right) \Big|_{x=0} \end{aligned} \quad (\text{A.146})$$

$$= \frac{m}{\hbar^2|\vec{k}|} \iint_{\mathcal{R}(U)} dzdy \left(\frac{\partial}{\partial y} U_{\text{Mag},\pm}(y) \frac{k_z}{|\vec{k}|} \right) \Big|_{x=0} \quad (\text{A.147})$$

The derivative in respect to y can be canceled using the corresponding integral and the previous equation becomes

$$\Delta\varphi_{\text{Mag},\pm} = \mp \frac{m\mu_n}{\hbar^2k} \int_{I,II} dz \left(\mu_n B_x(y) \frac{k_z}{k} \Big|_I - \mu_n B_x(y) \frac{k_z}{k} \Big|_{II} \right). \quad (\text{A.148})$$

Using the same parametrization as in appendix A.8.2 gives

$$\begin{aligned}
-\frac{\hbar^2 k \Delta\varphi_{\text{Mag},+}}{m\mu_n} &= \int_0^l dz \left(B_x(y) \frac{k_z}{k} \Big|_{\text{I}} - B_x(y) \frac{k_z}{k} \Big|_{\text{II}} \right) + \int_l^{2l} dz \left(B_x(y) \frac{k_z}{k} \Big|_{\text{I}} - B_x(y) \frac{k_z}{k} \Big|_{\text{II}} \right) \\
&\quad + \int_{2l}^L dz \left(B_x(y) \frac{k_z}{k} \Big|_{\text{I}} - B_x(y) \frac{k_z}{k} \Big|_{\text{II}} \right). \tag{A.149}
\end{aligned}$$

Jumping directly to the result as it is derived in appendix A.8.2 and by exchanging the the Casimir potential energy by the magnetic potential energy gives

$$-\frac{\hbar^2 k \Delta\varphi_{\text{Mag},+}}{m\mu_n} = \frac{\cos \alpha_{\text{I}} L}{\hat{y} - a} \int_a^{\hat{y}} dy B_x(y) - \frac{\cos \alpha_{\text{II}} L}{\hat{y} + a} \left(\int_0^a dy B_x(y) + \int_0^{\hat{y}} dy B_x(y) \right). \tag{A.150}$$

Assuming $B_x(y) = B_0 + by$ and dropping the constant B_0 gives

$$\Delta\varphi_{\text{Mag},\pm} = \mp \frac{m\mu_n}{\hbar^2 k} \left(\frac{y^2 - a^2}{a^2 y^2 \sqrt{L^2 + (y - a)^2}} + \frac{a^2 + y^2}{(y + a) \sqrt{L^2 + (a + y)^2}} \right). \tag{A.151}$$

For $L \gg (a - y)$ and $L \gg (a + y)$ this can be simplified to

$$\Delta\varphi_{\text{Mag},\pm} = \mp \frac{m}{\hbar^2 k} \mu_n b \frac{ayL}{a + y} \tag{A.152}$$

which features the same structure as the gravitational phase shift discussed in section 5.6.3.2.

For $\frac{\partial}{\partial x} \vec{B} \neq 0$: If a magnetic field changes only in x -direction the potential energy is given as

$$U_{\text{Mag},\pm} = \mp \mu_n B(x) \tag{A.153}$$

and the change in kinetic momentum for each component n is given by

$$\Delta q_{n,\pm} = \mp \frac{m}{\hbar^2 |\vec{k}|} \mu_n B(x) \frac{k_n}{|\vec{k}|}. \tag{A.154}$$

As in the last paragraph the situation is analog to gravity acting in the interferometer. If the area enclosed by path I and path II is oriented perpendicular to gravity no phase shift is expected. Indeed we see that $\Delta\varphi_{\text{Mag}} = 0$ if the yz -plane is chosen. Still, the gradient

A. Supplemental Information

should have an effect due to the slight deflection L_x of the neutron in the gradient field which is analog to the vertical drop due to gravity as discussed in section 5.6.3.2. The general phase shift is specified by equation (A.113) and the xy -plane is used for the calculation. The geometry is shown in figure A.22. This gives

$$\Delta\varphi_{\text{Mag,Vert},\pm} = \iint_{\mathcal{R}(U)} dx dy \left(\frac{\partial q_y(\vec{r})}{\partial x} - \frac{\partial q_x(\vec{r})}{\partial y} \right) \Big|_{z=0} \quad (\text{A.155})$$

$$= -\frac{m}{\hbar^2 |\vec{k}|} \iint_{\mathcal{R}(U)} dx dy \left(\frac{\partial}{\partial x} U_{\text{Mag}}(x) \frac{k_y}{|\vec{k}|} \right) \Big|_{x=0} \\ + \frac{m}{\hbar^2 |\vec{k}|} \iint_{\mathcal{R}(U)} dx dy \underbrace{\left(\frac{\partial}{\partial y} U_{\text{Mag}}(x) \frac{k_x}{|\vec{k}|} \right)}_{=0} \Big|_{x=0} \quad (\text{A.156})$$

$$= -\frac{m}{\hbar^2 |\vec{k}|} \iint_{\mathcal{R}(U)} dx dy \left(\frac{\partial}{\partial x} U_{\text{Mag}}(x) \frac{k_y}{|\vec{k}|} \right) \Big|_{x=0} \quad (\text{A.157})$$

By canceling the x -derivative with the corresponding integral, evaluating the result at path I or path II, and by using equation (A.124) the previous equation becomes

$$\Delta\varphi_{\text{Mag,Vert},\pm} = \mp \frac{m}{\hbar^2 k} \int_{I,II} dy \left(\mu_n B_x(x) \frac{k_y}{k} \Big|_I - \mu_n B_x(x) \frac{k_y}{k} \Big|_{II} \right). \quad (\text{A.158})$$

where $k_y = k \cos(\alpha)$. To evaluate the integral one follows the contour of the area $\mathcal{R}(U)$ enclosed by the two interfering paths as shown in figure A.22. In contrast to figure A.21, figure A.22 shows a view of the setup from the direction of the beam port.

In the enclosed area the integration along the mirror direction can be split in several regions. The parametrization for beam path I is

$$\left. \begin{aligned} x(y) &= \frac{L_x}{a-\hat{y}}(y-a) \\ dy &= \frac{a-\hat{y}}{L_x} dx \\ \cos(\alpha) &= \frac{L_x}{\sqrt{L_x^2 + (\hat{y}-a)^2}} \end{aligned} \right\} \mathcal{C}_{z1} \ \& \ \mathcal{C}_{z2} \ \& \ \mathcal{C}_{z3} \quad (\text{A.159})$$

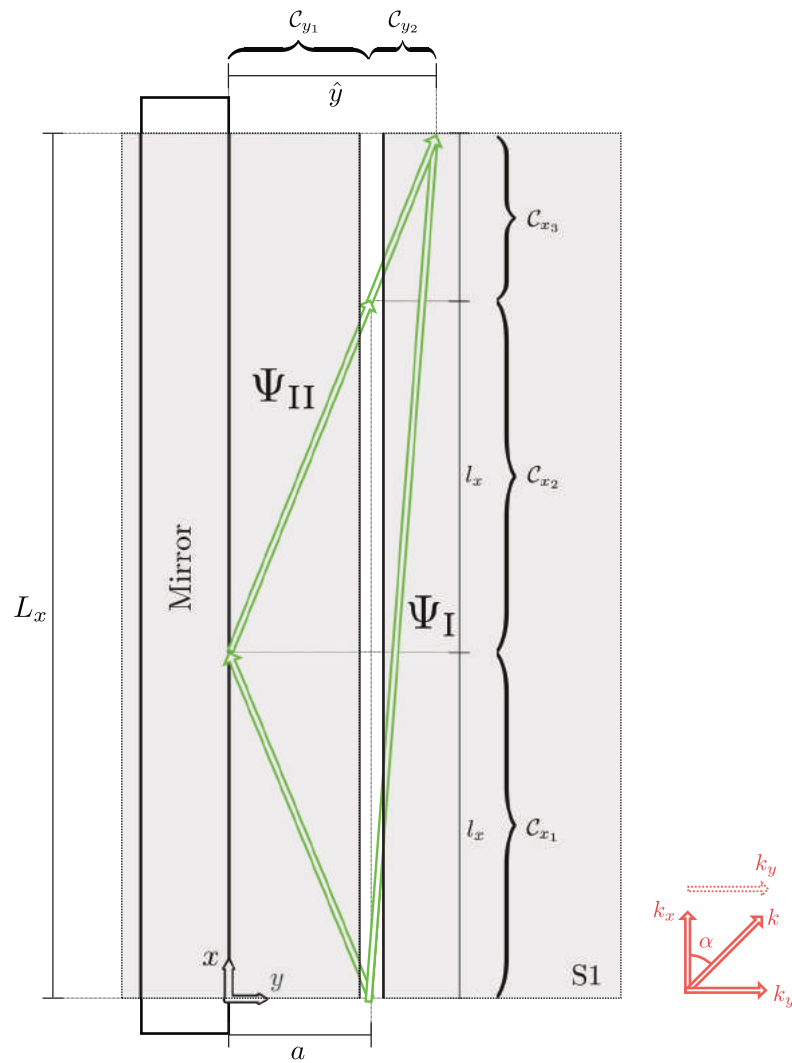


Figure A.22.: The integration contour that is used for the calculation of phase shifts in Lloyd's mirror for a magnetic field varying parallel to gravity.

A. Supplemental Information

and for beam path II is

$$\left. \begin{aligned} x(y) &= \frac{L_x}{\hat{y}+a}(a-y) \\ dy &= -\frac{a+\hat{y}}{L_x}dx \\ \cos(\alpha) &= \frac{L_x}{\sqrt{L_x^2+(\hat{y}+a)^2}} \end{aligned} \right\} \mathcal{C}_{z1}$$

$$\left. \begin{aligned} x(y) &= \frac{L_x}{a+\hat{y}}(a+y) \\ dy &= \frac{a+\hat{y}}{L_x}dx \\ \cos(\alpha) &= \frac{L_x}{\sqrt{L_x^2+(\hat{y}+a)^2}} \end{aligned} \right\} \mathcal{C}_{z2} \& \mathcal{C}_{z3}$$
(A.160)

For \mathcal{C}_{z1} , \mathcal{C}_{z2} and \mathcal{C}_{z3} one yields

$$\frac{\hbar^2 k \Delta \varphi_{\text{Mag,-}}}{m \mu_n} = \int_0^{\hat{y}} dy \left(B_x(x) \frac{k_y}{k} \Big|_{\text{I}} - B_x(x) \frac{k_y}{k} \Big|_{\text{II}} \right) \quad (\text{A.161})$$

$$= \int_0^a dy \left(B_x(x) \frac{k_y}{k} \Big|_{\text{I}} - B_x(x) \frac{k_y}{k} \Big|_{\text{II}} \right) + \int_a^{\hat{y}} dy \left(B_x(x) \frac{k_y}{k} \Big|_{\text{I}} - B_x(x) \frac{k_y}{k} \Big|_{\text{II}} \right) \quad (\text{A.162})$$

$$= - \int_{\frac{L_x a}{a+\hat{y}}}^{\frac{2L_x a}{a+\hat{y}}} dx \frac{a+\hat{y}}{L_x} \cos \alpha_{\text{II}} B_x(x) + \int_{\frac{L_x a}{a+\hat{y}}}^0 dx \frac{a+\hat{y}}{L_x} \cos \alpha_{\text{II}} B_x(x) \quad (\text{A.163})$$

$$\int_0^{L_x} dx \frac{a-\hat{y}}{L_x} \cos \alpha_{\text{I}} B_x(x) - \int_{\frac{2L_x a}{\hat{y}+a}}^{L_x} dx \frac{a+\hat{y}}{L_x} \cos \alpha_{\text{II}} B_x(x) \quad (\text{A.164})$$

The integration over path II in Term A.163 and the Term A.164 can be connected

$$\frac{\hbar^2 k \Delta \varphi_{\text{Mag,-}}}{m \mu_n} = \int_0^{L_x} dx \frac{a-\hat{y}}{L_x} \cos \alpha_{\text{I}} B_x(x) - \int_0^{L_x} dx \frac{a+\hat{y}}{L_x} \cos \alpha_{\text{II}} B_x(x) \quad (\text{A.165})$$

$$= \left(\frac{a-\hat{y}}{L_x} \cos \alpha_{\text{I}} - \frac{a+\hat{y}}{L_x} \cos \alpha_{\text{II}} \right) \int_0^{L_x} dx B_x(x) \quad (\text{A.166})$$

$$= \underbrace{\left(\frac{a-\hat{y}}{\sqrt{L_x^2+(\hat{y}-a)^2}} - \frac{a+\hat{y}}{\sqrt{L_x^2+(\hat{y}+a)^2}} \right)}_{\Delta I/\text{II}} \int_0^{L_x} dx B_x(x). \quad (\text{A.167})$$

$\Delta I/II$ is just the path difference between path I and path II. Assuming that the magnetic field has a linear gradient of the form $B(x) = B_0 + bx$ the integral can be solved. Note that the constant part B_0 would have dropped out in equation (A.157) and is thus not further considered for the phase shift. The integral can be solved as

$$\int_0^{L_x} B(x)dx = B_0L_x + \frac{1}{2}bL_x^2 \quad (\text{A.168})$$

and equation (A.167) becomes

$$\Delta\varphi_{\text{Mag},\pm} = \mp \frac{m\mu_n bL_x^2}{\hbar^2k} \frac{1}{2} \left(\frac{a - \hat{y}}{\sqrt{L_x^2 + (\hat{y} - a)^2}} - \frac{a + \hat{y}}{\sqrt{L_x^2 + (\hat{y} + a)^2}} \right). \quad (\text{A.169})$$

This phase shift is very small and can be neglected in all future considerations.

B. Thesis Information

B.1. Developed Software

— **CR39Analyse**

Mathematica package which handles datasets of scanned CR39 detectors. Images which are taken with an optical microscope are scanned for possible nuclear tracks. Tracks which are due to the nuclear reaction of neutrons in a converting boron layer are identified using a random forrest algorithm. The package handles image and data stitching to cover big area detectors and rudimentary analysis. After identifying possible tracks each track will get a dataset unique identifier. Results are saved in a rudimentary database format using the FileIO package.

— **LloydMonteCarlo**

Mathematica package to simulate the interference pattern of Lloyd's mirror considering several systematic effects. The probability density is calculated for the chosen model, beam characteristics are considered as for example the wavelength distribution, and from the resulting distribution a CR39 detector is simulated using MonteCarlo rejection drawing.

— **FileIO**

Mathematica package that implements a rudimentary database for config files and tracks files which are produced by the CR39Analyse package.

— **NeutronsAndMatter**

Mathematica package which calculates neutron absorption and scattering through matter for elements, molecules, and compounds.

— **BiDimAnalysis**

Mathematica package which interprets the raw data from the Bidim26 detection system. This includes ROIs and ToF spectra.

— **KurAnalysis**

Mathematica package which interprets the plain text files captured by the Kurri on-line detection system.

— **BeamTimeSupport**

Mathematica package which handles measurement metadata, complex measurement procedures, and automatically builds a measurement database.

B.2. Supervised Theses

— **Matthias Heumesser**

Diploma Thesis, *Kollimationssystem für ein Lloyd-Materiewellen-Interferometer*, 2016

— **Martin Mock**

Bachelor Thesis, *Aufbau und Erweiterung eines Vakuumsystems zur Erzeugung hoher elektrischer Felder für das q-Bounce Experiment*, 2016

— **Dominik Blöch**

Project Thesis, *Realisierung und Analyse eines Temperatursensor-Arrays für das Lloyd-Experiment*, 2016

— **Patrick Kappl**

Bachelor Thesis, *Vorbereitung einer Strahlzeit für ein Lloyd-Interferometer mit sehr kalten Neutronen*, 2015

— **Andreas Scheicher**

Project Thesis, *Transmissions Optimierung und ^3He basierte Detektion von sehr kalten Neutronen zur Implementierung eines Lloyd-Interferometers* 2015

— **David Bricher**

Project Thesis, *Velocity spectrum analysis of Very-cold neutrons at a Lloyd-Mirror Interferometer experiment*, 2015

— **Alexander Leopold**

Project Thesis, *Homogeneity considerations for the production of spatially resolving neutron detectors for the qBounce experiment on the μm -scale via a Physical Vapor Deposition unit*, 2014

— **Markus Spannring**

Bachelor Thesis, *Untersuchung des Überschlagverhaltens zwischen zwei planparallelen Platten bei bekanntem Abstand und in Abhängigkeit vom Druck*, 2013

— **Markus Spannring**

Project Thesis, *Kalibrierung der Logicbox*, 2013

— **Michael Iro**

Bachelor Thesis, *Construction of an apparatus for measuring strong electric fields at small distances and low pressure for the qBounce-Experiment*, 2013

— **Lukas Schrangl**

Project Thesis, *Systematische Untersuchung hoher elektrischer Felder zwischen Neutronenspiegeln für das qBounce-Experiment*, 2011

— **Jakob Micko**

Project Thesis, *Electric field studies of a square electrode configuration for qBounce*, 2018

List of Tables

3.1. Neutrons Characteristic Properties.	17
3.2. Thermal Neutron Scale.	19
3.3. Vertical Neutron Guide Characteristics.	22
3.4. PF2 Dimension Table.	24
5.1. Parameter for Optical Lloyd's Mirror.	55
5.2. Reflectivity of a Detector.	57
5.3. Time-Dependent Contribution to g	66
5.4. Sensitivity of Lloyd's Mirror to Gravitational Effects.	67
5.5. Phase Shift Systematic Effects Summary	77
5.6. Phase Shift Hypothetical Effects Summary	78
6.1. Lloyd's Mirror Setup Characteristics Comparison.	82
6.2. Maximal Bin Intensity.	95
6.3. Lloyd's Mirror Statistical Parameter Comparison.	96
6.4. Simulation Parameters.	99
6.5. Result of a Fit on the Simulation.	102
7.1. Very-Cold Neutron Beam Availability	111
7.2. Collimation Stage Results and Parameters.	121
7.3. Very-Cold Neutron Wavelength and Bandwidth Comparison.	123
7.4. Parameter for Brilliance at the PF2.	125
7.5. Parameter for Intensity Estimation at S1.	126
7.6. Measured Very-Cold Neutron Brilliance Comparison.	126
7.7. Entrance Slit Transmission Characteristics.	129
7.8. Relevant Monitored Environmental Quantities.	132
7.9. Background Measurement IDL001 Parameters.	133
8.1. CR39-based Detector Layer Functions.	138

LIST OF TABLES

8.2. Kinetic Energy of Daughter Particles for $n + B \rightarrow Li + \alpha$	139
8.3. Maximal Tracks per Microscope Image for Specific Cluster Abundance. . .	147
8.4. Image Characteristics for Optical Track Detection.	149
8.5. Classifier Training Set.	155
8.6. Classification Result.	157
A.1. Neutron Energy Availability	186
A.2. Neutron Energy Availability — Length Scale	186
A.3. Standard Calculation Parameter Table	188
A.4. Natural Constant Table	189
A.5. Compound & Element Table	189
A.6. Optical Potentials	190
A.7. Parameter Table on the Simulation.	191

List of Figures

2.1. Standard Model of Particle Physics Particles.	8
2.2. Energy Budget of the Universe.	10
3.1. Neutron Energies and Thermal Characterization.	18
3.2. Vertical Displacement due to Gravitation.	20
3.3. Cold Source Schematic at Institut Laue-Langevin.	21
3.4. PF2 UCN-Turbine, VCN-Cabin and VCN-Beam.	23
3.5. Spatial Dependence of the Wavelength Spectra at the PF2.	25
4.1. Double-slit Depiction.	29
4.2. Lloyd's Mirror Schematic.	30
5.1. Surface Interaction Geometry.	33
5.2. Relevant Geometric Quantities for Diffraction.	36
5.3. Single-slit Diffraction Pattern.	39
5.4. Straight Edge Geometry.	40
5.5. Straight Edge as Measured by Gaehler et al. 1981.	41
5.6. Green's Function Principle.	42
5.7. Plane Wave Lloyd's Mirror Representation.	44
5.8. Idealized Lloyd's Mirror Fringes.	46
5.9. Relative Higher Order Contributions.	47
5.10. Geometry for Lloyd's Mirror to Calculate Green's Function.	48
5.11. Boundary for Lloyd's Mirror Geometry.	49
5.12. Lloyd's Mirror Wave Function Derived Using Green's Identity.	50
5.13. Lloyd's Mirror Fringes.	51
5.14. Lloyd's Mirror Carpet for Finite Mirror.	53
5.15. Lloyd's Mirror Cut for Finite Mirror.	54
5.16. Difference Between Time-Dependent and Static Pattern.	54
5.17. Optical Lloyd's Mirror Compared to Theoretical Calculation.	56

LIST OF FIGURES

5.18. Reflectivity of Detector Coating.	58
5.19. Lloyd’s mirror Compared to a Straight Edge.	58
5.20. Scheme Two-path Interferometer.	60
5.21. Calculation of Sensitivity for a Phase Shift.	61
5.22. Derivative of the Pattern $P(y)$	62
5.23. Phase Sensitivity in Lloyd’s Mirror.	63
5.24. Mirror Reflection Phase Shift.	64
5.25. Phase Shifts Induced by Gravity.	65
5.26. Relative Phase shifts due to a Chameleon Field.	71
5.27. Statistical Sensitivity to the Chameleon Field.	72
5.28. Phase Shift due to an Axion Coupling.	73
5.29. Statistical Sensitivity to an Axion Coupling.	74
5.30. Axion Coupling Strength — Mass Limits.	75
6.1. Relevant Components and Quantities for Simulation.	79
6.2. Measurement Scheme.	80
6.3. Lloyd’s Mirror Period as Function of λ and L	81
6.4. Measurement Scheme Interferogram.	83
6.5. Convolved Probability Density.	84
6.6. Coherence Patch for Circular Aperture.	86
6.7. Coherent Region Plot.	87
6.8. Reflection Curve of a SiO ₂ -Mirror.	88
6.9. Spatial Beam Distribution.	90
6.10. Visibility Reduction for a Non-Monochromatic Beam.	92
6.11. Maxima Contained in Specific Visibility Region.	92
6.12. Statistic Characteristics of Two-Point Scheme.	93
6.13. Simulation Procedure.	97
6.14. Dependency of $\Psi_{\mathcal{L}}$ on the Spectrum Width.	98
6.15. Simulation of Lloyd’s Mirror.	100
6.16. Simulation of Lloyd’s Mirror with Propagation Region.	102
6.17. Misaligned Slit Geometry.	103
6.18. Visibility Drop for Misaligned Slit.	105
6.19. Rough Slit Geometry.	106
6.20. Visibility Drop for Rough Slit.	107
7.1. Experimental Schematic for a Lloyd’s Mirror Setup.	113

7.2. Implementation of the Beam-Shaping Section during Beam-Time *Test-2455*. 114

7.3. Spatial Distribution PF2 115

7.4. Spatial Distribution after M0. 117

7.5. Wavelength Distribution at the PF2 and Setup. 118

7.6. Angular Measurement Scheme. 119

7.7. Very-Cold Neutron Beam Scan. 120

7.8. Slits and Collimation. 121

7.9. Time of Flight Setup. 123

7.10. Setup for Intensity Extrapolation. 124

7.11. Proposed Interferometer Region. 128

7.12. Mirror Entrance Slit Setup. 130

7.13. Supporting Interferometer Monitor Systems. 131

8.1. CR39, ¹⁰B Detector Dimensions. 137

8.2. CR39-based Detector Scheme. 138

8.3. CR39-based Detector Hit by Reaction Product. 139

8.4. Example of an Exposed and Post Processed CR39. 140

8.5. CR39-based Detector Efficiency and Resolution. 142

8.6. Thin Film Coating Principle. 143

8.7. Coating Process Result 144

8.8. Average k -Constituent Cluster Number. 146

8.9. Average k -Constituent Cluster Number for $k \geq 1$ 147

8.10. Example CR39 Image 149

8.11. Single Image Sample Distribution 150

8.12. Image Normalization Value Distribution 151

8.13. Nuclear Track Candidate. 152

8.14. Manually Classified Nuclear Track Candidates. 154

8.15. Random Forest Scheme. 156

8.16. Classification Procedure. 158

8.17. Classification Procedure. 160

8.18. Classification Procedure Examples 1. ID0020. 162

8.19. Classification Procedure Examples 2. ID0067. 164

9.1. Proposed Changes to a Future Setup. 169

10.1. Simulation of Lloyd’s Mirror Concluding Remarks. 174

LIST OF FIGURES

A.1. Setup of the Optical Lloyd’s Mirror.	179
A.2. Fit Residuals for 7 Day Simulation.	180
A.3. Fit Residuals for 21 Day Simulation.	180
A.4. Stitched Scan for ID001.	181
A.5. CR39Analyse.m Track Detection Front-End.	182
A.6. CR39Analyse.m Threshold Definition.	183
A.7. CR39Analyse.m Track File IO.	183
A.8. CR39Analyse Track File Analysis.	184
A.9. CR39Analyse.m Machine Learning Parameter.	184
A.10.CR39Analyse.m Class Assignment.	185
A.11.CR39Analyse.m Training Classes Example.	185
A.12.Institut Laue-Langevin Brilliance.	187
A.13.Surface Integration for a Corner Geometry.	198
A.14.Lloyd’s Mirror Derivative.	204
A.15.Asymptotic Solution of Lloyd’s Mirror for $z \gg 1$ and $\delta \rightarrow 0$	205
A.16.Lloyd’s Mirror Probability Density for Non-Normal Incident.	206
A.17.Lloyd’s Mirror Probability Density for Non-Normal Incident at Negative Angles.	206
A.18.Huygen’s Principle applied to Lloyd’s Mirror.	207
A.19.Cut Through the Probability Density for a Finite Mirror.	208
A.20.Lloyd’s Mirror Phase Shift Calculation.	216
A.21.Lloyd’s Mirror Integration Contour.	218
A.22.Lloyd’s Mirror Integration Contour for a Magnetic Field.	225

Bibliography

- Adelberger, E. G., B. R. Heckel, S. Hoedl, C. D. Hoyle, D. J. Kapner and A. Upadhye (29th Mar. 2007). ‘Particle-Physics Implications of a Recent Test of the Gravitational Inverse-Square Law’. In: *Physical Review Letters* 98, pp. 131104–4 (see p. [13](#)).
- Afach, S., G. Ban, G. Bison, K. Bodek, M. Burghoff, M. Daum, M. Fertl, B. Franke, Z. D. Grujić, V. H elaine, M. Kasprzak, Y. Kermaidic, K. Kirch, P. Knowles, H. C. Koch, S. Komposch, A. Kozela, J. Krempel, B. Lauss, T. Lefort, Y. Lemi ere, A. Mtchedlishvili, O. Naviliat-Cuncic, F. M. Piegsa, Guillaume Pignol, P. N. Prashanth, G. Quemener, D. Rebreyend, D. Ries, S. Rocchia, P. Schmidt-Wellenburg, A. Schnabel, N. Severijns, J. Voigt, A. Weis, G. Wyszynski, J. Zejma, J. Zenner and G. Zsigmond (18th May 2015). ‘Constraining Interactions Mediated by Axion-like Particles with Ultracold Neutrons’. In: *Physics Letters B* 745, pp. 58–63 (see pp. [14](#), [74](#), [75](#), [170](#)).
- AG, Schott (7th Nov. 2016). *Optisches Glas 2016*. Annual Report, pp. 1–150 (see p. [189](#)).
- Allmendinger, F., M. Burghoff, W. Heil, S. Karpuk, W. Kilian, S. Knappe-Gr uneberg, W. M uller, U. Schmidt, A. Schnabel, F. Seifert, Yu Sobolev, L. Trahms and K. Tullney (21st Feb. 2013). ‘Searches for Lorentz Violation in 3He/129Xe Clock Comparison Experiments’. In: *Hyperfine Interactions* 215, pp. 15–23 (see p. [75](#)).
- Anderson, Carl D. (Mar. 1933). ‘The Positive Electron’. In: *Physical Review* 43, pp. 491–494 (see p. [12](#)).
- Aprile, E., F. Agostini, M. Alfonsi, K. Arisaka, F. Arneodo, M. Auger, C. Balan, P. Barrow, L. Baudis, B. Bauermeister, A. Behrens, P. Beltrame, K. Bokeloh, A. Brown, E. Brown, S. Bruenner, G. Bruno, R. Budnik, J. M. R. Cardoso, A. P. Colijn, H. Contreras, J. P. Cussonneau, M. P. Decowski, E. Duchovni, S. Fattori, A. D. Ferella, W. Fulgione, F. Gao, M. Garbini, C. Geis, L. W. Goetzke, C. Grignon, E. Gross, W. Hampel, R. Itay, F. Kaether, G. Kessler, A. Kish, H. Landsman, R. F. Lang, M. Le Calloch, D. Lellouch, C. Levy, S. Lindemann, M. Lindner, J. A. M. Lopes, K. Lung, A. Lyashenko, S. Macmullin, T. Marrod an Undagoitia, J. Masbou, F. V. Massoli, D. Mayani Paras, A. J. Melgarejo Fernandez, Y. Meng, M. Messina, B. Miguez, A. Molinario, M. Murra, J. Naganoma, K. Ni, U. Oberlack, S. E. A. Orrigo, E. Pantic,

BIBLIOGRAPHY

- R. Persiani, F. Piastra, J. Pienaar, G. Plante, N. Priel, S. Reichard, C. Reuter, A. Rizzo, S. Rosendahl, J. M. F. dos Santos, G. Sartorelli, S. Schindler, J. Schreiner, M. Schumann, L. Scotto Lavina, M. Selvi, P. Shagin, H. Simgen, A. Teymourian, D. Thers, A. Tiseni, G. Trincherro, O. Vitells, H. Wang, M. Weber, C. Weinheimer and Xenon100 Collaboration (Sept. 2014). ‘First Axion Results from the XENON100 Experiment’. In: *Physical Review D* 90, p. 062009 (see p. 14).
- Arfken, George B. and Hans J. Weber (22nd Oct. 2013). *Mathematical Methods for Physicists*. Academic Press. 1029 pp. (see pp. 42, 192).
- Baumann, J., R. Gähler, J. Kalus and W. Mampe (June 1988). ‘Experimental Limit for the Charge of the Free Neutron’. In: *Physical Review D* 37, pp. 3107–3112 (see p. 17).
- Berenji, B., J. Gaskins and M. Meyer (16th Feb. 2016). ‘Constraints on Axions and Axionlike Particles from Fermi Large Area Telescope Observations of Neutron Stars’. In: *Physical Review D* 93, pp. 015–13 (see p. 14).
- Bergmann, Ludwig and Clemens Schäfer (1992). *Lehrbuch Der Experimentalphysik III Optik*. Vol. v.3. Berlin: De Gruyter (see pp. 33, 36, 39).
- Berman, Paul R. (8th Jan. 1997). *Atom Interferometry*. Academic Press. 478 pp. (see p. 59).
- Bloch, Dominic (5th Jan. 2016). ‘Realisierung Und Analyse Eines Temperatursensor-Arrays Für Das Lloyd-Experiment’. Undergraduate. Vienna: Technical University Vienna. 1-60 (see p. 132).
- Born, Max and Emil Wolf (1970). *Principles of Optics*. 4th ed. London: Pergamon Press (see pp. 29, 30).
- Breiman, Leo (1st Oct. 2001). ‘Random Forests’. In: *Machine Learning* 45.1, pp. 5–32 (see pp. 153, 155).
- Bricher, David (8th Nov. 2015). ‘Velocity Spectrum Analysis of VCNs at a Lloyd-Mirror Interferometer Experiment’. Undergraduate. Vienna: Technical University Vienna. 1-49 (see pp. 114, 118, 123, 124, 188).
- Bruckner, H. (1999). *Goldmann-Lexikon Chemie: Grundlagen, Chemische Elemente, Organische Chemie, Grundstoffe Und Verfahren, Chemie Und Umwelt*. BLI, Bertelsmann Lexikographisches Institut (see p. 189).
- Brukner, Časlav and Anton Zeilinger (Nov. 1997). ‘Diffraction of Matter Waves in Space and in Time’. In: *Physical Review A* 56, pp. 3804–3824 (see pp. 42, 194, 195, 198).
- Bulatowicz, M., R. Griffith, M. Larsen, J. Mirijanian, C. B. Fu, E. Smith, William Snow, H. Yan and T. G. Walker (3rd Sept. 2013). ‘Laboratory Search for a Long-Range T-

- Odd, P-Odd Interaction from Axionlike Particles Using Dual-Species Nuclear Magnetic Resonance with Polarized Xe129 and Xe131 Gas'. In: *Physical Review Letters* 111, pp. 413–5 (see p. 75).
- Burrage, Clare, Edmund J. Copeland and E. A. Hinds (Mar. 2015). 'Probing Dark Energy with Atom Interferometry'. In: *Journal of Cosmology and Astroparticle Physics* 03, p. 042 (see p. 70).
- Cartan, Élie (1922). 'Sur Une Generalisation de La Notion de Courbure de Riemann et Les Espaces a Torsion'. In: *Comptes Rendus, Ac. Sc. Paris*, pp. 593–595 (see p. 13).
- Cassou, R. M. and E. V. Benton (Sept. 1978). 'Properties and Applications of CR-39 Polymeric Nuclear Track Detector'. In: *Nuclear Track Detection 2*, pp. 173–179 (see p. 138).
- Catena, Riccardo and Piero Ullio (1st Aug. 2010). 'A Novel Determination of the Local Dark Matter Density'. In: *Journal of Cosmology and Astroparticle Physics* 2010, pp. 004–004 (see p. 9).
- Chadwick, J. (1932). 'Possible Existence of a Neutron'. In: *Nature* (see p. 17).
- Clowe, D., M. Bradač and AH Gonzalez (2006). 'A Direct Empirical Proof of the Existence of Dark Matter'. In: *The Astrophysical Journal* (see p. 9).
- Cowley, J. M. (5th Dec. 1995). *Diffraction Physics*. Elsevier. 481 pp. (see pp. 31, 36, 65, 86).
- Cronenberg, Gunther (16th Nov. 2015). 'Frequency Measurements to Test Newton's Gravity Law within the qBounce Experiment'. Doctoral Thesis. Vienna: Technical University Vienna. 1-96 (see pp. 70, 72).
- De Broglie, Louis (1924). 'Recherches sur la théorie des quanta'. Doctoral Thesis. Migration - université en cours d'affectation. 127 pp. (see p. 30).
- DeBeer-Schmitt, Lisa, Lilin He and Ken Littrell (24th Jan. 2017). *Instrument CG-2*. White Paper, pp. 1–1 (see p. 186).
- Dianoux, A. J. (31st Aug. 2003). *Neutron Data Booklet*. Old City Publishing Science. 210 pp. (see pp. 18, 19, 34, 189, 190).
- Dolgov, A. D. (1st Dec. 1992). 'Non-GUT Baryogenesis'. In: *Physics Reports* 222.6. 00386, pp. 309–386 (see p. 4).
- Durstberger-Rennhofer, Katharina, Tobias Jenke and Hartmut Abele (3rd Aug. 2011). 'Probing the Neutron's Electric Neutrality with Ramsey Spectroscopy of Gravitational Quantum States of Ultracold Neutrons'. In: *Physical Review D* 84, pp. 036004–036005 (see p. 61).

BIBLIOGRAPHY

- Economou, E. N. (17th Apr. 2013). *Green's Functions in Quantum Physics*. Vol. 7. Berlin, Heidelberg: Springer Science & Business Media. 254 pp. (see pp. [194](#), [195](#)).
- Eder, K., M. Gruber, A. Zeilinger and R. Gähler (1989). 'The New Very-Cold-Neutron Optics Facility at ILL'. In: *Nuclear Instruments and Methods in Physics Research Section A: Accelerators, Spectrometers, Detectors and Associated Equipment* 284, pp. 171–175 (see pp. [18](#), [19](#), [80](#)).
- Einstein, A. (1st Jan. 1905). 'Über Einigen Die Erzeugung Und Verwandlung Des Lichtes Betreffenden Heuristischen Gesichtspunkt'. In: *Annalen der Physik* 322, pp. 132–148 (see p. [30](#)).
- (1916). 'Die Grundlage Der Allgemeinen Relativitätstheorie'. In: *Annalen der Physik* 354, pp. 769–822 (see pp. [3](#), [10](#)).
- Eskildsen, M. R., P. L. Gammel, E. D. Isaacs and C. Detlefs (1998). 'Compound Refractive Optics for the Imaging and Focusing of Low-Energy Neutrons'. In: *Nature* 391, pp. 563–566 (see p. [33](#)).
- Felber, J., R. Gähler, R. Golub and K. Prechtel (July 1998). 'Coherence Volumes and Neutron Scattering'. In: *Physica B: Condensed Matter* 252, pp. 34–43 (see pp. [85](#), [86](#)).
- Filter, Hanno (24th Sept. 2009). 'Neutronendetektor Auf CR-39 Basis'. Undergraduate. University of Heidelberg. 1–33 (see pp. [141–143](#)).
- Filter, Hanno, Mario Pitschmann and Hartmut Abele (2018). 'Solving Lloyd's Mirror Using Greens Functions'. Article (see p. [63](#)).
- Fixsen, D. J. (Dec. 2009). 'The Temperature of the Cosmic Microwave Background'. In: *The Astrophysical Journal* 707, pp. 916–920 (see p. [11](#)).
- Fleisher, R. L., P. B. Price and R. M. Walker (1975). 'Nuclear Tracks in Solids: Principles and Applications'. In: *Berkeley* (see p. [148](#)).
- Foot, R., H. Lew and R. R. Volkas (21st Sept. 1992). 'Electric Charge Quantization'. In: *arXiv.org* hep-ph (see p. [31](#)).
- Gähler, R., A. G. Klein and A. Zeilinger (Apr. 1981). 'Neutron Optical Tests of Nonlinear Wave Mechanics'. In: *Physical Review A* 23, pp. 1611–1617 (see pp. [40](#), [41](#)).
- Gähler, Roland and Anton Zeilinger (Apr. 1991). 'Wave-Optical Experiments with Very Cold Neutrons'. In: *American Journal of Physics* 59, pp. 316–324 (see p. [57](#)).
- Gea-Banacloche, J. (1999). 'A Quantum Bouncing Ball'. In: *American Journal of Physics* Volume 67, Issue 9, pp. 776–782 (see p. [161](#)).

- Gebhart, Valentin, Juliane Klatt and Stefan Yoshi Buhmann (1st Mar. 2016). ‘Casimir-Polder Interaction of Neutrons with Metal or Dielectric Surfaces’. In: *arXiv.org quant-ph* (see pp. [69](#), [70](#), [215](#)).
- Geltenbort, Peter (2013). *VCN-Beam Supplemental Information*. Email (see pp. [24](#), [116](#), [186](#)).
- Gibbs, R. L. (Jan. 1975). ‘The Quantum Bouncer’. In: *American Journal of Physics* 43, pp. 25–28 (see p. [161](#)).
- Golub, Robert, Steve K. Lamoureaux and David J. Richardson (1991). *Ultra-Cold Neutrons*. Bristol: Adam Hilger (see pp. [19](#), [33](#), [88](#), [190](#)).
- Grobov, A. V. and S. G. Rubin (25th Aug. 2015). ‘Large-Scale Regions of Antimatter’. In: *Physics of Atomic Nuclei* 78, pp. 617–619 (see p. [12](#)).
- Hakamata, T. (2006). *Photomultiplier Tubes-Basics and Applications: Hamamatsu Photonics KK (Electron Tube Division)*. Hamamatsu Photonics K.K. (see p. [191](#)).
- Hamilton, P., M. Jaffe, P. Haslinger, Q. Simmons, H. Müller and J. Khoury (Aug. 2015). ‘Atom-Interferometry Constraints on Dark Energy’. In: *Science* 349, pp. 849–851 (see pp. [70](#), [72](#), [170](#)).
- Harris, P. G., C. A. Baker, K. Green, P. Iaydjiev, S. Ivanov, D. J. R. May, J. M. Pendlebury, D. Shiers, K. F. Smith, M. van der Grinten and Peter Geltenbort (1st Feb. 1999). ‘New Experimental Limit on the Electric Dipole Moment of the Neutron’. In: *Physical Review Letters* 82, pp. 904–907 (see p. [17](#)).
- Heumesser, Matthias (22nd June 2016). ‘Kollimationssystem für ein Lloyd-Materiewellen-Interferometer’. Masters Thesis. Vienna: Technical University Vienna. 1-95 (see pp. [86](#), [89](#), [113](#), [114](#), [119–121](#), [126](#)).
- Hino, M., S. Tasaki, Y. Kawabata, T. Ebisawa, Peter Geltenbort, T. Brenner, J. S. Butterworth, R. Gähler, N. Achiwa and M. Utsuro (July 2003). ‘Development of a Very Cold Neutron Spin Interferometer at the ILL’. In: *Physica B: Condensed Matter* 335, pp. 230–233 (see p. [113](#)).
- Hino, Masahiro (2015). *VCN Technology*. Email (see p. [127](#)).
- Hinterbichler, Kurt and Justin Khoury (10th June 2010). ‘Screening Long-Range Forces through Local Symmetry Restoration’. In: *Physical Review Letters* 104, pp. 625–4 (see p. [170](#)).
- Hubble, Edwin (15th Mar. 1929). ‘A Relation between Distance and Radial Velocity among Extra-Galactic Nebulae’. In: *Proceedings of the National Academy of Sciences* 15.3, pp. 168–173. pmid: [16577160](#) (see p. [10](#)).

BIBLIOGRAPHY

- Ivanov, A. N. (17th Feb. 2016). *Lloyd's Mirror Interferometer as a Tool for Detection of Torsion*. Scientific Report. Vienna: Technical University Vienna, pp. 1–4 (see pp. [31](#), [75](#), [216](#), [218](#)).
- Ivanov, A. N., R. Höllwieser, Tobias Jenke, M. Wellenzohen and Hartmut Abele (16th May 2013). ‘Influence of the Chameleon Field Potential on Transition Frequencies of Gravitationally Bound Quantum States of Ultracold Neutrons’. In: *Physical Review D* 87, pp. 105013–17 (see p. [13](#)).
- Ivanov, A. N. and M. Wellenzohen (5th July 2016). ‘Einstein-Cartan Gravity with Torsion Field Serving as Origin for Cosmological Constant or Dark Energy Density’. In: *arXiv.org* gr-qc, p. 47 (see pp. [13](#), [14](#), [75](#)).
- Jaffe, Matt, Philipp Haslinger, Victoria Xu, Paul Hamilton, Amol Upadhye, Benjamin Elder, Justin Khoury and Holger Müller (3rd July 2017). ‘Testing Sub-Gravitational Forces on Atoms from a Miniature in-Vacuum Source Mass’. In: *Nature Physics* 98, pp. 21101–6 (see pp. [13](#), [70](#), [72](#)).
- Jenke, Tobias (16th Sept. 2011). ‘qBounce - Vom Quantum Bouncer Zur Gravitationsresonanzspektroskopie’. Vienna: Technical University Vienna. 1-101 (see p. [142](#)).
- Jenke, Tobias, Gunther Cronenberg, Hanno Filter, Peter Geltenbort, Martin Klein, Thorsten Lauer, Kevin Mitsch, Heiko Saul, Dominik Seiler, David Stadler, Martin Thahammer and Hartmut Abele (19th July 2013). ‘Ultracold Neutron Detectors Based on 10B Converters Used in the qBounce Experiments’. In: *Nuclear Inst. and Methods in Physics Research, A* 732, pp. 1–8 (see pp. [82](#), [137](#), [138](#), [141–143](#)).
- Joyce, Austin, Bhuvnesh Jain, Justin Khoury and Mark Trodden (30th June 2014). ‘Beyond the Cosmological Standard Model’. In: *arXiv.org* astro-ph.CO, pp. 1–98 (see p. [13](#)).
- Kappl, Patrick Michael (8th Feb. 2016). ‘Vorbereitung Einer Strahlzeit Für Ein Lloyd-Interferometer Mit Sehr Kalten Neutronen’. Undergraduate. Vienna: Technical University Vienna. 1-31 (see p. [131](#)).
- Khoury, Justin and Amanda Weltman (27th Feb. 2004). ‘Chameleon Cosmology’. In: *Physical Review D* 69, pp. 044026–044015 (see pp. [13](#), [70](#)).
- Klein, A. G. and S. A. Werner (1st Mar. 1983). ‘Neutron Optics’. In: *Reports on Progress in Physics* 46, pp. 259–335 (see p. [33](#)).
- Klein, Martin Oliver (26th July 2000). ‘Experimente Zur Quantenmechanik Mit Ultrakalten Neutronen Und Entwicklung Eines Neuen Detektors Zum Ortsaufgelösten Nachweis von Thermischen Neutronen Auf Großen Flächen’. Doctoral Thesis. Universität Heidelberg. 1-137 (see pp. [138](#), [141](#)).

- Knoll, Glenn F. (2010). *Radiation Detection and Measurement; 4th Ed.* 4th ed. New York, NY: Wiley (see p. 138).
- Kostelecký, V. Alan, Neil Russell and Jay D. Tasson (20th Mar. 2008). ‘Constraints on Torsion from Bounds on Lorentz Violation’. In: *Physical Review Letters* 100, p. 111102 (see p. 76).
- Krantz, Claude (2006). ‘Quantum States of Neutrons in the Gravitational Field’. Masters Thesis. Universität Heidelberg. 1-104 (see pp. 137, 142).
- Kumakhov, M. A. and V. A. Sharov (1992). ‘A Neutron Lens’. In: *Nature* 357, pp. 390–391 (see p. 33).
- Landau, Rubin H., Manuel José Páez and Cristian C. Bordeianu (2008). ‘A Survey of Computational Physics’. In: *A Survey of Computational Physics by Rubin H. Landau* (see p. 82).
- Lang, Christian B. and Norbert Pucker (7th June 2016). *Mathematische Methoden in der Physik*. Berlin, Heidelberg: Springer. 859 pp. (see pp. 97, 216).
- Langenbeck, Peter (1st Jan. 2014). *Interferometry for Precision Measurement*. SPIE-International Society for Optical Engineering. 243 pp. (see p. 31).
- Langhoff, P. W. (Aug. 1971). ‘Schrödinger Particle in a Gravitational Well’. In: *American Journal of Physics* 39, pp. 954–957 (see p. 161).
- Laue-Langevin, Institut (1986). *ILL YellowBook - 1986*. Institut Laue-Langevin, pp. 1–36 (see p. 186).
- (19th June 2008). *ILL Yellowbook - 2008*. Annual Report. Institut Laue-Langevin, pp. 1–69 (see pp. 18, 19, 21, 22, 24, 111, 112, 126, 186, 187).
- Lemmel, H., Ph Brax, A. N. Ivanov, Tobias Jenke, Guillaume Pignol, M. Pitschmann, T. Potocar, M. Wellenzohen, M. Zawisky and Hartmut Abele (Apr. 2015). ‘Neutron Interferometry Constrains Dark Energy Chameleon Fields’. In: *Physics Letters B* 743, pp. 310–314 (see pp. 70, 72).
- Lemmel, Hartmut (21st Dec. 2006). ‘Confinement Induced Neutron Phase’. Doctoral Thesis. Vienna: Technical University Vienna. 1-103 (see p. 52).
- Lloyd, Humphrey (1st Jan. 1831). ‘On a New Case of Interference of the Rays of Light’. In: *The Transactions of the Royal Irish Academy* 17, pp. 171–177 (see pp. 29, 30).
- Luschikov, V. I. and A. I. Frank (1978). ‘Quantum Effects Occurring When Ultracold Neutrons Are Stored on a Plane’. In: *JETP Lett.* (See p. 161).
- Majkrzak, C. F. (1984). ‘Interference Coatings for Neutrons’. In: *Applied Optics* 23, pp. 3524–3528 (see p. 122).

BIBLIOGRAPHY

- Mandel, L. and Emil Wolf (1995). *Optical Coherence and Quantum Optics*. Cambridge: Cambridge University Press (see p. 86).
- Manzin, G. (2011). *Bidim80 and Bidim26 for UCN*. Grenoble: Institut Laue - Langevin, pp. 1–3 (see pp. 24, 125, 188).
- Melnikov, Yuri A. and Max Y. Melnikov (2012). *Green's Functions: Construction and Applications*. Berlin: De Gruyter (see p. 198).
- Mohr, P. J., D. B. Newell and B. N. Taylor (2015). 'CODATA Recommended Values of the Fundamental Physical Constants: 2014'. In: *Journal of Physical and Chemical Reference Data* 45, p. 043102 (see p. 189).
- Morse, Philip McCord and Herman Feshbach (1st Jan. 1953). *Methods of Theoretical Physics*. Vol. 1. McGraw-Hill Science, Engineering & Mathematics. 997 pp. (see pp. 42, 43, 194–197).
- Nahrwold, Sophie Loise (14th Mar. 2005). 'Development of a Detector for Bound Quantum States of Neutrons in the Earths Gravitational Field'. Masters Thesis. Heidelberg: University Heidelberg. 1-82 (see pp. 137, 138, 141, 142, 148, 152).
- Nesvizhevsky, Valery V., H. Börner and Alexei M. Gagarski (2000). 'Search for Quantum States of the Neutron in a Gravitational Field: Gravitational Levels'. In: *Nuclear Instruments and Methods in Physics Research Section A: Accelerators, Spectrometers, Detectors and Associated Equipment* 440, pp. 754–759 (see pp. 137, 142).
- Oda, T., M. Hino, M. Kitaguchi, Hanno Filter, Peter Geltenbort and Y. Kawabata (July 2017). 'Towards a High-Resolution TOF-MIEZE Spectrometer with Very Cold Neutrons'. In: *Nuclear Instruments and Methods in Physics Research Section A: Accelerators, Spectrometers, Detectors and Associated Equipment* 860, pp. 35–41 (see pp. 23, 25).
- Patrignani, C. (2016). 'Review of Particle Physics'. In: *Chinese physics C* (see pp. 7–12, 14, 15, 17, 18, 189).
- Peccei, R. D. and Helen R. Quinn (June 1977). 'CP Conservation in the Presence of Pseudoparticles'. In: *Physical Review Letters* 38, pp. 1440–1443 (see p. 14).
- Penzias, A. A. and R. W. Wilson (July 1965). 'A Measurement of Excess Antenna Temperature at 4080 Mc/S.' In: *Astrophysical Journal* 142, pp. 419–421 (see p. 11).
- Peters, A., K. Y. Chung and S. Chu (Feb. 2001). 'High-Precision Gravity Measurements Using Atom Interferometry'. In: *Metrologia* 38, pp. 25–61 (see pp. 66, 67).
- Petit, G. and B. Luzum (2010). *IERS Technical Note No. 36*. IERS Conventions (see p. 68).

- Planck-Collaboration et al. (5th Feb. 2015). ‘Planck 2015 Results. XIII. Cosmological Parameters’. In: *arXiv.org astro-ph.CO*, A13 (see pp. [9](#), [11](#)).
- Pokotilovski, Yu N. (Nov. 2011). ‘Neutron Experiments to Search for New Spin-Dependent Interactions’. In: *Journal of Experimental and Theoretical Physics* 94, pp. 413–417 (see pp. [iii](#), [v](#), [4](#), [14](#), [31](#), [59](#), [73](#)).
- (12th May 2013a). ‘Potential of the Neutron Lloyd’s Mirror Interferometer for the Search for New Interactions’. In: *Journal of Experimental and Theoretical Physics* 116, pp. 609–619 (see pp. [31](#), [45](#), [46](#), [71](#), [72](#), [76](#), [78](#)).
- (26th Feb. 2013b). ‘Strongly Coupled Chameleon Fields: Possible Test with a Neutron Lloyd’s Mirror Interferometer’. In: *Physics Letters B* 719, pp. 341–345 (see pp. [iii](#), [v](#), [5](#), [31](#), [59](#), [64–66](#), [73](#), [170](#)).
- Poplawski, Nikodem J. (23rd June 2011). ‘Spacetime Torsion as a Possible Remedy to Major Problems in Gravity and Cosmology’. In: *Astronomical Review* 8, pp. 108–115 (see p. [14](#)).
- Powers, D. M. (2011). ‘Evaluation: From Precision, Recall and F-Measure to ROC, Informedness, Markedness and Correlation’. In: *Flinders University of South Australia* (see p. [159](#)).
- PPG-Industries (25th Apr. 2006). ‘CR-39 Product Bulletin’. In: pp. 1–5 (see p. [139](#)).
- Quintanilla, J. and S. Torquato (Nov. 1996). ‘Clustering Properties of D-Dimensional Overlapping Spheres’. In: *Physical Review E* 54, pp. 5331–5339 (see p. [147](#)).
- Rauch, H., Wolfgang Treimer and U. Bonse (Apr. 1974). ‘Test of a Single Crystal Neutron Interferometer’. In: *Physics Letters A* 47, pp. 369–371 (see p. [35](#)).
- Rauch, H., A Zeilinger, G. Badurek, A. Wilfing, W. Bauspiess and U. Bonse (20th Oct. 1975). ‘Verification of Coherent Spinor Rotation of Fermions’. In: *Physics Letters A* 54.6. 00382, pp. 425–427 (see pp. [68](#), [221](#)).
- Rauch, Helmut and Samuel A. Werner (2015). *Neutron Interferometry*. Oxford University Press, USA. 447 pp. (see pp. [33–36](#), [59](#), [60](#), [67](#), [76](#), [77](#), [221](#)).
- Read, J. I. (7th Apr. 2014). ‘The Local Dark Matter Density’. In: *arXiv.org astro-ph.GA*, p. 063101 (see p. [9](#)).
- Riess, Adam G., Alexei V. Filippenko, Peter Challis, Alejandro Clocchiatti, Alan Diercks, Peter M. Garnavich, Ron L. Gilliland, Craig J. Hogan, Saurabh Jha, Robert P. Kirshner, B. Leibundgut, M. M. Phillips, David Reiss, Brian P. Schmidt, Robert A. Schommer, R. Chris Smith, J. Spyromilio, Christopher Stubbs, Nicholas B. Suntzeff and John Tonry (1st Sept. 1998). ‘Observational Evidence from Supernovae for an

BIBLIOGRAPHY

- Accelerating Universe and a Cosmological Constant'. In: *The Astronomical Journal* 116, pp. 1009–1038 (see p. 10).
- Rueß, Frank J. (18th Oct. 2002). 'Quantum States in the Gravitational Field'. Masters Thesis. Heidelberg: Universität Heidelberg. 1-107 (see pp. 137, 142).
- Rutherford, Sir E. (1st July 1920). 'Bakerian Lecture: Nuclear Constitution of Atoms'. In: *Proc. R. Soc. Lond. A* 97.686, pp. 374–400 (see p. 17).
- Scheicher, Andreas (28th Jan. 2015). 'Transmission Optimierung Und ^3He Basierte Detektion von Sehr Kalten Neutronen Zur Implementierung Eines Lloyd-Interferometers'. Undergraduate. Vienna: Technical University Vienna. 1-33 (see pp. 124, 168).
- Schwinger, Julian Seymour, L. L. De Raad, K. A. Milton and W. Y. Tsai (1998). *Classical Electrodynamics*. Reading, MA: Perseus (see p. 193).
- Sears, V. F. (1982). 'Fundamental Aspects of Neutron Optics'. In: *Physics Reports* (see p. 33).
- Shull, C. G. (Mar. 1969). 'Single-Slit Diffraction of Neutrons'. In: *Physical Review* 179, pp. 752–754 (see pp. 33, 39).
- Stadler, David (4th Nov. 2009). 'Dynamik Ultrakalter Neutronen Im Gravitationsfeld Der Erde'. Masters Thesis. Heidelberg: University Heidelberg. 1-91 (see pp. 141, 142, 152).
- Steyerl, A. (Apr. 1975). 'A "Neutron Turbine" as an Efficient Source of Ultracold Neutrons'. In: *Nuclear Instruments and Methods* 125, pp. 461–469 (see p. 21).
- Steyerl, A., H. Nagel, F. X. Schreiber, K. A. Steinhauser, R. Gähler, W. Gläser, P. Ageron, J. M. Astruc, W. Drexel, G. Gervais and W. Mampe (June 1986). 'A New Source of Cold and Ultracold Neutrons'. In: *Physics Letters A* 116, pp. 347–352 (see pp. 112, 116).
- Thalhammer, Martin (2018). 'T.b.A'. Doctoral Thesis. Vienna: Technical University Vienna (see pp. 99, 148, 149, 161, 162).
- Werner, S. A. (1994). 'Gravitational, Rotational and Topological Quantum Phase Shifts in Neutron Interferometry'. In: *Classical and Quantum Gravity* 11, A207–A226 (see pp. 59, 65, 214).
- Westphal, Alexander (2nd June 2001). 'Quantum Mechanics and Gravitation'. Masters Thesis. Heidelberg: Universität Heidelberg. 1-147 (see p. 142).
- Wikipedia (2017). *Young's Interference Experiment* (see p. 29).
- Wolfram Research, Inc (2017). *Mathematica*. Champaign, Illinois (see pp. 101, 153, 155, 193).

- Young, Thomas (1807). *A Course of Lectures on Natural Philosophy and the Mechanical Arts. By Thomas Young*. London: Printed for J. Johnson (see p. 29).
- Zeilinger, Anton, Roland Gähler, C. G. Shull, Wolfgang Treimer and Walter Mampe (Oct. 1988). ‘Single- and Double-Slit Diffraction of Neutrons’. In: *Reviews of Modern Physics* 60, pp. 1067–1073 (see pp. 33, 39, 82, 112, 123, 126, 187).
- Ziegler, James (2013). *SRIM - The Stopping and Range of Ions in Matter* (see p. 139).

Acknowledgement

I like to acknowledge that this work would be impossible without support, contributions, and challenges from many sides.

Carina. Thank you for being there with me, for enduring the time I secludedly wrote this thesis and for your loving support!

Eva, Dietmar, and Leon. Thank you for supporting me thorough-out my life, shaping my thoughts and character by challenging discussions.

I like to thank **Hartmut Abele** to accepting me into his group and entrusting me with the responsibilities of this project. I like to thank **Eberhard Widmann** and **Mike Snow** for agreeing to assess the scientific value my thesis. I like to thank **Mario Pitschmann**, **Matthias Heumesser**, **Peter Geltenbort**, and **Tatsuro Oda** for the long, constructive, and pleasant collaboration on this project. I like to thank **Bella Wagner** for helping me with the complex topic of correct english gramma and spelling.

I like to thank my colleagues that graciously offered feedback to my thesis, the many students and colleagues with which I were allowed to work together and collaborate on this project, and colleagues and friends without which I would not haven been able to complete my PhD with a more or less sane mind.

I like to thank my colleagues from the Atominstitut, especially from the ATI workshops and the ATI secretary's office, from the Institut Laue-Langevin, from the Kyoto University, from the Japan Proton Accelerator Research Complex, from the University of Vienna, from the Technical University Munich, from Adelphi Technology Inc., and from the Doktoratskolleg Particles and Interactions.

Thank You!

© Dipl.-Phys. Hanno Filter, Wien 2018
E-Mail: hfilter@odeandiewelt.eu

TU Wien - Atominstitut
Stadionallee 2, 1020 Wien, Austria

Cover-Design: Florian Clewe, Rotterdam

I gratefully acknowledge support from the Technical University Vienna, the Doktoratskolleg Particles and Interactions, and the Institut Laue-Langevin.

The registered version of this thesis can be found at <http://katalog.ub.tuwien.ac.at/AC15102743> and the original version directly at the Technical University of Vienna Library.

fdk Π



TECHNISCHE
UNIVERSITÄT
WIEN



Kurzfassung

Lloyd's Spiegel wie er von Humphrey Lloyd 1831 beschrieben wurde ist ein vielseitiges optisches Instrument. Heutzutage findet es vor allem in den Gebieten der Unterwasserakustik und der optischen Oberflächenanalyse Verwendung. In dieser Arbeit wird die Machbarkeit einer Umsetzung von Lloyd's Spiegel mit sehr kalten Neutronen untersucht.

Aufgrund offener Fragen wie z.B. der scheinbaren Inkompatibilität von Allgemeiner Relativitätstheorie und Quantenmechanik, dem Phänomen der Dunklen Materie und der Dunklen Energie, und der Antimaterie-Materie Asymmetrie, werden neuartige Experimente benötigt, die Einblick geben in bisher nicht untersuchte Parameterbereiche. Eine Umsetzung von Lloyd's Spiegel mit sehr kalten Neutronen könnte einen solchen Einblick eröffnen, wie in Pokotilovski (2011) und in Pokotilovski (2013) vorgeschlagen.

In dieser Arbeit wird das quantenmechanische Verhalten von Neutronen untersucht, die eine Region mit einem vertikal ausgerichteten Spiegel durchqueren, um Bedingungen einer experimentellen Umsetzung abzuleiten. Darauf aufbauend wird eine Simulation des erwarteten Interferogram vorgestellt, um die benötigte Messzeit abzuschätzen. In Übereinstimmung mit den theoretischen Überlegungen wird ein Neutronenoptik Aufbau, wie er am Institut Laue-Langevin umgesetzt wurde und welcher den Neutronenstrahl für das Interferometer aufbereitet, vorgestellt. Abschließend werden Entwicklungen einer orts aufgelösten Detektion von Neutronen mithilfe von Bor-beschichteten CR39 Plättchen präsentiert, wie sie für dieses Experiment benötigt werden.

Abstract

The Lloyd's mirror as described by Humphrey Lloyd in 1831 is a simple but powerful instrument in optical studies. Today's foremost applications are the optical inspection of flat surfaces and as a tool in underwater acoustics. This thesis discusses and investigates the feasibility of an implementation of Lloyd's mirror with very-cold neutrons.

Due to current open questions in physics as for example the apparent incompatibility of general relativity and quantum mechanics, the phenomenon of dark energy and dark matter, and matter antimatter asymmetry, novel experimental insights into yet unexplored parameter spaces are needed. Lloyd's mirror realized with matter wave especially very-cold neutrons could offer such new insights as proposed in Pokotilovski (2011) and in Pokotilovski (2013).

In this thesis the quantum mechanical behavior of neutrons that transverse a region in front of a mirror is studied theoretically to infer the requirements of an experimental realization. It is concluded with a simulation of the expected interferogram to estimate the required measurement time. In accordance with the theoretical studies, the results of an experimental realization of the required beam preparation section at the very-cold neutron beam at the PF2 at the Institut Laue-Langevin are presented. Finally, a spatial detection mechanism using boron-based CR39 imaging plates adapted to the needs of this experiment is demonstrated.

